UCL
Université catholique de Louvain

Université catholique de Louvain
Ecole Polytechnique de Louvain
Institute of Mechanics, Materials and Civil Engineering (iMMC)

Time dependent plasticity and strain localization in nanocrystalline metallic thin films

Guerric Lemoine

Thesis committee

Prof. Laurent Delannay, Université catholique de Louvain, Belgium (Supervisor)
Prof. Thomas Pardoen, Université catholique de Louvain, Belgium (Supervisor)
Prof. Jean-Pierre Raskin, Université catholique de Louvain, Belgium
Prof. Marc Geers, Technische Universiteit Eindhoven, The Netherlands
Prof. Javier Segurado, Universidad Politécnica de Madrid, Spain
Prof. Thierry Massart, Université Libre de Bruxelles, Belgium
Prof. Hervé Jeanmart, Université catholique de Louvain, Belgium (President)

Louvain-la-Neuve, April 2018.

Acknowledgements

Cette section marque la fin d'une belle aventure qui n'aurait pu être possible sans le soutien inconditionnel et enthousiaste de mes deux promoteurs, Laurent et Thomas, deux rois de l'optimisme et de la sérénité. J'ai appris énormément à vos côtés. Je vous remercie pour vos conseils, pour toutes vos idées, votre bienveillance et la passion que vous transmettez au quotidien. Un merci particulier à Laurent pour la quantité exceptionnelle de temps que tu m'as accordée, pour ton aide pour comprendre les subtilités de fortran et pour toutes ces suggestions d'amélioration que ton petit côté perfectionniste m'a suggérées. Merci également de m'avoir proposé ce poste d'assistant qui m'a permis de découvrir une autre facette de moi-même.

I gratefully thank Professor Marc Geers, Professor Javier Segurado, Professor Thierry Massart and Professor Jean-Pierre Raskin who have kindly accepted to review my thesis as well as for their questions and feedback, which have helped me greatly in improving the manuscript.

J'ai eu la chance d'évoluer au sein de deux pôles de recherche: IMAP et MEMA, ce qui signifie deux fois plus de collègues, deux fois plus de rires, deux fois plus de tartes, deux fois plus de teambuildings, deux fois plus de drinks et de barbecues. Merci à tous d'avoir égayé mes journées. Merci à tous mes collègues de bureau pour leur bonne humeur et leur soutien: Bruno, Sébastien, Christophe, Xavier, Arnaud, Thomas T., Romain et Marie-Stéphane. Spéciales dédicaces à Arnaud, mon incroyable encadrant de mémoire, à Romain pour toutes les pauses sucrées et à Marie-Stéphane pour tous les résultats de sa thèse et nos discussions biberon! Merci à Marieme pour toutes nos discussions et notre soutien mutuel lors de la rédaction, on se retrouve bientôt chez e-Xstream!

Je remercie chaleureusement Maxime qui a partagé avec tant de générosité ses connaissances en modélisation. Tu m'as guidé dans mes premières aventures avec ABAQUS, GMSH, Python ou encore Linux, me permettant de développer l'expertise nécessaire pour affronter tous les défis de modélisation de ma thèse. Du côté expérimental, rien n'aurait été possible sans la guidance de Mickey, le didactique "Artisan" des micromachines, le maître incontesté de la bonne humeur, de la patience et du pragmatisme en cleanrooms. Merci également pour toutes nos discussions techniques ou plus personnelles! Merci aussi à Romain et Adeline pour tous les dépôts AJA.

Merci à ma famille et à tous les amis qui m'ont manifesté leur soutien pendant ces longues soirées de rédaction.

Je ne peux trouver les mots pour exprimer ma gratitude envers Julie, la femme de ma vie. Tu m'as soutenu du début à la fin même si je t'avais dit "non, je ferai jamais une thèse!". Tu as su rivaliser d'ingéniosité pour me remotiver quand j'étais dans le(s) creux de la vague. Tu as réussi à garder le

sourire malgré ces longs week-ends et ces tardives nuits de rédaction pendant la grossesse. Du fond du coeur, merci! Merci Arthur d'avoir décidé de pointer le bout de ton nez! Tu as été la motivation sans laquelle je n'aurai sûrement pas clôturé si rapidement!

Guerric Lemoine

Contents

CHAPTER 1

Introduction

Novel designs of devices requiring nanocrystalline materials in the form of thin films are constantly proposed in order to accompany the constant race towards technological miniaturization. Thin films are here material samples with a reduced thickness from a single atomic layer to a few microns. In spite of an incomplete understanding of the mechanisms governing their deformation, thin films are nowadays present everywhere such as in micro- electromechanical systems (MEMS), nano- electromechanical systems (NEMS), solar cells and protective or functional coatings. Mechanical integrity of the films is crucial to ensure the reliability of the devices under interest. Compared to their bulk counterparts, thin films exhibit a higher yield strength but generally suffer of a lack of ductility. Owing to the very fine microstructure, thin films involve also moderate to high strain rate sensitivity, which can lead to creep manifestations which impact on various applications.

In order to uncover the mechanisms that give rise to the unique properties of nanocrystalline thin films and to their propensity to creep, the scientific community has proposed over the last decade a large variety of nanomechanical testing methods. One of these methods, developed at UCLouvain in the years 2005-2006, was extensively used to study the tensile and creep/relaxation response of thin metallic films. The underlying idea of this nanomechanical lab-on-chip technique is to use internal stresses, created during the deposition of a silicon nitride beam in order to load a specimen after etching of the underneath sacrificial layer. The main advantage of this technique is that hundreds of creep/relaxation tests are simultaneously carried out without monopolizing any external actuating/loading equipment and without using any time consuming calibration procedures. This internal stress actuated testing method

allows also the determination of activation volume during relaxation, giving a signature of the dominant relaxation mechanism.

Time dependent relaxation/creep mechanisms are amplified in nanocrystalline materials compared to traditional microcrystalline systems due to the dominance of thermally activated mechanisms and the difficulty to activate classical dislocations based plasticity (Meyers et al., 2006). The analysis of relaxation in thin films, especially when freestanding, does not only offer a system of fundamental interest due to the inherent simplicity of the microstructure (often one grain in thickness), sharp crystallographic textures, and the magnified effect of the free surfaces, but it also has important applications in membrane and coating technologies. Creep in freestanding films affects the operation of several MEMS devices such as RF-MEMS switches (Modlinski et al., 2004b). Also thin coatings involving large internal stresses could relax over long periods by creep.

Nickel (Ni) is the only material experimentally studied in this thesis (while other materials are investigated using a modelling approach). The first reason is the industrial interest for this material. Due to their enhanced properties (i.e. high hardness, corrosion resistant behaviour and wear resistance), nanocrystalline nickel films have been studied for their potential applications as catalysts and micromechanical switches or actuators. Additional motivation for the selection of a FCC metal has been provided by the fruitful characterization campaign on palladium thin films, carried out by Colla (2014) during her thesis. Pd was used as model material to study the mechanical behaviour of FCC nanocrystalline metals and we presumed that the gained experience would possibly help to understand the tensile and creep/relaxation behaviour of other FCC metals. The main experimental objective is to adapt the on-chip microtensile method to obtain a stable process for the testing of freestanding Ni films. Next to the selection of the proper fabrication process, several practical questions arise when dealing with lab-on-chip experiment: what is the influence of the design on the extracted stress and strain? Does the etching step affect the measurement? How can we explain the experimental scatter generally observed at very small strains (Vayrette et al., 2015)? It is also important to establish the impact of viscoplasticity on the experimental data. To answer all these questions, the lab-on-chip technique has been for the first time since its patenting, modelled through finite elements simulations.

The present thesis constitutes mainly a contribution to earlier work at UCLouvain. During the last decade, the **lab-on-chip** technique has been successfully applied to Al thin films (Coulombier, 2012), Pd thin films (Colla, 2014) and Cu thin films (Vayrette et al., 2015; Lapouge et al., 2017). These works constitute a source of scientific questioning. Some of these experimental results are not yet fully understood while some original observations have to be assessed by modelling approaches. Indeed, the full potential of these films can only be achieved if their mechanical behaviour is completely understood.

Coupling experimental observations and modelling is thus of prime interest. For instance, Colla et al. (2015) have reported surprisingly high dislocation activity in Pd thin films during loading and subsequent creep/relaxation which contrasts with other experimental and modelling studies, suggesting different deformation mechanisms or more discrete slip events. Modelling of such small scale systems is challenging as the validity limit of continuum approaches is nearly reached. The next major question to be examined in this thesis is if is it possible to reproduce the experimental mechanical behaviour of the Pd nanocrystalline films, relying on a continuum model and assuming only dislocation-based mechanisms as suggested from the TEM characterization. As the strain rate sensitivity is magnified at nanoscale, it is key to identify physically based constitutive equations able to capture the influence of dislocations on viscoplasticity. These constitutive laws are incorporated in the crystal plasticity code previously available at UCLouvain, in order to reach this objective.

The control of the **ductility** of thin metallic films is a major issue in a variety of technologies involving flexible electronics, MEMS and deformable coatings. Lab-on-chip experiments on Cu thin films have revealed a dependence of the ductility on the strain rate, leading to an improved ductility in creep/relaxation than in uniaxial tensile loading. Ductility is considered in this thesis, as the capacity of a material to withstand plastic localization. The last questions to be addressed in this thesis are: how can we model plastic localization in metallic thin films? As dislocation and/or grain-boundaries based deformation mechanisms can be activated when the film thickness decreases, what is the proper way to tackle the complexity of the grain size and thickness effect? Can we isolate the key features that can lead to enhanced ductility?

After the introduction, this thesis is organized as follows. The second chapter is dedicated to the elements of the state of the art necessary to understand the developments made in this thesis and to justify the interest of the questions that are asked. Therein, an overview of the deformation mechanisms in nanograined metals is presented as well as the influence of grain size on various mechanical properties such as yield strength, strain hardening and ductility. The fundamental concept of thermally activated deformation mechanisms is then presented and the modelling approaches of plasticity in nanocrystalline materials and of ductility are successively reviewed. After summarizing the mechanical testing methods dedicated to thin films, the third chapter focusses on the internal stress actuated microtensile testing method developed at UCLouvain. The concept of the technique is exposed and we attempt to adapt the fabrication process to Ni thin films. The basic data reduction scheme is then assessed using finite element modelling and some possible issues are emphasized. In the two last chapters, great efforts are devoted to the modelling of experimental results gathered with the on-chip technique. In the fourth chapter, a dislocation based crystal plasticity model is developed to study the

tensile and relaxation behaviour of Pd thin films. The model predictions are discussed and compared with the experimental results. A parametric study is then performed. Finally, an imperfection based model is presented in the fifth chapter in order to study plastic localization in thin films. The model is validated towards literature examples and the impact of several features on the ductility is investigated.

The succession of chapters does not reflect the chronology of the present thesis. Originally, the envisaged approach was mainly experimental, combining lab-on-chip experiments with extensive TEM observations. This methodology was rapidly dismissed due to long-term unavailability of deposition and lithography devices in cleanroom facilities. While continuing to attempt experimental developments, I became increasingly interested in numerical and theoretical models. My efforts were then focussed on the modelling of experimental results already available at UCLouvain. The dislocation based crystal plasticity model was developed to analyse the mechanical behaviour of Pd thin films, gathered experimentally by Colla (2014). At this point, the adaptation of the lab-on-chip technique was still unsuccessful and the next stage of my thesis became the analysis of strain localization in metallic thin films. Relying on an imperfection model, this study was devoted to analyse the influence of key material parameters on the ductility with decreasing film thickness and a phenomenological approach was adopted, discarding the use of advanced material models such as the one presented in chapter 4. Despite all the failed attempts, the lab-on-chip technique was finally not abandoned and efforts were expended to the FE simulations of the experimental technique for driving the development of a new stress and strain extraction procedure. Such structural analysis requires only the macroscopic mechanical response of materials, without any insights of the meso- or micro-scale behaviour.

The research carried out in the framework of this doctoral thesis has led to the following scientific output:

Publications in international journals

1. **G. Lemoine**, M-S. Colla, H. Idrissi, T. Pardoen, L. Delannay, *Dislocation and back stress dominated viscoplasticity in freestanding sub-micron Pd films.* Acta Materialia, Vol. 111, p. 10-21 (2016);

2. **G. Lemoine**, T. Paroden, L. Delannay, *Localized necking in nanocrystalline metallic thin films under static and relaxation conditions*, to be submitted.

International conference contributions

1. **G. Lemoine**, T. Paroden, L. Delannay, *Localized necking in nanocrystalline metallic thin films under static and relaxation conditions*, 27th International Workshop on Computational Mechanics of Materials, Leuven (2017);

2. **G. Lemoine**, M-S. Colla, H. Idrissi, T. Pardoen, L. Delannay, *Dislocation and back stress dominated viscoplasticity in free-standing sub-micron Pd films.* ICACM 2016 Symposium, Compiègne (2016);

3. **G. Lemoine**, M-S. Colla, H. Idrissi, T. Pardoen, L. Delannay, *Dislocation and back stress dominated viscoplasticity in freestanding sub-micron Pd films.* 15th European Mechanics of Materials Conference, Brussels (2016);

4. **G. Lemoine**, M-S. Colla, H. Idrissi, T. Pardoen, L. Delannay, *Crystal Plasticity based modelling of Viscoplasticity in Nanocrystalline FCC Thin Films.* Euromech Colloquium 570, Multiscale analysis of the impact of microstructure on plasticity and fracture in interface-dominated materials, Houffalize (2015);

5. **G. Lemoine**, M-S. Colla, B. Amin-Ahmadi, H. Idrissi, N. Schryvers, J-P Raskin, T. Pardoen, L. Delannay, *Study of creep/relaxation in nanocrystalline FCC thin films through internal-stress-actuated microtensile testing method.* 13th International Conference on Creep and Fracture of Engineering Materials and Structure, Toulouse (2015);

6. L. Delannay, H. Tummala, **G. Lemoine**, T. Pardoen, M. Fivel, *Influence of Grain Shape on Dislocation Slip Activity Inside Free-Standing Thin Films.* 4th International Conference on Material Modelling, Berkeley (2015);

7. **G. Lemoine**, M-S. Colla, J-P Raskin, T. Pardoen, L. Delannay, *Crystal plasticity based modelling of strain hardening and creep in nanocrystalline FCC thin films.* 4th International Symposium on Computational Mechanics of Polycrystals, Düsseldorf (2014);

8. **G. Lemoine**, M-S. Colla, H. Idrissi, J-P.Raskin, T. Pardoen, L. Delannay, *Crystal plasticity based modelling of strain hardening and creep in nanocrystalline freestanding Pd films.* 14th European Mechanics of Materials Conference, Gothenburg (2014);

9. **G. Lemoine**, M-S. Colla, J-P Raskin, T. Pardoen, L. Delannay, *Crystal plasticity based modelling of strain hardening and creep in nanocrystalline freestanding Pd films.* 35th Risø International Symposium on Materials Science. New Frontiers of Nanometals, Roskilde,(2014);

10. T. Pardoen, Thomas, M. Coulombier, M-S. Colla, **G. Lemoine**, R. Vayrette, M. Ghidelli, J-J Blandin, S. Gravier, L. Delannay, J-P. Raskin, *Size dependent plastic localization in thin nanocrystalline or amorphous metallic films.* MRS fall meeting, Boston (2014).

CHAPTER 2

State of the art - Background

Compared to their coarse-grained (CG) counterparts, nanocrystalline (NC) metals usually present excellent mechanical performances in terms of strength and fatigue resistance but they often suffer of a lack of ductility. Many nanocrystalline systems show also, owing to their very fine microstructure (grain sizes in the range of $\sim 10-20$ nm to $\sim 100-200$ nm), moderate to high strain rate sensitivity at room temperature. Thin films, especially when freestanding, offer a system of fundamental interest to study NC metals owing to nanograined columnar microstructures frequently involving a single grain along the film growth direction and sharp crystallographic textures. Furthermore, thin films are nowadays widely used in the microelectronic industry and for surface functionalization. Applications in MEMS devices and in membrane technology often involve very thin films. In order to ensure the reliability and the integrity of all possible applications, the study of the mechanical properties and the related deformation mechanisms is essential. Another motivation is to guide the processing of thin film materials with better performances.

In this chapter, the deformation mechanisms of NC metals are presented and differences or similarities with CG metals are underlined. As the grain size decreases, thermally activated mechanisms play an increasingly important role in setting the stress-strain response. The framework of thermal activation is detailed in the second section, followed by the effects of the deformation mechanisms on the yield strength and on the strain hardening capacity. The ductility in NC metals is then briefly reviewed. After these experimental observations, several modelling approaches of NC metals are given. Finally, predictive models for plastic instability are presented to investigate the influence of strain hardening, strain rate sensitivity and imperfection on the ductility.

2.1 Deformation mechanisms

Due to their small grain size, NC metals deform via different mechanisms from those observed in their CG counterparts. As the grain size decreases, GB-mediated deformation mechanisms appear and compete or cooperate with dislocations-mediated mechanisms. Figure 2.1 depicts several deformation mechanisms identified in NC metals by direct TEM observations or by atomistic studies. Dislocation-mediated mechanisms are represented in grains A-D and a-c while GB-mediated accommodation mechanisms are illustrated in grains 1-4. The significance of each deformation mechanism changes with decreasing grain size and initial defects density. Moreover, more than one deformation mechanism may be active at a determined grain size, resulting in complex interplay between deformation mechanisms and difficult experimental observations.

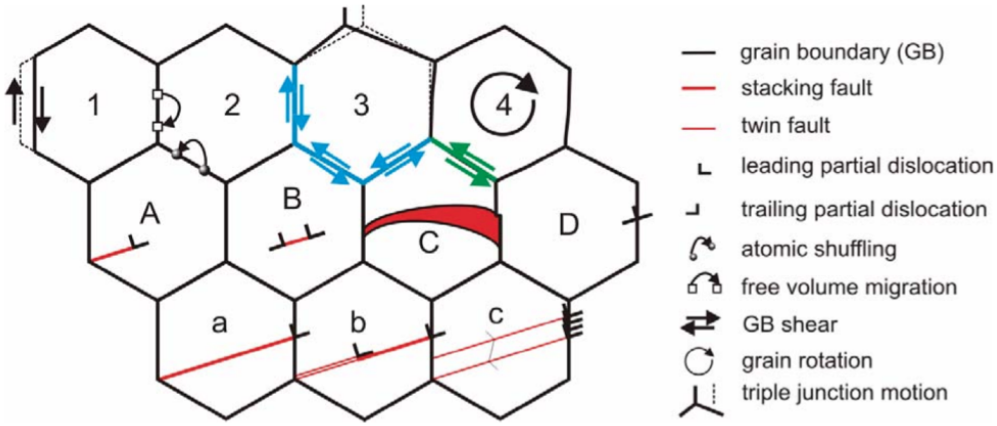

Fig. 2.1: Schematic representation of various possible deformation mechanisms in NC FCC metals. Courtesy of Christian Brandl.

Deformation mechanisms in NC metals have been extensively studied by TEM or HRTEM. However, dislocation behaviour observed by HRTEM may not be active in bulk materials. The TEM thinning process can alter the microstructure and generate large surface/volume ratio which may strongly influence the dislocation activity. Owing to mirror forces from free surfaces, a small grain adjacent to the free surface tends indeed to be free of dislocations. Of course, some types of GBs inside NC materials can stabilize dislocations. Furthermore, the observed dislocation-based mechanisms combined with the emergence of new GB-based mechanisms are in good agreement with the low to moderate strain hardening capacity and the magnified strain rate sensitivity of NC FCC metals.

In this section, the most important results from atomistic simulations and HRTEM investigations are highlighted. This section does not aim to be com-

prehensive. Further details about the deformation mechanisms in NC metals can be found in (Meyers et al., 2006; Zhu et al., 2012).

2.1.1 Dislocation-mediated mechanisms

In some respects, NC and CG metals accommodate mechanical deformation in a similar way, as emphasized by Yuan et al. (2015). Both experimental and atomistic studies have indicated that dislocation mediated plasticity prevails inside nanograins as for CG metals (Bitzek et al., 2008; Chen et al., 2012). However, in contrast with CG metals, dislocations, whether perfect or partial, originate predominantly from GBs and no more from conventional Franck-Read sources which cease to operate in the NC domain (Bitzek et al., 2008; Wang et al., 2010). Also, unlike CG materials, no pile-ups and very little dislocation debris are generally found after deformation in such materials (Dalla Torre et al., 2002; Kumar et al., 2003a). In-situ TEM (Hugo et al., 2003; Kumar et al., 2003a) as well as MD simulations (Van Swygenhoven et al., 2006) have shown that once emitted from GB, dislocations cross the entire grain and are absorbed and/or transmitted at the opposite GB. During the propagation of a dislocation, GB ledges or misfit regions may act as obstacles. GBs act thus as sources and sinks for dislocations.

Through statistical analysis of MD simulations, the group of Helena Van Swygenhoven discovered that triple junctions are highly probable sites for dislocation nucleation as they tend to be regions where both high stress concentrations and high density of structural defects take place (Van Swygenhoven et al., 1999; Van Swygenhoven, 2002; Derlet et al., 2003; Van Swygenhoven et al., 2006; Velasco et al., 2011). Their work also revealed that the shear stress required for the dislocation nucleation from triple junctions was lower than that for bowing out and propagation. Dislocation sources are thus already available at GB triple junctions well before the shear stress in a slip system reaches the CRSS for dislocation slip. This view of dislocation sources is also supported by the fact that GBs are generally in non equilibrium (Meyers et al., 2006). Such boundaries provide a large number of excess dislocations (compared to GB at equilibrium) and can even enable grain boundary sliding or grain rotation at room temperature (see section 2.1.2). Specifically, dislocations sources are dislocation segments that have emerged from triple junction and are pinned at each end of the adjacent GBs. Although depinning of these dislocation segments can be thermally assisted, experimental observations indicated that it is largely mechanically driven (Van Petegem et al., 2006). Note that pinning of dislocations can also be overcome by dislocation cross-slip. Taken together, these results suggest that dislocation mediated plasticity is determined by dislocation propagation instead of nucleation.

In the last decade, some High Resolution Transmission Electron Microscopy (HRTEM) investigations found that some systems exhibit nevertheless signifi-

cant dislocation accumulation in NC metals. Wu and colleagues (Wu and Ma, 2006; Wu et al., 2007) cold-rolled NC Ni at liquid nitrogen temperature and observed dislocations trapped in the grain interior as well as near GBs. More recently, surprisingly high dislocation activity and storage were observed at room temperature in NC Pd thin films (Colla et al., 2015) but also in NC Ni (Lee et al., 2013) and Pt (Wang et al., 2010).

Asaro, Krysl and Kad (AKK) developed a model describing the nucleation of partial and perfect dislocations from GBs in NC metals. The AKK model assumes the existence of a dislocation in a GB from which a partial or perfect segment which is emitted into the GI. They derived the nucleation stress by balancing the line energy of the segment with the work done by the two residual dislocation segments created along the GB, see Figure 2.2. The critical resolved shear stress is given by

$$\frac{\tau_{CRSS}}{\mu} = \kappa \frac{(d - \delta_{eq})}{d} + \frac{1}{3}\frac{b}{d} \tag{2.1}$$

where μ is the shear modulus, κ is the stacking fault energy normalized by μb, δ_{eq} is the equilibrium spacing of partial dislocations and b is the Burgers vector. A perfect dislocation can be emitted when

$$\frac{\tau_{CRSS}}{\mu} = \frac{b}{d}. \tag{2.2}$$

A transition from perfect to partial dislocation is therefore expected. Note also the inversely proportional relation between the stress and the grain size instead of the classical Hall-Petch relationship assuming that the stress of polycrystalline metals varies as a function of $d^{-1/2}$.

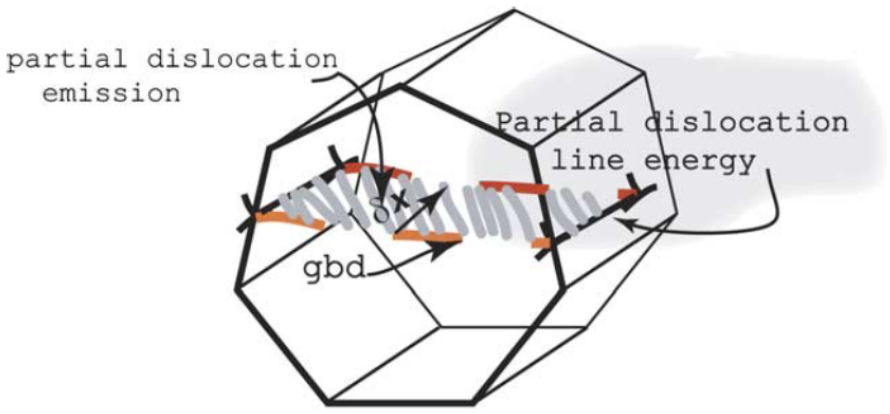

Fig. 2.2: Schematic illustration of the AKK model developed by Asaro et al. (2003) for the emission of stacking faults from a GB.

Wu and Ma (2006) and Lohmiller et al. (2014) have reported intensive perfect dislocations activity in NC metals while Liao et al. (2004) observed predominant partial dislocations activity in NC Al containing stacking fault bounded by partial dislocations. Whether partial or full dislocations are predominating, is driven by the ratio of stable and unstable stacking fault energy (SFE) (Swygenhoven et al., 2004). Note also that deformation twinning is also a possible deformation mechanism in NC metals. Yamakov et al. (2002) have shown that as a first partial dislocation is emitted, the formation of a deformation twin is possible if a second partial of the same type as the first one is emitted on a adjacent slip plane (see grain a-c in Figure 2.1). Deformation twinning was revealed by HRTEM for instance, in NC Al even if Al has a high SFE (Chen et al., 2003; Zhu et al., 2008).

The reduced number of dislocation sources and the presence of free surfaces in NC metals can lead to a state called "dislocation starvation" where dislocations annihilate at the free surface, preventing their storage inside the grain (Greer et al., 2005; Greer and De Hosson, 2011). New dislocations have to be continuously nucleated to sustain further deformation. These phenomenons have been recently addressed by El-Awady (2015) through discrete dislocation dynamics (DDD) simulations on single micro- and nano-crystals. His study pointed out that the product $d\rho_0$ is a key parameter with ρ_0 the initial dislocation density and d, the grain size. When $d\rho_0$ is very small, a pure dislocation starvation regime is expected with no dislocation accumulation. When $d\rho_0$ is moderate, the dislocations exhaust from their mutual interactions and leads to exhaustion hardening where the nucleation of new dislocation is mandatory to sustain flow (Benzerga, 2008). Classical forest hardening is recovered at large $d\rho_0$.

2.1.2 Grain boundaries-mediated mechanisms

As the grain size decreases, GB-mediated deformation mechanisms appear and progressively dominate the mechanical response. Different thermally activated GB-mediated mechanisms involving GB motion (see grain 1 in Figure 2.1), GB sliding (grain 2), triple junction migration (grain 3), GB rotation (grain 4), GB diffusion or grain growth, can then cooperate or compete with regular dislocation-based mechanisms.

Several mesoscopic models argued that GBs in NC metals are highly disordered or even amorphous regions (see section 2.5). Rather, the GBs in nanometals appear to have structures fundamentally similar to those encountered in CG metals. HRTEM observations on NC Ni (d = 30 nm) and on NC Pd (d = 5 nm) highlighted the maintained crystallinity in the GBs. Van Swygenhoven and coworkers observed also highly structured GB in MD simulations of NC Ni and Cu with grain size below 20 nm (Van Swygenhoven et al., 2000, 2001).

GB sliding is expected to become the dominant deformation mechanism below $d \sim 10$ nm (Schiotz and Jacobsen, 2003). Such GB activity is facilitated by atomic shuffling or stress-assisted free volume migration (see grain 2 in Figure 2.1). This mechanism requires other cooperative processes such as GB migration, triple junction motion, grain rotation or GB dislocations accommodation to ensure geometrical compatibility and release the stress built up in the vicinity of the grain (Zhu et al., 2007). Employing the concept of thermally-activated shear, Conrad and Narayan (2000) proposed that the macroscopic shear rate $\dot{\gamma}$ produced by independent, atomic shear events at the GBs is given by:

$$\dot{\gamma} = \frac{6\delta\nu_D}{d} \sinh\left(\frac{V\tau_{eff}}{k_B T}\right) \exp\left(\frac{-\Delta F}{k_B T}\right) \tag{2.3}$$

where $\delta \sim 3b$ is the GB width, ν_D is the Debye frequency, d, the grain size, $V = b^3$ is the activation volume for an atomic shear, k_B is the Boltzmann constant and ΔF is the Helmholtz free energy. However this approach and the one proposed by Kim et al. (2001) do not consider the deformation accommodation. This issue was addressed well before by Raj and Ashby (1971) in their work explaining the superplasticity of metals. Their model assumes that plastic accommodation between adjacent grains occurs only by diffusion, leading to the following Newtonian viscous flow like expression of the shear rate $\dot{\gamma}$:

$$\dot{\gamma} = \frac{64\delta\Omega D_b}{k_B T} \left(\frac{1}{d^3}\right) \tau \tag{2.4}$$

with D_b the boundary diffusion coefficient and Ω the atomic volume.

Even if GB sliding has been proposed by several groups to deform NC metals and to explain the inverse Hall-Petch effect, clear experimental evidences of this mechanism are difficult to obtain (Hugo et al., 2003; Ivanisenko et al., 2009). Only indirect arguments are provided such as the lack of texture formation (GB sliding is assumed to randomize lattice rotations) or the retention of equiaxed grains (Markmann et al., 2003; Sergueeva et al., 2007). Shan et al. (2004) have also observed grain rotation during in-situ TEM straining of NC Ni with $d \sim 10$ nm.

Another deformation mechanisms is GB motion which can contribute to grain growth during deformation. Strain driven GB motion for NC Ni at room temperature has been reported by Farkas et al. (2008) while GB migration coupled with shear strain was revealed in other MD simulations (Velasco et al., 2011). Experimentally, Rupert et al. (2009) observed stress-driven GB migration as well as grain growth in NC aluminium thin films. Recently, Wang et al. (2017) Rottmann and Hemker (2017) performed in situ TEM and observed stress induced GB migration in NC gold and NC Cu freestanding films respectively.

Grain growth or grain coarsening constitutes a last GB accommodation mechanism. Due to their non-equilibrium state, NC metals can be prone to grain coalescence through GB motion even at room temperature (Ames et al., 2008). The micro-indentation study of Zhang et al. (2005) on NC Cu at different temperature suggests that grain growth is a stress-driven rather than a diffusion driven mechanism in NC metals. Grain coarsening reduces strength upon deformation (Mompiou et al., 2013). In addition to GB migration, grain growth can also be induced by adjacent grains rotation arising from local GB sliding (see grain 4). This rotation induced coarsening produces high dislocation density regions at the previous locations of the GBs (Shan et al., 2004).

2.2 Thermally activated deformation mechanisms

As the grain size decreases, thermal activation may become significant. Conventional dislocation multiplication from Franck-Read sources becomes rather limited. As a consequence, stress level increases and other thermally activated deformation mechanisms start to operate, replacing the Franck-Read process based on a purely athermal mechanically driven propagation of dislocation loops.

Similarly to atoms, defects such as dislocations are in constant motion at non zero temperature, oscillating around their mean position, defined by a minimum energy state. Deformation can be seen as dislocations moving from a minimum energy state to another. Between these two minima, an energy barrier has to be overcome that represents the difficulty to depin a dislocation from a specific obstacle. Work is required to move the dislocation over the energy barrier, and this work is supplied by the applied stress. However, the energy of the dislocation is actually oscillating around the minimum due to the available thermal energy and so the effective height of the energy barrier to overcome must be compared with the available thermal energy. This viewpoint is the foundation of the theoretical framework of thermal activation. Largely inspired by the works of Kocks et al. (1975), Argon (2008), Ramesh (2009), this section provides a theoretical background on thermal activation of dislocation motion in the presence of discrete obstacles and on strain rate sensitivity analysis.

One way to evaluate the energy barrier is to consider a system deforming by small increments of shear strain $\Delta\gamma$. Figure 2.3 represents the glide resistance diagram as a function of the area swept by the dislocation. Each deformation increment is associated to the swept area, Δa, between two successive short range obstacles. Short range obstacles resistance is represented here by sinusoidal hills and valleys although this approach remains valid for any resistance

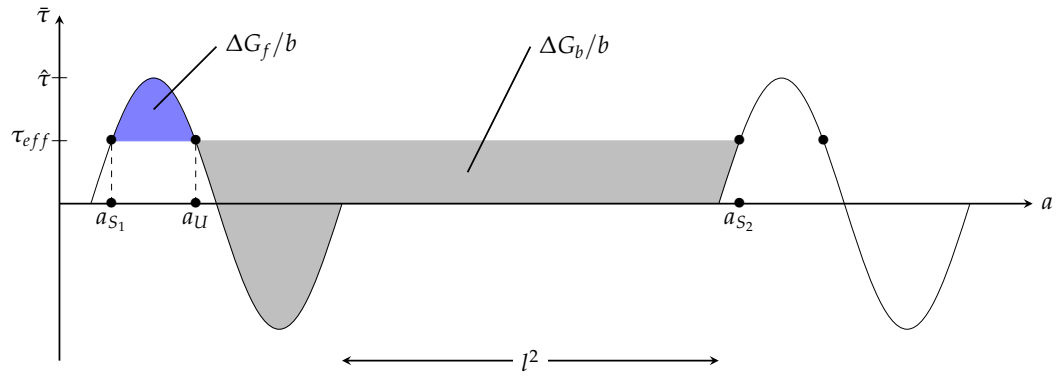

Fig. 2.3: Schematic sinus-like glide resistance $\bar{\tau}$ as a function of the area a swept during dislocation motion. S_1 and S_2 illustrate two successive stable equilibrium positions due to short range obstacles whereas U corresponds to an unstable equilibrium position. Equilibrium is achieved when the effective applied stress τ_{eff} equals the glide resistance. The activation energy for forward and reverse jumps ΔG_f and ΔG_b are also represented.

profile. The glide resistance to dislocation motion is

$$\bar{\tau} \equiv \frac{1}{V}\frac{\partial F}{\partial \gamma} = \frac{1}{b}\frac{\partial F}{\partial a}. \tag{2.5}$$

where V is the volume of the system, F is the Helmholtz free energy and b is the Burgers vector.

Under an effective applied stress τ_{eff}, the dislocation travels between two successive stable positions S, from left to right under a positive driving force $b\,(\tau_{eff} - \bar{\tau})$. In some regions (S and U), the effective applied stress and the glide resistance balance one another. Position S is a stable equilibrium while U is unstable because the dislocation would again be under positive driving force after thermal fluctuation. The energy barrier to overcome between the stable and unstable equilibrium positions, ΔG, that must be supplied by thermal fluctuation at a given stress and a given temperature is

$$\Delta G = \Delta F - \Delta W \tag{2.6}$$

$$= b\int_{a_S}^{a_U} (\bar{\tau} - \tau_{eff})\mathrm{d}a. \tag{2.7}$$

The escape of dislocation from these obstacles is a statistical process assisted by thermal fluctuation, generally referred as *thermal fluctuation* and modelled by a Arrhenius-type probability law.

Over most of the regime of practical interest, dislocations move in a jerky manner (Kocks, 2001). Gliding dislocations spend most of their time trapped at pinning points and dislocations are assumed to move in a negligible time between two successive obstacles. The dislocation velocity is controlled by

the release rate of dislocations either by thermal activation or by a change in applied stress. Reverse jumps of dislocations over activation barriers may become important at low stresses. A reverse jump would bring a dislocation back from the stable position S_2 to the unstable position U, from where it would, under positive driving force, jump back to S_1. This can happen under the action of thermal fluctuation, despite the adverse influence of the applied stress. The usual Arrhenius-type rate equation can no longer apply. A general rate equation for the net rate of thermally activated release of dislocations, P, taken into account possible back jumps at constant stress, is given by (Kocks et al., 1975)

$$P = \nu_G \left[\exp\left(-\frac{\Delta G_f}{k_B T}\right) - \exp\left(-\frac{\Delta G_b}{k_B T}\right) \right] = \frac{1}{t_w} \tag{2.8}$$

with ν_G the Granato frequency, k_B the Boltzman constant, T the temperature, ΔG_f and ΔG_b, the forward and backward activation energies, and t_w the waiting time spent in front of an obstacle. ΔG_b can be approximated by:

$$\Delta G_b = \Delta G_f + \tau_{eff} b a \tag{2.9}$$

with a the area swept out after a successful jump, roughly l^2. l is the average distance between discrete obstacles, in the order of $1000b$ or $10b$ for stronger and weaker obstacles respectively. Introduction of equation (2.9) in (2.8) yields to

$$P = \nu_G \exp\left(-\frac{\Delta G_f}{k_B T}\right) \left\{ 1 - \exp\left(-\frac{\tau_{eff} b a}{k_B T}\right) \right\}. \tag{2.10}$$

If the forward and reverse work are equal and opposite, the sinus hyperbolic law, frequently used in the literature, can be recovered from equation (2.10) assuming a square wave resistance diagram.

For steady state mobile density ρ_m, slip rate $\dot{\gamma}$ can be expressed as:

$$\dot{\gamma} = \frac{b \rho_m l}{t_w + t_{run}}. \tag{2.11}$$

In the jerky glide regime, the running time t_{run} can be neglected and the dependence of the slip rate $\dot{\gamma}$ on the effective resolved shear stress τ_{eff} arising from dislocation glide is finally given by:

$$\dot{\gamma} = b \rho_m l \nu_G \exp\left(-\frac{\Delta G_f}{k_B T}\right) \left\{ 1 - \exp\left(-\frac{\tau_{eff} b a}{k_B T}\right) \right\}. \tag{2.12}$$

When $\Delta G_f(\tau_{eff} = 0)$ is large (as here $0.2 - 2\mu b^3$), the stress dependence of the exponential is so large that, the stress dependence of the pre-exponential term can be ignored (Frost and Ashby, 1982). $\dot{\gamma}_0 = b \rho_m l \nu_G$ can be treated as a constant, hence

$$\dot{\gamma} = \dot{\gamma}_0 \exp\left(-\frac{\Delta G_f}{k_B T}\right) \left\{ 1 - \exp\left(-\frac{\tau_{eff} b a}{k_B T}\right) \right\}. \tag{2.13}$$

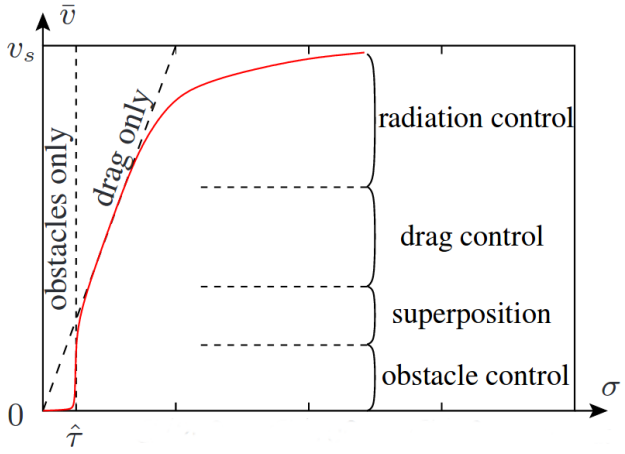

Fig. 2.4: Representation of the kinetics of dislocation motion, by the average dislocation velocity $\bar{\nu}$ as a function of applied stress. Image taken from (Ertürk, 2012).

For short-range obstacles, which are especially sensitive to thermal activation, the free enthalpy of activation can be expressed by the phenomenological relationship (Kocks et al., 1975):

$$\Delta G = F_0 \left\{ 1 - \left(\frac{\tau_{eff}}{\hat{\tau}} \right)^p \right\}^q \tag{2.14}$$

where F_0 represents the total energy barrier to be overcome with thermal fluctuation when no stress is applied. The parameter p describes the tail of the short-range glide resistance profile and q the shape of the top. These parameters vary in the following range

$$0 < p \leq 1 \qquad\qquad 1 \leq q \leq 2. \tag{2.15}$$

Selecting $p = 1/2$ and $q = 3/2$ has been demonstrated by Ono (1968) to correctly describe a variety of short-range glide resistance profiles. The mechanical threshold stress $\hat{\tau}$ is the flow stress required to overcome the localized obstacles at the absolute zero temperature, when thermal activation is impossible $\Delta G = 0$. Below $\hat{\tau}$, the jerky glide regime applies but above $\hat{\tau}$, dislocations move in a continuous manner sustained by viscous drag forces, see Figure 2.4. When stress exceeds this maximum glide resistance $\hat{\tau}$, dislocations will not be able to find any equilibrium positions and large scale slip occurs. In this regime, the velocity of dislocations is linearly dependent on the applied stress. Further increase of the applied stress activates additional dissipative processes that limit the maximum velocity reachable by dislocations.

For non idealized short range obstacles, the glide resistance diagram is asymmetric and some free energy can be stored after dislocation motion. Averaged over a large distance, this energy storage can lead to non zero long-range internal glide resistance τ_i which cannot be overcome by thermal activation.

The term $(\tau - \tau_i)$ is the component of the stress above the athermal component which is usually denoted τ_{eff}, the effective stress or the thermal stress. Another view of the effective stress is that dislocations experience long-range interactions associated with internal or back-stress τ_i and short-range stress associated to τ_{eff}. In CG crystals, the internal stress results from long-range elastic interactions of mobile dislocations with the substructure and exhibits long-wavelength spatial fluctuations. The effective stress is related to short-range interactions with localized obstacles such as forest dislocations or GBs and exhibits short-range fluctuations. Note that stress reduction tests allow to experimentally separate the effective and internal stress contributions (Milička, 1999). Stress reductions experiments carried out on electrodeposited NC Ni have revealed high values for the effective stress as compared to CG metals (Van Petegem et al., 2006).

Thermally activated phenomena are often quantified by the strain rate sensitivity exponent or by the activation volume. Regardless of the involved mechanisms, the activation volume V^* is defined as

$$V^* \equiv -\frac{\partial \Delta G}{\partial \tau_{eff}} \tag{2.16}$$

at constant temperature and constant microstructure. Neglecting the reverse jumps, the rate equation reduces to an Arrhenius-type law and the activation volume writes

$$V^* = k_B T \frac{\partial \ln \dot{\gamma}}{\partial \tau_{eff}}. \tag{2.17}$$

Because τ_{eff} is related to the stress experienced by the defect involved in the thermal activation, the apparent activation volume is commonly computed from the macroscopic measurement of σ and ε, by $V_{app} = M k_B T \frac{\partial \ln \dot{\varepsilon}}{\partial \sigma}$. There is no consensus on the value of the Taylor factor M to be used for NC metals. In the literature, 3 or $\sqrt{3}$ are used. Based on the Schmidt law, some authors argued that $M = 2$ is in any case, the lower bound for the Taylor factor for mechanisms involving dislocation motion and that $M = 3$ is still valid (Blum and Eisenlohr, 2017). Other researchers used the Von Mises yield theory to justify $M = \sqrt{3}$ (Wei, 2007). The apparent strain rate sensitivity exponent m_{app} is also largely employed in the literature and is defined, assuming a power law rate dependence, by

$$m_{app} = \frac{\partial \ln \sigma}{\partial \ln \dot{\varepsilon}_p} \tag{2.18}$$

where σ is the stress and $\dot{\varepsilon}_p$, the plastic strain rate. From this definition arises a inversely proportional relation between V_{app} and m_{app}.

The activation volume can be seen as the signature of a thermally activated mechanism. For instance, conventional dislocation based mechanisms are characterized by $V^* = 100 - 1000\ b^3$ while only $1\ b^3$ is required for diffusion based mechanisms. During the last decade, the strain rate sensitivity of

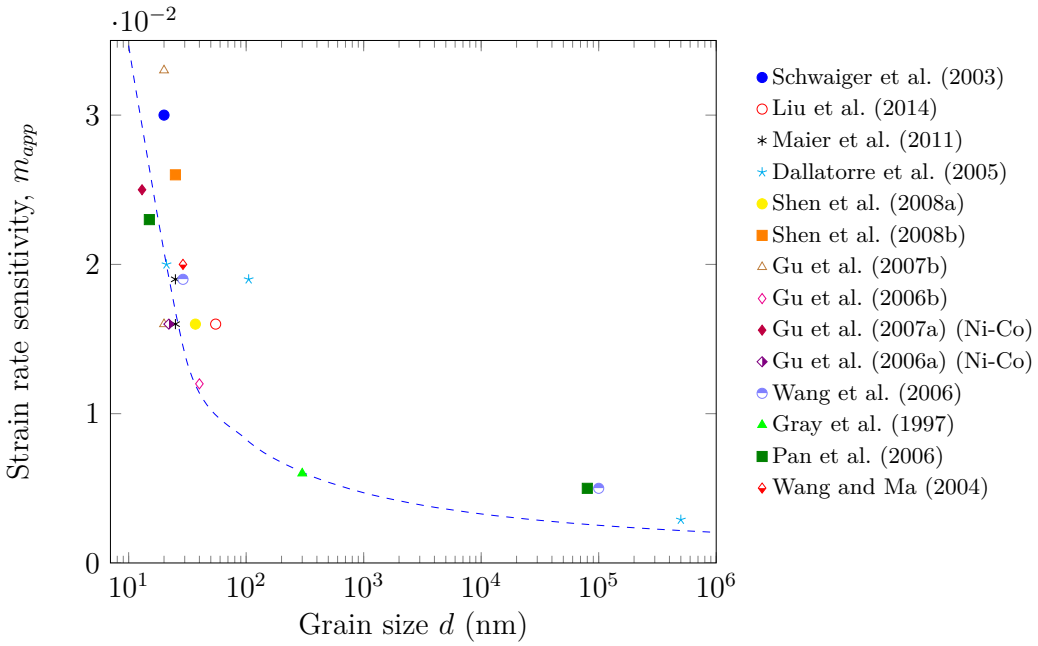

Fig. 2.5: Strain rate sensitivity of Ni as a function of grain size. The reference and its first author corresponding to each data point are also given in the plot.

NC metals has been extensively studied by strain rate jumps, nanoindentation or lab - on - chip technique. Figure 2.5 depicts the evolution of the strain rate sensitivity, m_{app}, of Ni as a function of the grain size. Data have been compiled from the literature. As the grain size decreases, the GB-mediated mechanisms progressively replace the dislocation-based mechanisms, resulting in a magnified strain rate sensitivity for FCC metals in the NC domain. As seen in Figure 2.5, m lies under 0.05. So grain boundary sliding ($m \sim 0.5$) and diffusion creep ($m = 1$) are not dominating the mechanical response for $d > 10$ nm as expected by atomistic simulations (see section 2.1.2). Interplay between dislocation- and GB- mediated mechanisms is rather expected.

2.3 Yield strength and strain hardening

In NC polycrystals, the spread of the grain size distribution is such that the smallest grains can be extremely resistant to plasticity while other grains, better oriented or larger, can yield much earlier, leading to a high stress heterogeneity and a long elasto-plastic transition, see e.g. (Li et al., 2012; Yuan et al., 2015). The concept of yield stress is thus not obviously defined anymore and must be given at a representative level of plastic strain (Saada and Kruml, 2011) or at representative tangent modulus (Rajagopalan et al., 2010).

Nevertheless, NC metals follow an Hall-Petch trend down to grain size of 10-20 nm. The well-known Hall-Petch strengthening of FCC polycrystals is

given by

$$\sigma_Y = \sigma_0 + k_{HP}\ d^{-n_{HP}} \tag{2.19}$$

where σ_Y is the yield strength, σ_0 and k_{HP} are material constants, d is the grain size and n_{HP} is an exponent comprised between 0.4 and 1. Conventional Hall-Petch relationship relying on pile-up theory sets $n_{HP} = 0.5$. Deviations from the original Hall-Petch strengthening have been recorded with grain size reduction. This is sometimes named as the Hall-Petch breakdown. At very small grain sizes, some authors reported also a softening or an "inverse" Hall-Petch effect (Chokshi et al., 1989; El-Sherik et al., 1992; Conrad and Narayan, 2000). Deviations start when the traditional intragranular dislocation mechanisms become limited and that GBs start playing a more prominent role. The inverse Hall-Petch effect is often interpreted in terms of GB sliding or diffusion processes associated with the large interface density when the grain size is very small.

The dislocation based mechanisms observed in NC metals, do generally not lead to dislocation accumulation in the grain interior and therefore efficient isotropic strain hardening is absent (Kumar et al., 2003b; Skrotzki et al., 2013). Furthermore, conventional strain hardening mechanisms like forest hardening have rarely been observed and dynamic recovery eliminates the few dislocations stored inside the nanograins (Meyers et al., 2006; Sun et al., 2015). The influence of such low strain hardening on the ductility of materials is dramatic.

Nevertheless strain hardening capacity can be enhanced by the presence of twins or by strain heterogeneity resulting from the grain size distribution and inducing back-stresses and kinematic hardening. The presence of twin boundaries promote dislocation storage and can significantly increase the strain hardening capacity of NC materials (Zhu et al., 2012). Some NC Pd and Al films exhibit a significant strain hardening capacity and a significant increase in the strength with decreasing thickness (Haque and Saif, 2003; Colla et al., 2012). The large apparent strain hardening at the onset of plasticity is shown to be a gradual elastic-plastic transition, inducing a significant kinematic hardening contribution (Haque and Saif, 2003; Rajagopalan et al., 2010). Recent experimental and numerical investigations have shown that the generated back-stresses can lead to backward creep or even strain recovery under zero mechanical stress (Rajagopalan et al., 2007, 2008; Van Petegem et al., 2006).

2.4 Ductility

Nanocrystalline metals often suffer of a lack of ductility (Meyers et al., 2006; Dao et al., 2007; Pineau et al., 2016). Ductility represents the ability for a material to deform plastically without strain instability such as diffuse or localized necking, nor failure by damage. The limited ductility is commonly attributed

to high strength combined with a low strain hardening capacity (Meyers et al., 2006; Sharon et al., 2013). The same applies to thin films which are usually not only nanocrystalline but are also affected by their free surface (Haque and Saif, 2003; Espinosa et al., 2004; Nicola et al., 2006; de Boer et al., 2008a). The low strain hardening originates from the small volume available for dislocation accumulation for grain size typically smaller than 1μm. Extrinsic factors such as geometrical imperfections in thin films can also trigger instability (Coulombier et al., 2010). The relative magnitude of geometrical imperfections is magnified in thin films: roughness or grain boundary grooving, even with amplitudes in the nanometer range, constitute significant imperfections, so do initial texture inhomogeneities (Viatkina et al., 2005). A variety of softening mechanisms can also act to accelerate plastic localization. For instance, plastic instabilities may be promoted by progressive damage accumulation or by lattice reorientation during deformation, leading to soft texture.

Ma (2006) has reviewed 8 techniques to tailor a nanostructure in order to achieve coexisting high strength and high ductility at room temperature. Three of these routes of improvement are suitable for pure NC metals or pure metallic thin films. A first way to achieve a good trade-off between high strength and ductility is mixing up the length scales by creating bimodal or multimodal grain size distribution. The combination of micro- and nano- grains results in high kinematic hardening and high strain gradients between neighbouring grains which delay plastic instability (Ma, 2006). The second approach involves growth twins. Growth twins effectively block dislocation motion and prevent dynamic recovery, unlike GBs or dislocation cells. The associated increase of strain hardening improves the ductility. Strain hardening capacity and strain rate sensitivity enhancement constitute a last improvement route. In NC metals, the activation of rate-dependent GB or dislocation based mechanisms commonly magnifies the strain rate sensitivity at the expense of the strain hardening capacity. Experimental confirmation of such improvement routes are given in the next paragraph.

Due to nanocrystalline plasticity mechanisms, many thin films exhibit moderate to high strain rate sensitivity at room temperature which may help restoring the ductility. Results on Au thin films with moderate to high ductility have been reported by Jonnalagadda et al. (2010) and Hosseinian et al. (2016). These experimental studies highlight a competition between several deformation mechanisms, leading to an improved ductility when strain rate is low, as illustrated in Figure 2.6. During tensile tests under low strain rates, 0.85 μm and 1.76 μm thick freestanding Au films with 44 nm grain size uniformly elongated to $\sim$6% compared to $\sim$2% at higher strain rates. In Hosseinian et al. (2016), the strain achieved during relaxation of 100 nm thick films with 30 nm grain size is about ten times larger than the monotonic tensile strain to failure ($\sim$1%). Over the relaxation time, a progressive transition operates from intergranular and transgranular dislocation motions to grain-boundary diffusion

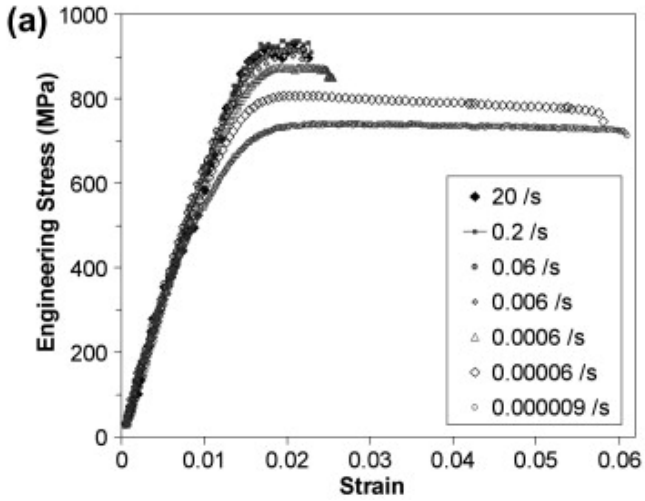

Fig. 2.6: Stress-strain curves of Au thin films illustrating the effect of strain rate on the ductility of thin films. Image reproduced from (Jonnalagadda et al., 2010).

based mechanisms, improving the ductility. Stable extreme local ductility inside the necks of pure Al thin films has been observed by Coulombier (2012). Tensile tests were performed on 150 - 400 nm thick films using the on-chip test method (Gravier et al., 2009). The good resistance to unstable flow has been attributed to a high rate sensitivity caused by thermally activated grain growth deformation mechanisms combined with dislocation activity at grain boundaries (Legros et al., 2008; Mompiou et al., 2013). Similar ductility has also been reported by Gianola et al. (2006, 2008) on pure Al. Some Pd thin films with ∼30 nm in plane grain size and growth nanotwins, deposited by Colla (2014), exhibited a high strain rate sensitivity and a significant strain hardening capacity attributed to back stresses due to dislocation/twin boundary interactions. The nanotwins act indeed as barriers to dislocation motion as well as sources for dislocation storage and multiplication via specific TB/dislocation interactions, providing an additional contribution to the strain hardening capacity (Idrissi et al., 2011; Wang et al., 2012b; Colla et al., 2015). The expected high ductility has been confirmed by on-chip test method, up to 12% in the best cases while reaching strengths above 1 GPa (Colla et al., 2012; Colla, 2014; Colla et al., 2015). This positive influence of growth nanotwins on strain rate sensitivity and strain hardening is well known for bulk Cu where a high strength ductility balance is observed (e.g. (Lu et al., 2009; Dao et al., 2006; Zhu et al., 2007, 2011)). Furthermore Anderoglu et al. (2010) have reported surprisingly high uniform plastic flow in nanotwinned Cu foils.

2.5 Micromechanical modelling of nanocrystalline metals

In order to predict the mechanical properties of NC materials, computational models linking the macroscopic properties and the nanoscale effects are needed. While the atomistics and molecular dynamics (MD) seem to give the most suitable frameworks to simulate the nanoscale effects, they suffer of time and size scales limitations. Only few grains undergoing much higher strain rate than experimentally reachable strain rate can be simulated, preventing internal relaxation and potentially resulting in artefacts in the mechanical behaviour (Van Swygenhoven, 2008). These limitations make it impossible to directly compare the numerical results and experimental observations. This is why atomistic or MD simulations are limited to the prediction or the validation of the possible deformation mechanisms.

Growing interest of scientific community has thus been attracted to continuum micromechanics modelling as an analysis tool to explore the mechanical properties of NC and UFG materials at a macroscopic level and their possible improvements. Nevertheless, continuum models assume scale separation between the structural elements (atoms, dislocations, ...) and the considered volume, as well as homogeneity of deformation. The validity of this continuum hypothesis is debated in the literature. In some cases, atomistic and continuum models are combined to introduce atomistic fed materials parameters into micromechanical models (see e.g. the quasicontinuum method (Miller and Tadmor, 2002; Curtin and Miller, 2003) or the Finite Element Atomistics (FEAt) method (Kohlhoff et al., 1991)). As stated by Mishnaevsky and Levashov (2015), "micromechanical modelling of NC materials pushes in fact the borders of traditional continuum mechanics seeking to incorporate physical effects into purely mechanical concepts". In this section, an overview of micromechanical of NC and UFG metallic materials is presented. Composite and multigrains based models are reviewed.

Compared to coarse-grained materials, NC and UFG materials present a high volume content of boundary surface which has led several models to consider these metals as two-phase (or even three-phase) composite materials. The mechanical response of grain interior and of GBs is distinguished and the macroscopic response is then obtained by the rule-of-mixture in which the relative volume fraction of the phases varies with the grain size.

One of the earliest modelling approach based on the rule-of-mixture was proposed by Meyers and Ashworth (1982). Their model relies on a mantle-core description of grains in which plastic deformation is initiated in the GB-region mantle at the localized stress concentrations arising from elastic incompatibilities and at dislocation sources in GBs. The GB was assigned lower yield strength and higher work hardening rate than grain interior core. This ap-

proach later extended by Fu et al. (2001) assumed that the thickness of the GB mantle is grain size dependent. The relevance of this assumption for NC metals can be questioned. The grain size dependency on the thickness of the GB mantle is not observed experimentally nor in MD simulations (Van Swygenhoven et al., 1999; Yamakov et al., 2002; Kumar et al., 2003a).

Carsley et al. (1995) considered NC material as a two-phase composite consisting of squared grains with bulk properties (following a Hall-Petch equation for the grain-size dependence of the strength), and of a GB phase which represent a metallic glass material. This model applied on Ni, Fe and Cu captured some deviation from the conventional Hall-Petch slope at small grain sizes.

Kim et al. (2001) developed a cubic cell composite model consisting of a crystallite and a GB phase (see Figure 2.7(a)). The deformation of the grain interior is considered as the superposition of diffusional flow (Coble creep and Nabarro-Herring creep) and dislocation glide. The GB phase controlled by diffusional deformation mechanism only is described by a viscous Newtonian behaviour. This model introduced also the notions of critical grain size in the grain interior phase below which the dislocation based mechanism is not activated and of upper limit of the stress in the GB phase, set to be the strength of the material in the amorphous state. The breakdown of the Hall-Petch relation with decreasing grain size is simulated and interpreted in terms of predominance of diffusional mechanisms.

Different composite models are based on the so-called grain boundaries affected zones (GBAZ) approach, as worked out by Schwaiger et al. (2003). The GB phase is presented as a sharp GB surrounded by a GBAZ with varied properties (see Figure 2.7(b)). Based on MD simulations of NC metals, a GBAZ in a NC or UFG material is assumed to span a grain size independent distance of about 7–10 lattice parameters away from the GB. In their work, Schwaiger and collaborators studied the strain-rate sensitivity of NC Ni with two-dimensional model of hexagonal grains separated by GBAZ softer than the grain interior, using a simple power-law type rate-dependent plastic law with linear hardening.

Following the GBAZ approach, Li and Weng (2007, 2013) developed a secant-viscosity composite model where both constituent phases are elastic–viscoplastic. The viscoplastic behavior follows a unified constitutive law involving a grain-size dependent yield stress for the grain interior. The model was applied to calculate the grain-size dependence of flow stress, strain-rate sensitivity, and activation volume of NC metals.

As the grain size decreases, the influence of the grain size distribution becomes predominant and simple cubic or hexagonal unit cells become insufficiently representative of the real NC microstructure. The complex interplay between deformation mechanisms asks for quasi-real representation of microstructure (e.g. multigrains aggregate or Voronoï representations).

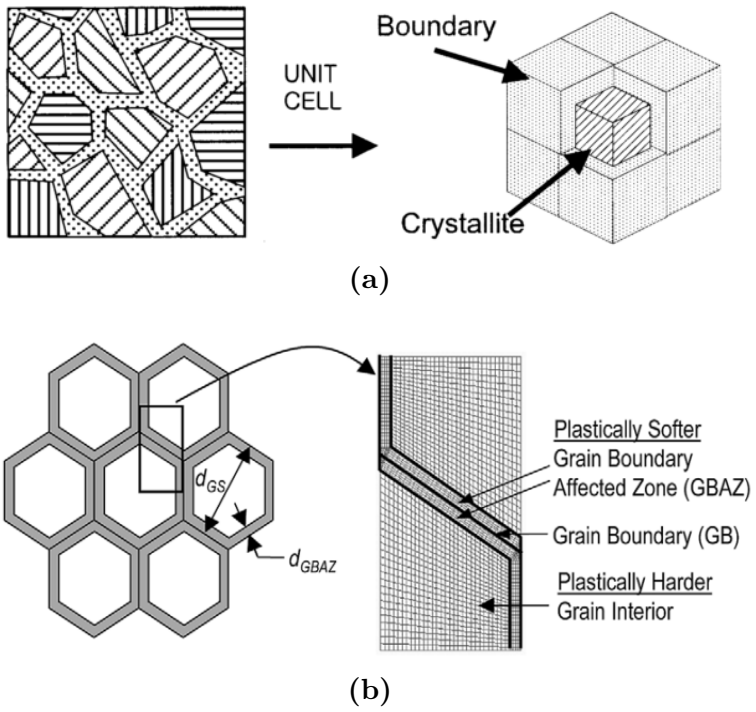

Fig. 2.7: Illustrations of unit cells models of NC metals: cubic composite unit cell of Kim et al. (2001) (a) and 2D grains of hexagonal shape separated by the GBAZ proposed by Schwaiger et al. (2003) (b).

The work of Fu et al. (2001) was one of the first FE plasticity calculation of polycrystalline aggregate accounting for grain size effects in a physically-based manner. The simulated polycrystalline aggregates are represented in Figure 2.8. Relying on the mantle-core approach developed by Meyers and Ashworth (1982), the authors incorporated GB sliding and took into account the dislocation accumulation rate at GBs and in the grain interior. Deviation of the Hall-Petch slope in the NC domain was observed in their simulations. Fu et al. (2004) further extended their model, using crystal plasticity either in both phases or only in the grain interior while the work hardening GB region responded to a Voce equation, and neglecting this time, GB sliding.

The AKK model describing the deformation mechanisms based on the emission of perfect or partial dislocations, along with deformation twins from GBs and GB sliding was proposed by Asaro, Krysl and Kad (Asaro et al., 2003; Asaro and Suresh, 2005). Zhu et al. (2005, 2006) extended further the AKK model with a aggregate approach. The authors investigated the effect of grain size distribution through log-normal distributions on the mechanical response of NC Ni. The model takes also into account thermal activation and grain size dependent transition between these mechanisms, suggesting plausible interpretation of the increasing strain rate sensitivity in NC metals.

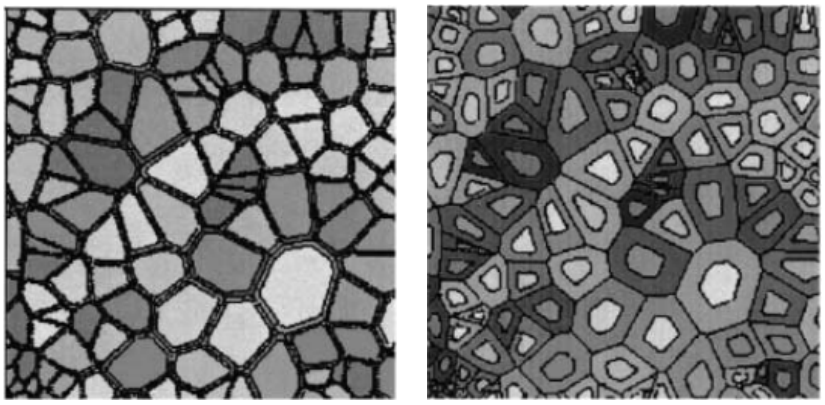

(a) $d = 10\mu$m **(b)** $d = 1\mu$m

Fig. 2.8: Polycrystalline aggregates used by Fu et al. (2001), illustrating the grain size dependence assumption of the GB mantle thickness.

Wei and Gao (2008) proposed an extension of the model of Zhu et al. (2005) by introducing elasticity and GB diffusion. Their model relied also on a more rigorous dislocation-emission rate at GBs in NC materials. Combining all the main deformation mechanisms, the study of these competing deformation mechanisms at NC grain size revealed a substantial increase of the strain-rate sensitivity as the dominant deformation mechanisms shift from the grain interior to GBs but also a rate-dependent strain rate sensitivity. A mesoscopic continuum model of a 2D polycrystal with deformation mechanisms including single crystal plasticity for the grain interior, GB diffusion and GB sliding was then presented by Wei et al. (2008), the same year. This extension accounts for the coupling between GB processes and dislocation activity within the grains.

Wei et al. (2006) established a FE-based 2D plane-strain model to study the deformation and failure behaviour of FCC NC metals. The polycrystal is represented by a Voronoï tessellation in which each grain is decomposed into a grain interior and an amorphous 0.5 nm thick GB. GB are simulated with a rate-dependent amorphous model which accounts for cavitation at triple junctions and related failure phenomena while crystal plasticity is applied for the grain interior with CRSS based on the AKK model. Wei and coworkers concluded that a transition from the grain interior dominated shearing to GB dominated shearing and cavitation occurs as the grain size decreases from 50 nm to 10 nm.

Gürses and El Sayed (2011a,b) derived a variational two-phase constitutive model based on the GBAZ approach. The grain interior in which dislocation mediated plasticity dominates, is modelled with rate-independent crystal plasticity relying on a specific yield criteria based on the AKK model which accounts for the transition from partial dislocation to full dislocation mediated plasticity. In the GBAZ regions modelled with rate-dependent isotropic porous

plasticity, mechanisms other than dislocations, such as atomic shuffling, GB sliding and void initiation and growth are operative. Using the Taylor assumption, the authors studied the mechanical behaviour and rate-dependence of NC Ni and NC Cu.

Lebensohn et al. (2007) presented a micromechanical model based on FFT method to study the effects of grain size, strain rate and pressure on the local and macroscopic mechanical behaviour of NC materials under quasi-static and shock loadings. NC metals are represented by a RVE of self-similar polycrystals with different submicronic grain size. Each crystal is divided in two phases: grain interior and GB. Crystal viscoplasticity with Hall-Petch grain size dependence of CRSS is used for the grain interior and J2 isotropic viscoplasticity for the GBs (compatible with the diffusion controlled mechanisms at GBs) is assumed. The model reproduced the increased strain rate sensitivity of NC FCC metals and captured an inverse Hall-Petch effect at grain size lower than 10 nm.

Mercier et al. (2007) integrated elasticity in the Kim et al. (2001) approach to study the transition to the inverse Hall-Petch effect. NC materials are represented by an aggregate of spherical grains in which grain size is distributed following a log-normal probability function. Macroscopic response is computed using the Taylor-Lin assumption.

Shi and Zikry (2009) developed a dislocation density grain boundary interaction (DDGBI) approach, incorporating the Raj-Ashby GB sliding model (Raj and Ashby, 1971). Dislocation emission, absorption and transmission are considered, assuming that the dislocation–density interactions occur between slip systems on each side of the GB interface. Additively splitting the total dislocation-density into immobile and mobile dislocation density, rate dependent dislocation based crystal plasticity is used with a initial dislocation densities dependence on GB misorientations. They observed that the GB sliding contribution increases with decreasing grain size and that GB sliding can change the direction of crack growth. Following a similar approach of the DDGBI model, Aoyagi et al. (2014) considered the effect of the GB and dislocation sources to analyse the grain size effect on the yield strength of UFG severe plastically deformed metals.

Assuming that, once nucleated, dislocations cross the grain and are absorbed at the opposite GB, Warner and Molinari (2006) implemented a FE-based semi-discrete crystal plasticity model. The introduction of discrete slip events in grains captured the extraordinary hardening observed in the microplastic regime of NC metals. This model neglects dislocation interactions in the grain interior and assumes that successive slip events require increasing stress. This later assumption is compatible with the stress-reduction experiments of Van Petegem et al. (2006) in which the effective stress is observed to increase with deformation.

Li et al. (2009a, 2012) developed the quantized crystal plasticity (QCP) model. Based on results of MD simulations, the material deforms by grain-averaged shear strain/stress jumps resulting from discrete slip events. The authors implemented QCP into FE model of 1000 grains polycrystals. The simulated polycrystals are characterized by a grain to grain distribution of CRSS at which slip event occurs and a grain to grain distribution of the local plastic strain jump by a single slip event across an entire grain. QCP model successfully predicted the stress-strain response of NC metals and their propensity to plastic localisation.

The model proposed by Yuan et al. (2015) added a physical background on the spatial distribution of CRSS assumed in the QCP model. They developed a geometrically based, statistical model for the characteristic CRSS needed to activate a dislocation source at GB, which give rise to a generalized extreme value distribution of CRSS. CRSS of each slip system can moreover vary both spatially and temporally, changing after each discrete slip event. A Hall-Petch-type scaling ($\sigma \propto d^{-0.63}$) emerges from their simulations, due to the grain size limitations on the dislocation sources length. Their model produced significant strain hardening in the macroscopic response and predicted a strong texture influence in the NC domain.

Other advanced models including non equilibrium grain boundaries and GB defects have been reviewed by Mishnaevsky and Levashov (2015).

The main challenge of the micromechanical modelling of NC metals is the proper selection of the constitutive laws to correctly represent the peculiarities of NC materials and of all their possible deformation mechanisms. A large panel of deformation mechanisms has been envisaged to model NC materials, from conventional crystal plasticity to diffusive accommodation mechanisms and discrete slip events. Moreover, the complex competition or cooperation interactions between these mechanisms and their grain size dependence are difficult to observe and are not yet fully understood despite the insights given by atomistic/ MD simulations and inverse analysis.

2.6 Modelling of plastic localization

The prediction of plastic localization is of prime interest for industrial metal forming processes but plays also a central role in the design of flexible electronics or thin films technologies. The localization of plasticity is an instability which leads to a transition from a uniform to a non-uniform mode of deformation while the loading remains uniform. Two types of instabilities are distinguished: diffuse necking an localized necking (or localized band). According to Barata da Rocha et al. (1985), ductility (i.e. the maximum allowable strain) in industrial stamping processes is not determined by diffuse but by localized necking. Upon loading, diffuse necking initiates when geometric softening due

to local area reduction of the sheet overcomes strain hardening. The neck develops progressively and considerable extension is still possible after the onset of diffuse necking. Upon additional deformation, the necking region further localizes until a sharp localized band starts to form. The length of the localized band is of the order of the sheet thickness while the length of the diffuse neck scales with the sheet width. The scaling factor for the length of the diffuse neck can evolve with deformation and can depend on the stress state as well, see (Pardoen et al., 2004).

In the past sixty years, various theoretical necking models have been developed that focus either on diffuse or localized necking. These necking models successfully predicted the formability of metallic sheets, characterized by the so-called forming limit diagram (FLD), representing the major and minor strains corresponding to necking for any monotonic proportional strain paths. In practice, the FLD is a very useful tool because necking usually occurs prior to failure in ductile metals. The first models for diffuse and localized necking under biaxial loading were respectively proposed by Swift (1952) and Hill (1952) for rigid plastic and defects-free materials. The onset of diffuse necking is predicted when an increment of deformation no longer corresponds to a rise in the load $dF_i = 0$ for $i = 1, 2$ simultaneously, see Figure 2.9(a). This is the maximum force criterion, frequently attributed to Swift (1952). Several years later, Hill (1991) has raised issues with the original work of Swift and proposed a slightly different formulation. Diffuse necking can be expected when the major strain reaches ε_{11}^{inst} given by

$$\varepsilon_{11}^{inst} = \frac{2n\left(1+\rho+\rho^2\right)}{\left(1+\rho\right)\left(2\rho^2-\rho+2\right)} \tag{2.20}$$

where $\rho = \varepsilon_{22}/\varepsilon_{11}$ and n is the strain hardening. For uniaxial loading, the maximum force criterion reduces to the well-known Considère criterion:

$$\varepsilon_{11}^{inst} = n. \tag{2.21}$$

For the modelling of localized necking, Hill (1952) assumed that a region of the sheet is subjected to a proportional in-plane loading, characterized by the forces per unit width, referred as tension: $T_1 = \sigma_{11}h$ and $T_2 = \sigma_{22}h$, as depicted in Figure 2.9(b). The localized necking condition postulates that necking starts when the major tension reaches a maximum i.e. $dT_1 = 0$. Differentiating the equation, this condition writes

$$\frac{dT_1}{T_1} = \frac{d\sigma_1}{\sigma_{11}} + \frac{dh}{h} \tag{2.22}$$

$$= \frac{d\sigma_{11}}{\sigma_{11}} + d\varepsilon_{33} \tag{2.23}$$

$$= \frac{d\sigma_{11}}{\sigma_{11}} - (1+\rho)d\varepsilon_{11} = 0, \tag{2.24}$$

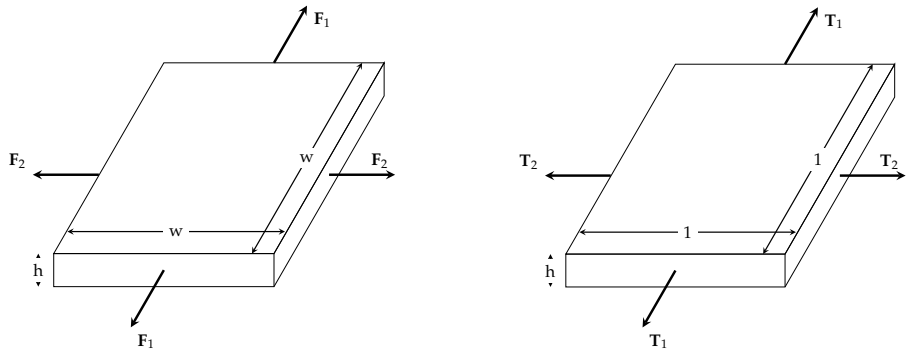

(a) Swift's model **(b)** Hill's model

Fig. 2.9: Schematic illustrations of the sheet patch considered by Swift (1952) (a) and by Hill (1952) (b). The in-plane dimensions of the displayed sheet patch are of unit length in (b). The sheet patch is subjected to the forces F_1, F_2 in (a) while force by unit width called tension, T_1,T_2 are applied in (b).

leading to

$$\frac{1}{\sigma_{11}}\frac{d\sigma_{11}}{d\varepsilon_{11}} = 1 + \rho. \tag{2.25}$$

For a purely plastic material following a Hollomon law, the left side of the equation corresponds to the dimensionless strain hardening and gives

$$\frac{1}{\sigma_{11}}\frac{d\sigma_{11}}{d\varepsilon_{11}} = \frac{n}{\varepsilon_{11}}. \tag{2.26}$$

Finally, the major and minor strains corresponding to localized necking are given by

$$\varepsilon_{11}^{inst} = \frac{n}{1+\rho} \qquad \text{and} \qquad \varepsilon_{22}^{inst} = \frac{n\rho}{1+\rho}. \tag{2.27}$$

In uniaxial tension, $\rho = -0.5$ and

$$\varepsilon_{11}^{inst} = 2n \tag{2.28}$$

which is twice the strain corresponding to diffuse necking. Hill's localized necking model reduces to Swift's model for plane strain deformation, $\varepsilon_{11}^{inst} = n$. Hill's localized necking condition may in fact be obtained from Swift analysis of diffuse necking if only the thickness decreases to accommodate the elongation strain when localized necking sets in. As pointed out by Lian and Zhou (1989), diffuse necking is indeed based on providing extra thickness strain by both in-plane strain-rates while localized necking is based on providing extra thickness strain by elongation in the major deformation direction only.

The previous analysis are insensitive to changes in strain rates. Hart (1967) proposed an instability criteria taking into account both strain hardening and strain rate sensitivity for uniaxial tension:

$$\varepsilon_{11}^{inst} = \frac{n}{1-m}. \tag{2.29}$$

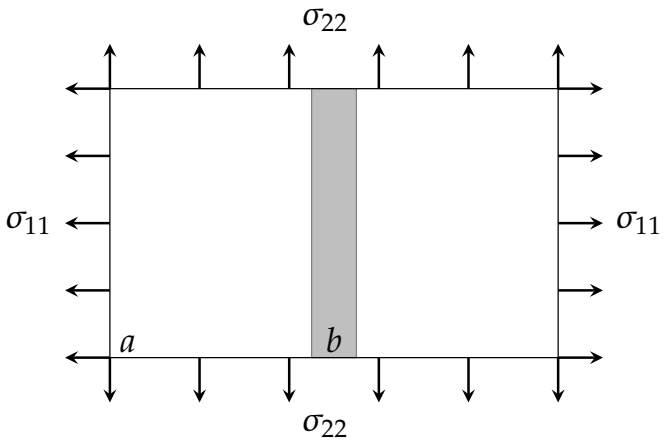

Fig. 2.10: Schematic representation of the imperfection based model developed by (Marciniak and Kuczyński, 1967). The presence of an initial band with reduced thickness (zone b) within an homogeneously deforming zone a is assumed. The sheet is subjected to biaxial loading.

Several researchers such as Ghosh (1977) and Hutchinson and Neale (1977) have critically reconsidered the work of Hart and have formulated their own criteria. As a matter of fact, Hart's approach does not reveal any dependence on material imperfection and largely underestimates the effect of strain rate sensitivity on ductility, unable to reproduce the experiments, see the collection of data of Woodford (1969). Even if Hart addresses these critics in a subsequent publication (Lin et al., 1981), it seems that how effective strain hardening and strain rate sensitivity stabilize the localization process is still a matter of debate (Sharon et al., 2013).

These criteria captured some interesting experimental trends observed in the FLDs but their use with advanced material models seems limited by necessary and fastidious, analytical developments. To overcome these restrictions, imperfection based approaches may be a solution. In their original paper, Marciniak and Kuczyński (1967) postulated the presence of an initial groove with reduced thickness, of infinite length and oriented perpendicular to the major strain direction, in which localized necking is supposed to occur during loading. It is assumed that the region outside the groove deforms under proportional deformation and some geometrical compatibility conditions are imposed. Note that in general, localized necking in the groove does not correspond to a plane strain deformation mode due to geometrical compatibility conditions. They prevent the groove from undergoing plane strain deformation, except if a plane strain state is explicitly imposed outside the groove. However at the onset localized necking, the deformation mode is very close to plane strain because the strain rate along the major strain direction becomes much larger than in the minor strain direction.

Hutchinson and Neale (1978a) extended the Marciniak-Kuczinsky (MK)

model by considering all the possible initial orientation of the groove. This is essential to obtain realistic predictions for the negative minor strain region of the FLD. For the positive minor strain region, the minimum strain at instability always corresponds to the groove orientation normal to the loading direction and the original MK approach applies which saves unnecessary computation time. Using the extended MK approach, Hutchinson and Neale (1978b) have again demonstrated that the strain rate sensitivity effect on ductility is significant even for low strain rate sensitivity exponents. Their studies on rate- independent and dependent materials have revealed that the onset of plastic instability is affected by the constitutive model. J_2 deformation and flow theory give distinct results.

Since the seventies, the extended MK framework has been extensively employed to better understand the localized necking and predict the formability of sheets. Barlat (1987) extended the MK model to take into account any anisotropic yield locus and so to study the influence of the yield locus on the ductility of metallic sheets. Different yield surfaces described either by a phenomenological Von Mises equation or by the procedure of Taylor/Bishop and Hill (TBH) for polycrystalline aggregates were investigated. The Taylor-Bishop-Hill yield locus predicted quite realistic FLD while the Von Mises yield locus resulted in overestimation. The impact of the yield surface shape has been further explored by Lian et al. (1989). Their study demonstrated that the shape of the right-side of the FLD is strongly affected by the yield surface shape between plane strain deformation and equibiaxial stretching. Yao and Cao (2002) pointed out that formability is also affected by kinematic hardening by considering both isotropic and kinematic hardening within the MK framework.

Compared to classical continuum plasticity models, crystal plasticity models allow a better agreement between experimental FLDs and numerical predictions by taking into account the evolution of crystallographic texture. However several studies have shown that depending on the initial texture, the formability may or not be influenced by texture evolution. Different crystal plasticity models and homogenization scheme have been successfully used: rate independent crystal plasticity (Tóth et al., 1996; Knockaert et al., 2002) and rate dependent crystal plasticity (Inal et al., 2005) under Taylor assumption, or viscoplastic self consistent model (Signorelli et al., 2009). The MK model has been recently extended by Eyckens et al. (2009, 2011) to take into account through thickness shear encountered in single point incremental forming.

Other types of localization model include bifurcation type model and perturbation type model. Bifurcation analysis gives a general framework to obtain criteria without requirement of initial imperfection or threshold value at which localized necking occurs. According to this approach, a criterion for diffuse necking is given by the loss of positivity of the second order work (Hill, 1957). Localized necking or shear banding is predicted by the loss of ellipticity of the

governing differential equations (Rudnicki and Rice, 1975; Hill and Hutchinson, 1975). As soon as softening occurs in rate-independent materials, the equilibrium equations lose ellipticity and the problem becomes ill-posed in a conventional continuum framework. As an example, FEM simulations of localized necking may result in a high mesh sensitivity due to the occurrence of strain jumps along discontinuity lines/planes (Sluys, 1998). For a proper formulation, enhanced (regularized) theories are necessary, by means of higher-order time derivatives (viscoplasticity) or higher-order spatial derivatives (strain gradient models). For viscoplastic material, the ellipticity is indeed preserved and strain fields remain continuous even in the presence of strain softening (Needleman, 1988).

When plastic localization starts, very large plastic gradients develop, leading to strain gradient plasticity effects. A very large density of geometrically necessary dislocations (GNDs) is indeed required to accommodate the plastic gradients associated to the development of a neck or a localized band in metal sheet. The accumulation of GNDs leads to an additional strain hardening source compared to a purely isotropic hardening contribution dictated by the accumulation of statistically stored dislocations only. This kind of stabilization effect has been studied by Niordson and Redanz (2004) and by Niordson and Tvergaard (2005) using 2D FE simulations relying on the strain gradient plasticity model of Fleck and Hutchinson (2001).

Significant effort has been devoted to the prediction the FLDs of CG metallic sheets for industrial stamping but little attention has been paid on the ductility of metallic films with UFG or NC grain sizes. A strain gradient plasticity approach dedicated to metallic thin films with columnar grains has been followed by Brugger et al. (2010) in order to investigate the effect of the thickness, grain shape and surface constraints on ductility. Their study pointed out that even if a reduction of the film thickness leads to a lower necking resistance due to higher yield strength, this deleterious effect can be compensated by the strain gradient effect. Recently, Pardoen (2014) developed an enhanced closed form 1D imperfection based localization analysis in order to investigate the mechanics of diffuse necking in metallic films in uniaxial tension. His model relies on a description of the localization process in a finite length specimen using either a 2- or 3- zones model, following the linear approach of Hutchinson and Neale (1977). A strain gradient plasticity contribution to the hardening of rate sensitive materials was incorporated in the model along with possible creep or relaxation deformation mechanisms. Linking the plastic flow parameters to the microstructure and film thickness, this model showed that the ductility can dramatically drop for either very small grain sizes and/or film thickness due to the high strength and to the presence of imperfections. Ductility at small grain size can however be recovered owing to an increased rate sensitivity resulting from thermally activated mechanisms, in agreement with experimental observations.

2.7 Thin film mechanical testing

The last decade has seen a rapid development of a wide variety of testing methods for the mechanical characterization of thins films, permitting nearly all types of macroscale mechanical tests to be performed at the nanoscale. Tensile testing as well as bending, fracture and fatigue experiments are nowadays commonly performed. Several reviews have recently covered the topic of nano-mechanical testing (Gianola and Eberl, 2009; Dehm et al., 2017). This section summarizes the miniaturized deformation strategies developed over the last decade and provides some examples of the on-chip approach, following the short review proposed by Pineau et al. (2016).

When testing freestanding thin films, the main difficulty is the extraction, manipulation and positioning of the samples. The characterization methods can be roughly classified in three categories. In the first approach, thin films are removed from a patterned template, attached to a nanomanipulator and transferred to the testing frame where they are glued or welded at anchors. The second opposite approach consists in bringing the loading device to the test specimen still attached to the original frame. The last category is generally referred as the "on-chip" approach. On-chip means that the material is directly characterized on the test platform on which it is deposited, with the loading devices and the measurement sensors partially or totally embedded on the testing frame. Other conventional techniques devoted to the measurement of mechanical properties of thin films are nanoindentation or the wafer curvature measurement method under thermal cycles (Nix, 1989) but these techniques are not adapted for freestanding thin films. Figure 2.11 represents a series of nanomechanical testing methods which have been successfully applied to freestanding thin films. Various experimental set ups transpose a miniaturized version of macroscopic tensile tests. The first microtensile mechanical testing systems have been imagined by Sharpe et al. (1997) and Tsuchiya et al. (1998) (see Figure 2.11(a)). Electrostatic and piezoelectric external actuators have been used to pull on the films. As depicted in Figure 2.11(b), the nano-manipulator used to transfer thin ribbons can also actuate the force for deforming the test material, while gluing or welding the opposite side of the sample to a force sensor (Prakash et al., 2011). After focus ion beam (FIB) machining, specimens are connected to specific gripper or AFM equipments which pull them in tension (Kiener et al., 2008; Jang and Greer, 2011). Such set ups allow direct *in situ* observations within a scanning electron microscope (SEM). Similar approach has been developed by Kang and Saif (2010) for thin films. One of the major difficulties in the techniques (a-c) cited above is the proper connection between specimens and external loading devices. A small misalignment of the specimen induces off-axis loading and invalidates indeed the accurate extraction of stress and strain (Kang et al., 2010).

Microelectromechanical systems (MEMS) can be advantageously used to

circumvent these issues as specimens, actuators and strain sensors can be directly integrated on the testing frame. Figures 2.11(d-f) provides examples of tensile testing methods based on MEMS fabrication techniques. Figure 2.11(d) show the MEMS-based testing approach proposed by Haque and Saif (2002). An external piezo-actuator is still required to pull on the sample which is directly deposited on a supporting beam structure, specially designed to minimize misalignment. Espinosa et al. (2007) have proposed a fully integrated MEMS based method with both actuation and sensing embedded on the test stage. The technique illustrated in Figure 2.11(e), relies on electrostatic or electrothermal actuators. These testing stages enable transmission electron microscope (TEM) imaging as the back etching of the wafer under the specimen allows *in situ* characterization, see e.g. (Hosseinian et al., 2016). On-chip actuation of elementary tensile testing structures has been proposed at UCLouvain. The underlying idea of this technique, schematically represented in Figure 2.11(f), is to use internal stress generated in one film to deform another film. Chapter 3 extensively describes this technique as it is the main testing technique used in this thesis. All previous on-chip methods require micro- and nano-fabrication techniques as lithography and etching in order to prepare the samples and the associated testing stage.

Other loading configurations have also been suggested. Espinosa et al. (2004) have developed a nanoindentation based method, represented in Figure 2.11(g), to test free-standing clamped beams under purely uniaxial tensile conditions within the gauge sections. The stress is related to the nanoindentor load while interferometry measurement is used to extract the strain. The bulge test, shown in Figure 2.11(h) consists in deflecting a thin membrane by means of a pressurized fluid and involves biaxial loading conditions which can vary from plane strain to equibiaxial stretching depending on the aspect ratio of the membrane, see e.g. (Xiang and Vlassak, 2006; Nicola et al., 2006).

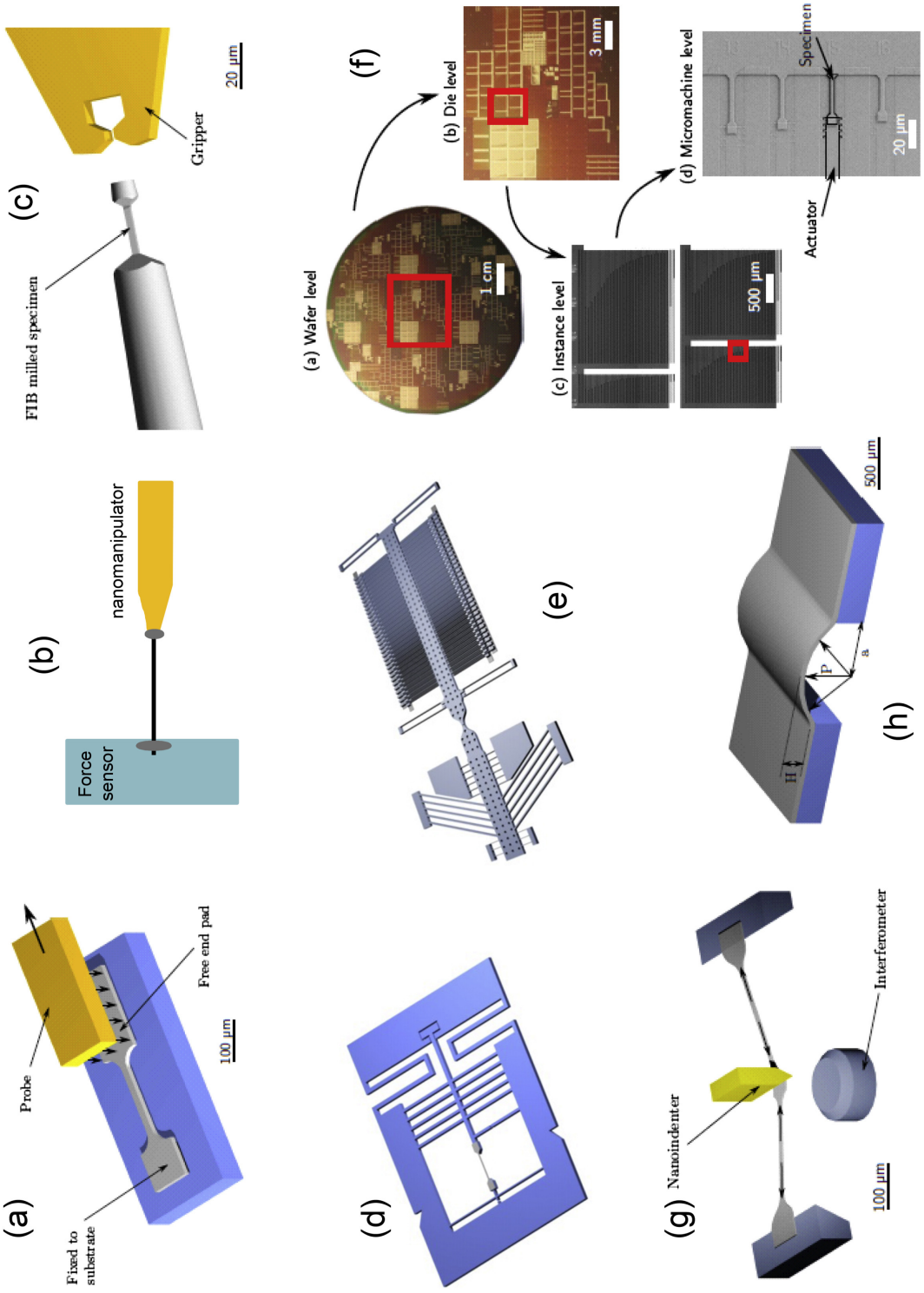

Fig. 2.11: Various set ups for testing the mechanical properties of freestanding thin films: (a) tensile stage by Tsuchiya and co-workers, (b) nanomanipulator directly used to apply deformation, (c) FIB machined micro grips, (d) MEMS based test frame by Haque and Saif, (e) MEMS tensile stage by Espinosa and collaborators, (f) the UCLouvain on-chip testing laboratory, (g) tensile loading through deflection, (h) bulge test configuration. Image reproduced from Pineau et al. (2016).

CHAPTER 3

Contribution to the UCLouvain on-chip nanomechanical test method

The continuous progress in micro- and nano-fabrication techniques has opened new fields of applications for nanoscale objects such as sub-micron thin films. For several years, major effort has been devoted to the understanding of the mechanical behaviour and deformation mechanisms of materials at such small scale. The impact of these researches also concerns other fields like coatings and thin membranes. For supporting this new research domain, the scientific community has designed new testing devices able to extract the mechanical behaviour of nanoscale objects.

The versatile on-chip MEMS-based method, developed at UCLouvain in the year 2007-2008, is devoted to the deformation behaviour of freestanding thin films. It relies on micro-fabrication techniques used to produce MEMS. In this chapter, the basic concept of the technique is briefly presented and the data reduction scheme is subsequently detailed. Then, some contributions of the present thesis are presented. First, I have adapted the fabrication process to the specific application on nickel films. Next, the UCLouvain on-chip technique is for the first time analysed through finite element modelling. The aim of this analysis is to answer the following question: how does the chosen design influence the extracted stress and strain as well as the loading path? Errors between the real and the extracted mechanical behaviour are computed and some design guidelines are given. Afterwards, improved data reduction schemes are proposed in order to precisely extract the strain and the stress

in the specimen. Finally, the effect of plasticity and viscoplasticity is investigated and the last subsection aims at providing an estimate of the strain rate undergone during the release of the specimen.

3.1 The concept

The underlying idea of the on-chip technique is to use internal stress generated during the deposition of an "actuator" beam in order to pull on another thin material sample (see Figure 3.1). When the underneath sacrificial layer is etched away, the actuator is free to contract and thus to stretch the sample until force equilibrium is reached (Gravier et al., 2009). The present testing method differs from the majority of techniques presented in the literature (see section 2.7) as hundreds of elementary tests are simultaneously carried out on a single 3 inch silicon wafer; each elementary structure providing one point of the stress-strain curve. Using the micro- and nano-fabrication techniques, it is easy to reproduce a high number of elementary structures. It also gives the possibility to control and progressively vary the deformation state inside different specimens without the need to build a complex multi-purpose testing stage. The main drawback of the technique is that the sample cannot be analysed *in situ* due to process requirement. So some relaxation might already occur between the time of release and the first measurement.

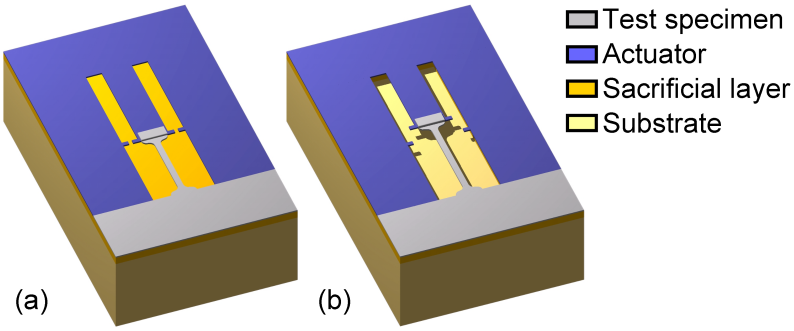

Fig. 3.1: Elementary internal stress actuated uniaxial tensile test structure, (a) before release, (b) after release. Direct measurement of the cursor displacement allows to recover one point of the stress-strain curve.

An elementary tensile testing structure, called "micromachine", is built on top of a silicon wafer (see fig 3.2). First, a sacrificial layer is deposited over the entire substrate without patterning. The actuator layer is deposited on top of the sacrificial layer. The material of this layer involves high tensile internal stresses in order to provide the actuating force. This actuator layer is patterned by lithography techniques. Then, the specimen layer is deposited and also patterned, see Figure 3.2(f). The sacrificial layer is etched away to release the structure. The specimen beam is deformed in tension owing to the contraction

of the actuator, see Figure 3.2(g). During the release step, the actuator beam relaxes elastically acting as a spring while the force in the specimen beam force raises until force equilibrium is reached. The stress and the mechanical strain in the specimen can be directly inferred from the displacement u measured between dedicated cursors (see Figure 3.1(b) and section 3.2). Different levels of stress can be imposed by changing the length or the width of the actuator and/or of the test specimen, allowing the determination of a full stress strain curve from small strain elastic behaviour up to fracture.

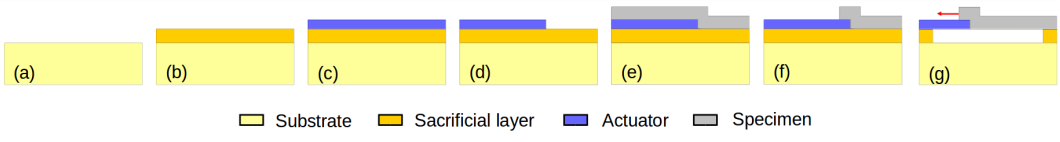

Fig. 3.2: Processing steps used to prepare tensile structures. (a) substrate, (b) deposition of the sacrificial layer, (c) deposition of the actuator, (d) patterning of the actuator, (e) deposition of the specimen layer, (f) patterning of the specimen and (g) release

The selected material of each layer has to fulfil some specific requirements. The actuator layer has to contain a high level of tensile internal stress and the internal stress gradient through the thickness has to be negligible to avoid out-of-plane deformation. The actuator has to be a though material which only deforms elastically without any visco-elastic or plastic effects to provide an accurate mechanical analysis. The choice of the specimen layer is dictated by scientific or practical interest. The specimen can contain tensile or compressive internal stresses. Under these conditions, the specimen and the actuator can actually be made of the same material if it respects all the requirements. The sacrificial layer has to be easily removed by a selective etching solution without harming the actuator nor the specimen layers. The selection of the material of each layer, envisaged in this thesis, is presented in section 3.3.

3.2 Mechanical analysis

In the case of uniaxial tension, the stress σ^s and the mechanical strain ε^s_{mech} in the specimen can be directly inferred from the displacement u measured between a moving and a fixed cursor using scanning electron microscopy, from the knowledge of the Young's modulus of the actuator, and from the mismatch strain of both the actuator ε^a_{mis} and the test specimen ε^s_{mis}. These mismatch strains result from the fabrication process and from the deposition steps. The experimental approach is presented in this section. The mechanical analysis starts by considering the actuator. Then, the analysis of the stress state in the specimen subjected to uniaxial tension is presented. The characteristic dimen-

sions and properties of actuator and sample layers are respectively denoted by the subscript $()^a$ and $()^s$.

The total strain in the actuator ε_a is assumed to be the sum of the mechanical strain ε^a_{mech} and the mismatch strain ε^a_{mis}:

$$\varepsilon^a = \varepsilon^a_{mech} + \varepsilon^a_{mis}. \tag{3.1}$$

By convention, a contraction of the actuator is associated to a positive displacement $u > 0$. The strain in the actuator ε^a writes:

$$\varepsilon^a = ln\left(\frac{l^a_{nom} - u}{l^a_{nom}}\right) \simeq \frac{-u}{l^a_{nom}} \tag{3.2}$$

where l^a_{nom} is the nominal initial length (i.e. before release) of a constrained actuator and u is the displacement measured at the actuator cursor after the release. As the actuator remains elastic during deformation, the stress σ^a is directly determined from Hooke's law:

$$\sigma^a = E^a \varepsilon^a_{mech} \tag{3.3}$$

where E^a is the Young's modulus of the actuator. Using equation (3.3), it is possible to calculate the load F corresponding to a constrained actuator of cross section area, A^a:

$$\begin{aligned} F = A^a\sigma^a = A^a E^a \varepsilon^a_{mech} &= A^a E^a \left(\varepsilon^a - \varepsilon^a_{mis}\right) \\ &= A^a E^a \left(\frac{-u}{l^a_{nom}} - \varepsilon^a_{mis}\right). \end{aligned} \tag{3.4}$$

If we now consider uniaxial tension in the specimen, the total deformation of the specimen ε^s which can deform up to large deformation is given by:

$$\varepsilon^s = \varepsilon^s_{mech} + \varepsilon^s_{mis} = ln\left(\frac{l^s_{nom} + u}{l^s_{nom}}\right) \tag{3.5}$$

where l^s_{nom} is the nominal length (i.e. before release) of the specimen. The stress inside the specimen of cross section area, A^s, can be inferred directly from the force equilibrium, i.e. $F = \sigma^a A^a = \sigma^s A^s$. This leads to:

$$\sigma^s = \frac{F}{A^s} = \frac{A^a}{A^s} E^a \left(\frac{-u}{l^a_{nom}} - \varepsilon^a_{mis}\right). \tag{3.6}$$

Equations (3.5) and (3.6) provide one point of the specimen stress-strain response. By varying the geometrical dimensions of the elementary test structure, it is possible to cover a large range of stresses and strains in the specimen, giving access to the full stress-strain curve of the specimen. As a consequence, the design includes micromachines with varying dimensions. Specifically, long

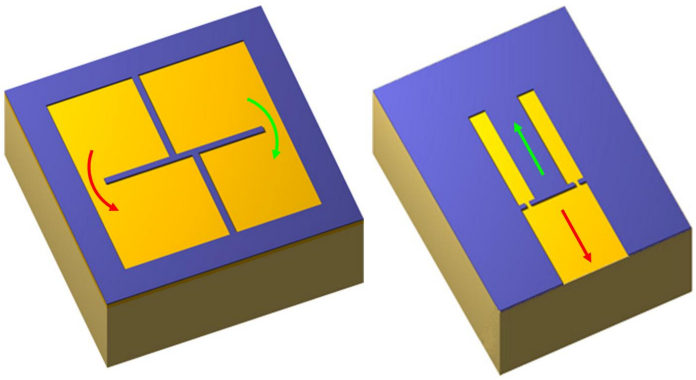

Fig. 3.3: Rotating sensor (a) and free beam (b) structures before release. The red (green) arrows represent the motion of the structure after the release of a film with compressive (tensile) internal stress.

specimens and short actuators provide small stress, deforming only elastically the sample while short specimens and long actuators involve higher stress, possibly leading to plasticity in ductile materials. The effect of width and thickness ratio is similar. Typical widths are 10-15 μm and 1-6 μm for the actuator and specimen beams, respectively. The total length of the structure (actuator and specimen) is between 500 and 2000 μm.

The design and error analysis have been detailed in Gravier et al. (2009). The most important sources of error on the stress extraction comes from the errors on the measurement of u and ε_a^{mis}. While u is measured by direct SEM observation, the mismatch strain of the actuator and of the specimen is calculated from the analysis of free beam structures, auto-actuated structures, rotating sensors or by the measurement of internal stresses. These dedicated structures are located close to the tensile testing structures, giving locally access to the internal stress and allowing the evaluation of its homogeneity on the substrate.

Before patterning, the mismatch strain can be determined using wafer curvature measurements in order to compute the internal stress σ_{Stoney} and then recover the mismatch strain:

$$\sigma_{Stoney} = \frac{1}{6}\frac{E^{sub}}{1-\nu^{sub}}\frac{\left(h^{sub}\right)^2}{h^f}\Delta\kappa. \tag{3.7}$$

where $E^{sub}/(1-\nu^{sub})$ is the biaxial modulus of the silicon substrate, h^{sub} is the substrate thickness, h^f the film thickness and $\Delta\kappa$ is the variation of the sample curvature (due to equibiaxial stress), measured by profilometry. The corresponding deformation is given by:

$$\varepsilon_{mis}^a = \sigma_{Stoney}\frac{1-\nu^a}{E^a}. \tag{3.8}$$

Using for instance free actuators consisting in a beam connected to an anchor on one side (see Figure 3.3(a)), the mismatch strain inside the actuator can be probed after the release and ε^a_{mis} writes:

$$\varepsilon^a_{mis} = \ln\left(1 - \frac{u^{free}}{l^{free}_{nom}}\right) \tag{3.9}$$

where u^{free} is the displacement measured at the actuator cursor after the release of a free actuator ($u < u^{free}$) and l^{free}_{nom} is the nominal length a free actuator. As a matter of fact, in the case of a free actuator, as no external loading is applied, the mechanical stress is zero. After the release and subsequent total relaxation of the internal stress, the total strain is thus exactly equal to the mismatch strain.

Another kind of structures used to locally measure the internal stress are the rotating sensors. As depicted in Figure 3.3(a), these structures consist of a central beam perpendicular to two clamped arms. When the structure is released from the substrate, the arms contract or extend. The mismatch strain is then inferred from the deviation of the central beam using analytical formula or FE simulations (He et al., 2008).

In the case of auto-actuated structures, the test devices are designed identical as the uniaxial tensile testing structures but the actuator and specimen beams are constituted of the same material. ε^a_{mis} is derived from the cursor displacement as for classical uniaxial tensile testing structures. Assuming that both the actuator and the specimen remain elastic, force equilibrium conditions lead to

$$\varepsilon^a_{mis} = \frac{A^s \ln\left(\frac{l^s_{nom}+u}{l^s_{nom}}\right) + A^a \frac{u}{l^a_{nom}}}{A^s - A^a}. \tag{3.10}$$

The accuracy on u is considered to be less than 50 nm when using high magnification FEG SEM micrographs. The current accuracy estimation of the mismatch strain is about 5% using dedicated test structures near the set of tensile structures, such as free actuators and self-actuators. This leads to an error on the stress of around 10%. Regarding the measurement of the strain, only the error on u is critical, resulting in less than 5% relative error on the strain.

3.3 Contribution to the fabrication process and material selection

In the last decade, there has been a growing interest towards the use of nanocrystalline nickel films for their potential applications in micro-mechanical switches and actuators due to their mechanical and catalytic properties. Nanocrystalline nickel present also high corrosion and wear resistance properties.

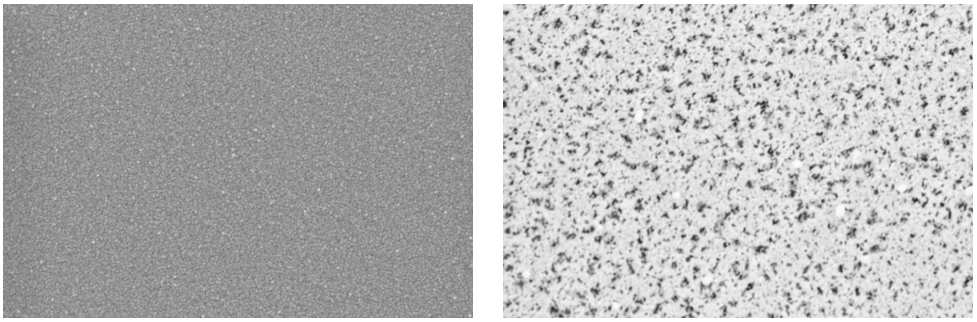

(a) After deposition **(b)** After 1 min etching of HF 73%

Fig. 3.4: Plane view of the Ni films before and after HF 73% etching during 1 min. Note the surface heterogeneity after HF etching.

In the present thesis, specific layers and fabrication steps have been investigated to adapt the lab-on-chip technique to Ni. Despite several attempts, no viable fabrication process for Ni on-chip structures has been found. Nevertheless, the details of the proposed process used to produce test structures dedicated to Ni are described in this section as a way to keep memory of the critical aspects for future developments. Figure 3.2 illustrates the fabrication process. The whole process has been performed in the WINFAB class 100 cleanroom facilities.

Substrate selection. The substrates used in WINFAB cleanrooms are pure {100} monocrystalline Si wafers with a diameter of 3 inches and a thickness equal to 380 μm, polished on the front face. Wafers with monotonic curvature are selected by profilometry in order to accurately measure the radius of curvature of the substrate and get a precise value of the internal stresses using equation 3.7.

Sacrificial layer. This layer has to be etched away by wet or dry etching without damaging the actuator nor the specimen layer. The first attempt was to use 1 μm thick silicon dioxide sacrificial layer and a wet release using hydrofluoric acid, HF 73%. The best compromise between layer quality and etching time is to use plasma enhanced chemical vapour deposition (PECVD) to deposit the SiO_2 layer. The precursor gases were composed of 100 sccm of SiH_4, 700 sccm of N_2O and 350 sccm of N_2. The deposition was made at 300°C and was densified during 20 minutes at 800°C. Nevertheless the selectivity of HF etchant for the Ni layer (i.e. the ratio of the etching rate of the sacrificial layer and of the specimen) was low. HF etching profoundly modified the surface state and the roughness of the Ni layer as shown in Figure 3.4. A second successful attempt was to use the silicon substrate itself as sacrificial layer and TMAH or XeF_2 etching. For TMAH etching, $\langle 100 \rangle$ directions were oriented at an angle of 45° with respect to the Si flat.

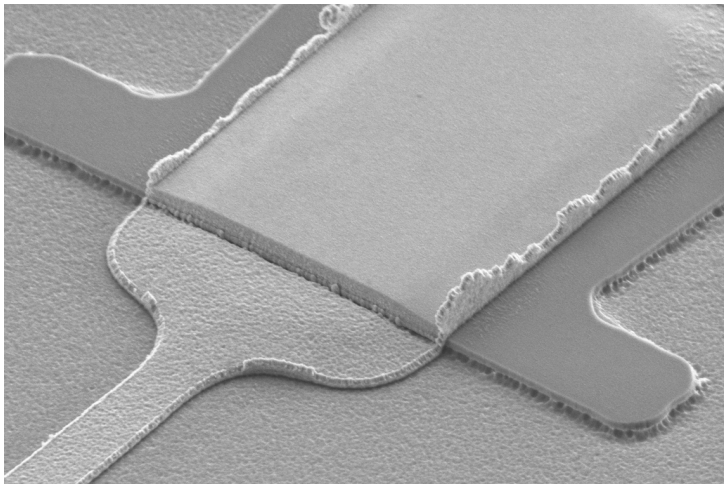

Fig. 3.5: Illustration of the overetching of the Si sacrificial layer due to the selectivity of SF_6 gas. The overetching was such that the Ni layer does not overlap the actuator, resulting in no anchor between the 2 layers.

Actuator layer deposition and patterning. As previously mentioned, the actuator dimensions and mechanical properties are the key elements to load the specimen and to extract its mechanical behaviour. This layer has to present a high level of tensile internal stress and to be as uniform as possible over the entire wafer. Hence, a low pressure chemical vapour deposition (LPCVD) Si_3N_4 layer was deposited at 800°C on top of the sacrificial layer in a Koyo VF-1000LP. The precursor gases were 30 sccm of SiH_2Cl_2 and 120 sccm of NH_3 at a pressure of 35 Pa in the tube. The induced tensile internal stresses were observed to be thickness independent and around ∼1 GPa. The thickness uniformity was very good, varying by approximately $1-3$ nm over the entire wafer. As the LPCVD method was used, Si_3N_4 was deposited on both sides of the substrates. Prior to the actuator patterning on the front face, this layer was totally etched on the back face by dry etching with SF_6 and internal stress was measured by profilometry. Then a positive photolithography was used for the patterning of the actuator layer. A positive photoresist (AZ6612) was deposited on the actuator layer. After prebaking at 110°C for 90s, the photoresist is exposed to UV light with a patterning mask during 3.4s. The exposed photoresist is then dissolved in a TMAH-based solution (AZ 726 MIF) during 60s. A post-exposure bake of 90s at 130° densified the remaining photoresist. The photolithography was followed by a SF_6 plasma etching, patterning the Si_3N_4 layer. To prevent overetching of the Si sacrificial layer due to the low selectivity of SF_6 (as illustrated in Figure 3.5, the last 20 nm of Si_3N_4 were etched by CHF_3 plasma. The remaining photoresist was removed with acetone.

Specimen layer deposition and patterning. Only pure Ni films have been investigated in this thesis. The Ni films were patterned using lift-off pho-

tolithography. In contrast to the positive lithography of the actuator, a negative photoresist (AZ5214E) was first deposited and patterned. After prebaking at 110°C for 90s, the photoresist was exposed to UV light with a patterning mask during 2s. A post-baking of 40s at 120°C was then performed, followed by a flood exposure without mask during 6s. The negative photoresist was then developed in the AZ 726 MIF solution. The Ni was then deposited non-conformally over the resist. The material deposited on the photoresist was then lifted off by dissolving the resist in acetone within an ultrasonic bath while the material deposited between the resist remains on the substrate. Ni films were first deposited using e-beam evaporation. The intrinsic magnetic field of Ni deviates the electron beam and thus did not allow a proper control of the deposition rates. High internal tensile stresses[1] were generated over 1 GPa, leading to cracking issues in many locations (e.g. at corners, see Figure 3.6). In order to circumvent these difficulties, 300 nm thick Ni thin films were fabricated by direct current magnetron sputtering in a chamber from AJA under an argon (Ar) plasma pressure of 6 mTorr, at room temperature. To ensure a good uniformity, the samples were rotated at 45 rpm and put at a relatively large sputtering distance (122 mm) from the high purity Ni target (99.99% purity). Deposition time was 120 min while the sputtering power was 50W. To ensure the adhesion of the overlapping region between the Ni and the Si_3N_4 beams, Ni was deposited on top of a thin TiO_2 adhesion layer deposited by RF sputtering (chamber pressure 2 mTorr and sputtering power 50W during 15 min). The Multi-beam Optical Stress Sensor (MOSS) technique, described in Figure 3.7, was used to evaluate the internal stress during and after the deposition. A CCD camera, mounted inside the AJA deposition chamber, continuously detects the position of an array of 3×4 parallel laser beams, reflected off the cantilevered sample. The variation of sample curvature is given by:

$$\Delta\kappa = Y\ \frac{D - D_0}{D_0} \tag{3.11}$$

where D is the average distance between the reflected spots, D_0 is the initial average distance between the spots and Y is an optical parameter equal to 0.68 m^{-1} for the AJA chamber. The curvature variation is related to the internal stress by the Stoney's equation:

$$\frac{E^{sub}}{1-\nu^{sub}}\frac{\left(h^{sub}\right)^2}{6}\Delta\kappa = h^f\sigma_{MOSS} = \int_0^{h^f}\sigma_{incr}(h)\mathrm{d}h. \tag{3.12}$$

σ_{MOSS} is the average internal stress in the film. When $h^f\sigma_{MOSS}$ is plotted as a function of h^f, its derivative is the incremental internal stress in the film $\sigma_{incr}(h)$, describing the evolution of the internal stress during deposition and

[1] The internal stresses of the evaporated Ni films were determined by wafer curvature measurement on a non-patterned wafer of the same deposition batch. Patterned layers lead indeed to high inaccuracies in the determination of the wafer curvature.

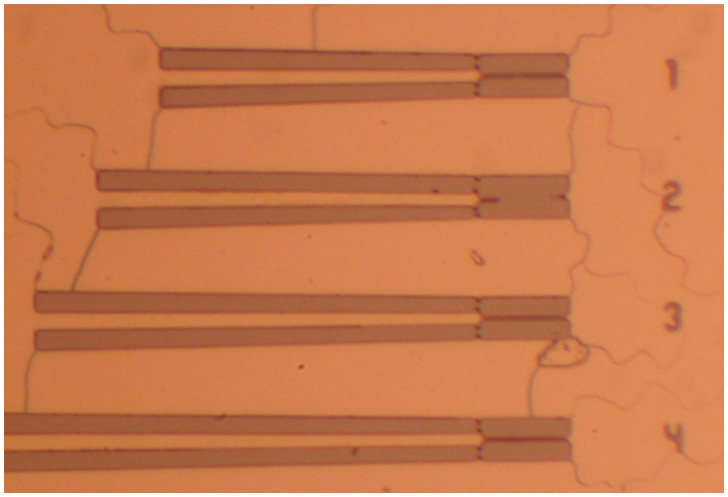

Fig. 3.6: Illustration of the underetching of the Si sacrificial layer due to the selectivity of SF_6 gas. The underetching was such that the Ni layer does not overlap the actuator, resulting in no anchor between the 2 layers.

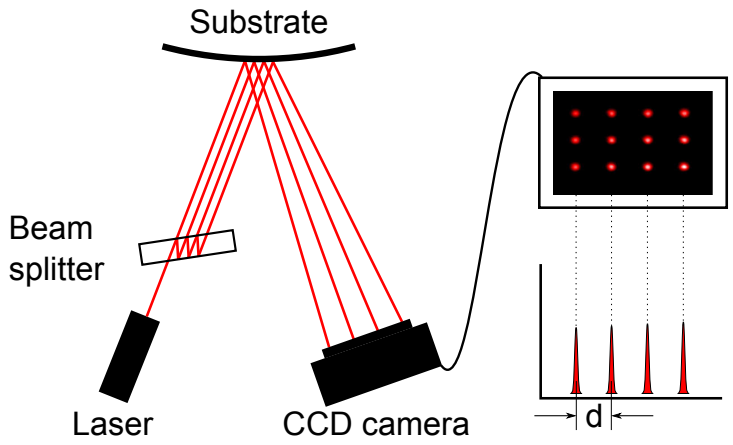

Fig. 3.7: Sketch of the Multi-beam Optical Stress Sensor (MOSS). If internal stresses are generated during the deposition process, the substrate curvature will change. The stress inside a thin film can be computed from the variation of substrate curvature via equation (3.12). To measure the curvature accurately, parallel laser beams are reflected on the substrate and continuously detected by a CCD camera. When the substrate bends, the mean spacing between the spots in the CCD varies and the variation of curvature is directly proportional to the spots distance variation.

possible subsequent relaxation. At the end of the deposition, the mean internal stress inside the Ni layer σ_{MOSS} was around 400 MPa which is a significant reduction compared to the stress level of the first attempts (1 GPa). It is worth to mention that the patterning masks used in this thesis did not allow an *in situ* monitoring of the internal stress. As the whole wafer was patterned, no sufficiently large plane surface was indeed available for the laser beams

reflection and the internal stress was thus measured on plain wafers. The new mask design proposed in 2017 includes now a dedicated area for MOSS measurements.

Release. The final step of the process allows the loading of the Ni specimens after etching of the sacrificial layer. The release was conducted in a TMAH (Tetrametylammonum hydroxide) solution (10% vol) at a fixed temperature of 90°C. The TMAH solution dissolves selectively the Si substrate without any alteration of the Ni and Si_3Ni_4 layers. The etching rate for the $\langle 100 \rangle$ direction was 1μm/min. Note that the TMAH etching is an anisotropic etching which depends on the atomic densities of the Si crystalline planes. This means that freestanding beams can be obtained only if they are oriented along the (100) planes which is at an angle of 45° with respect to the flat of the wafer. Once the etching was completed, the sample was immersed for 10 minutes in deionized water at 50°C to stop etching and to reduce thermal gradient. Afterwards, the sample was left for 2×10 minutes in water at room temperature. As the release was performed in a wet environment, a supercritical drying was required to avoid the stiction of the structures on the underneath substrate. Release by XeF_2 has also been investigated. As XeF_2 etching is inhibited by silicon dioxide and altered by water, a HF 2% cleaning was therefore performed followed by a drying at 110°C during 20 min. The sample was then subjected to 15 pulses of 3s cycle of 2 Torr of XeF_2 etchant.

Even if these two release techniques were successful, no viable micromachines were obtained, except for some samples with very small l^a_{nom}/l^s_{nom} ratio corresponding to the elastic domain. Fracture at the overlap or in the sample was systematically observed, as illustrated in Figure 3.8. The critical aspects for future Ni micromachines development and some possible solutions are listed hereafter but have not been implemented due to the extended unavailability of some equipments in the clean rooms facilities.

- The control of internal stress in the Ni thin film is of prime importance. Adeline Delvaux has recently deposited 100 nm thick Ni thin films exhibiting nearly no internal stress (less than 50 MPa) by magnetron sputtering at room temperature. A sputtering power of 50W under an Ar plasma pressure of 2 mTorr was imposed.

- An adhesion layer between Ni and Si_3N_4 should not be omitted to ensure adherence between the two layers.

- A complete CHF_3 etching of the Si sacrificial layer is advised.

- XeF_2 release is recommended. This dry etching prevents the supplementary CPD step and the temperature variation associated to TMAH etching, affecting mechanical response and delaying the first observation.

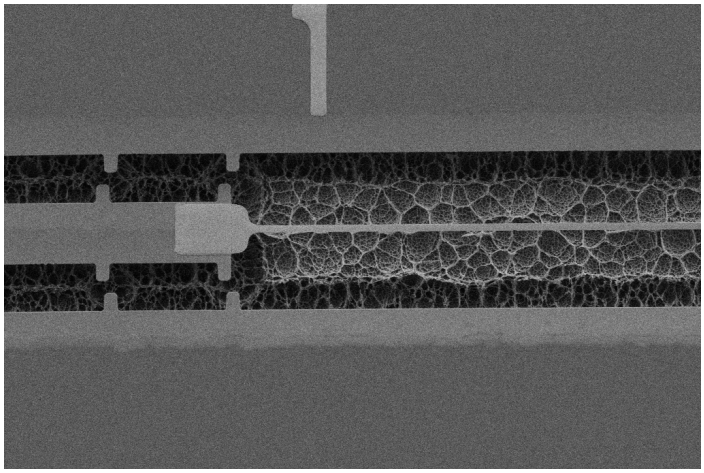

(a)

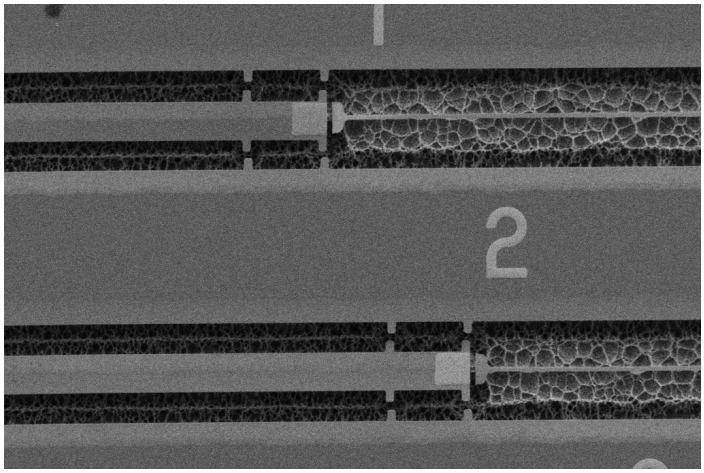

(b)

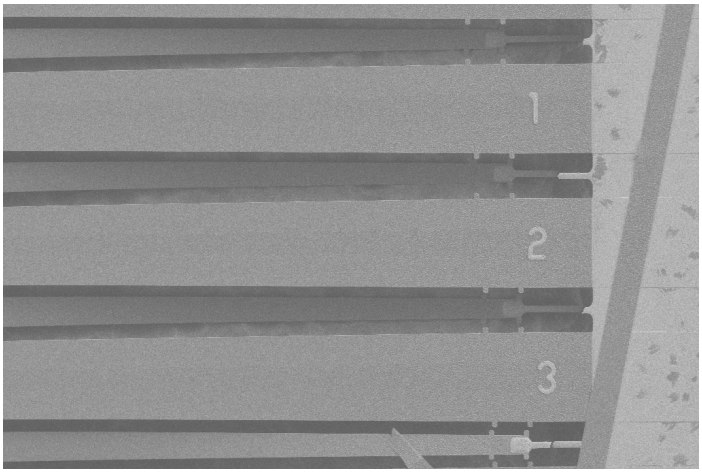

(c)

Fig. 3.8: SEM images of Ni micromachines after XeF_2 release. Figure (a) shows a viable micromachine characterized by very small l^a_{nom}/l^s_{nom} ratio, leading to an elastic loading of the sample. Figures (b) and (c) illustrates the systematic rupture at the overlap (b) or in the sample (c).

3.4 Finite element modelling

The basic data reduction scheme for the extraction of the stress and strain of freestanding beams subjected to uniaxial tension has been exposed in the previous section. In this formulation, an elementary test structure is modelled as two adjacent rectangular beams perfectly connected and perfectly clamped on two external fixed parts. In reality, geometry is not so simple. The specimens are dog-bone shaped: such design ensures uniaxial tension condition along the gauge length and avoids stress concentration at the edges of the gauge. Furthermore, isotropic etching of the sacrificial layer induces the under-etching of the actuator and specimen fixed parts which become partly freestanding. The contribution of all these freestanding parts on the measured displacement u can lead to non-negligible errors on the extracted stress and strain as well as an increase of the experimental dispersion. Despite the awareness of these issues, the impact of the dog-bone and under-etched parts on the extracted value of stress and strain has never been quantified even if Vayrette et al. (2015) and Ghidelli et al. (2017) have proposed some improved data reduction schemes. In order to address these issues, lab-on-chip experiments are performed through finite element simulations. The main objectives of this study are: (i) to quantify the error induced by the under-etched parts and the dog-bone on the stress and strain inferred from the cursor displacement through the original data reduction scheme (Gravier et al., 2009), (ii) to evaluate the relevance of an analytical correction approach on the measured displacement, (iii) to assess the robustness of the structures allowing the determination of the mismatch strain ε_{mis} which is the main source of error on the stress.

In this section, finite element models are used to simulate the test structures from internal stress generation to the progressive release process and the eventual subsequent relaxation. FE simulations are performed using the software ABAQUS while 2D models of the on-chip structure are developed on GMSH (Geuzaine and Remacle, 2009). The present FE modelling focusses on the latest generation of on-chip structures in which the dog-bone shape differs from the previous generations (Vayrette et al., 2015). The dimensions of the structure vary as follows in the new generation: specimen length l^s_{nom} =50-100-200-400 μm, specimen width w^s =1-0.5,2.5-4 μm, actuator length l^a_{nom}, thirty values ranging from 50 to 1500 μm, widths of the tapered actuator: w^a_{min} =10 μm and w^a_{max} =14 μm. Test structures are grouped in instances for which w^s and l^s_{nom} are constant. Nine instances are simulated and model dimensions are limited to the following values tabulated in Table 3.1. As depicted in Figure 3.9, half structures are meshed with second order plane stress triangular elements and the bottom line of the mesh has zero displacement along its normal, corresponding to mirror symmetry conditions. The cursors present on the actuator are not represented here and the displacement of the cursor is instead monitored by the displacement of the interface between the actuator and the specimen in the FE model (see Figure 3.9).

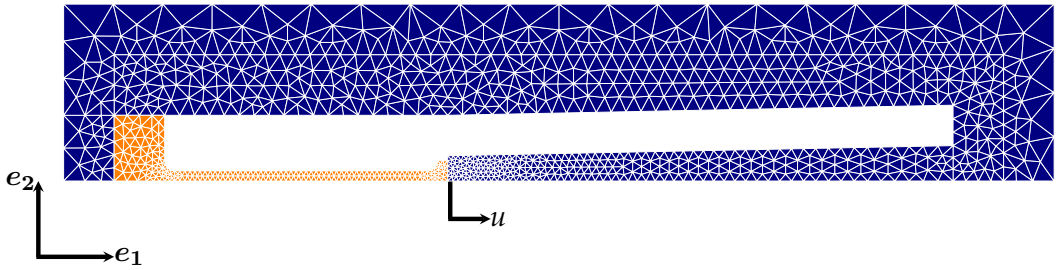

Fig. 3.9: 2D-model of an on-chip structure. Actuator material is represented in blue whereas the specimen material is in orange. The mesh is generated with GMSH. The displacement u is monitored by the displacement of the interface between the actuator and the specimen.

l^s_{nom} [μm]	w^s [μm]	l^a_{nom} [μm]		
50	1.5	50	100	200
200	2.5	250	280	360
400	4	450	550	650
		750	850	950
		1075	1225	1500

Table 3.1: Dimensions of the actuator and specimen FE models

As the underlying idea of the lab-on-chip technique is to use the internal stress created during the deposition of the actuator to pull on another specimen film, biaxial internal stresses are generated by thermal loading while all the nodes of the mesh remain fixed. Even if the origin of the internal stress in the specimen and actuator layer are not precisely known, the present FE model assumes only thermal stresses. Thermal expansion coefficient and temperature variation are chosen such as to build a equibiaxial stress corresponding to the 1075 MPa typically, measured experimentally after the deposition of the actuator. The elastic properties of the actuator have been taken from the measurement performed on the LPCVD Si_3N_4, with a Young's modulus E^a and a Poisson coefficient ν^a equal to 250 GPa and 0.3, respectively.

During the etching step, the different parts of the on-chip structure are progressively released and free to deform: the specimen and actuator beams, the specimen dog-bone shapes, the under-etched specimen and actuator anchoring parts due to the isotropic etching of the underlying sacrificial layer. The etching of the sacrificial layer is simulated by progressively releasing initially blocked node sets. It is assumed that the etching front progresses at constant velocity υ, corresponding to the etching rate, from the edges towards the center of the sample. The progressive release process can be visualized in Figure 3.10 for $\upsilon = 0.181\mu$m/s. The total etching time is decomposed in several time intervals t_k - t_{k+1}. The node set $NSET_k$ associated to the etching time interval t_k - t_{k+1}, contains all nodes n_j of the mesh which have met the

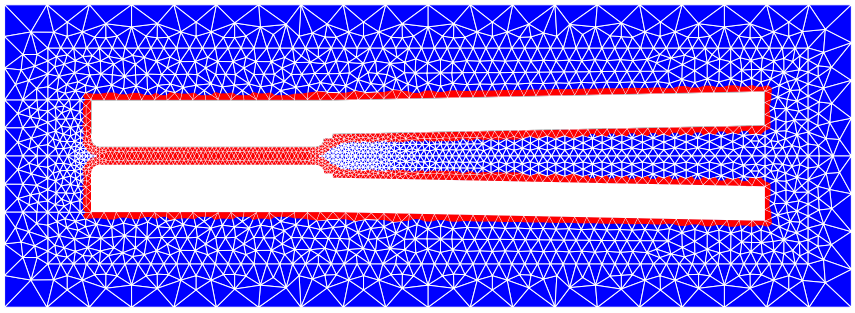

(a) $t = 28s$: the specimen is fully released and freestanding.

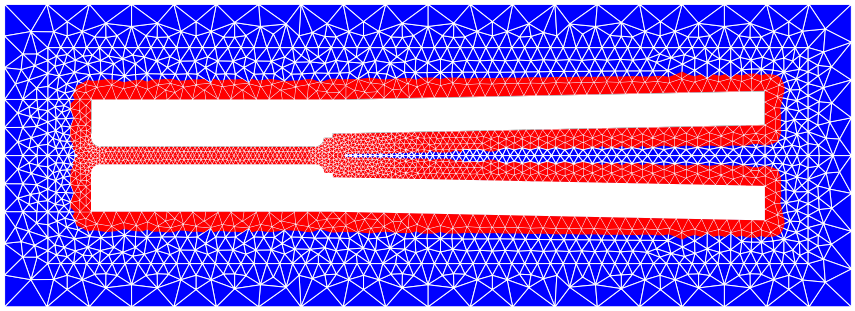

(b) $t = 32s$

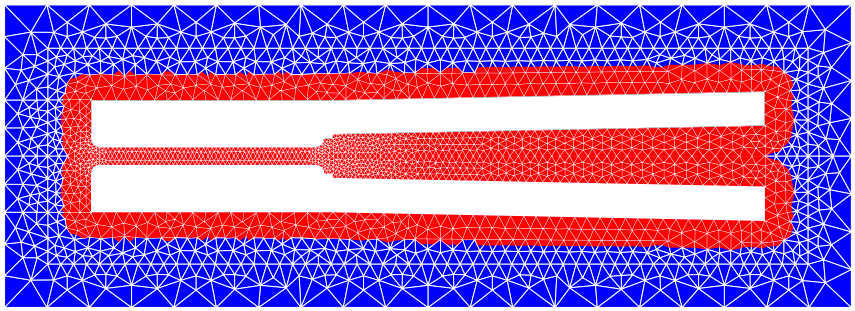

(c) $t = 38s$: the actuator is fully released and freestanding.

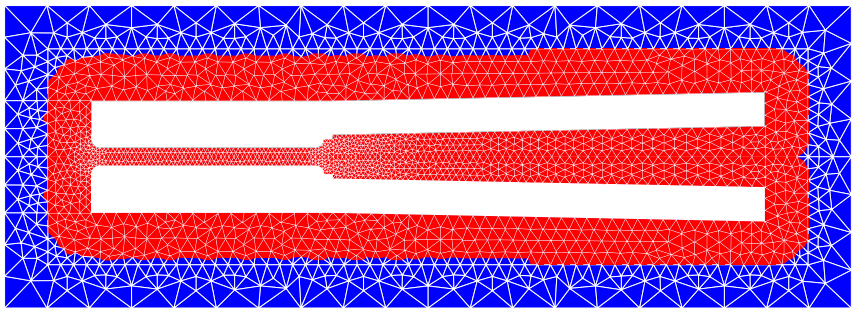

(d) $t = 50s$: the under-etching of the anchoring part further increases.

Fig. 3.10: Visualization of the progressive etching process on the undeformed mesh by successive release of initially blocked node sets. Colors red and blue correspond respectively to released and blocked mesh nodes.

etching front during this laps of time:

$$NSET_k = \{n_j\} \mid vt_k < d_{n_j} \leq vt_{k+1}. \tag{3.13}$$

The distance d_{n_j} associated to the jth mesh node of coordinate (x_{n_j}, y_{n_j}) is the minimum distance of the node to the periphery of the unreleased structure, consisting of the infinitely many points (x_i, y_i) along its length:

$$d_{n_j} = \min_i \left(\sqrt{\left(x_{n_j} - x_i\right)^2 + \left(y_{n_j} - y_i\right)^2} \right). \tag{3.14}$$

d_{n_j} is computed using the Python package Shapely dedicated, to the analysis and manipulation of planar geometries. The simulation includes an over-etching time, corresponding to supplementary etching occurring still after complete release of the actuator. As depicted in Figure 3.10(a), the specimen is earliest released. In Figures 3.10(b) and 3.10(c), the etching front further progresses and the actuator becomes fully released after a laps of time corresponding to $w^a_{max}/2v$. Additional time increases the under-etching of the anchoring parts of the specimen and actuator, see Figure 3.10(d).

3.5 Results

The lab-on-chip method is a versatile technique which can be used for the mechanical characterization of elastic material or elasto-(visco)-plastic material. Nowadays, oxide layers such as silicon, vanadium or zinc oxides are actively studied at UCLouvain for possible applications in coating technologies while previous experimental campaigns have successfully characterized the mechanical behaviour of Al (Coulombier et al., 2010), Pd (Colla, 2014) and Cu (Lapouge et al., 2016) thin films.

Elastic and (visco)-plastic materials are thus investigated in the next subsections. The elastic, plastic and viscoplastic material response are characterized by the material parameters tabulated in Table 3.2. The lab-on-chip experiment is carried out by performing 15×9 FE simulations corresponding to the 9 instances described in Table 3.1. A silicon oxide sacrificial layer is assumed and the etching rate of silicon oxide is set equal to $v = 0.181$ μm/s, corresponding to an HF 47% etching process. A total etching time of 50s is imposed and subdivided into 50 time intervals. An over-etching time of 12s is assumed. The total etched distance is equal to $vt \sim 9\mu$m, typically observed at the under-etched anchoring parts during experiments. The mean stress and strain in the gauge region are recovered by volume averaging of the stress and strain in the gauge region. The macroscopic stress and strain are also inferred from the cursor displacement u following the original data reduction scheme (Gravier et al., 2009) using equations equations (3.5) and (3.6). For the sake of simplicity, the mean stress and strain in the gauge will be referred to from

Actuator	
Elastic	$E^a = 250$ GPa $\nu^a = 0.3$
Specimen	
Elastic	$E^s = 120$ GPa $\nu^s = 0.3$
Plastic	$\sigma_f = \sigma_0(1 + k_S p)^{n_S}$ $\sigma_0 = 400$ MPa $k_S = 250$ $n_S = 0.1$
Viscoplastic	$\sigma_f = \sigma_0(1 + k_S p)^{n_S} (\dot{p}/\dot{p}_0)^m$ $\sigma_0 = 400$ MPa $k_S = 250$ $n_S = 0.1$ $m = 0.05$ $\dot{p}_0 = 0.001$

Table 3.2: Material parameters used for the simulation of the elastic, plastic and viscoplastic materials.

now as σ^s and ε^s whereas the stress and strain extracted from the measured displacement u will be denoted $\sigma^s|_u$ and $\varepsilon^s|_u$. In order to evaluate the impact of the simplified data reduction scheme, relative errors ϵ on the stress and the strain are computed as

$$\epsilon_\varepsilon = \frac{\varepsilon^s - \varepsilon^s|_u}{\varepsilon^s} \qquad \text{and} \qquad \epsilon_\sigma = \frac{\sigma^s - \sigma^s|_u}{\sigma^s}. \tag{3.15}$$

The nominal stress is used to compute ϵ_σ in order to avoid the propagation of the error related to the strain.

3.5.1 Purely elastic material

A model material with a linear elastic behaviour is studied first. Internal stresses of 1075 MPa and 171.5 MPa are generated respectively within the actuator and the specimen. As equibiaxial internal stresses are considered, the mismatch strain of the actuator and of the specimen are obtained using equation (3.8): $\varepsilon^a_{mis} = -0.00301$ and $\varepsilon^s_{mis} = -0.001$ respectively. The simulation results are presented in Figure 3.11(a). The continuous orange curve represents the mechanical behaviour extracted from the gauge region while

the marked lines represent the stress-strain curve ($\varepsilon^s|_u$, $\sigma^s|_u$) from 4 different instances. As expected, the stress state analysis reveals that the initial transverse stress along the direction $\boldsymbol{e_2}$ vanishes after the complete release of the specimen, corresponding to uniaxial tensile loading in the $\boldsymbol{e_1}$ direction. Please refer to Figure 3.9 for the definition of the axes. As the initial stress state in the actuator is equibiaxial before the release, the validity of equation (3.6) may be questioned. During the etching, the actuator is progressively released. Whereas the material remains constrained along the direction $\boldsymbol{e_1}$, the actuator width is free to contract in order to relax the internal stress along the direction $\boldsymbol{e_2}$. This contraction along $\boldsymbol{e_2}$ hinders elongation along $\boldsymbol{e_1}$ (due to the Poisson effect) and this lowers the initial tensile internal stress:

$$\sigma_0^a = \sigma_{biaxial}^a - \nu^a \sigma_{biaxial}^a = -E^a \varepsilon_{mis}^a, \tag{3.16}$$

corresponding to the tensile stress at zero strain in equation (3.6). Furthermore, the evolution of σ^a with ε^a in the FE simulations, follows equation (3.6).

The simplified data reduction scheme clearly underestimates the real stress σ^s (volumetric average). The stress-strain curves ($\varepsilon^s|_u$, $\sigma^s|_u$) deviate from linearity at small strains and vary from an instance to another, highlighting the influence of the specimen geometry. Note that the deviation from linearity originates only from the measured displacement and not from any viscous relaxation. Such dispersion in the results is also observed experimentally, see e.g. (Vayrette et al., 2015). As represented in Figure 3.11(b), very large relative errors on the stress, up to ϵ_σ =10, are observed for $l_{nom}^a < 500\mu$m. As l_{nom}^a increases, ϵ_σ can decrease down to ∼1%. The relative error on the strain ϵ_ε ranges between 0.1 and 10% as depicted in Figure 3.11(c). ϵ_ε decreases with increasing specimen width w^s while the specimen length l_{nom}^s does not really influence the precision. The actuator length has a limited impact on ϵ_ε: after some variation below $l_{nom}^s = 500\mu$m, the relative error remains constant. As a matter of fact, the precision of ($\varepsilon^s|_u$, $\sigma^s|_u$) varies with the dimensions of the actuator and of the specimen.

Careful analysis of the stress state within actuators with $l_{nom}^s < 500\mu$m indicates that the stress field is not uniform and that Saint Venant's Principle may thus not apply in such cases. This principle states that: *The stresses and strains in a body at points that are sufficiently far from points of application of load depends only on the static resultant of the loads and not on the distribution of loads.* The extraction of the σ^s should thus be limited to actuator sufficiently long in order to minimize the influence of the non-uniform actuator field. The actuator anchoring part is under-etched, leading to a distribution of load along a distance around $w_{max}^a + 2w_w + 2vt \sim 50\mu$m for the present simulations (w_w will be defined in section 3.5.1.2 and is represented in Figure 3.14). $l_{nom}^a = 500\mu$m appears to be a relevant lower bound for the actuator length.

The precision errors can lead to misinterpretation of the experimental data. A common procedure for determining the Young's modulus of a material pre-

senting the stress-strain curve in Figure 3.11(a), is to exclude the data points below $\varepsilon = 0.005$ and to obtain the slope of the linear regression of the data points. Such approach leads to the determination of an apparent Young's modulus ranging from 105 GPa to 135 GPa whereas $E^s = 120$ GPa.

3.5.1.1 Structure for the determination of the mismatch strain

The determination of the mismatch strain in the actuator is a critical issue as it directly impacts the extracted stress level inside the specimen. Different methodologies have been presented in section 3.3 to extract the mismatch strain from dedicated structures. The robustness of these structures for the determination of the proper mismatch strain is assessed through FE simulations. The first approach consists in the measurement of the displacement of a trapezoidal free beam which is anchored at one of its edges. The case of an Si_3N_4 free beam with equibiaxial internal stresses equal to 1075 MPa is investigated. The release of free beams of different lengths is simulated during 50s up to complete relaxation of the internal stress. $\varepsilon^a_{mis}|_u$ is then computed from equation (3.9). Figure 3.12(a) represents the variation of ε^a_{mis} as a function of the free beam length l^{free}_{nom}. $\varepsilon^a_{mis}|_u$ decreases with increasing free beam length but is overestimated for any free beam length. Note again the dramatic influence of $l^{free}_{nom} < 500\mu$m on the extracted values. Figure 3.12(b) illustrates the influence of the over-etching time t_{over} on the extracted $\varepsilon^a_{mis}|_u$. As the over-etching time decreases, the contribution of the under-etched part decreases, leading to $\varepsilon^a_{mis}|_u$ almost equal to its true value for long free actuator beams (relative error is less than 3%). This approach is however not suitable for all materials due to possible stress gradient over the layer thickness. The free beams lie no more in a plane but present an out of plane curvature, making it difficult to accurately measure the displacement.

Another possibility is to use auto-actuated structures in which the specimen and the actuator consist of the same material. These dedicated structures are characterized by a specimen length $l^s_{nom} = 1000\mu$m, a specimen width w^s= 1.5 or 2.5 μm and actuator length l^a_{nom} varying from 1000 to 1500 μm. $\varepsilon^a_{mis}|_u$ is given in this specific configuration by equation (3.10) and the corresponding values for the actuator and the specimen simulated in the previous paragraphs, are reported in Figures 3.12(c) and 3.12(d) as a function of l^a_{nom}. The long actuators allows reaching an excellent precision of $\sim 3 \times 10^{-3}$ for the averaged $\varepsilon^a_{mis}|_u$.

3.5.1.2 Corrected data reduction scheme

In order to precisely determine the stress and strain inside the specimen, Vayrette et al. (2015) and Ghidelli et al. (2017) have proposed corrected data reduction schemes on their own. This section presents their correction models and outlines their limitations. A new analytical correction model is then

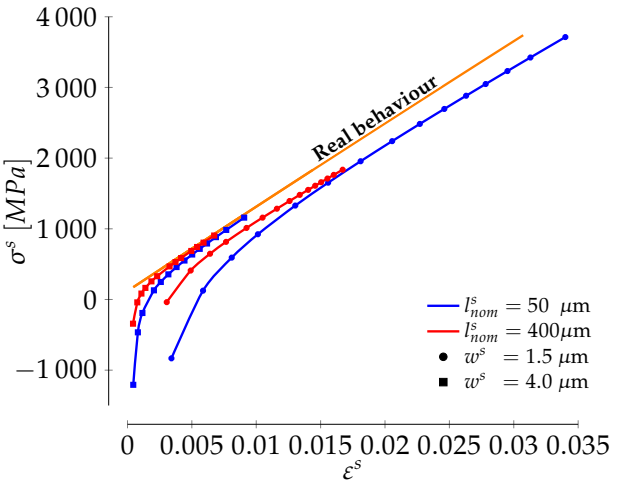

(a) Stress-strain curve

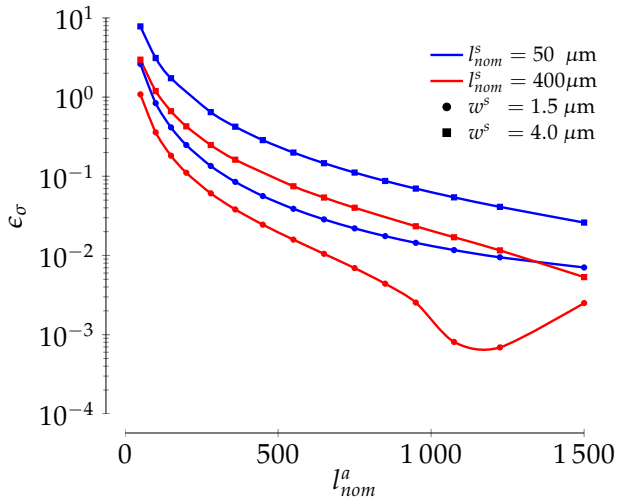

(b) Relative error on σ^s

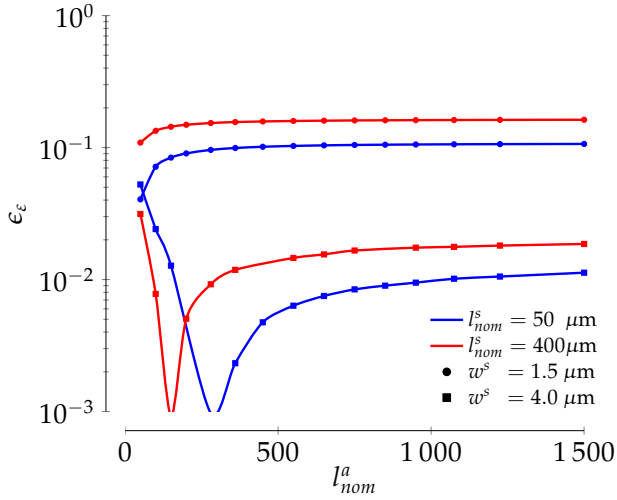

(c) Relative error on ε^s

Fig. 3.11: (a) Comparison between the real behaviour and the extracted stress-strain curves for 4 different instances; (b-c) relative errors on the extracted stress ϵ_σ and strain ϵ_ε for the case of a purely elastic material.

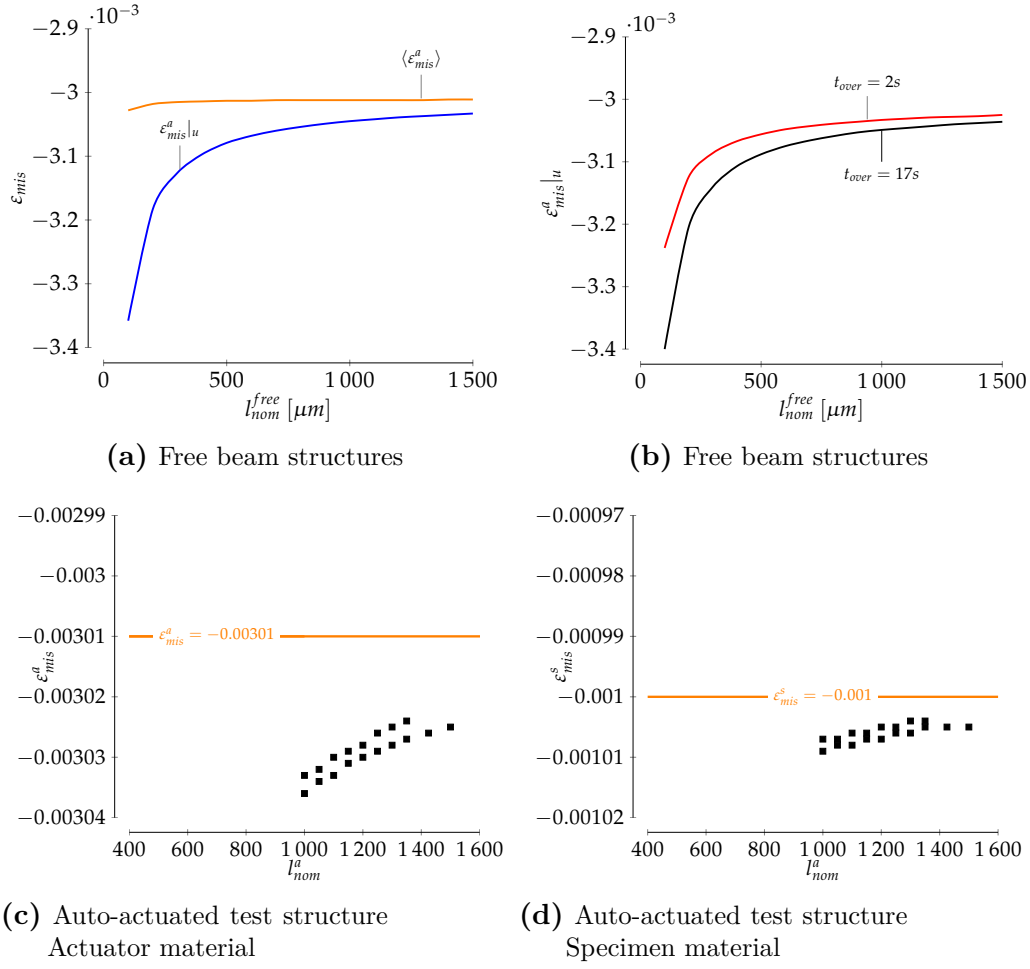

(a) Free beam structures

(b) Free beam structures

(c) Auto-actuated test structure Actuator material

(d) Auto-actuated test structure Specimen material

Fig. 3.12: Predicted mismatch strains extracted from dedicated structures: free beam structures and auto-actuated test structures.

presented and compared to the FE predictions.

Vayrette et al. (2015) considered the contributions of all the freestanding parts of the test structures as illustrated in Figure 3.13. A elementary structure is decomposed into seven sub-regions: the actuator beam, the specimen dogbone region and gauge length, the overlap region and the under-etching zones due to the underlying sacrificial layer. A full 1D description of the system taking into account the influence of each deforming part of the structure is formulated by modelling the 8 sub-regions in series. The measured displacement u is expressed as the sum of discrete displacement associated to each freestanding sub-region i at the same side of the cursor:

$$u = -\left(u^a_{ue} + u^a\right) \tag{3.17}$$

$$u = u^s_{over} + u^s_{dg_L} + u^s_{gauge} + u^s_{dg_R} + u^s_{ue}. \tag{3.18}$$

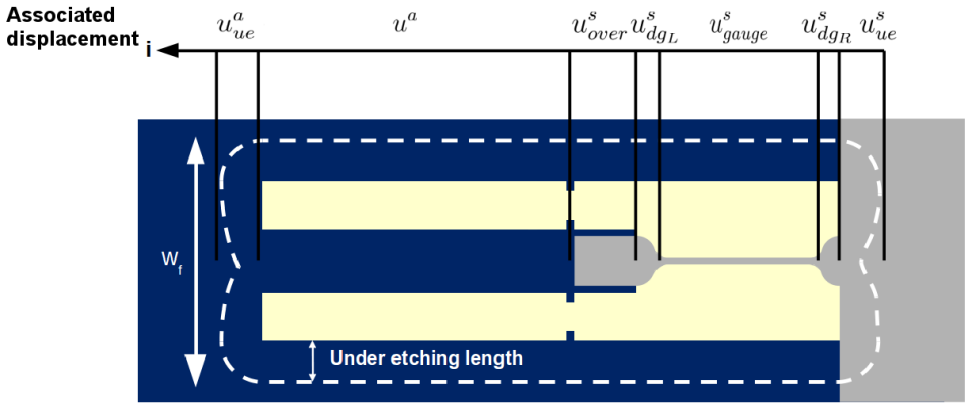

Fig. 3.13: Schematic representation of the correction model proposed by Vayrette et al. (2015) for one elementary uniaxial tensile testing structure.

Using the small strain formalism, the mechanical strain of sub-region i writes

$$\varepsilon^i_{mech} = \varepsilon^i - \varepsilon^i_{mis} = \ln\left(1 + \frac{u^i}{l^i}\right) - \varepsilon^i_{mis} \approx \frac{u^i}{l^i} - \varepsilon^i_{mis}. \tag{3.19}$$

Once force equilibrium is reached after the release, the force F in each subregion i is equal: $F = |\sigma^i A^i|$. The accurate extraction of F is fundamental for a precise determination of the stress in the gauge specimen. The contribution of the overetched region of the actuator, u^a_{ue} has to be removed. As the actuator layer behaves like a linear spring, Hooke's law gives

$$F = A^i E^a \left(\frac{u^i}{l^i} - \varepsilon^i_{mis}\right). \tag{3.20}$$

Assuming that the geometrical features of the two actuator sub-regions are known, the force equilibrium leads the following expression of the displacement beam u^a:

$$u^a = \frac{l^a_{ue}\varepsilon^a_{mis}\left(\dfrac{A^a_{nom}}{A^a_{ue}} - 1\right) - u}{\dfrac{A^a_{nom}}{A^a_{ue}}\dfrac{l^a_{ue}}{l^a_{nom}} + 1} \tag{3.21}$$

where A^a_{ue} is estimated equal to $w^f h^a$ (see figure 3.13 for the definition of w^f). F is then computed using equation (3.20), giving access to each value of the stress σ^i.

The strain in the gauge length is finally determined by a dichotomy method. The specimen Young's modulus E^s is iteratively adapted until the sum of the computed displacement of all the specimen sub-regions matches with the measured displacement u. A key limitation of this approach is that the identified E^s varies from an on-chip structure to another, loosing the intrinsic uniqueness of the Young's modulus definition. This approach may also not be practical for plastic and visco-plastic materials.

In the same vein, Ghidelli et al. (2017) recently proposed a simpler corrected data reduction scheme where the effect of under-etching and of the change of thickness along the specimen width are included. The under-etching leads to an effective beam length longer than the nominal value. The effective actuator length l^a_{eff} is the sum of the nominal actuator length l^a_{nom} and of the under-etching length l^a_{ue}, estimated to distance vt covered by the etching front during the release :

$$l^a_{eff} = l^a_{nom} + l^a_{ue}. \tag{3.22}$$

The measured displacement u can be decomposed into two contributions: the contraction of the actuator beam u^a and a displacement related to the under-etched zone contraction u^a_{ue}:

$$u = u^a + u^a_{ue} \tag{3.23}$$

in which u^a_{ue} is estimated as the displacement of a free beam of equivalent length l^a_{ue}:

$$u^a_{ue} = -\varepsilon^{mis}_a l^a_{ue}. \tag{3.24}$$

The displacement change corresponding to the contraction of the actuator beam can be extracted by combining equations (3.23) and (3.24).

Neglecting the overlap region, the measured displacement is decomposed on the specimen side as follows

$$u = u^s_{gauge} + u^s_{db} + u^s_{ue} \tag{3.25}$$

where u^s_{gauge} is the true displacement imposed to the gauge section of the specimen, u^s_{db} is the displacement of the dogbone parts of the specimen and u^s_{ue} is the under-etching displacement associated to the specimen. According to Vayrette et al. (2015), u^s_{db} and u^s_{ue} can be estimated by a simple 1D isoforce approach for an elastic material as:

$$u^s_{db} = u\left(\frac{w^s}{w^{eff}_{db}}\right)\left(\frac{l^s_{db}}{l_{tot}}\right) \tag{3.26}$$

$$u^s_{ue} = u\left(\frac{w}{w^{eff}_{ue}}\right)\left(\frac{l^s_{ue}}{l_{tot}}\right) \tag{3.27}$$

where w^{eff}_{db} and w^{eff}_{ue} are, respectively, the effective width of the dogbone and the effective width of the under-etching zone while l^s_{db} is the dogbone length and $l_{tot} = l^s_{nom} + l^s_{db} + l^s_{ue}$, the total length of the specimen. Direct estimation of w^{eff}_{db} and w^{eff}_{ue} is avoided by simplifying equations (3.26) and (3.27). The displacement imposed to the gauge length writes finally:

$$u^s_{gauge} = u - u\Omega(l^s_{db} + l^s_{ue})/l^s_{tot} \quad \text{with} \quad \Omega = w^s/w^s_{eff} \tag{3.28}$$

where w^s_{eff} is the effective width of the specimen. Ghidelli et al. (2017) select $\Omega = 0.3$ in order to ensure that the elastic regime in the computed stress-strain curve intersects the origin ($\varepsilon^s = 0, \sigma^s = 0$). The mechanical strain and

stress in the specimen can finally be calculated by replacing respectively u by u^s_{gauge} in equation (3.5) and u by u^a in equation (3.6) where A^s can also be corrected to take into account the possible thickness variation of the specimen induced by shadow effect of the photoresist during the specimen deposition by sputtering. This approach needs again some extension for plastic and visco-plastic materials.

In this thesis, the data reduction scheme has been improved by integrating all the geometrical features of the freestanding test structures in a more systematic way, excluding any fitting approach. Correction factors are proposed based on force equilibrium. Following Vayrette et al. (2015), a on-chip structure is decomposed in several subregions i: the actuator, the actuator under-etched region, the specimen gauge, the specimen dogbones, the specimen under-etched regions and the specimen region linking the dogbone to the actuator. The influence of the overlap region is neglected. Assuming small strains, the elastic strain ε^i_{mech} of geometrical subregions i of the actuator or of the specimen can be determined by

$$\varepsilon^i_{mech} = \frac{F}{E^i h^i w^i(x)} \tag{3.29}$$

where F is the applied force, h^i the layer thickness and $w^i(x)$ is the width of each region i as a function of x, which is the distance between the boundaries of each region i. The corresponding displacement is obtained by integrating the deformation ε^i_{mech} over the characteristic length of the region, l^i

$$u^i_{mech} = \int_0^{l^i} \varepsilon^i_{mech} dx. \tag{3.30}$$

The width corresponding to the dog-bone region of the specimen, w^s_{dg} writes

$$w^s_{dg}(x) = w^s + 2R - 2\sqrt{R^2 - (R-x)^2} \tag{3.31}$$

while the width characterising the under-etched region of the specimen w^s_{ue} is assumed to span all the etched surface

$$w^s_{ue}(x) = \min\left(w^s + 2R, 2\sqrt{(vt)^2 - (vt-x)^2}\right) + 2\sqrt{(vt)^2 - (vt-x)^2} + 2w_w. \tag{3.32}$$

For the sake of simplicity, the etch front near the specimen dog-bone is supposed to be circular. The width of the under-etched region of the actuator is given by

$$w^a_{ue}(x) = \min\left(w^a_{max}, 2\sqrt{(vt)^2 - (vt-x)^2}\right) + 2\sqrt{(vt)^2 - (vt-x)^2} + 2w_w \tag{3.33}$$

and the trapezoidal shape of the actuator leads to

$$w^a(x) = w^a_{min} + \frac{(w^a_{max} - w^a_{min})}{l^a_{nom}} x. \tag{3.34}$$

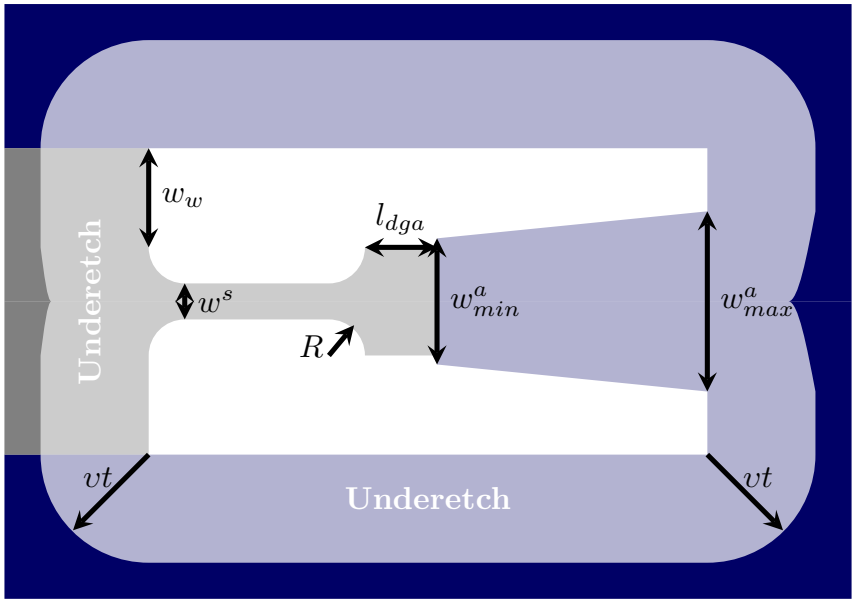

Fig. 3.14: Schematic representation of a test structure indicating the characteristic dimensions used in the correction model proposed in this thesis.

Thereupon, the ratio of displacement of the geometrical subregions of the specimen to the specimen gauge zone π^s is given by

$$\pi^s = \frac{u^s_{ue,mech} + u^s_{dg,mech} + u^s_{dga,mech}}{u^s_{mech}} = \frac{l^s_{nom}}{w^s}\left[2\int_0^R \frac{dx}{w^s_{dg}(x)} + \int_0^{\upsilon t} \frac{dx}{w^s_{ue}(x)} + \frac{l^s_{dga}}{w^s_{dg}}\right] \tag{3.35}$$

and the ratio of displacement associated to the elasticity of the under-etched region of the actuator to the gauge zone π^s is

$$\pi^a = \frac{u^a_{ue,mech}}{u^a_{mech}} = \frac{l^a_{nom}}{(w^a_{max} - w^a_{min})\ln(w^a_{max}/w^a_{min})} \int_0^{\upsilon t} \frac{dx}{w^a_{ue}(x)}. \tag{3.36}$$

The *dga* region corresponds to the rectangle linking the dog-bone to the actuator (see Figure 3.14). Parameters π^s and π^a are geometrical coefficients, independent of the applied force and of the material properties. However, the total deformation is the sum of mechanical and mismatch strain which leads to:

$$\varepsilon^i_{mech} = \varepsilon^i - \varepsilon^i_{mis} \tag{3.37}$$

By integrating equation (3.37) over each l_i and introducing the coefficients π^i, the displacement of the actuator and of the specimen are finally obtained:

$$u^a = \frac{u - \varepsilon^a_{mis}\upsilon t + \pi^a \varepsilon^a_{mis} l^a_{nom}}{1 + \pi^a}, \tag{3.38}$$

$$u^s = \frac{u - \varepsilon^s_{mis}\left(2R + l_{dga} + \upsilon t\right) + \pi^s \varepsilon^s_{mis} l^s_{nom}}{1 + \pi^s} \tag{3.39}$$

where u is the measured displacement of the cursor, corresponding to the sum of the displacement of all the subregions of the actuator or of the specimen. The present approach needs further extension for plastic and visco-plastic materials.

The present correction and the ones proposed by Vayrette et al. (2015) and Ghidelli et al. (2017) are compared to the FE predictions for the lab-on-chip simulations presented in Figure 3.11. The relative errors ϵ_σ and ϵ_ε are computed and represented in Figure 3.15 as a function of actuator length for an instance with $l^s_{nom} = 50\mu$m and $w^s = 1.5\mu$m. As depicted in Figure 3.15, the three correction procedures improve the precision on the extracted stress and strain. For $l^a_{nom} > 500\mu$m, the correction model presented in this thesis gives the best results for σ^s. The relative error ϵ_σ is improved by more than one order of magnitude (see Figure 3.15(a)). Note that the $u^a_{ue} = -\varepsilon^{mis}_a l^a_{ue}$ assumption of Ghidelli et al. (2017) is not confirmed by FE analysis: in the under-etched actuator part, the stress is not fully relaxed and the mean strain in this zone is not equal to ε^a_{mis}. In Figure 3.15(b), the corrections on ε^s computed from the present model and from Ghidelli et al. (2017) are similar while the correction factor of Vayrette et al. (2015) was not computed due to its physical irrelevance. The relative error ϵ_ε decreases by a factor 3 to 5. The previous observations remain valid for each instance. The impact of the under-etched actuator regions is not properly captured for small actuator length as any analytical correction model relies on Saint Venant's Principle.

3.5.2 Elasto-plastic material

Metallic thin films are often studied using the lab-on-chip technique and one may wonder what is the influence of plasticity on the accuracy of the measurements. A plastic material is now investigated. The strain hardening follows a Swift law:

$$\sigma_f = \sigma_0(1 + kp)^n \tag{3.40}$$

where σ_f is the flow stress and p is the accumulated plastic strain. The material parameters are listed in Table 3.2. The lab-on-chip simulations are performed and the results of the simulations are depicted in Figure 3.16(a). The internal stress reaches 405 MPa within the specimen and plasticity takes place before the release of the actuator. Nevertheless, the elastic regime is accessible as observed in Figure 3.16(a). This is due to the fact that the stress along the width direction $\boldsymbol{e_2}$ relaxes during the release. Consequently, the initial stress along the specimen length direction $\boldsymbol{e_1}$ reduces and becomes lower than the stress after thermal loading. The $(\varepsilon^s|_u,\ \sigma^s|_u)$ data are spread and strongly differs from an instance to another, as observed experimentally by Colla et al. (2012). The relative errors on the stress are above 3% for any instance and reaches more than 10 % for the smallest w^s, as represented in Figure 3.16(c). The relative error on the strain is limited to less than 1% (see Figure 3.16(e)). Plastic deformation occurs mainly in the specimen gauge which exhibits the narrowest section, limiting the influence of the dog-bone and the under-etched

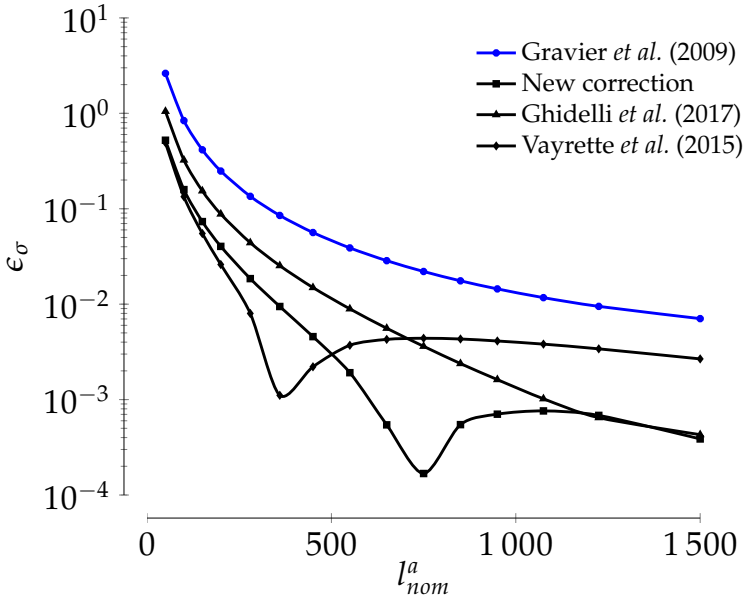

(a) Relative error on σ^s

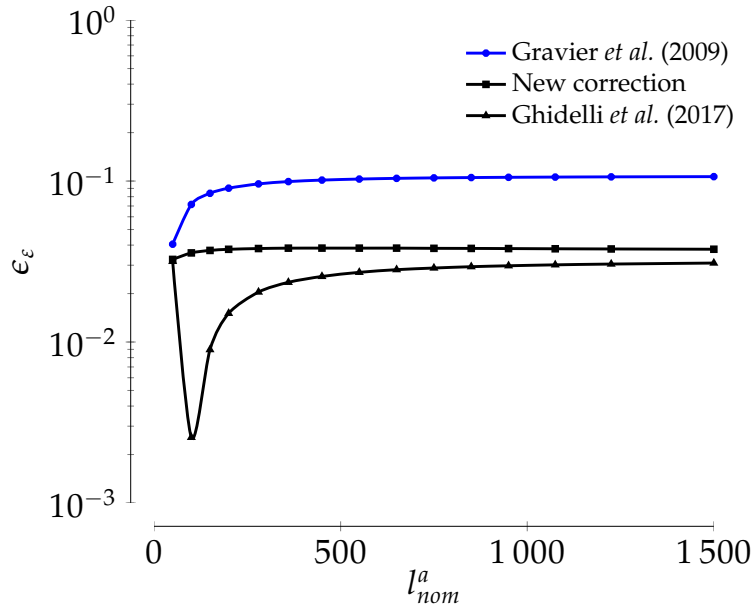

(b) Relative error on ε^s

Fig. 3.15: Relative errors on the stress (a) and strain (b) as a function of the actuator length l^a_{nom}, computed based on the original data reduction scheme (Gravier et al., 2009), the new correction procedure, the correction of Ghidelli et al. (2017) and of Vayrette et al. (2015) for a purely elastic material. $l^s_{nom} = 50\mu$m and $w^s = 1.5\mu$m.

specimen anchoring parts. Auto-actuated structures gives a mean mismatch strain $\varepsilon^s_{mis} \sim 0.0037$ while its true value is equal to 0.00237, indicating that such dedicated structures are not suitable for the extraction of ε^s_{mis} in an elasto-plastic material.

As depicted in Figures 3.17(a) and 3.17(a), any correction model worsens ϵ_ε in comparison with the original data reduction scheme while the same conclusions as in the previous section can be drawn for ϵ_σ. The actuator remains indeed purely elastic.

3.5.3 Elasto-viscoplastic material

Thin films are often subjected to creep and relaxation due to their magnified strain rate sensitivity which can be detrimental in applications. Previously, Al, Cu and Pd thin films were experimentally characterized in relaxation using the lab-on-chip technique. Due to process requirement, the first displacement was generally recorded after 2 or 3h. The question to be examined in this section is what is the impact of viscoplasticity on the extracted stress and strain?

A viscoplastic material is studied with the following viscoplastic law:

$$\sigma_f = \sigma_0(1 + k_S p)^{n_S}(\dot{p}/\dot{p}_0)^m \tag{3.41}$$

where $\dot{p}$ is the accumulated plastic strain rate. The material parameters are listed in Table 3.2. The release of the on-chip structure is simulated and afterwards, the simulation continues for 3 hours. The results are presented in Figure 3.16(b) with the corresponding errors in Figure 3.16(d) and 3.16(f). The stress and strain curves of 2 elementary structures are represented. The points marked with a red dot correspond to the first data measured experimentally. Important stress relaxation takes place before the first measurement. The extracted $(\varepsilon^s|_u,\, \sigma^s|_u)$ are not representative of the release. Each elementary structure underwent a different tensile loading and subsequent relaxation paths. As can be seen in the graph, the four structures exhibit different yield strengths indicating that they have undergone different loading rates. In previous studies, the strain hardening capacity of metallic thin films was quantified in terms of the incremental strain hardening exponent,

$$n_{incr} = \frac{d\ln\sigma}{d\ln p} \tag{3.42}$$

and in terms of the strain hardening rate

$$\Theta = \frac{d\sigma}{dp}. \tag{3.43}$$

based on a "stress-strain" curve corresponding to the measurements obtained 3 hours after release. So the incremental strain hardening exponent and the hardening rate reported by Colla et al. (2012) do not have the anticipated

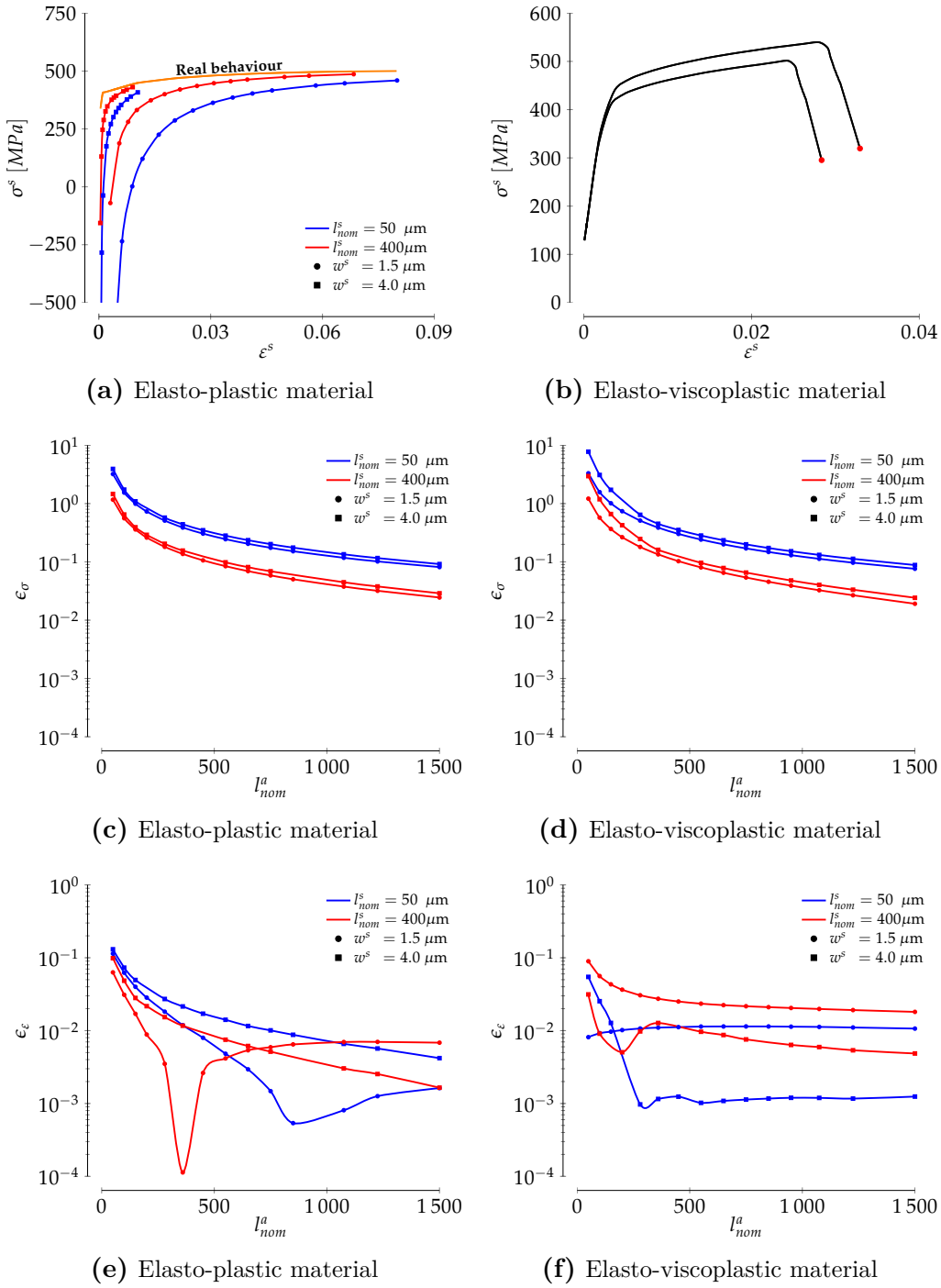

(a) Elasto-plastic material **(b)** Elasto-viscoplastic material

(c) Elasto-plastic material **(d)** Elasto-viscoplastic material

(e) Elasto-plastic material **(f)** Elasto-viscoplastic material

Fig. 3.16: (a) Comparison between the real behaviour and the extracted stress-strain curves for 4 different instances; (b) Influence of 3 hours relaxation on the extracted stress and strain; Relative errors on the stress (c-d) and strain (e-f) as a function of the actuator length l^a_{nom}.

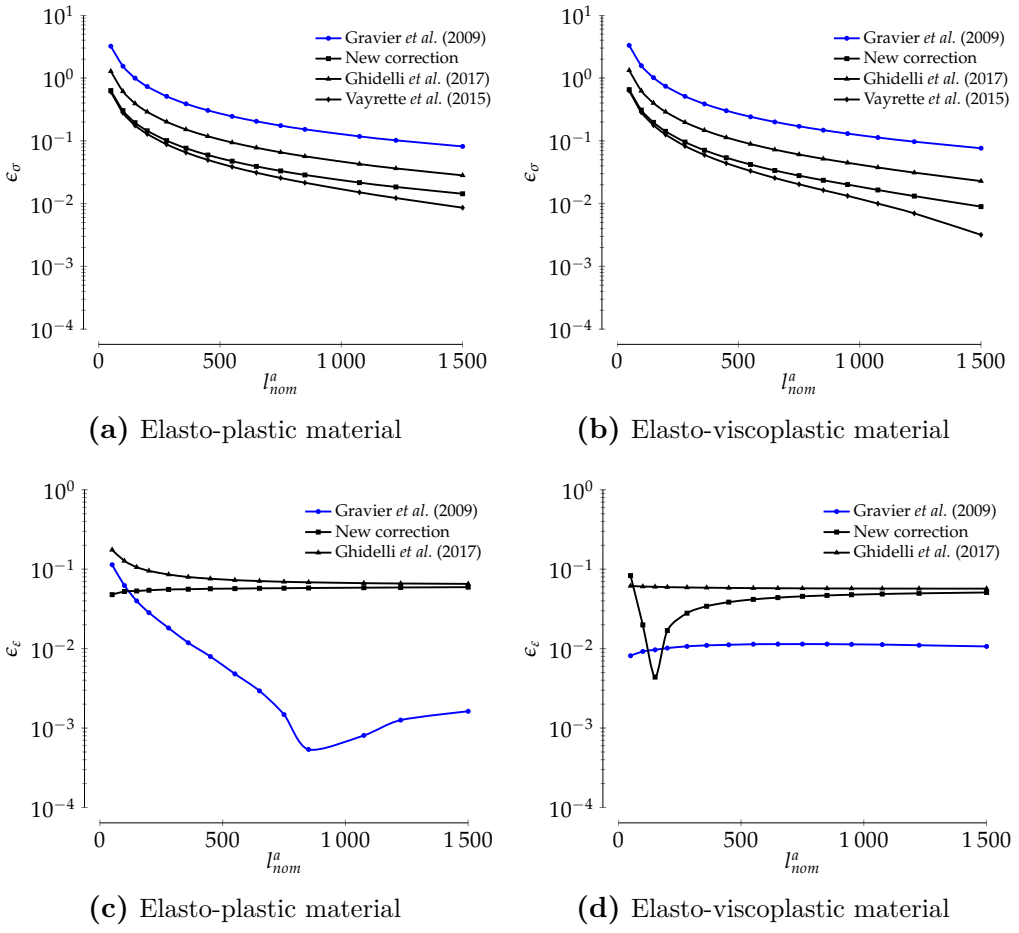

(a) Elasto-plastic material **(b)** Elasto-viscoplastic material

(c) Elasto-plastic material **(d)** Elasto-viscoplastic material

Fig. 3.17: Relative errors on the stress (a) and strain (b) as a function of the actuator length l^a_{nom}, computed based on the original data reduction scheme (Gravier et al., 2009), the new correction procedure, the correction of Ghidelli et al. (2017) and of Vayrette et al. (2015) for an elasto-(visco)plastic material. $l^s_{nom} = 50\mu$m and $w^s = 1.5\mu$m.

meaning. The analysis of strain hardening in viscoplastic materials requires indeed careful thoughts as each elementary structure experiences a different loading rate and a different relaxation rate. The stress relaxation slope is quiet sharp and this is due to the fact we impose the same thickness for the actuator and the specimen. Experimentally, the specimen is between 2 and 6 times thicker than the actuator, leading to more compliant relaxation rates. As observed in Figure 3.16(b), it is worth to mention that the spring-like relaxation is not purely linear. After the complete release of the actuator, etching still continues during a laps of time $t_{over} = 12$s and the under-etching of the anchoring parts keeps increasing, leading to a non-linear relaxation behaviour. Extrapolation of the linear relaxation behaviour will thus not allow to recover the mechanical behaviour during loading.

As reported in Figures 3.16(d) and 3.16(f), the correction procedure leads to the same observations as for elasto-plastic material and confirms the inadequacy of an elasticity based correction approach for plastic materials.

3.5.3.1 Strain rate

Modelling of the mechanical behaviour of thin films represents a logical continuation of the lab-on-chip experiments. If representative volume elements or homogenization techniques are employed, strain rate constitutes an input data of prime importance for viscoplastic models. The strain rate undergone by a specimen in an test structure was found to vary with the length of the actuator and the specimen. This section aims at quantifying the strain rate undergone by the specimen during the release step and comparing the analytical models proposed by Vayrette et al. (2015) for elastic materials to the FE predictions. Before that, the evolution of the actuator shape design and its influence on the strain rate are presented.

The original design of lab on-chip structures involves rectangular actuator beams. For a constant sacrificial layer etching rate υ, a perfect rectangular actuator beam of width w^a becomes instantaneously freestanding after a etching time equal to $w^a/2\upsilon$. In reality, the deposition of the sacrificial layer is not uniform over the whole substrate, leading to local variation of the chemical composition and density of the sacrificial layer. During the release step, some regions of the actuator beam subjected to higher local etching rates become freestanding while others remain attached to the substrate. The release of the actuator beam and the specimen mechanical loading are then sequential, uncontrolled and probably very fast. In order to solve these issues, Vayrette et al. (2015) have introduced structures with a tapered shape actuator. Figure 3.18 is a schematic drawing of such structure with a tapered actuator of maximum width w^a_{max}, minimum width w^a_{min} and length l^a_{nom} .

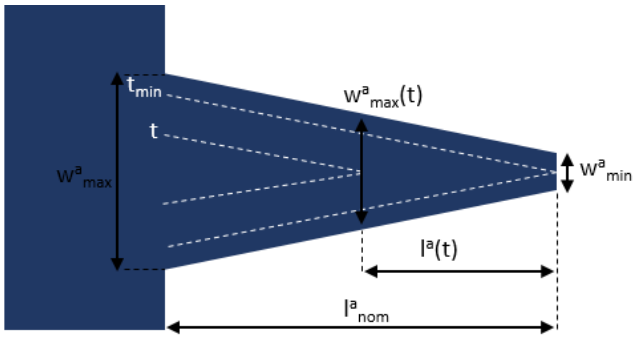

Fig. 3.18: Schematic illustration of tapered actuator proposed by Vayrette et al. (2015) for controlling the strain rate.

The mechanical loading starts at time t_{min} while the actuator is fully released at time t_{max} which are the durations required to etch a length of, respectively, $w^a_{min}/2$ and $w^a_{max}/2$. For $t > t_{min}$, the in-plane dimensions of the

freestanding part of the tapered actuator, $w^a_{max}(t)$ and $l^a(t)$, increase linearly with time:

$$w^a_{max}(t) = 2\upsilon t, \tag{3.44}$$

$$\frac{l^a(t)}{l^a_{nom}} = \frac{2\upsilon t - w^a_{min}}{w^a_{max} - w^a_{min}}. \tag{3.45}$$

This simple design modification allows a controlled progressive release of the actuator beam avoiding excessive release rates in some sections. As the actuator width evolves linearly from w^a_{min} to w^a_{max} , the specimen strain and stress during the release can be computed using equations (3.5) and (3.6), respectively. As the actuator has a trapezoidal shape and the force is constant along the actuator, the actuator cross-sectional area A^a injected in equation (3.5) is the product of the actuator thickness h^a and the average freestanding actuator beam width, $w^a(t) = (w^a_{max}(t) + w^a_{min})/2$.

Relying on a small strain formulation,Vayrette et al. (2015) considered two extreme cases in order to estimate the strain rate imposed during the release step. The upper limit of the strain rate is derived by considering that the actuator has fully relaxed its internal stress at the end of etching step, leading to $\varepsilon^a = \varepsilon^a_{mis}$). Based on the associated displacement, the upper limit of the strain rate writes

$$\dot{\varepsilon}_{max} = \frac{1}{l^s_{nom}}\frac{\mathrm{d}u}{\mathrm{d}t} = -\varepsilon^a_{mis}\frac{l^a_{nom}}{l^s_{nom}}\left(\frac{2\upsilon}{w^a_{max} - w^a_{min}}\right). \tag{3.46}$$

In this case, the strain rate is time independent. $\dot{\varepsilon}_{max}$ linearly increases with increasing ε^a_{mis} , υ, l^a_{nom}/l^s_{nom} and is inversely proportional to $w^a_{max} - w^a_{min}$.

The second approach consists in expressing the specimen strain rate from a purely elastic formalism of the mechanical equilibrium between the sample and the actuator at each time t. Assuming elastic strains and combining equations (3.5) and (3.6) leads to:

$$u = l^s_{nom}\left(\frac{\sigma^s}{E^s} + \varepsilon^s_{mis}\right) \tag{3.47}$$

$$= l^s_{nom}\left(\frac{F}{E^s A^s} + \varepsilon^s_{mis}\right) \tag{3.48}$$

$$= l^s_{nom}\left(\frac{E^a A^a}{E^s A^s}\left(-\frac{u}{l^a(t)} - \varepsilon^a_{mis}\right) + \varepsilon^s_{mis}\right) \tag{3.49}$$

$$u\left(\frac{l^s_{nom}}{l^a(t)}\frac{E^a A^a(t)}{E^s A^s} + 1\right) = l^s_{nom}\varepsilon^s_{mis} - \frac{l^s_{nom}E^a A^a(t)}{E^s A^s}\varepsilon^a_{mis}. \tag{3.50}$$

The actuator area is given by

$$A^a(t) = h^a\left(2\upsilon t + w^a_{min}\right)/2. \tag{3.51}$$

Introducing (3.45) and (3.51) in (3.50), the strain rate finally writes:

$$\begin{aligned} \dot{\varepsilon} = \frac{1}{l^s_{nom}}\frac{\mathrm{d}u}{\mathrm{d}t} &= \frac{1}{l^s_{nom}}\frac{B\mathrm{d}A - A\mathrm{d}B}{B^2} \\ \text{with } u(t) &= \frac{A}{B} = \frac{E^sA^s\varepsilon^s_{mis} - \varepsilon^a_{mis}E^ah^a\left[\upsilon t + w^a_{min}/2\right]}{\frac{E^sA^s}{l^s_{nom}} + E^ah^a\frac{w^a_{max} - w^a_{min}}{l^a_{nom}}\frac{\upsilon t + w^a_{min}/2}{2\upsilon t - w^a_{min}}} \end{aligned} \tag{3.52}$$

In this case, the strain rate evolves with time as well as with the geometrical and material features of the actuator and specimen beams.

Figure 3.19 depicts the variation of strain rate as a function of l^a_{nom}/l^s_{nom} and as a function of time for the force equilibrium based approach for 170 nm thick copper films. The HF etching rate of LPCVD silicon oxide is equal to $\upsilon = 0.181$ μm/s. The actuator thickness is equal to $h^a = 100$nm and the beam widths are: $w^a_{min} = 8\mu$m, $w^a_{max} = 10\mu$m and $w = 1.4\mu$m.

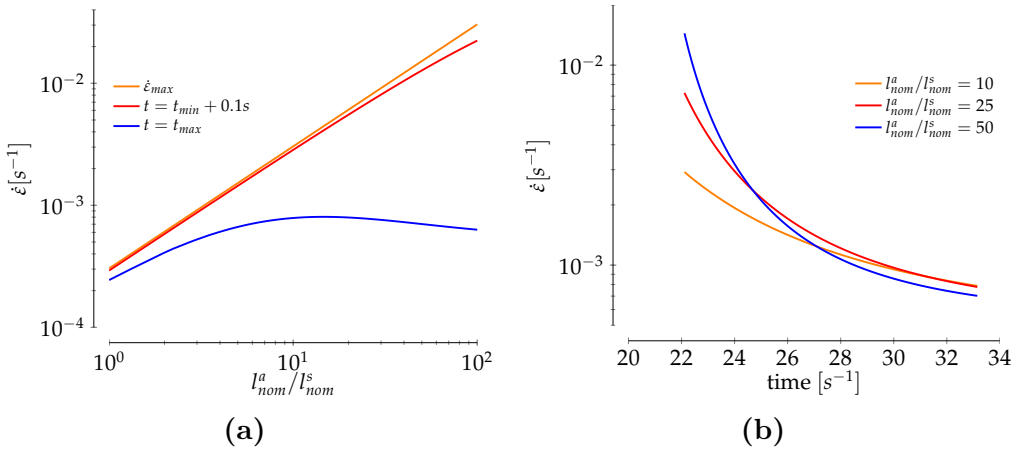

Fig. 3.19: Variation of the strain rate as a function of l^a_{nom}/l^s_{nom} for 170 nm thick copper films, following equations (3.46) and (3.52) (a) and as a function of time (b).

The strain rate undergone by the elastic material in section 3.5.1 and by the viscoplastic material in section 3.5.3 are computed for different actuator and specimen dimensions. Strain rates are determined by the derivative of a cubic spline interpolating the strain as a function of the release time. Figure 3.20 represents the strain rate obtained by FEM simulations and by equations (3.46), denoted $\dot{\varepsilon}_{max}$, and (3.52), denoted by Vayrette. In the elastic case, the strain rate decreases with release time while the strain rate is relatively constant for the viscoplastic material. The force equilibrium approach of Vayrette et al. (2015) are in concordance with the elastic FE results but slightly overestimated the strain rate. This can be explained by the contributions of the dogbones and the under-etched parts which are not taken into account. Even if the approach of Vayrette et al. (2015) relies on elasticity, the strain rates

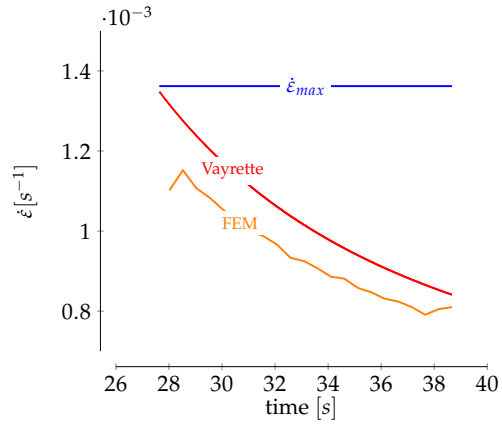

(a) $l^s_{nom} = 200\ \mu$m, $l^a_{nom} = 1000\ \mu$m and $w^s = 1.5\ \mu$m, elastic

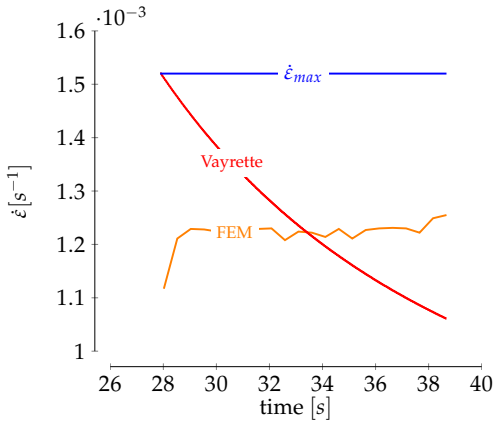

(b) $l^s_{nom} = 200\ \mu$m, $l^a_{nom} = 1000\ \mu$m and $w^s = 1.5\ \mu$m, viscoplastic

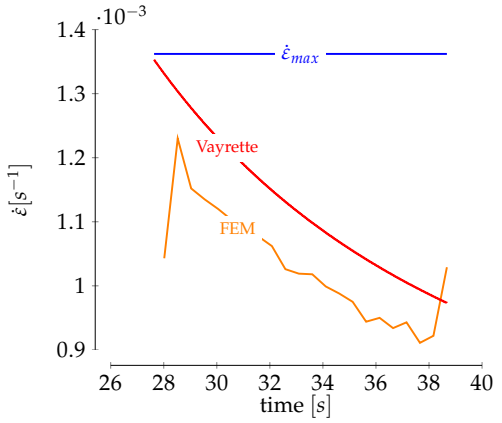

(c) $l^s_{nom} = 100\ \mu$m, $l^a_{nom} = 500\ \mu$m and $w^s = 1\ \mu$m, elastic

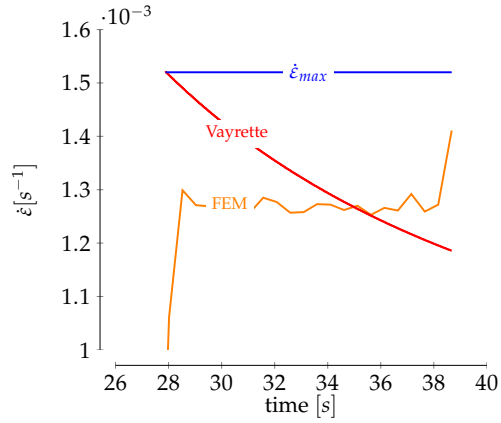

(d) $l^s_{nom} = 100\ \mu$m, $l^a_{nom} = 500\ \mu$m and $w^s = 1\ \mu$m, viscoplastic

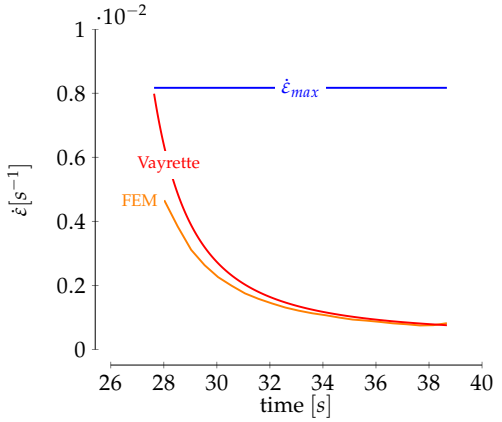

(e) $l^s_{nom} = 50\ \mu$m, $l^a_{nom} = 1500\ \mu$m and $w^s = 2.5\ \mu$m, elastic

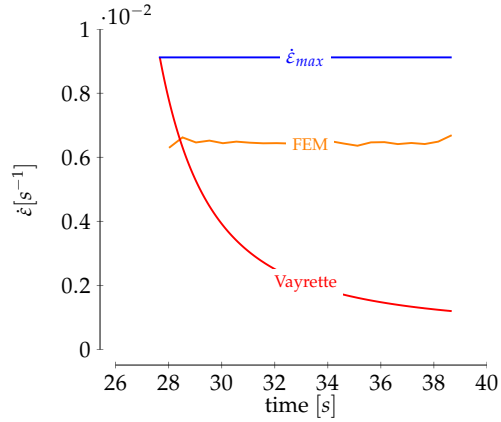

(f) $l^s_{nom} = 50\ \mu$m, $l^a_{nom} = 1500\ \mu$m and $w^s = 2.5\ \mu$m, viscoplastic

Fig. 3.20: Comparison of the strain rate applied to the specimen during the release obtained by FEM simulations and by equations (3.46) and (3.52) proposed by Vayrette et al. (2015) for different actuator and specimen dimensions. The case of an elastic and an elasto-viscoplastic material are considered.

in the viscoplastic case lie always between the minimum and maximum values predicted by (3.52).

3.6 Conclusion

This chapter has introduced the on-chip microtensile testing method developed at UCLouvain. The fabrication process has been detailed to the specific application of Ni thin films. All the lab-on-chip production attempts were unsuccessful and consequently, the critical aspects for future Ni lab-on-chips development have been listed. Nevertheless, the on-chip method will remain central in the rest of the thesis as several questions have arisen from the previous characterization campaigns on metallic thin films.

Lab-on-chips have for the first time been modelled using FEM and the whole on-chip experiment has been simulated from the generation of internal stresses to the release of the structure and eventual subsequent relaxation. The structure design has been found to profoundly influence the stress and strain extracted from the basic data reduction scheme.The contribution of the dog-bones and the under-etched anchoring parts of the actuator and of the specimen have a non negligible impact on the measured displacement, resulting in a large scatter of the data from an instance to another and in possible erroneous determination of material characteristic such as Young's modulus. Small actuator lengths lead to the most significant errors on the stress, due to the violation of the Saint Venant's Principle. The analysis has revealed that long actuator and wide specimen beams are best suited to lower the uncertainties on the displacement. In the same vein, the structures dedicated to the determination of the mismatch strain ε_{mis} have been simulated and the impact of the dimensions on the extracted ε_{mis} has been investigated. Auto-actuated structures have to be privileged to ensure the proper characterization of ε_{mis} of pure elastic material while free beams are more suitable for (visco)plastic materials. Also limiting the over-etching time increases the accuracy of the measure. A new analytical correction model has been proposed and the limitations of previous improved data reduction schemes have been outlined. The present correction model improves the precision on the stress and on the strain by a factor 10 and 3-5 respectively. However the new correction procedure is strictly limited to elastic deformation. If the use of small specimen beams is needed (in order to avoid buckling of films with compressive internal stresses), FE simulations should be performed to recover the correct displacement. Viscoplasticity has finally been studied and the influence of the on-chip structure dimensions on the strain rate has been revealed, highlighting the fact that each elementary test structure follows a specific loading path and revealing the impact of over-etching time on the relaxation behaviour.

Through the last years, the evolution of the elementary on-chip structure has been driven by user "appreciations" and experiences. The very long auto-

actuated structures dedicated to the determination of ε_{mis} present in oldest generation have been for instance, replaced by shorter structures in the last generation and the shape of the dog-bone has been modified. From the present analysis, it is recommended to systematically couple further design developments with FE simulations to prevent issues with the data reduction scheme but also stress concentration leading to premature failure of the specimen.

CHAPTER 4

Dislocation and back stress dominated viscoplasticity in freestanding sub-micron Pd films

In contrast with the insights given by MD simulations, Colla et al. (2015) have observed that dislocation storage occurs in nanocrystalline Pd thin films and that hardening by dislocation interactions cannot be excluded. In this chapter, a dislocation-based crystal plasticity model is developed in order to study the mechanical and creep/relaxation behaviour of polycrystalline metallic thin films and investigate whether or not the experimental observations can be explained based solely on dislocations. The model accounts for the confinement of plasticity due to grain boundaries and for the anisotropy of individual grains, as well as for the significant viscoplastic effects associated to dislocation dominated thermally activated mechanisms. Numerical predictions are assessed based on experimental tensile test followed by relaxation on freestanding Pd films, gathered using an on-chip test technique. The dislocation-based mechanism assumption captures all the experimental trends, including the stress-strain response, the relaxation behaviour and the dislocation density evolution, confirming the dominance of a dislocation driven deformation mechanism for the present Pd films with high defects density. The model has also been used to address some original experimental evidences involving back stresses, Bauschinger effect, backward creep and strain recovery.

This chapter reproduces the following article (with minor additions):

Lemoine, G., Delannay, L., Idrissi, H., Colla, M.S., Pardoen, T., 2016. Dislocation and back stress dominated viscoplasticity in freestanding sub-micron Pd films. *Acta Materialia* 111, 10–21. doi:10.1016/j.actamat.2016.03.038.

4.1 Introduction

Creep and relaxation in nanocrystalline (NC) metallic thin films is a major issue in many applications such as in micro- or nano-electromechanical systems (MEMS/NEMS) devices (Modlinski et al., 2004a,b), in flexible electronic systems and in thin membrane technology. NC metals usually present excellent mechanical performance in terms of strength and fatigue resistance but they often suffer of a lack of ductility (Meyers et al., 2006; Dao et al., 2007; Pineau et al., 2016). Many NC systems show also, owing to their very fine microstructure (grain sizes in the range of $\sim$ 10-20 nm to $\sim$ 100-200 nm), moderate to high strain rate sensitivity at room temperature (Jonnalagadda et al., 2010) which may help restoring the ductility (Pardoen, 2014) but can lead to detrimental creep / relaxation effects in applications. These viscoplastic effects are also reinforced by the high internal stress levels induced by high stress heterogeneities during deformation (Van Petegem et al., 2006; Rajagopalan et al., 2007; Lonardelli et al., 2009).

Rate dependent plasticity mechanisms, controlled by either dislocation slip, diffusion or grain boundary (GB) motion are magnified in sub-micron and NC metals (Kumar et al., 2003b). Other advanced models including non equilibrium grain boundaries and GB defects have been reviewed by Mishnaevsky and Levashov (2015). Due to the large amount of internal interfaces combined to large local stress and small volume available for dislocation accumulation, thermally activated mechanisms substitute the regular forest dislocation type plasticity in NC metals. The same applies to thin films which are usually not only NC but are also affected by their free surface. At sub-micron scales, the well-known Hall - Petch strengthening involving intragrain nucleation and propagation of dislocations breaks down. As the grain size decreases, different thermally activated mechanisms involving GB rotation (Liu et al., 2011), GB sliding (Ivanisenko et al., 2009), grain growth (Gianola et al., 2006; Legros et al., 2008), GB dislocations (Mompiou et al., 2013) or GB migration (Rupert et al., 2009), can cooperate or compete with regular dislocation-based mechanisms. Several analytical or mesoscopic computational models have been developed, based on phase mixture assumptions (Gürses and El Sayed, 2011b; Li and Weng, 2013; Kim et al., 2001) or on dislocation and/or GB based deformation (Brandl et al., 2011; Li et al., 2009b; Shi and Zikry, 2009; Li et al., 2009a; Ertürk et al., 2014). Different composite models are based on the so-called grain boundaries affected zones (GBAZ) approach, as worked out for instance by Schwaiger et al. (2003), conceiving NC material as a two phase composite

of a stronger grain interior and softer grain boundaries, see also (Gürses and El Sayed, 2011b; Li and Weng, 2013). Zhu et al. (2005) have developed a polycrystal model based on the Asaro-Krysl-Kad model (Asaro et al., 2003; Asaro and Suresh, 2005) with mechanisms including the emission of perfect and partial dislocations and grain boundary sliding, and with thermal activation and grain size dependent transition between these mechanisms. Brandl et al. (2011) suggest also that dislocation-mediated rather than GB-mediated plasticity is the rate-limiting process determining the flow stress when thermal activation of dislocation mechanisms is considered. All these models capture fairly well the enhanced strain rate sensitivity of NC metals and the inverse Hall-Petch effect.

It is still debated to which extent plasticity can be dominated by dislocation glide in NC metals. Nevertheless, experimental investigations pointed out that the deformation seems to be controlled by dislocation interactions with pinning points, as for coarse metals (Van Petegem et al., 2006). However, no pile-ups and very little dislocation debris are generally found after deformation in such materials (Dalla Torre et al., 2002; Kumar et al., 2003a). In-situ TEM (Hugo et al., 2003; Kumar et al., 2003a) as well as molecular dynamics simulations (Van Swygenhoven et al., 2006) have shown that once nucleated, dislocations cross the grain and are absorbed and/or transmitted at the opposite grain boundary. Grain boundaries act thus as source and sinks for dislocations. Depending on the grain size distribution and on the distribution of dislocation density from one grain to another, a transition between classical dislocation activity and GB dislocation nucleation plasticity progressively occurs. Recent investigations found nevertheless significant dislocation accumulation in NC Ni (Wu et al., 2009; Lee et al., 2013), Pt (Wang et al., 2010) and NC Pd thin films (Colla et al., 2015). The typical deposition processes of the latter Pd films can lead to a high densitiy of defects in terms of e.g. growth twins, GBs, vacancies. The presence of pre-existing dislocations or growth twins in the as-deposited films presumably favours additional dislocation storage by providing the necessary pinning sites for further accumulation.

Thin films, especially when freestanding, offer a system of fundamental interest owing to nanograined columnar microstructures frequently involving a single grain along the film growth direction and sharp crystallographic textures (Nix, 1989). Some Pd and Al films exhibit a significant strain hardening capacity and a significant increase in the strength with decreasing thickness (Haque and Saif, 2003; Colla et al., 2012). The large apparent strain hardening at the onset of plasticity is shown to be a gradual elastic-plastic transition (Haque and Saif, 2003; Rajagopalan et al., 2010). The largest grains yield much earlier than the smallest ones, inducing a significant kinematic hardening contribution. This Bauschinger effect, due to internal stresses, is revealed also by backward creep during interrupted unloading experiments on NC Ni (Van Petegem et al., 2006). These experiments also demonstrate high values

for the effective stress and for the internal stress as compared to coarse grained metals. Recent experimental and numerical studies on Al and Au thin films have also shown that plastic strain can be recovered under zero applied stress conditions (Rajagopalan et al., 2007; Lonardelli et al., 2009; Rajagopalan et al., 2008; Koslowski, 2010). The experimental results conducted by Rajagopalan et al. (2007, 2008) and Lonardelli et al. (2009) reveal that time dependent strain recovery results from significant internal stress generated by highly heterogeneous stress distribution.

In this chapter, a dislocation-based crystal plasticity model is developed. The model accounts for the confinement of plasticity due to grain boundaries and for the anisotropy of individual grains, as well as for the significant viscoplastic effects associated to dislocation dominated thermally activated mechanisms. The goal of this study is to capture the grain size and external dimensions effects and provide a better quantitative understanding of the experimental mechanical behaviour of nano-grained Pd films with different thickness in terms of dislocation density, strain rate sensitivity or activation volume evolutions and back stresses. The model is identified and validated based on experimental measurements obtained by the on-chip test method (Gravier et al., 2009; Coulombier et al., 2012). The specific tensile and relaxation results used in this study are original (except for the data on the thinnest film), confirming earlier data (Colla et al., 2012). The following issues are addressed:

1. Is it possible to reproduce the experimental mechanical behaviour of the Pd NC films, assuming only dislocation-based mechanisms as suggested from the TEM characterization (Colla et al., 2015; Wang et al., 2012a) ?

2. Is a crystal plasticity model with simple phenomenological description of the rate sensitivity and only dislocation-based hardening rich enough to capture: the film thickness effect, the dislocation density evolution and the relaxation behaviour of NC metallic thin films?

3. Does the model generate a sufficiently heterogeneous stress distribution, able to induce backward creep or even strain recovery?

4. What is the influence of the texture on the creep/relaxation behaviour?

The outline of the chapter is the following. In section 2, the lab-on-chip tests results on Pd are presented, motivating the main assumptions of the model. The model and the crystal plasticity framework are described in section 3. Section 4 contains the results and discussion with parameter identification and validation. Finally a parametric study is presented in section 5 in order to widen the scope of the study.

4.2 Lab-on-chip uniaxial tensile test results

The present study is motivated by the uniaxial tension response of three NC e-beam evaporated Pd films with thicknesses equal to 90, 200 and 480 nm. The experimental campaign was performed by Colla (2014) using the on-chip test method (Gravier et al., 2009) and additional characterization tools (see Colla et al. (2015); Idrissi et al. (2011); Wang et al. (2012a). As shown in Figure 4.1, the latter technique relies on self-actuated micromachines created by the deposition, etching and partial release of several layers on a silicon substrate. Tensile internal stress is generated during the deposition of the actuator. Then, the underlying sacrificial layer is etched away and the actuator pulls on the Pd specimen which can deform up to large plastic strains whereas the actuator remains elastic. Indeed its cross section area A^{actu} is larger than the sample cross-section area A^{sample}. Hence, the tensile stress inside the Pd sample may be deduced from the contraction of the actuator ΔL, the Young's modulus of the Si_3N_4 actuator $E^{actu} = 240$ GPa and the initial lengths of the sample L_0^{sample} and actuator L_0^{actu}. The tensile stress in the test specimen is given by (see Vayrette et al. (2015) for a more detailed mechanical analysis):

$$\sigma_{11}^{sample} = \frac{A^{actu}}{A^{sample}}\sigma_{11}^{actu} \simeq \frac{A_0^{actu}}{A_0^{sample}}\left(1 + \frac{\Delta L}{L_0^{sample}}\right) E\frac{\Delta L}{L_0^{actu}}. \tag{4.1}$$

Here, we have assumed a constant actuator cross-section and we have assumed that the sample deformation is mostly plastic so that volume is preserved. The loading of each micromachine is varied by using different L_0^{actu}/L_0^{sample} ratios.

Etching of the sacrificial layer is fast and the initial loading rate is around $3\ 10^{-3}\ s^{-1}$ for 10 s, with a dependence on sample length. Then, the actuator behaves as a linear spring which slowly contracts while the sample (still loaded in tension) undergoes viscoplastic elongation. Due to process requirements, the first experimental measurement of ΔL is made 3 hours after the release, in a scanning electron microscope. Measurements are then repeated after relaxation times varying from a few hours to several months. At all times, the actuator follows a linear force-displacement relationship and equation (4.1) remains valid. These conditions thus correspond to a creep test performed on a sample attached to a linear spring (Coulombier et al., 2012).

Based on transmission electron microscopy observations (Colla et al., 2015, 2012; Colla, 2014), the thinnest and the thickest of the three Pd films were found to have similar distribution of the in-plane grain diameter D. The grain size distribution is represented in this study using a log-normal distribution, as commonly used in numerical approaches (Zhu et al., 2005; Gürses and El Sayed, 2011a; Zhu et al., 2006). The probability density function $P(D)$ of a log-normal grain size distribution is given by:

$$P(d) = \frac{1}{\sqrt{2\pi}\sigma D}\ \exp\left(-\frac{1}{2}\left(\frac{\log(D/D_0)}{\sigma}\right)^2\right) \tag{4.2}$$

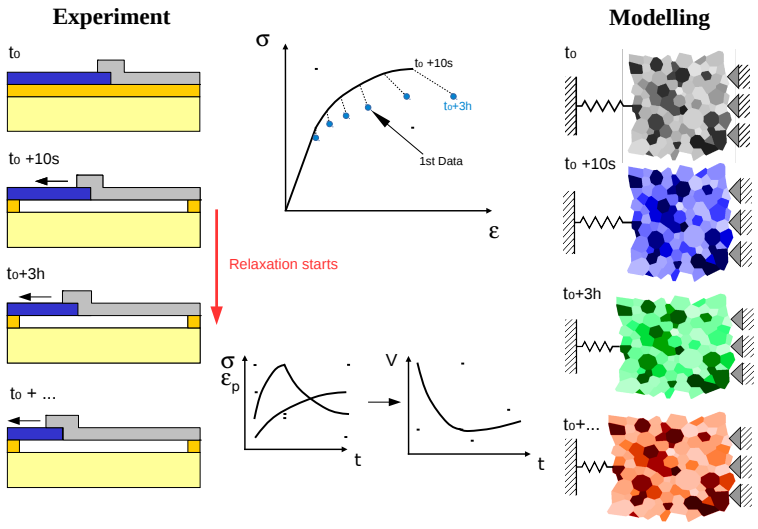

Fig. 4.1: Description of the Lab-on-chip technique and the equivalent simulation setup.

where σ and D_0 are determined based on the mean grain size $\bar{D}$ and the variance $Var[D]$ using

$$\bar{D} = D_0 \exp \frac{\sigma^2}{2} \qquad Var[D] = D_0^2 \exp(\sigma^2) \left(\exp(\sigma^2) - 1 \right). \tag{4.3}$$

The experimental grain size distribution is correctly reproduced with $\bar{D} = 30\ nm$ and $Var[D] = 100\ nm^2$.

The initial dislocation density in the as-deposited film was measured by counting extra half planes on inverse fast Fourier transforms (IFFTs) generated from high resolution TEM (HRTEM) images using masks applied on each g vector (Colla et al., 2015). The method for counting the dislocations is based on a number of [110] HRTEM images of selected regions taken at different defocus. Furthermore, because dislocations could exhibit edge component in different planes, special attention was paid to avoid multiple counting of the same dislocations in IFFTs images obtained with different g vectors. Using this method, the initial dislocation density measured in the as-deposited films was found equal to $4 \pm 0.7\ 10^{16}\ m^{-2}$ (see Colla et al. (2015) for more details). It is worth noting that some nanograins were almost free of dislocations as can be seen in the HRTEM of Figure 4.2.

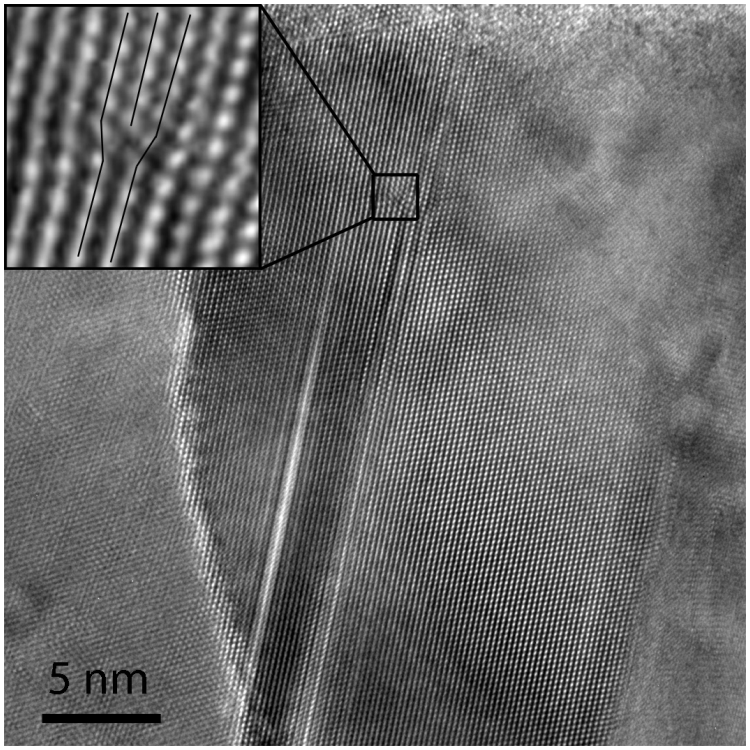

Fig. 4.2: HRTEM image of one nanograin with a lateral diameter of 21 nm obtained in as-deposited 310 nm thick Pd film. Note the homogenous contrast free from dislocations. Only one dislocation in the upper left part can be observed (see the high magnification insert).

4.3 Model

4.3.1 Modelling of dislocation glide

It is assumed that plasticity is produced in the Pd films only by dislocation glide, which occurs in a jerky manner (Kocks, 2001). Dislocations spend most of their time trapped at pinning points: the time spent gliding between two successive obstacles is negligible. The strain rate is hence controlled by the rate at which dislocations are released from pinning points, and this is triggered either by thermal activation or by a change in applied stress. When the effective shear stress τ^α resolved onto the α^{th} slip system is low, dislocations may undergo backward jumps over activation barriers. Then, the usual Arrhenius-type rate equation does not apply. Instead, following Kocks et al. (1975) and Frost and Ashby (1982), the dislocation slip rate on the slip system may be expressed as:

$$\dot{\gamma}^\alpha = \dot{\gamma}_0 \exp\left(-\frac{\Delta G}{k_B T}\right)\left\{1 - \exp\left(-\frac{\tau^\alpha ba}{k_B T}\right)\right\}. \tag{4.4}$$

Here, k_B is the Boltzman constant, T is the temperature, $\dot{\gamma}_0$ is a reference slip rate and $\tau^\alpha ba$ is the difference between the free enthalpy available for,

respectively, forward and backward jumps. ΔG is the free enthalpy allowing a mobile dislocation to overcome short-range obstacles:

$$\Delta G = F_0 \left\{ 1 - \left(\frac{\tau^\alpha}{\hat{\tau}} \right)^p \right\}^q . \tag{4.5}$$

The constant F_0 is of the order of $0.2 - 2\mu b^3$ whereas selecting $p = 1/2$ and $q = 3/2$ has been demonstrated by Ono (1968) to correctly describe a variety of short-range glide resistance profiles.

In the present study, τ^α remains below the mechanical threshold $\hat{\tau}$, which corresponds to the jerky glide regime. We do not consider the high stress regime in which dislocations glide is hindered by viscous drag forces. A simplified strain hardening law is adopted (Kocks and Mecking, 2003) according to which $\hat{\tau}$ evolves as a function of the total dislocation density ρ:

$$\hat{\tau} = \tau_{nucl} + 0.5\mu b \frac{1}{d_{eff}} + 0.3\mu b\sqrt{\rho}. \tag{4.6}$$

In (4.6), the term τ_{nucl} has been introduced in order to account for the much larger effective yield stress of grains that are initially free from any mobile dislocation. For instance Bei et al. (2008) have shown experimentally that dislocation-free Mo single crystal have a yield strength approaching the theoretical strength, independent of their size, same as for whiskers (e.g. Brenner (1956)) . Molecular dynamics simulations on Cu single crystal have revealed that the stress required for dislocation nucleation from an interface (heterogeneous nucleation) in the absence of traditional dislocation sources is controlled by the theoretical shear strength (Spearot et al., 2009; Tschopp et al., 2007). Hence, we use $\tau_{nucl} = \mu/10 = (C_{11} - C_{12} + 2C_{44})/40$ when grains are initially dislocation-free and $\tau_{nucl} = 0$ otherwise.

In the present samples, the small effective grain size d_{eff} is the initial mean spacing between dislocation pinning points. The stress needed to bow dislocation segments is assumed to scale with $1/d_{eff}$ (Sinclair et al., 2006; Delincé et al., 2007). With the increase of the dislocation density inside plastically deforming crystals, the mean free path of gliding dislocations is soon determined by dislocation interactions, i.e. by the last term in the previous equation.

Following e.g. Estrin and Mecking (1984) and Kocks and Mecking (2003), the dislocation density evolves as a function of the accumulated plastic slip according to:

$$\dot{\rho} = \left(k_1\sqrt{\rho} - k_2 \left\{ 1 - \left(\frac{k_B T}{F_0} \ln\left(\frac{\dot{\Gamma}_0}{\dot{\Gamma}} \right) \right)^{1/q} \right\}^{-1/p} \rho \right) \dot{\Gamma} \tag{4.7}$$

where $\dot{\Gamma} = \sum_\alpha |\dot{\gamma}^\alpha|$. The rate of dislocation storage increases proportionally to the square root of ρ whereas the recovery term is strain rate and temperature dependent (Kocks, 2001; Kocks and Mecking, 2003). k_1 and k_2 are constants.

4.3.2 Micro-to-macro modelling of crystal plasticity

Before presenting the scale transition modelling from individual crystal to the macroscopic response, the fundamental hypothesis of the crystal plasticity framework are recalled. Experimental observations underlying the theory of crystal plasticity in metals deforming solely by dislocation slip can be summarised as follows (Delannay et al., 2006):

- Dislocation slip is a stress-driven process which occurs along well-defined crystallographic planes and directions.
- As dislocation sweep through the crystal lattice, the material is sheared, the volume remains constant and the crystal lattice is globally unaffected.
- Lattice deformations are elastic and the related amplitude is two orders of magnitude lower than plastic strains.
- In addition to elastic stretches, the crystal lattice rotates so as to fulfil local kinematic constraints.

To distinguish elastic and plastic strains, it is common to rely on a multiplicative decomposition of the gradient tensor $\boldsymbol{F}$:

$$\boldsymbol{F} = \boldsymbol{R}_\star \boldsymbol{U}_{el} \boldsymbol{F}_p. \tag{4.8}$$

$\boldsymbol{F}_p$ transforms the initial configuration into a fictitious intermediate configuration corresponding to a crystal deformed by slip only (see Figure 4.3). The subsequent transformation may in turn be decomposed into a symmetric tensor, $\boldsymbol{U}_{el}$ representing elastic stretch and an orthogonal tensor $\boldsymbol{R}_\star$ representing lattice rotation. The latter rotation is a state variable of the model. It is important, on the one hand, because it determines the macroscopic texture development; on the other hand because the stress tensor is attached to the crystal lattice and a proper account of the lattice rotation ensures objectivity of the the theory.

In all metals, elastic strains are infinitesimal which implies $\boldsymbol{U}_{el} = \boldsymbol{I} + \boldsymbol{\varepsilon}_{el}$ (with $\|\boldsymbol{\varepsilon}^{el}\| \ll 1$). Under this assumption, the velocity gradient tensor $\boldsymbol{L}$ is expressed as follows:

$$\boldsymbol{L} = \dot{\boldsymbol{F}}\boldsymbol{F}^{-1} \simeq \boldsymbol{R}_\star \left(\dot{\boldsymbol{\Omega}}_\star + \dot{\boldsymbol{\varepsilon}}_{el} + \boldsymbol{L}_p \right) \boldsymbol{R}_\star^T, \tag{4.9}$$

where $\dot{\boldsymbol{\Omega}}_\star = \boldsymbol{R}_\star^T \dot{\boldsymbol{R}}_\star$ is the lattice spin. The plastic velocity gradient $\boldsymbol{L}_p$ is considered as the sum of the shear rates along the different slip systems:

$$\boldsymbol{L}_p = \sum_\alpha \left(\boldsymbol{b}^\alpha \otimes \boldsymbol{m}^\alpha \right) \dot{\gamma}^\alpha \tag{4.10}$$

where $\boldsymbol{b}^\alpha$ is the normalized Burgers vector, $\boldsymbol{m}^\alpha$ is the slip plane normal of the α^{th} slip system. The dislocation slip rates are computed based on the rate

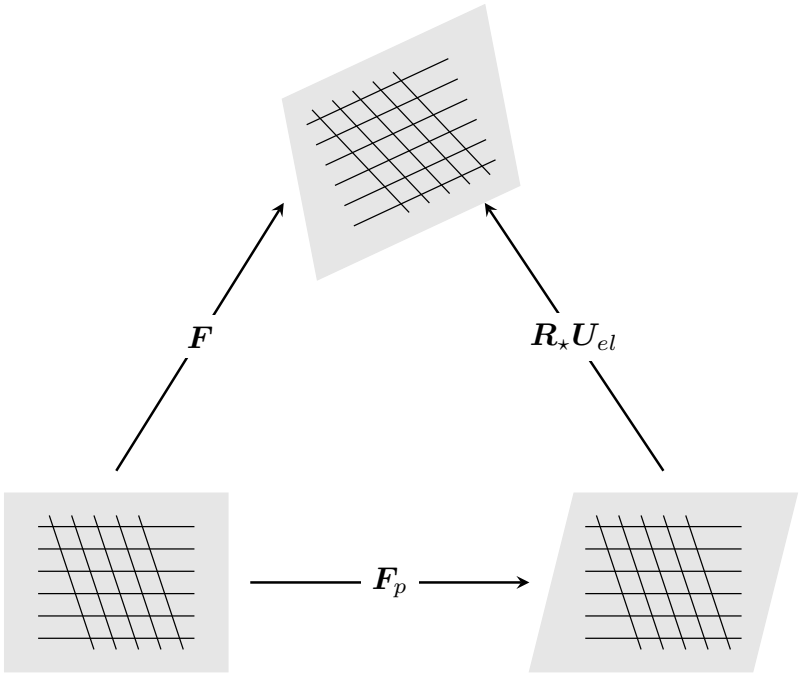

Fig. 4.3: Decomposition of a crystal's deformation into the elastic and the plastic components.

equation (4.4) while considering that the Cauchy stress $\boldsymbol{\sigma}$ evolves proportionally to the elastic strain rate but also due to the lattice rotation:

$$\mathcal{C} : \dot{\boldsymbol{\varepsilon}}_{el} = \dot{\boldsymbol{\sigma}} + \boldsymbol{\sigma}\dot{\boldsymbol{\Omega}}_\star - \dot{\boldsymbol{\Omega}}_\star\boldsymbol{\sigma}. \tag{4.11}$$

Both the elastic stiffness operator $\mathcal{C}$ and $\boldsymbol{\varepsilon}^{el}$ are considered to rotate with the crystal lattice. The lattice spin $\dot{\boldsymbol{\Omega}}_\star$ is obtained by a fully-implicit time integration of the skew-symmetric part of the velocity gradient $\boldsymbol{L}$ which involves an iterative solution of the plastic velocity gradient $\boldsymbol{L}_p$. Note that equation (4.11), obtained from the time derivative of second Piola-Kirchhoff stress demonstrates that the lattice rotation and the objectivity are constitutively prescribed in the crystal plasticity framework.

The deformation of individual grains still remains to be defined since it is different from the known macroscopic deformation. The so-called Multisite homogenization scheme is used in the present study. This model is a "2-site" grain interaction framework derived from the ALAMEL model suggested for the prediction of cold rolling textures by Van Houtte et al. (2005). Scale transition based on such "2-site" modelling of grain interactions was also proposed by Evers et al. (2002) (see Roters et al. (2010) for a complete review). As illustrated in Figure 4.4, we consider pairs of (sub-)grains interacting across a planar grain boundary of normal $\boldsymbol{n}^{GB}$. Stress balance across the interface is achieved by allowing some heterogeneity of strain: the two subregions undergo opposite relaxations relative to the macroscopic deformation. In the present

study, where grains have columnar shape across the film thickness, the velocity gradient tensors of the two subregions are expressed by:

$$\boldsymbol{L}^{I} = \boldsymbol{L}^{macro} + \dot{\gamma}^{(R1)} \left(\boldsymbol{t}^{GB} \otimes \boldsymbol{n}^{GB} \right) + \dot{\gamma}^{(R2)} \left(\boldsymbol{n}^{film} \otimes \boldsymbol{n}^{GB} \right) + \dot{\gamma}^{(R3)} \left(\boldsymbol{n}^{GB} \otimes \boldsymbol{n}^{GB} \right), \tag{4.12}$$

$$\boldsymbol{L}^{II} = \boldsymbol{L}^{macro} - \dot{\gamma}^{(R2)} \left(\boldsymbol{t}^{GB} \otimes \boldsymbol{n}^{GB} \right) - \dot{\gamma}^{(R2)} \left(\boldsymbol{n}^{film} \otimes \boldsymbol{n}^{GB} \right) - \dot{\gamma}^{(R3)} \left(\boldsymbol{n}^{GB} \otimes \boldsymbol{n}^{GB} \right), \tag{4.13}$$

where $\boldsymbol{n}^{film}$ is the film normal direction and $\boldsymbol{t}^{GB} = \boldsymbol{n}^{GB} \times \boldsymbol{n}^{film}$ is the tangent to the grain boundary that is inside the plane of the film. Hence, the local strain heterogeneity is averaged out over every cluster of two subregions. The amplitude of the relaxation rates, represented by $\dot{\gamma}^{(R1)}$, $\dot{\gamma}^{(R2)}$ and $\dot{\gamma}^{(R3)}$, is computed by minimizing the deformation energy of the two subregions. This is approximately fulfilled by requiring that:

$$\begin{aligned} \left(\boldsymbol{\sigma}^{I} - \boldsymbol{\sigma}^{II} \right) \; : \; \left(\boldsymbol{t}^{GB} \otimes \boldsymbol{n}^{GB} \right) &= \left(\boldsymbol{\sigma}^{I} - \boldsymbol{\sigma}^{II} \right) \; : \; \left(\boldsymbol{n}^{film} \otimes \boldsymbol{n}^{GB} \right) \\ &= \left(\boldsymbol{\sigma}^{I} - \boldsymbol{\sigma}^{II} \right) \; : \; \left(\boldsymbol{n}^{GB} \otimes \boldsymbol{n}^{GB} \right) \\ &= 0, \end{aligned} \tag{4.14}$$

where $\boldsymbol{\sigma}^{I}$ and $\boldsymbol{\sigma}^{II}$ represent the Cauchy stress, which is assumed uniform inside one of the two subregions. Details about the numerical implementation of the model can be found elsewhere (Bardel et al.). The orientation of the planar interface is different for each cluster. The sampling of grain boundary normals $\boldsymbol{n}^{GB}$ is generated randomly and isotropically inside the plane of the film. The lattice disorientation of adjacent grains is considered to be random. Starting from a large sampling of grain orientations that is representative of the initial texture (Melchior and Delannay, 2006), the lattice orientations of the subregions are randomly selected and associated in pairs at the onset of the simulation. In section 4.5.3, an alternative hypothesis is tested about the partitioning of stresses and strains throughout the polycrystalline aggregate. In this second approach, we rely on the Taylor assumption, according to which all grains undergo the same deformation. This induces a different stress within each grain so that the equilibrium equations are not satisfied across grain boundaries.

4.4 Results

4.4.1 Parameters identification

The value of k_1 and k_2 should be determined by comparison of the simulations and experiments. Here, three different experimental results of Pd thin films are used for determining the parameters. To this end, freestanding unpassivated thin films are considered. When the film is freestanding and unpassivated, the results are representative of the film behaviour alone, free of constraints. Otherwise, artefacts may come from the confinement of the film by the substrate or by the passivation layers acting as obstacle to deformation glide.

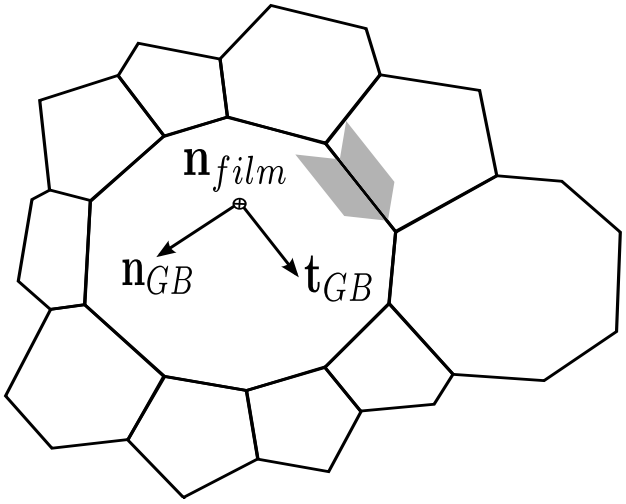

Fig. 4.4: Illustration of the multisite model considering short-range interaction of adjacent grains.

The 90 nm, 200 nm and 480 nm thick Pd films are considered. Note that the results for the 200 nm and 480 nm are original and different from those in Colla et al. (2012). The difference lies in the layer that is used in the process to ensure adhesion between the Pd and Si_3N_4. In the present tests, Ti layer is used and etched away with the sacrificial layer, avoiding the artefact due to an adhesion layer. The creep/relaxation response was also characterized for these tests . Microstructure parameters have been determined from extensive TEM observations (Colla et al., 2015, 2012; Colla, 2014). It has been observed that the in-plane grain size distribution is the same for each film, independent of thickness. They exhibit grains with columnar morphology and involve generally only one grain across the thickness. As previously mentioned, some nanograins are free of dislocations (see Figure 4.2). Following Duhamel et al. (2010), we assume that the probability of having no mobile dislocation inside a columnar grain of volume $V = \pi D^2 H/4$ may be expressed as a Poisson law: $\exp(-\rho_0 V/l_0)$ where ρ_0 is the initial polycrystalline average of the dislocation density and the characteristic dislocation length, l_0, is set equal to the length of the largest circular loop inside a sphere of volume V:

$$l_0 = \pi d_{eff} \qquad \text{where} \qquad d_{eff} = \sqrt[3]{\frac{6}{4} D^2 H}. \tag{4.15}$$

According to equation (4.15), the effective mean grain size increases thus with increasing film thickness and is equal to 48 nm, 63 nm and 85 nm for respectively 90 nm, 200 nm and 480 nm thick films. The grain size distributions for the considered film thickness are depicted in Figure 4.5. The initial dislocation density ρ_0 is assumed to be equal to $4\ 10^{15}\ m^{-2}$. TEM observations have revealed a larger initial dislocation density but all the dislocations with edge component have been included in these measurements. This means that im-

mobile dislocations which are not contributing to the plasticity such as dipoles, locks or dislocations pinned at the grain boundaries or twin boundaries have been taken into account in HRTEM measurements. Hence, it is thus reasonable to use a smaller ρ_0 for crystal plasticity simulations. The effective grain size distributions of a film exhibiting a log-normal in-plane grain size distribution are illustrated in Figure 4.5, for different films thickness: 90, 200 and 480 nm. Different probability functions of having no dislocation inside a grain are also represented in Figure 4.5. From this figure, it can be seen that the proportion of grains free from dislocations increases with decreasing thickness.

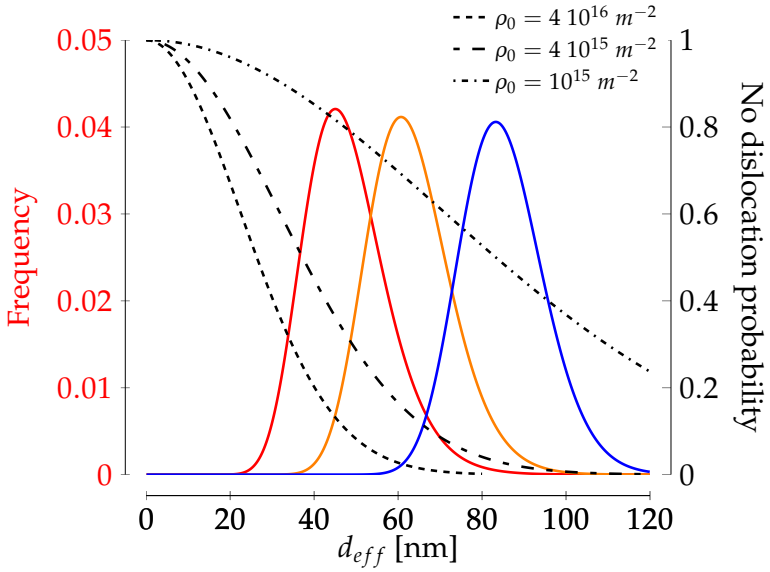

Fig. 4.5: Effective grain size distribution (continuous lines) and probability of having no dislocation inside a grain (dashed lines) as a function of the effective grain size. The gaussians correspond to, from left to right, film thicknesses of 90, 200 and 480 nm.

The following characteristic material parameters apply to the Pd films. Elastic constants are: $C_{11} = 227.1\ GPa$, $C_{12} = 176\ GPa$ and $C_{44} = 71.7\ GPa$. The actual Young's modulus of a polycrystalline film depends on texture, which in turn tends to depend on its thickness. However, no marked texture has been observed in these Pd films. The viscoplastic parameters are chosen as follows: $p = 0.5$ and $q = 1.5$ as suggested by Ono (1968). The activation energy F_0 requires $0.5\mu b^3$ to overcome the short range obstacle without any aid from external stress for pure FCC metals (Frost and Ashby, 1982). The parameter $\dot{\gamma}_0$ has been estimated to be $10^8\ s^{-1}$ (Kocks et al., 1975) which is in agreement with the value used by Wang et al. (2013) in their study of creep in NC metals. The remaining model parameters k_1 and k_2 have been adjusted to fit experimental stress-strain curves.

The loading path undergone during a on-chip tensile test (moderately fast loading and subsequent 3h relaxation) is applied to a representative polycrystal

Table 4.1: Material parameters used in this work

	Description	Value	Unit	References
C_{11}	Elastic constant	227.1	GPa	(Freund and Suresh, 2003)
C_{12}	Elastic constant	176.0	GPa	(Freund and Suresh, 2003)
C_{44}	Elastic constant	71.7	GPa	(Freund and Suresh, 2003)
μ	Shear modulus	45	GPa	-
b	Burgers vector length	0.275	nm	-
p	Glide resistance profile parameter	0.5	-	(Ono, 1968)
q	Glide resistance profile parameter	1.5	-	(Ono, 1968)
F_0	Activation energy	$0.5\mu b^3$	J	(Frost and Ashby, 1982)
ρ_0	Initial dislocation density	$4\ 10^{15}$	m^{-2}	-
$\dot{\gamma}_0$	Reference slip rate	10^8	s^{-1}	-
$\dot{\Gamma}_0$	Reference slip rate	$12\dot{\gamma}_0$	s^{-1}	-
k_B	Boltzmann constant	$1.38\ 10^{-23}$	J/K	-
a	Area swept out for reverse jump	$3000\ b^2$	m^2	(Kocks et al., 1975)
k_1	Fit parameter	15.7	nm	-
k_2	Fit parameter	27.24	-	-

consisting of 1000 grains with random crystallographic texture. The optimized parameters for dislocation evolution were obtained in such a way as to fit at best the three experimental stress-strain curves depicted in Figure 4.6. The same parameters are used for each film thickness, see Table 4.1. Only the effective grain size and the proportion of grains having no dislocation vary in accordance with the experimental distribution (Figure 4.5).

The results shown in Figure 4.6 demonstrate that the model, based on dislocation accumulation and recovery, and on the main microstructural features measured experimentally is able to reproduce the experimental trends with only realistic parameter values. The yield strength of each film thickness is well captured, except for the 480 nm thick film where the yield stress is slightly overestimated. The experimental uncertainty is the largest for the thinnest film so that tuning parameters for this case would not be justified.

The relaxation results are compared to the predictions of the model which was subjected to fast loading and subsequent relaxation under the constraint of the spring as in the experiments, in Figure 4.7. Experimental relaxation/creep responses too are also fairly well captured by the model. This shows that relaxation/creep is well predicted with the same set of material parameters and thus

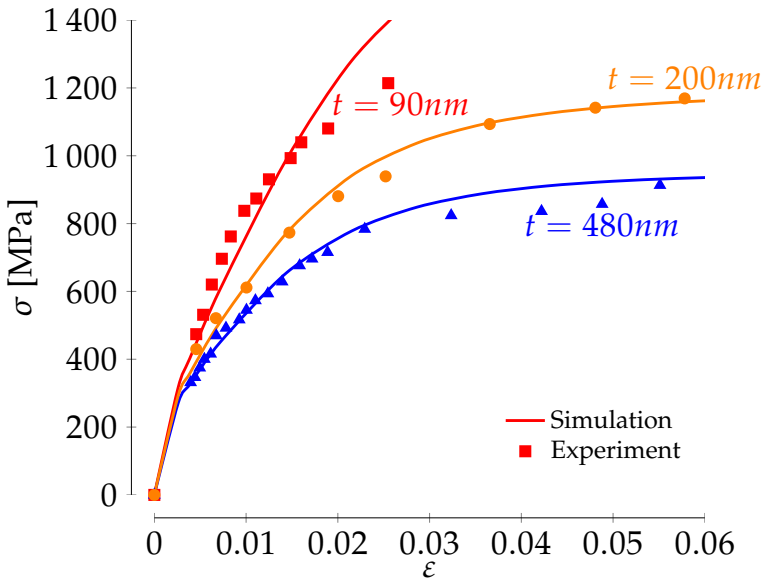

Fig. 4.6: Comparison between the experimental and predicted stress-strain curves for 90, 200 and 480 nm thick Pd films after moderately fast loading and subsequent 3h relaxation. The symbols represent the experimental data.

without adoc fitting based on the relaxation/creep results or on the dislocation evolution. For the 480nm thick film, the accuracy of the relaxation/creep prediction increases with the amplitude of the pre-strain. When $\varepsilon_{3h} = 0.023$ and $\varepsilon_{3h} = 0.012$, the simulation creep rate is smaller than the experimental one. If we consider the mean value of the creep rate during the whole process, both simulations and experiments indicate that (i) for a fixed initial pre-strain, the mean creep rate decreases when the film thickness increases; (ii) for a fixed film thickness, the mean creep rate increases with the amplitude of the pre-strain. When analysing the results, we must keep in mind that experiments involve increase of strain under a decreasing stress and the dependence of such mixed relaxation/creep response on the ratio of the sample and the actuator lengths makes it difficult to quantitatively compare the responses of films with different thicknesses.

As shown in Figure 4.8, the polycrystalline averaged dislocation density increases when deformation is applied, keeps increasing during the three first hours of relaxation and finally decreases upon relaxation. The dislocation density raises by a factor 9 for the 90 nm thick film with $\rho_0 = 4\ 10^{15} m^{-2}$. This feature is qualitatively compatible with the experimental observations of dislocation density increase during loading and dislocation density decrease during subsequent relaxation (Colla et al., 2015). The qualitative experimental trend is depicted in Figure 4.8. If $\rho_0 = 10^{16} m^{-2}$ is assumed, the dislocation density increases by a factor 2.5 which is more in agreement with the experimental value.

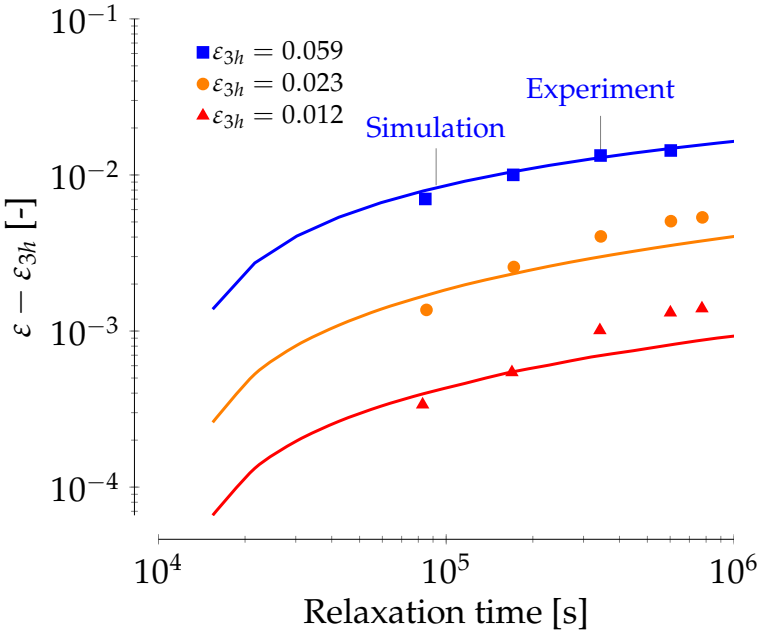

(a) 480 nm thick film

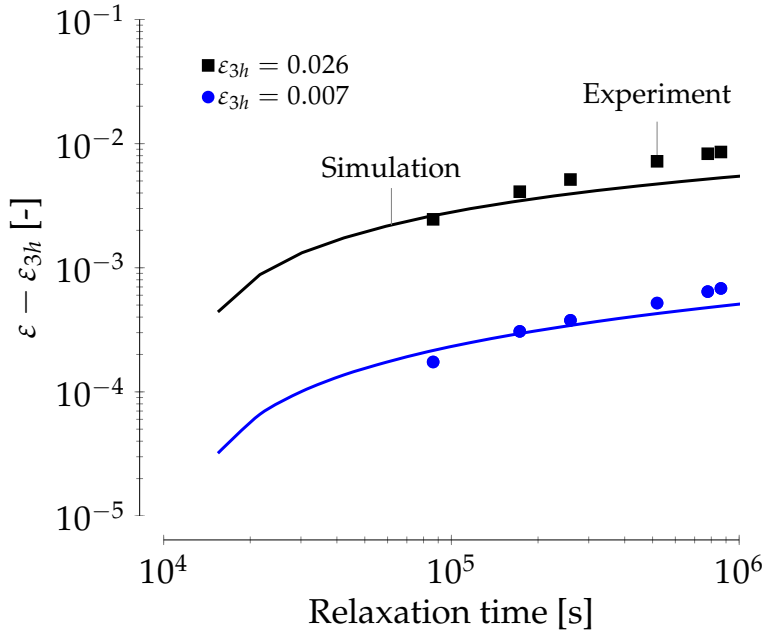

(b) 90 nm thick film

Fig. 4.7: Comparison between the experimental and predicted relaxation response for 90 and 480 nm thick films at different initial relaxation pre-strains ε_{3h}. The symbols represent the experimental data.

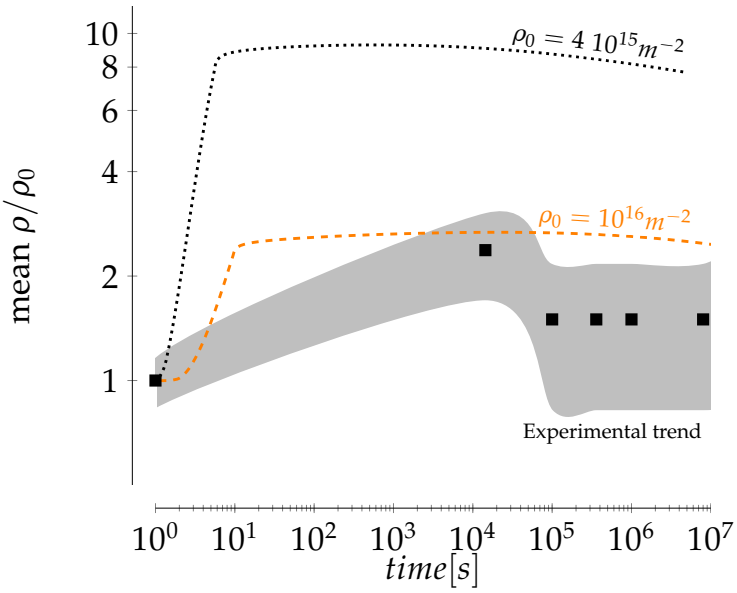

(a) Dislocation evolution

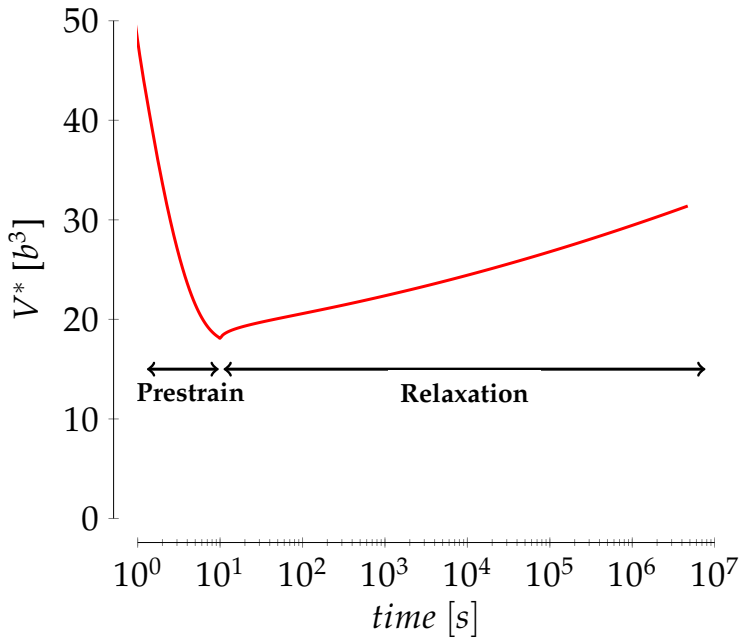

(b) Activation volume evolution

Fig. 4.8: (a) Grain volume averaged dislocation density evolution of 90, 200 and 480 nm thick Pd films versus relaxation time for different initial dislocation density, ρ_0. The relaxation pre-strain is 0.02. (b) Mean activation volume V^* as a function of simulation time t for 90 nm thick film under uniaxial tension and subsequent spring like relaxation. The relaxation starts after 10 s.

A side result of this modelling effort is in the data extraction from experimental measurements which are only available after 3 hours of relaxation. In reality, the film experiences first a fast loading at an estimated strain rate between 5 10^{-4} and 5 10^{-3} s^{-1}, taken here $\dot{\varepsilon} = 3\ 10^{-3}\ s^{-1}$, as depicted in Figure 4.9. The films creep then for 3 hours following the behaviour imposed by the elastic actuator. These results highlight the predominance of relaxation/creep on the experimentally measured mechanical behaviour. Depending on the actuator length, the magnitude of the creep strain varies and a large strain is reached during relaxation of the 480 nm thick film for instance.

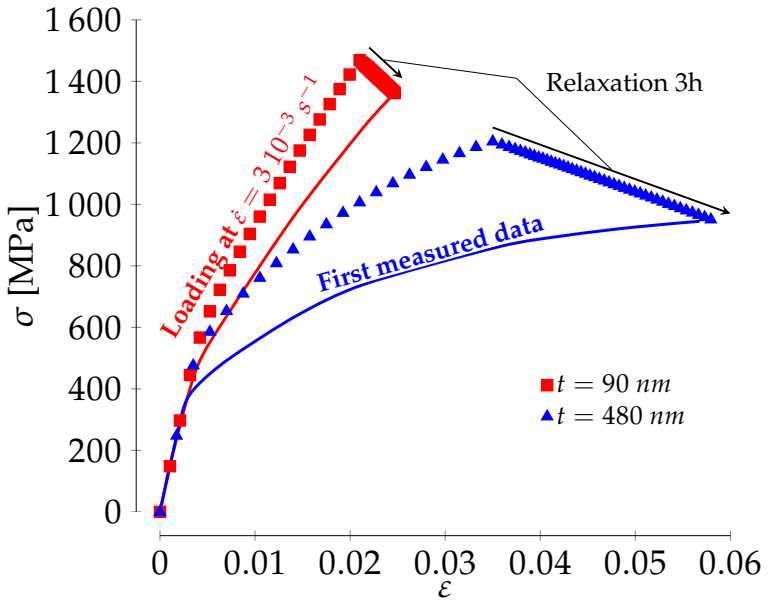

Fig. 4.9: Comparison between the predicted stress-strain curves after 3 hours relaxation and during the loading and the subsequent relaxation for 90 and 480 nm thick Pd films

4.4.2 Discussion

The results shown in Figure 4.6, 4.7 and 4.8 demonstrate that the present crystal plasticity model is able to reproduce, with a limited number of tuning parameters, the relaxation/creep behaviour, the dislocation density evolution and the film thickness effect. Conforming to TEM observations, the model includes a description of the main microstructural features and it assumes that dislocation-based mechanisms dominate. Furthermore, valid predictions can be obtained without resorting on a gradient plasticity formulation (see e.g. (Brugger et al., 2010)). The only length scale that enters the present model is the grain size in the mechanical threshold expression (4.6).

Plasticity of NC metallic films has been modelled with different approaches. However most of the previous studies involved GB-mediated plasticity mecha-

nisms. They often assumed a composite material with a thick grain boundary phase (Gürses and El Sayed, 2011b; Li and Weng, 2013; Kim et al., 2001) and considered the competition of several plasticity mechanisms (Kim et al., 2001; Shi and Zikry, 2009; Zhu et al., 2005, 2006). The present model assumes that plasticity is achieved by dislocation slip only, which is an assumption used also in the quantized crystal plasticity (QCP) approach (Li et al., 2009a, 2012) The assumption that kinematic hardening results form the interaction of soft and hard grains was already suggested by Li et al. (2009a, 2012) who considered widely scattered critical resolved shear stresses in order to capture experimental trends. The originality of the present contribution may be summarized as follows: (i) the distribution of soft and hard grains is here directly correlated to the grain size distribution and the dislocation density distribution; (ii) thermal activation is here taken into account through the physics-based rate equation (4.4); (iii) the scale transition based on the ALAMEL model is for the first time successfully applied to thin films with columnar grains.

The validity of a dislocation based crystal plasticity model at such small grain size can be questioned. As presented in section 4.3.2, the present crystal plasticity framework assumes that deformation occurs by dislocation slip only. Such model may also be extended to include other mechanisms such as mechanical twinning or phase transformation. A fundamental assumption is that the Burgers vector is really small compared to the grain size, allowing to consider the effects of dislocation slip averaged over time and space as a continuum shear. Based on the mechanism of dislocation nucleation and propagation through the entire grain proposed by Van Swygenhoven et al. (2006) for NC metals, the QCP theories of Li et al. (2009a) and Yuan et al. (2015) rely also on the crystal plasticity framework. In contrast to the repeated statements in the literature that NC metals do not accumulate dislocations during deformation (Hugo et al., 2003; Van Swygenhoven et al., 2006), Colla et al. (2015) have observed an huge dislocation activity and storage. The scientific community has sometimes expressed scepticism with respect to such high observed dislocation density. Apart from experimental errors, the measured dislocation densities are nevertheless not in conflict with a simplified approach of the Taylor equation $\sigma = M\hat{\tau} = M\alpha\mu\sqrt{\rho}$ during relaxation if a Taylor factor $M = 3$ and $\alpha = 0.3$ are considered. $\rho_0 \sim 10^{16}$ has also been observed by Wang et al. (2010) in NC Pt and by Lee et al. (2013) in NC Ni. As the stress is maintained during *in situ* TEM characterization (as employed these authors and Colla et al. (2015)), loss of dislocations by recovery during full unloading of the sample prior to TEM observation is avoided and higher ρ may be found than usual. In contrast to the discrete single slip events of the QCP models, such high dislocation density allows a continuous treatment of dislocation interactions at a grain scale. For grains initially free from dislocations, the stress required for dislocation nucleation τ_{nucl} is assumed to reach the theoretical shear strength. This nucleation stress was found to vary between $\mu/30$ and $\mu/10$ as a function of the Schmid factor (Spearot et al., 2009). Such lim-

ited impact on τ_{nucl} is neglected in the present model. Still, the nucleation of a dislocation is predominantly triggered by the local stress concentrations in the GBs (Bitzek et al., 2008). The corresponding nucleation stress can be considerably reduced albeit such effect is not considered in this work.

In this chapter, the mechanical response of Pd thin films is investigated using a micro-macro averaging scheme based on the ALAMEL model. This choice was made because the ALAMEL model is much more computationally efficient than CPFEM which was tested first. When starting this research, other scale transition schemes were considered such as a crystal-plasticity-based finite-element method (CPFEM) allowing full-field calculations over large samplings of grains constituting representative volume elements (RVEs) of the microstructure and texture (e.g. (Delannay et al., 2006; Segurado and Llorca, 2013)). In order to reproduce the experimental grain size distribution, the proposed model microstructure consisted of a periodic Laguerre-Voroinoï tessellation (100 grains), which was meshed adaptively so that grain boundary regions were finely discretized. As the experimental stress-strain curves were obtained after 3h relaxation due to process requirement, moderately fast loading and subsequent spring-like relaxation was applied to the RVE. Each experimental point in Figure 4.6 represents a specific loading path such that every iteration of the fitting procedure based on the Nelder algorithm (Nelder and Mead, 1965) consisted of 36 FEM simulations (12 by film thickness). From a computational viewpoint, such procedure was not efficient and efforts have then been devoted to the Multisite scale transition method. More efficient optimization procedure by means of CPFEM can nevertheless be applied to circumvent the time consuming approach followed in this thesis. An inverse optimization strategy based on the Levenberg-Marquardt method was recently proposed by Segurado and coworkers to determine the single crystal properties from the experimental mechanical behaviour of polycrystals under various loadings (Herrera-Solaz et al., 2014). The iterative optimization process began using simple RVE containing less than 100 grains in which each grain is represented by one element and changed progressively to more realistic RVEs once the optimization algorithm has reached the optimum solution for this RVE. This hierarchical approximation was shown to be very efficient to reduce the computational effort. Furthermore, this Levenberg-Marquadt optimization strategy was found to be robust with respect to the chose of the initial guesses while a minimum critical input information has to be provided in order to ensure the validity of the results (Herrera-Solaz et al., 2015).

In addition to the grain size dependent plasticity, thickness size effects have been reported for face-centered cubic (FCC) metallic thin films: flow strength increases with decreasing thickness, see e.g (Venkatraman and Bravman, 1992). The influence of Pd film thickness is successfully captured by our model. This external geometric size effect can be attributed to the reduced number of grains across the thickness (one or a few) and to the presence of free surfaces. The

dislocation-based crystal plasticity model does not take into account the presence of free surfaces and the dislocation starvation mechanism. The observed film thickness effect originates in our model only from the definition of the equivalent effective grain size and the associated proportion of grains free from dislocations. In other word, even though the crystal plasticity model misses several discrete deformations mechanisms such as intragrain back stress, these are not dominating the mechanical response of the film.

The strain rate sensitivity is often quantified by the apparent strain rate sensitivity exponent or by the apparent activation volume. The apparent strain rate sensitivity exponent m is defined by

$$m = \frac{\partial \ln \sigma}{\partial \ln \dot{\varepsilon}_p} \tag{4.16}$$

where σ is the stress and $\dot{\varepsilon}_p$, the plastic strain rate. Regardless of the involved mechanisms, the apparent activation volume may be defined as

$$V = M k_B T \frac{\partial \ln \dot{\gamma}}{\partial \sigma} \tag{4.17}$$

with M, the Taylor factor, k_B, the Boltzmann constant, T, the temperature and $\dot{\gamma}$, the slip rate. The apparent activation volume is commonly computed from the macroscopic measurement of σ and ε. During the last decade, the strain rate sensitivity of NC metals has been extensively studied by strain rate jumps, nanoindentation or on-chip technique. These studies reported a variety of rate sensitivity exponents, m, for NC and ultrafine grained fcc metals, such as Ni (Schwaiger et al., 2003; Wang et al., 2006; Dalla Torre et al., 2002; Maier et al., 2011; Liu et al., 2014), Cu (Duhamel et al., 2010; Cheng et al., 2005; Lu et al., 2005; Wang and Ma, 2003), Al (Gianola et al., 2006; Coulombier et al., 2012), Au (Jonnalagadda et al., 2010; Emery and Povirk, 2003) and Pd (Coulombier et al., 2012), most of which are of the order of 0.015-0.07 except for Au which can reach 0.15. The data compiled by Wei (2007) clearly shows a monotonical increase of m with decreasing grain size. Different values for m and V can arise for different initial strains indicating a change of relaxation mechanism and/or of the energy barrier to overcome short range obstacles. V is indeed related to the pinning distance (see equation (4.19)). The strain rate sensitivity exponent and the activation volume are directly related to the plastic deformation mechanisms. Due to the dense grain boundaries network in NC materials, enhanced strain rate sensitivity is not surprising because bulk dislocation forest based mechanisms ($V \sim 100 - 1000b^3$ and $m \sim 0 - 0.005$) are progressively replaced by thermally activated grain boundary-dislocation interaction mechanisms ($V \sim 1 - 10b^3$ and $m \sim 0.1 - 1$) (Meyers et al., 2006).

On the basis of the variation of ε^p and σ with time during relaxation, one can determine the apparent activation volume using equation (4.17). As a first simple means to analyse the plastic strain and stress versus time t

data, a logarithmic variation is assumed. An imposed logarithmic variation of ε^p and σ with t leads to a constant average apparent activation volume V independent of time (Caillard and Martin, 2003). If M is taken equal to $\sqrt{3}$ as proposed for FCC NC materials (Asaro and Suresh, 2005), V ranges from 21 to 32 b^3, depending on the relaxation pre-strain. These values are consistent with the values reported by Colla et al. (2015) for NC Pd, again confirming the predominance of dislocation-based mechanisms in these films. The true activation volume for recovery, V^* i.e. for a relaxation mechanism based on the depinning of dislocations, can be expressed by (Argon, 2008):

$$V^* = b\lambda\Delta y^* \tag{4.18}$$

where λ is the distance between the pinning points and Δy^* is the activation distance, i.e. the distance over which a dislocation has to jump to overcome the energy barrier which retains it trapped at its pinned position. The distance between pinning points is related to the dislocation density ρ:

$$\lambda = \beta\rho^{-1/2}, \tag{4.19}$$

where β is a geometric factor approximately varying between 1 and 2. Activation volume is thus a microscopic local quantity which is better defined as the derivative of the activation energy with respect to the effective stress at constant temperature:

$$V^* = -\left(\frac{\partial\Delta G}{\partial\tau^\alpha}\right)_T = F_0\frac{pq}{\tau^\alpha}\left(\frac{\tau^\alpha}{\hat{\tau}}\right)^p\left\{1-\left(\frac{\tau^\alpha}{\hat{\tau}}\right)^p\right\}^{q-1}. \tag{4.20}$$

Equation (4.17) can be recovered by assuming a simple Arrhenius-type relation between the slip rate and the activation energy. Note that the grain size dependence of $\hat{\tau}$ introduces a similar effect for the activation volume which in turn magnifies the strain rate sensitivity at small grain size, due to the inverse proportionality between V^* and m. On the basis of equation (4.20), the variation of the true activation volume with time is determined for each grain. The stress used here is the mean resolved shear stress on the 12 octahedral slip systems. Figure 4.8(b) represents the variation of the mean true activation volume with time, calculated for the 90 nm thick film loaded up to 2% deformation. The activation volume decreases with increasing plastic pre-strain. This agrees with the idea that V^* depends on dislocation density. After the ten first seconds of deformation, V^* tends to increase with subsequent plastic strain during relaxation as observed experimentally. A moderate increase of V^* by a factor $\sim$1.5 is observed upon the 40 days of relaxation. This increase can thus be associated to a decrease in ρ, again in accordance with the dislocation evolution obtained by simulation (see Figure 4.8(a)) and with the experimental observations (Colla et al., 2015).

4.5 Parametric study

Now, starting from the identified set of parameters, the effects of strain rate, grain size distribution and texture will be studied.

4.5.1 Strain rate effect

As previously discussed, the deformation mechanisms are thermally activated and the strain rate sensitivity is taken into account by the generalized rate equation with a phenomenological description of the activation energy. Figure 4.10(a) depicts the strong strain rate sensitivity of 200 nm thick NC Pd film, even at room temperature.

For the simulations, the loading strain rate is assumed to be equal to $3\ 10^{-3}\ s^{-1}$. During the first step of the on-chip test, the loading rate is dictated by the release rate of the rectangular actuator which is progressive but not completely controlled. The realistic range of strain rate is in between $5\ 10^{-4}$ to $5\ 10^{-3}\ s^{-1}$. The influence of the strain rate can be seen in Figure 4.10(a) and (b) where the realistic range of stress and strain have been shaded. Figure 4.10(b) represents the evolution of the relaxed strain ($\varepsilon - \varepsilon_{pr}$ with ε_{pr}, the strain reached before relaxation) as a function of the loading strain rate. The influence of strain rate on the measured strain after 3 hours of relaxation is really limited. In order to overcome this limitation, test structures with tapered shape actuators have been produced in the last generation of on-chip test structures (Vayrette et al., 2015).

4.5.2 Grain size distribution and texture effect

In NC metals, the grain size distribution is of prime importance. Plastic deformation is not only affected by the mean grain diameter but also by the grain size distribution, see e.g. (Koslowski, 2010). The smallest grains can indeed be extremely resistant to glide while larger grains can deform by more conventional dislocation mechanisms, leading to stress heterogeneities, huge levels of back stress and long elasto-plastic transition (Saada and Kruml, 2011). Furthermore, in thin films or when dimensions are reduced, the probability of finding dislocations sources becomes low and they are harder to activate (Benzerga and Shaver, 2006). The grain size distribution was shown to be a key parameter for the generation of stress heterogeneities, allowing strain recovery upon unloading. To understand the effect of grain size distribution, fast loading and subsequent relaxation simulations on 200 nm thick film with in-plane mean grain size $\bar{D} = 30$ nm are performed with varying variance $Var[D]$. Inversely to Zhu et al. (2006) who did not take into account a proportion of grains having initially no dislocation, the ultimate tensile strength increases with increasing variance, see Figure 4.11. Despite the fact that the proportion of large grains increases, a larger number of grains are free of dislocations, resulting in an

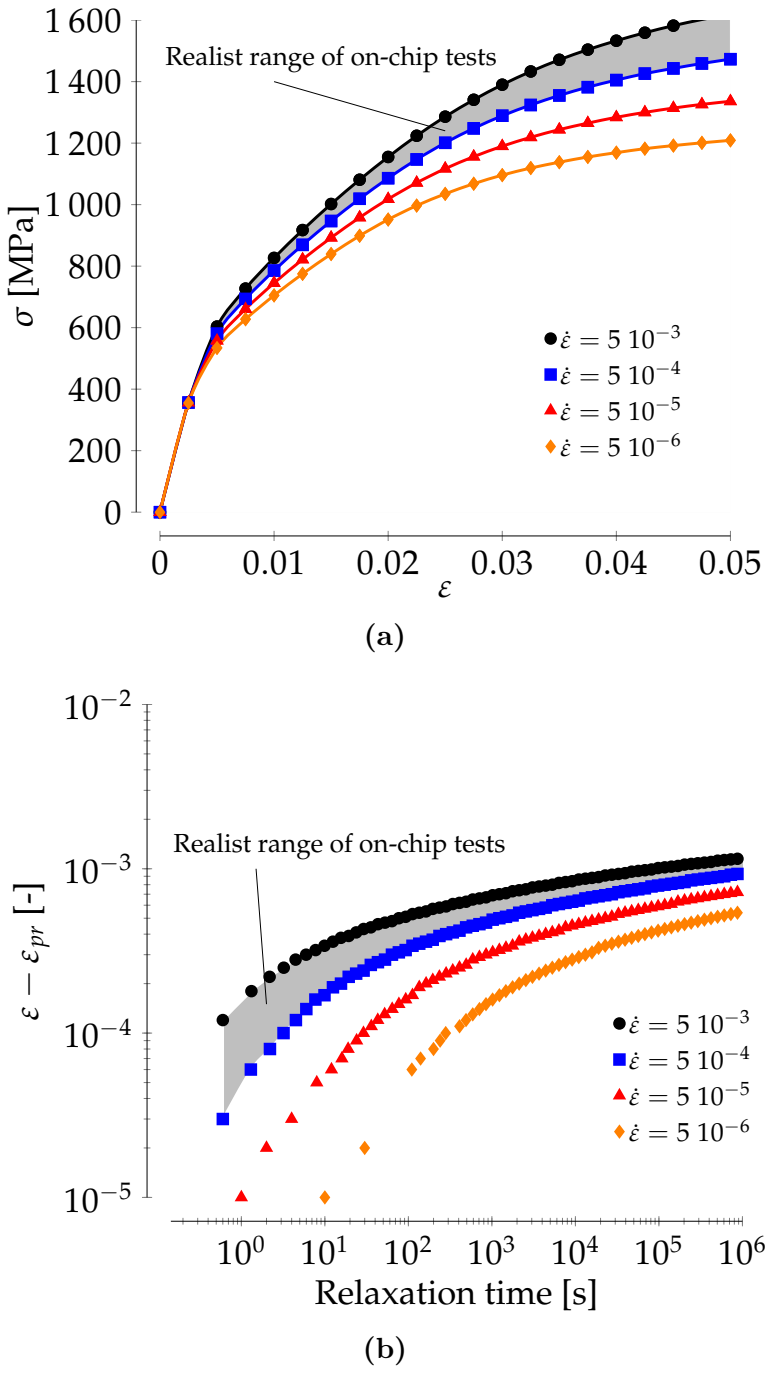

Fig. 4.10: (a) Effect of the strain rate sensitivity on the mechanical response of 200 nm thick Pd film with mean in-plane grain size $\bar{D} = 30$ nm and variance $Var[D] = 100\ nm^2$ when subjected to uniaxial tension. (b) Effect of the strain rate sensitivity on the relaxed strain of 200 nm thick Pd film when subjected to uniaxial tension and subsequent relaxation.

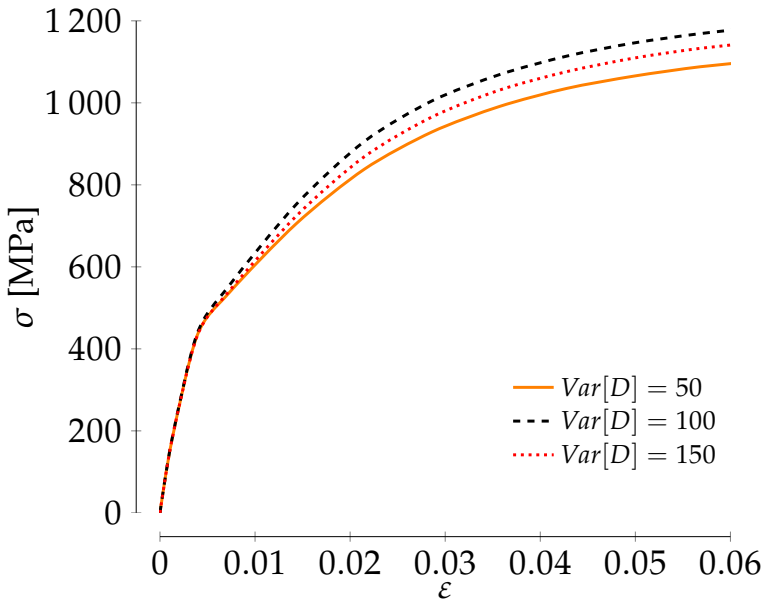

Fig. 4.11: Effect of the grain size distribution on the mechanical response of 200 nm thick Pd film with mean in-plane grain size $\bar{D} = 30$ nm when subjected to fast loading and subsequent three hours relaxation.

improved strength. For $Var[D] = 150$, this tendency wipes off and the grain size influence becomes dominant, resulting in a lower strength due to the higher proportion of large grains.

Metallic thin films are usually characterized by the presence of very sharp crystallographic texture whereas the films tested experimentally present nevertheless no marked crystallographic texture. A slight fibre texture is still observed with the (011) direction oriented parallel to the 90 nm thick film normal, with no in-plane preferential orientation. An increased Pd deposition rate weakens the possible (011) texture component, leading to a more random texture as for the 200 nm and 480 nm thick films (Colla, 2014). Texture development can occur during thickening of the film and during post-deposition annealing. It can also depend on the deposition method, see (Wang et al., 2012b). For instance, Pd deposition by sputtering can lead to a slight (011) fibre through the thickness. Different insights on texture development in thin films can be found in the literature (Thompson and Carel, 1995). The choice of the substrate and of the deposition conditions is of prime importance. Thin film textures can roughly be classified into random textures and fibre textures for which one crystallographic direction of all the grains are aligned with the substrate normal (Suwas and Ray, 2014). The influence of such perfect crystallographic fibre texture on the mechanical behaviour is shown in Figure 4.12 for films with different thickness. Texture has limited impact on the mechanical response of the film during loading or after relaxation. In-plane crystallographic desorientations do not affect such sub-micron film subjected to

	$\sigma^y_{textured}/\sigma^y_{random}$	r	$E_{textured}/E_{random}$
	480 nm		
(001)	0.83	0.26	0.85
(011)	1.04	2.05	1.03
(111)	0.97	3.82	1.08
	200 nm		
(001)	0.85	0.32	0.85
(011)	1.03	2.16	1.03
(111)	0.98	3.88	1.08
	90 nm		
(001)	0.89	0.45	0.85
(011)	1.04	1.63	1.03
(111)	0.97	2.53	1.08

Table 4.2: Yield strength $\sigma^y_{textured}$, averaged Lankford coefficient r and effective Young's modulus $E_{textured}$ of three different fibre textures for each film thickness.

uniaxial tension. In order to evaluate the plastic anisotropy, the yield strength $\sigma^y_{textured}$ and the Lankford coefficient r defined by

$$r = \frac{\dot{\varepsilon}^p_{22}}{\dot{\varepsilon}^p_{33}}, \tag{4.21}$$

are evaluated for (001),(011) and (111) fibre textures. The tangent modulus approach is used here to determine the yield strength due to the long elasto-plastic transition (Rajagopalan et al., 2010): $\sigma^y_{textured}$ is defined as the stress at which the strain hardening rate Θ becomes smaller than one third of the Young's modulus. The results tabulated in Table 4.2, reveal a high plastic anisotropy. The averaged Lankford coefficients strongly differ from 1, corresponding to a purely isotropic response ($r_{random} \sim 1.5$ for the three films). The softest grains have a (001) direction perpendicular to the loading direction while the hardest grains present a (011) direction parallel to the film normal. The influence of the texture on the effective Young modulus is also marked, in agreement with the Zener ratio AR:

$$AR = \frac{2C_{44}}{C_{11} - C_{12}} = 2.81 \tag{4.22}$$

which quantifies the degree of elastic anisotropy and suggests that Pd is highly anisotropic.

4.5.3 Internal stress and recovery

In order to evaluate the internal stress levels, stress reduction simulations are performed on the 90 nm thick Pd films with grain size distribution characterized by a mean in-plane grain size, $\bar{D} = 30$ nm and a variance, $Var[D] = 100$

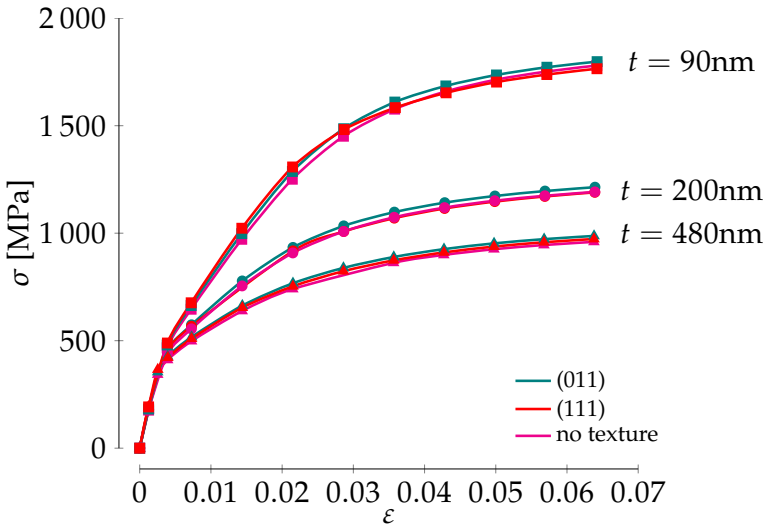

Fig. 4.12: Effect of the crystallographic texture on the mechanical response of Pd film with different film thickness, constant mean in-plane grain size $\bar{D} = 30$ nm and variance $Var[D] = 100$ when subjected to fast loading and subsequent three hours relaxation. Random, (011) and (111) fibre textures are considered.

nm^2. The polycrystal is loaded up to 3 % strain using a constant strain rate 10^{-3} s^{-1}. The specimen is then unloaded very rapidly by an amount $\Delta\sigma$, followed by a subsequent creep period of 3 minutes. As can be seen in Figure 4.13, forward and backward creep are observed as experimentally shown on NC Ni by Van Petegem et al. (2006) and Sun et al. (2015). This figure represents the mean creep rate normalized by the loading strain rate as a function of the hold stress normalized by the maximum stress reached during the loading. This significant kinematic hardening contribution results from the heterogeneity of deformation leading to high internal stress levels. Internal stress in single phase pure polycrystals results from the anisotropy of individual crystals and the obstacles to dislocation motion. Microstructural features play thus a key role in the plastic response of NC metals. The kinematic hardening contribution in this model arises from the difference of crystallographic orientation and from the initial dislocation density within grains. As mentioned already in Section 4, No intragrain back stresses are considered in this model. The Taylor and ALAMEL assumptions have been compared in Figure 4.13. The Taylor model assumes that each grain undergoes the macroscopic applied deformation. This results in higher stress heterogeneities to accommodate the imposed strain and leads to backward creep at higher positive hold stress after unloading. Following Van Petegem et al. (2006), both effective and internal stresses have been evaluated. In a simplified picture, the stress applied to deform plastically a crystal can be decomposed into an effective stress σ^* and an internal athermal stress σ_i. The ratio $\sigma^*/\sigma_i \sim 0.5$ is in qualitative good agreement with experimental evidence but slightly larger than what is measured in nc Ni ($\sigma^*/\sigma_i \sim 0.3$) (Van Petegem et al., 2006), indicating a lower internal

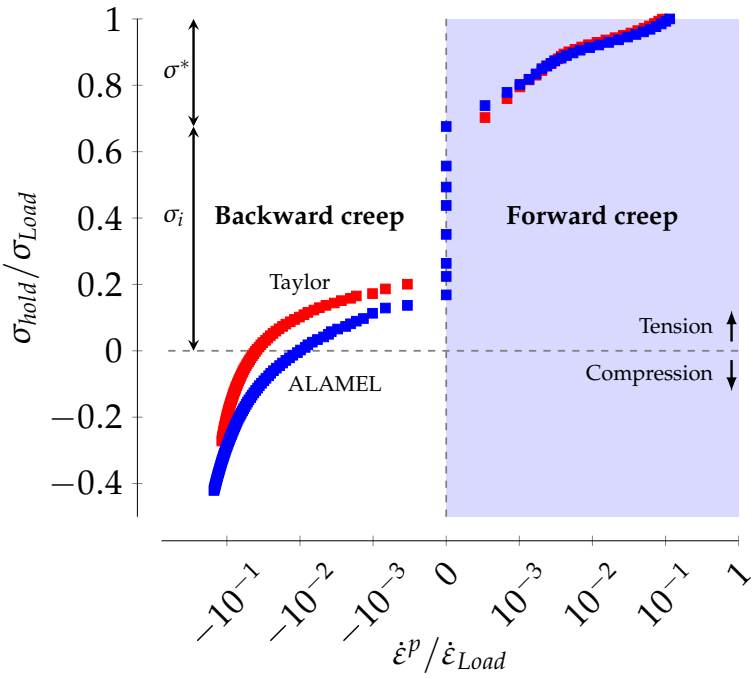

Fig. 4.13: Normalized creep rate as a function of the normalized hold stress after unloading for 90 nm thick Pd films using Taylor and ALAMEL model.

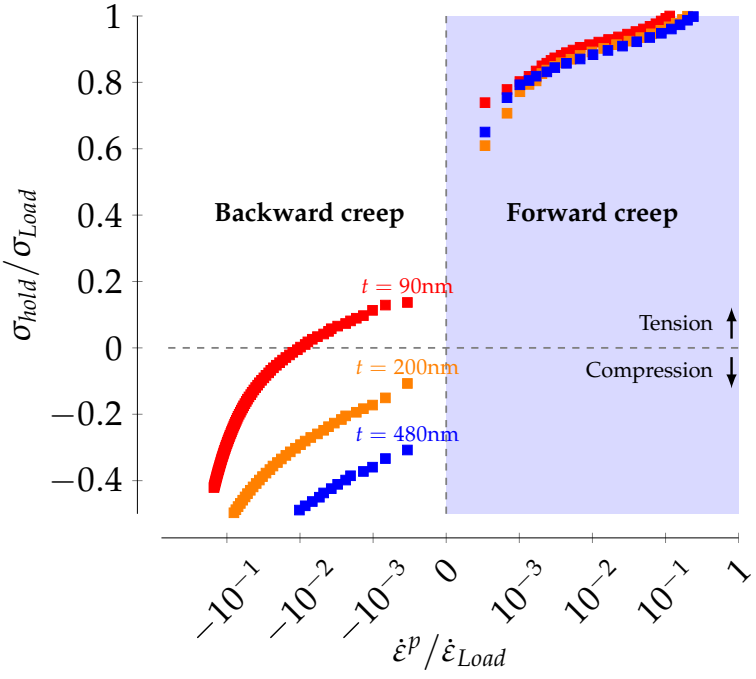

Fig. 4.14: Normalized creep rate as a function of the normalized hold stress after unloading for Pd films with mean in-plane grain size $\bar{D} = 30$ nm and variance $Var[D] = 100$, and different thickness

stress level. Viscoplastic effects are thus predominant in this dislocation-based model. Note also that the high internal stress level and the backward creep observed in the simulation results are in qualitative agreement with the experimental strain recovery results on the Pd films obtained in collaboration with the group Prof. T. Saif, which showed a small Bauschinger effect at positive stress upon unloading and a small strain recovery after 2 hours, see in (Colla, 2014). More characterizations on Pd films under unloading conditions should be made to confirm this trend.

Recent experimental and numerical studies on Al and Au thin films have shown that plastic strain can be recovered under zero applied stress conditions (Rajagopalan et al., 2007; Lonardelli et al., 2009; Rajagopalan et al., 2008; Koslowski, 2010). These experimental results reveal that time dependent strain recovery results from highly heterogeneous stress distribution. Sufficiently small and large grains are required in order to generate the stress heterogeneity and to allow recovery. Such recovery experiment has been simulated in the present study. Small and slow strain recovery is indeed predicted by the model. The influence of the film thickness on recovery is depicted in Figure 4.14. Thinner films result in higher proportion of grains initially free of dislocation. This induces higher stress heterogeneity, leading to the initiation of backward creep for higher hold stress after unloading.

4.6 Conclusion

The dislocation-based crystal plasticity model presented in this chapter for metallic thin films takes into account the strain rate sensitivity, the effects of grain size distribution and assumes only dislocation-based thermally activated deformation mechanisms. The model has been assessed against experimental data on sub-micron Pd films gathered using the lab-on-chip technique. Not only the effect of the film thickness is captured but also the relaxation response and the dislocation density evolution are correctly captured.

The dislocation-based deformation mechanism assumption allows the proper reproduction of all the experimental trends, highlighting the dominance of a pure dislocation controlled deformation mechanism for thin films with high defects density. The log-normal grain size and free dislocation grain distributions, combined with the crystallographic anisotropy, generate sufficiently heterogeneous stress distribution to observe backward creep and strain recovery, without any complex kinematic hardening formulation. One of the key element is the presence of hard grains initially free of mobile dislocations. According to the model, texture created during the deposition of a thin film does not significantly influence the creep behaviour and the stress heterogeneity. Furthermore, the model can be used to the data reduction analysis from the on-chip test technique.

According to the model, texture created during the deposition of a thin film does not significantly influence the creep behaviour and the stress heterogeneity.

CHAPTER 5

Localized necking in nanocrystalline metallic thin films under static and relaxation conditions

5.1 Introduction

From a reliability viewpoint, ductility in nanocrystalline metallic thin films is a critical issue in many applications such as in micro- or nano-electromechanical systems (Spearing, 2000; Iker et al., 2006), in thin membrane technology and in flexible electronics (Lacour et al., 2003; Béfahy et al., 2007). NC metals and thin films generally suffer of a lack of ductility. Nevertheless, counter-examples of large ductility in NC thin films have been reported in the literature and presented in section 2.4. Despite the increasing yield strength, necking can be delayed in NC materials by strain hardening or strain rate sensitivity enhancement. Additional source of necking stabilization is the storage of a geometrically necessary dislocation (GND) density. Numerical simulations relying on a strain gradient plasticity (SGP) theory have shown that the incorporation of plastic strain gradients can very significantly delay the occurrence of strain instabilities when the characteristic dimension of the specimen is on the order or below the characteristic length of the gradient model (Niordson and Redanz, 2004; Niordson and Tvergaard, 2005; Pardoen, 2014).

As a summary, in small scale systems, an important synergy exists between

film thickness and mechanical properties. As the film thickness decreases, the grain size decreases proportionally, resulting in a larger yield stress, a lower strain hardening capacity unless SGP become significant too, and an increased strain rate sensitivity due to thermally activated mechanisms. All these interconnected effects can affect positively or negatively the ductility of freestanding films. Necking can also be delayed due to delocalization effects resulting from the presence of a soft underlying substrate (Lacour et al., 2003; Lambricht et al., 2013) but this is not addressed here as the present chapter only focus on freestanding films.

In this chapter, an enriched Marciniak-Kuczynski (MK) type imperfection based plastic localization model is developed to address necking issues during static loading or time dependent relaxation which can be both met in application. 3D finite element (FE) simulations on tensile samples with rectangular sections performed by Tvergaard (1993) have shown that specimens with a width over thickness ratio higher than 3 are prone to localized necking without the emergence of diffuse necking. The notions of diffuse and localized necking have been defined in section 2.6. When the thickness is small compared to the width, the specimen is more sensitive to perturbations allowing deformation to easily concentrate over a length comparable to the thickness. The influence of geometry on necking behaviour is well-known for coarse-grained metals and it holds also in the case of ultrafine grained or nanocrystalline metals see e.g. (Espinosa et al., 2004) or (Zhao et al., 2008). Espinosa et al. (2004) have reported localized necking with no clear diffuse necking in freestanding submicron FCC films involving width over thickness ratio between 5 and 20 which are commonly encountered in thin films applications. Compared to the earlier analysis of Hutchinson and Neale (1978a), devoted to the synergy between imperfection, strain hardening and rate sensitivity, the present study aims at accounting also for SGP effects, for grain size dependent strength and rate sensitivity, for elasticity and for the possible contributions of creep mechanisms. Comparisons will be made with experimental data with the aim, either to validate the approach, either to help the interpretation of experimental data. The objective of this study is to provide a better understanding of the complex interplay between different competing or cooperating mechanisms. The model is devoted to localized necking in which the length of the neck scales with the thickness of the specimen. The problem of diffuse necking has been addressed in an earlier study by Pardoen (2014) relying on a simpler 1D imperfection model, thus not adapted to study the localization process in thin inclined necking bands. This chapter is organized as follows: the imperfection based model is first presented, followed by the constitutive laws. The SGP model is then validated towards the FE simulations of Niordson and Tvergaard (2005) and the experimental results of Jonnalagadda et al. (2010). A parametric study is finally carried out with a special attention to the prediction of instability for copper thin films tested using the Lab-on-chip technique.

5.2 MK model

The localized necking analysis is based on the Marciniak and Kuczyński (1967) model that postulates the existence of a material imperfection such as a groove or a narrow band with slightly diminished thickness, across the width of the film as depicted in Figure 5.1(a). In its modified form proposed by Hutchinson and Neale (1978a), the band is oriented at an angle ϕ with respect to the tensile direction $\mathbf{e}_1$. The quantities inside and outside the band are here denoted by the superscripts $()^{in}$ and $()^{out}$, respectively. The imperfection factor f is defined as the ratio of the initial thicknesses inside and outside the band $f = h_0^{in}/h_0^{out}$.

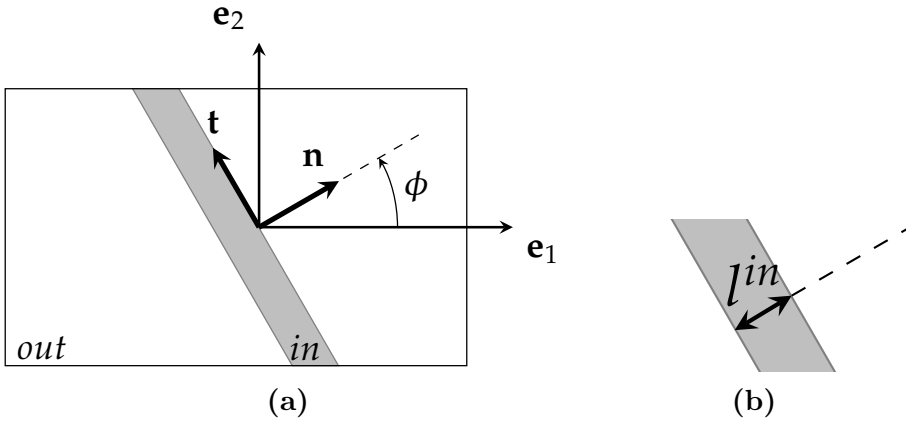

Fig. 5.1: (a) A thin solid with an initial thickness imperfection band (in) oriented at an angle ϕ with respect to the main loading direction and (b) zoom on the band for the definition of the band length l^{in}.

The present model considers the localization process in a finite length specimen with a volume fraction of the band f_b given by

$$f_b = \frac{\alpha f}{1/\eta - \alpha + \alpha f} \tag{5.1}$$

where α is the ratio of the initial length of the band over the initial specimen thickness and η is the specimen thickness over length ratio. The band orientation ϕ differs from its initial state, ϕ_0 and varies with the deformation outside the band which is assumed homogeneous.

$$\tan(\phi) = \frac{\mathrm{F}_{11}^{out}}{\mathrm{F}_{22}^{out}} \tan(\phi_0) \tag{5.2}$$

where the deformation gradient tensor $\mathbf{F}$ is computed from the velocity gradient tensor $\mathbf{L} = \dot{\mathbf{F}}\mathbf{F}^{-1}$. The velocity gradient tensors components of the two zones are expressed by:

$$\mathbf{L}^{out} = \mathbf{L}^{macro} - \frac{f_b}{1-f_b}\Big(\dot{\gamma}_{nn}\,(\mathbf{n}\otimes\mathbf{n}) + \dot{\gamma}_{tn}\,(\mathbf{t}\otimes\mathbf{n}) + \dot{\gamma}_{33}\,(\mathbf{e}_3\otimes\mathbf{e}_3)\Big), \tag{5.3}$$

$$\mathbf{L}^{in} = \mathbf{L}^{macro} + \Big(\dot{\gamma}_{nn}\,(\mathbf{n}\otimes\mathbf{n}) + \dot{\gamma}_{tn}\,(\mathbf{t}\otimes\mathbf{n}) + \dot{\gamma}_{33}\,(\mathbf{e}_3\otimes\mathbf{e}_3)\Big), \tag{5.4}$$

where $\mathbf{e}_3$ is the film normal direction, $\mathbf{n}$ is the band normal direction and $\mathbf{t} = \mathbf{n} \times \mathbf{e}_3$ is tangent to the band. The heterogeneity of the velocity gradient is thus introduced using three variables: $\dot{\gamma}_{nn}$, $\dot{\gamma}_{33}$ and $\dot{\gamma}_{tn}$ while ensuring that

$$\mathbf{L}^{macro} = (1 - f_b)\mathbf{L}^{out} + f_b\mathbf{L}^{in} \tag{5.5}$$

The components of $\mathbf{L}^{macro}$ and the $\dot{\gamma}_{nn}$, $\dot{\gamma}_{33}$ and $\dot{\gamma}_{tn}$ variables are determined by enforcing that the film out-of-plane stresses are nil, $\sigma_{33}^{out} = \sigma_{33}^{in} = 0$, and by balancing forces across the planar interfaces between zones *in* and *out*:

$$\left(h^{in}\boldsymbol{\sigma}^{in} - h^{out}\boldsymbol{\sigma}^{out}\right) : (\mathbf{n} \otimes \mathbf{n}) = 0 \tag{5.6}$$

$$\left(h^{in}\boldsymbol{\sigma}^{in} - h^{out}\boldsymbol{\sigma}^{out}\right) : (\mathbf{n} \otimes \mathbf{t}) = 0 \tag{5.7}$$

where the thickness of each zone evolves according to the out-of-plane deformation: $h^{out} = h_0^{out}\mathrm{F}_{33}^{out}$ and $h^{in} = h_0^{in}\mathrm{F}_{33}^{in}$. When the macroscopic loading mode corresponds to uniaxial tension along $\mathbf{e}_1$, $\sigma_{22}^{macro} = (1 - f_b)\sigma_{22}^{out} + f_b\sigma_{22}^{in} = 0$ is enforced as well.

If a symmetric $\boldsymbol{L}^{macro}$ is imposed, if follows that the spin tensor $\boldsymbol{W}^{macro} = 1/2(\boldsymbol{L}^{macro} - (\boldsymbol{L}^{macro})^T) = 0$ while the strain rate tensor $\boldsymbol{D}^{macro} = 1/2(\boldsymbol{L}^{macro} + (\boldsymbol{L}^{macro})^T) = \boldsymbol{L}^{macro}$. Note that inside and outside the band, the skew part of the velocity gradient is non zero. More specifically, the velocity gradient tensors components of the two zones write:

$$L_{tn}^{out} = D_{tn}^{macro} + W_{tn}^{macro} - \frac{f_b}{1 - f_b}\,\dot{\gamma}_{tn}, \tag{5.8}$$

$$= \underbrace{D_{tn}^{macro} - \frac{1}{2}\,\frac{f_b}{1 - f_b}\,\dot{\gamma}_{tn}}_{D_{tn}^{out}} + \underbrace{W_{tn}^{macro} - \frac{1}{2}\,\frac{f_b}{1 - f_b}\,\dot{\gamma}_{tn}}_{W_{tn}^{out}} \tag{5.9}$$

$$L_{tn}^{in} = D_{tn}^{macro} + W_{tn}^{macro} + \dot{\gamma}_{tn}, \tag{5.10}$$

$$= \underbrace{D_{tn}^{macro} + \frac{1}{2}\,\dot{\gamma}_{tn}}_{D_{tn}^{in}} + \underbrace{W_{tn}^{macro} + \frac{1}{2}\,\dot{\gamma}_{tn}}_{W_{tn}^{in}} \tag{5.11}$$

The onset of localized necking is assumed to occur when the thickness strain rate is much larger inside the band than outside. The following necking criterion is used:

$$|D_{33}^{in}|/|D_{33}^{out}| > 1000. \tag{5.12}$$

This point of instability is characterized by a given value of the macroscopic elongation F_{11}^{macro} which is expected to depend on the initial inclination of the band ϕ_0. All initial band orientation ϕ_0 between 0° and 90° are considered and the localization strain is defined as the earliest occurrence of necking $\varepsilon_{ins} = min_{\phi_0}\mathrm{F}_{11}^{ins}$.

The localization model is solved numerically using an implicit time integration procedure.

5.3 Constitutive laws

The total strain rate $\boldsymbol{D}$ is assumed to be the sum of two parts: an elastic strain rate $\boldsymbol{D}_{el}$ and an inelastic strain rate $\boldsymbol{D}_p$ including the (visco-)plastic and creep/relaxation contributions. The Cauchy stress $\boldsymbol{\sigma}$ is computed assuming isotropic elasticity:

$$\overset{\triangledown}{\boldsymbol{\sigma}} = \boldsymbol{C} : \boldsymbol{D}_{el} \tag{5.13}$$

with $\boldsymbol{C}$ being the isotropic elastic tensor which depends on the Young modulus E and the Poisson's ratio ν. $\overset{\triangledown}{\boldsymbol{\sigma}}$ is the Jaumann rate of the Cauchy stress which allows properly dealing with rigid-body rotation to satisfy the objectivity requirement at large plastic strains, defined as

$$\overset{\triangledown}{\boldsymbol{\sigma}} = \dot{\boldsymbol{\sigma}} - \boldsymbol{W}\boldsymbol{\sigma} + \boldsymbol{\sigma}\boldsymbol{W}. \tag{5.14}$$

As J_2 plasticity is assumed, the plastic yielding behaviour is independent of hydrostatic pressure and the plastic flow rule governs the evolution of the inelastic strain:

$$\boldsymbol{D}_p = \lambda \boldsymbol{s} \tag{5.15}$$

in which the scalar λ is called the plastic multiplier and $\boldsymbol{s}$ is the deviatoric part of the Cauchy stress:

$$\boldsymbol{s} = \boldsymbol{\sigma} - \frac{1}{3}(tr\ \boldsymbol{\sigma})\mathbf{1} \tag{5.16}$$

The plastic multiplier is given by:

$$\lambda = \frac{3}{2}\frac{\dot{p}}{\sigma_{eq}} \tag{5.17}$$

where σ_{eq} is the von Mises equivalent stress defined by

$$\sigma_{eq} = \sqrt{\frac{3}{2}\boldsymbol{s} : \boldsymbol{s}} \tag{5.18}$$

and $\dot{p}$ is the accumulated inelastic strain rate

$$\dot{p} = \sqrt{\frac{2}{3}\boldsymbol{D}_p : \boldsymbol{D}_p}. \tag{5.19}$$

The scalar p is the accumulated plastic strain defined by:

$$p(t) = \int_0^t \dot{p}\ dT. \tag{5.20}$$

As several deformation mechanisms are considered, the material constitutive law is solved in an incremental manner using a modified return mapping

algorithm. The total strain increment $\boldsymbol{D}\Delta t$ is imposed. The values of the variables at time t_n are known and the goal is to find the values of the variables at $t_n + \Delta t$. In the first step of the calculation, the increment is assumed to be purely elastic. The elastic predictor at time $t + \Delta t$, $\boldsymbol{\sigma}^{trial}$ is defined as

$$\boldsymbol{\sigma}^{trial} = \boldsymbol{\sigma}|_{t_n} + (\boldsymbol{C} : \boldsymbol{D}|_{t_n} + \boldsymbol{W}\boldsymbol{\sigma}|_{t_n} - \boldsymbol{\sigma}\boldsymbol{W}|_t)\,\Delta t. \tag{5.21}$$

For the classical (visco-)plastic deformation mechanism with accumulated plastic strain p_{dislo}, a yield function F is defined by:

$$F = \sigma_{eq} - \sigma_f \tag{5.22}$$

where σ_f is the flow stress. If $F^{trial}|_{t_n+\Delta t} > 0$, this plasticity mechanism is activated and plasticity develops during the increment such as to fulfil $F|_{t_n+\Delta t} = 0$. The choice of the yield function requires specific attention as it reflects the deformation mechanisms. A survey of the viscoplastic physics-based yield stress models suggests that as a good approximation, a threshold exists to activate plastic deformation. This suggestion is also in agreement with experiments. Uniaxial tensile tests at different strain rates, generally reveal a saturation of the mechanical response around a master curve at low strain rate, at least at low homologous temperature.

The first elastic predictor is incorrect because creep mechanisms involve no threshold stress and plastic correction phase is subsequently imposed. Using the plastic flow rule, the problem reduces to solving the following equation:

$$\sigma_{eq}^{trial} - 3G\Delta p - \sigma_{eq} = 0 \tag{5.23}$$

where the accumulated inelastic strain increment Δp is the sum of the contributions of all the deformation mechanisms:

$$\Delta p = \Delta p_{dislo} + \Delta p_{other}. \tag{5.24}$$

As these contributions vary with the applied equivalent stress, equation (5.23), the hardening and creep laws are solved iteratively using Newton's method to find the values of Δp_{dislo}, Δp_{other} and σ_{eq}.

Plastic strain gradients result in the storage of geometrically necessary dislocations (GNDs) (Fleck et al., 1994). Plastic strain gradients arise either in response to either inhomogeneous loading (bending for instance), or because the plastic response of the material is inhomogeneous due to its heterogeneous microstructure or its multiphase nature. GNDs are then required to accommodate the lattice curvature associated to non-uniform plastic strain fields while they act also as obstacles for the mobile dislocations, contributing to the deformation. Following Pardoen (2014), the strain gradient plasticity effects are taken into account through the introduction of the phenomenological generalized plastic strain rate $\dot{p}^*_{dislo}$. $\dot{p}^*_{dislo}$ is a combination of the conventional plastic

strain rate $\dot{p}_{dislo}$ and of the plastic strain gradients $\dot{p}_{dislo,k}$. Both linear and quadratic forms have been proposed for $\dot{p}^*_{dislo}$ as well as different decompositions for the gradients. A single parameter theory closely related to the strain gradient theory initially proposed by Aifantis (1984), has been selected here:

$$(\dot{p}^*_{dislo})^2 = (\dot{p}_{dislo})^2 + (l^*)^2 \; \dot{p}_{dislo,k} \; \dot{p}_{dislo,k} \tag{5.25}$$

where the material characteristic length l^*, required for dimensional consistency, sets the scale at which the gradients and thus the density of GNDs, start to significantly contribute to hardening (Fleck and Hutchinson, 2001; Evans and Hutchinson, 2009). The physical meaning of the material length scale l^* is still an open question (Kuroda and Tvergaard, 2010). Furthermore, l^* has no exact physical interpretation as the selected constitutive model is purely phenomenological in contrast for instance with other SGP models with a more physical background (Gao et al., 1999). Appropriate value of l^* can be obtained by fitting experimental results such as Fleck et al. (1994); Evans and Hutchinson (2009). In the framework of crystal plasticity, Geers et al. (2007) have suggested length scales which evolve with the dislocation densities.

Plastic strain gradients essentially develop inside the band. Outside the band, the accumulated generalized plastic strain $p^{out,*}_{dislo}$ is equal to the classical accumulated plastic strain p^{out}_{dislo}. The plastic gradient $\dot{p}_{dislo,k}$ is assumed normal to the band and is approximated by the difference in plastic strain rate between zone *out* and *in* over a geometrical characteristic length corresponding to a part of the current length of the neck, l^{in}/β. The length of the band, illustrated in Figure 5.1(b), is defined as the smallest in-plane dimension of the band (i.e. along the $\boldsymbol{n}$ direction). Based on equation (5.25), the quadratic form of the generalized plastic strain rate is then estimated by

$$\left(\dot{p}^{in,*}_{dislo}\right)^2 = \left(\dot{p}^{in}_{dislo}\right)^2 + \left(\frac{\beta l^*}{l^{in}}\right)^2 (\dot{p}^{out}_{dislo} - \dot{p}^{in}_{dislo})^2 \tag{5.26}$$

where β is a fitting parameter. Hence, there is only one non dimensional parameter affecting the contribution of the gradient which writes

$$\frac{\beta l^*}{l^{in}} = \frac{\beta}{\alpha} \frac{l^*}{h^{in}_0} \frac{f}{F^{in}_{nn}} \tag{5.27}$$

where α is the ratio between the initial length of the neck and the initial thickness. When modelling localized necking, it is common to take $\alpha = 1$. Inside the band, the strain hardening contribution is controlled by the accumulated generalized plastic strain $p^{*,b}_{dislo}$ as given by integrating the generalized plastic strain rate (5.26).

5.4 Model assessment

5.4.1 Assessment of the band orientation

The present model has been validated first based on the results obtained by Hutchinson and Neale (1978a) for a rate-independent rigid plastic material following an Hollomon type hardening law:

$$\sigma_f = k_H p^{n_H} \tag{5.28}$$

In their model as well as for Marciniak and Kuczyński (1967), an infinite metallic sheet is considered and the velocity gradient outside the band reduces to

$$\mathbf{L}^{out} = \mathbf{L}^{macro}. \tag{5.29}$$

The velocity gradient inside the band when f_b tends to zero, reduces to:

$$\mathbf{L}^{in} = \mathbf{L}^{out} + \Big(\dot{\gamma}_{nn} \left(\mathbf{n} \otimes \mathbf{n} \right) + \dot{\gamma}_{tn} \left(\mathbf{t} \otimes \mathbf{n} \right) + \dot{\gamma}_{33} \left(\mathbf{e}_3 \otimes \mathbf{e}_3 \right) \Big). \tag{5.30}$$

Figure 5.3 shows the strains outside the band at instability for a material behaving following equation (5.28) with $n_H = 0.22$ as a function of the initial band orientation, and compares the results obtained by Hutchinson and Neale (1978a) and by the present model. There is a good match between the two models. Furthermore, the minimal strain at necking corresponds to a current band orientation of $\sim 34°$ for the two models. Note that the criterion used by Hutchinson and Neale (1978a) for the occurrence of plastic localization differs from the one assumed in the present model and this can explain the slight differences:

$$\frac{dp^{out}}{dp^{in}} = 0. \tag{5.31}$$

5.4.2 Assessment towards SGP finite element simulations

The SGP model is identified and validated based on the FE simulations of Niordson and Tvergaard (2005). The latter simulations consist of a 2D plane strain model of a tensile test on a rectangular specimen with a material described by a finite version of the Fleck and Hutchinson (2001) SGP theory (details of the constitutive model can be found in Niordson and Tvergaard (2005)). The hardening is described by a rate dependent Swift law:

$$\sigma_f = \sigma_0 \left(1 + k_{S_1} p^*_{dislo}\right)^{n_S} \left(1 + k_{S_2} \dot{p}_{dislo}\right)^{m_S} \tag{5.32}$$

with, for the calculations of interest here, $E/\sigma_0 = 250$, $k_{S_1} = k_{S_2} = 250$, and n_S equal to 0.05, 0.1 or 0.2. A small strain rate sensitivity $m_S = 0.005$ is imposed.

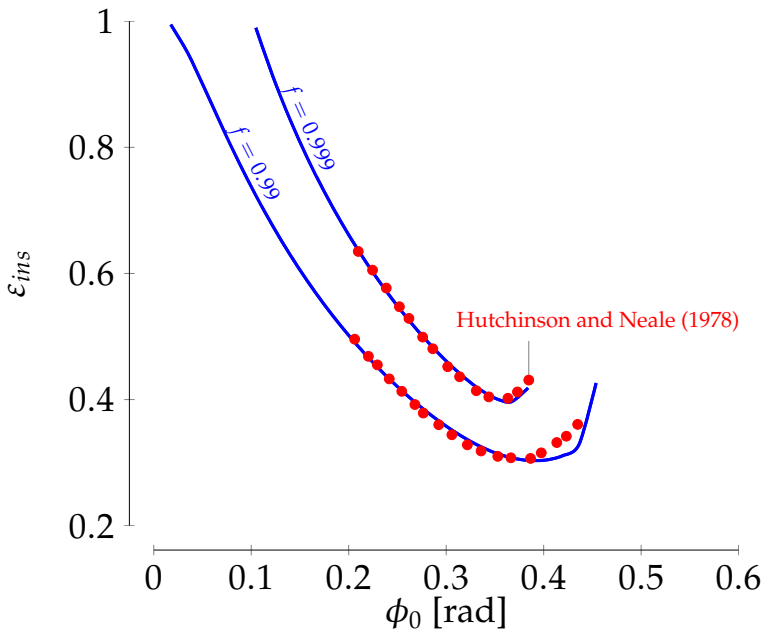

Fig. 5.2: Strains at instability ε_{ins} as a function of the initial band orientation ϕ_0 for the present model and the work of Hutchinson and Neale (1978a).

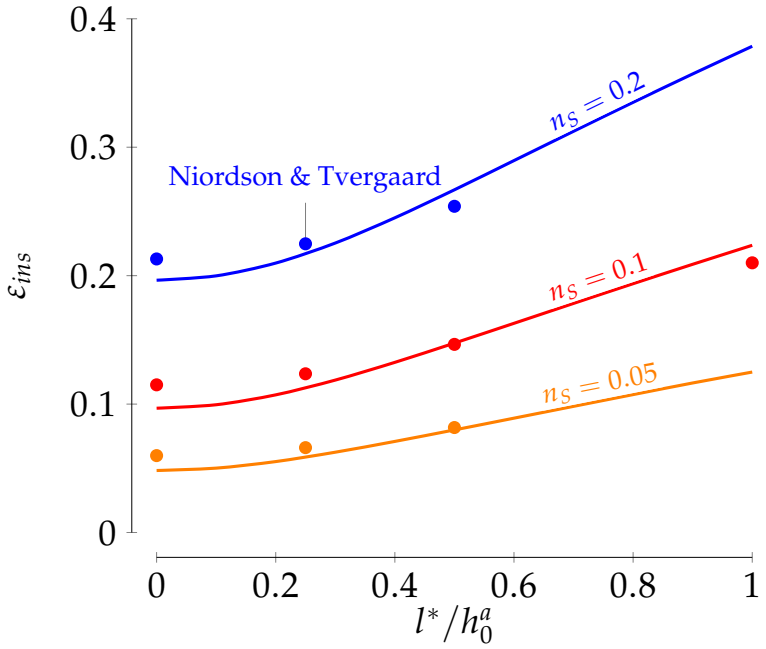

Fig. 5.3: Comparison between the strain at instability for n_S =0.05, 0.1 and 0.2 and various l^* normalized by the initial thickness h_0^{out}. $f = 0.995$, $E/\sigma_0 = 250$, $\beta = 6$. The discrete points are the results of Niordson and Tvergaard (2005).

Figure 5.3 compares the sample averaged necking strains versus l^* (normalized by h_0^{out}) of Niordson and Tvergaard (2005) and the results obtained with the present model in plane strain tension for different values of n_S, with the same imperfection, i.e. $f = 0.995$. In plane strain tension, the minimum value of the localized necking strain is obtained for an initial angle $\phi_0 = 0$ corresponding to the imperfection orientation used by Niordson and Tvergaard (2005). The only adjustment parameter β was set equal to 6. The present model captures the same tendency as the SGP FE simulations. The difference in necking strain can be attributed to the difference of geometry. In the modelling approach of Niordson and Tvergaard (2005), the width over length is imposed to 1/3 while here the thickness over length $\eta = 0.01$ is imposed. The present model captures quite well the stabilizing effect caused by SGP.

5.4.3 Comparison to experimental results on Au thin films

Jonnalagadda et al. (2010) have reported the stabilization of the necking process in 0.85 μm and 1.76 μm thick nanograined freestanding Au films at low strain rates. The strain at necking was small, below 2 % except for the lowest strain rates equal to 6×10^{-5} s^{-1} and 9×10^{-6} s^{-1}, reaching up to 6 % elongation. The strain rate sensitivity was found to increase for strain rates below 10^{-4} s^{-1} from 0.01 and 0.05, highlighting a transition in the dominant deformation mechanism. Low strain rate allowed indeed the activation of a primary creep type deformation mechanism which progressively dominates the mechanical response. These tensile tests have been simulated with the MK model, assuming a rate dependent Swift hardening law

$$\sigma_f = \sigma_0 \left(1 + k_{S_1} p_{dislo}\right)^{n_S} \left(1 + k_{S_2} \dot{p}_{dislo}\right)^{m_S} \tag{5.33}$$

and the contribution of one creep mechanism. The selected creep law is given by:

$$\dot{p}_{other} = K \sigma_{eq}^N \tag{5.34}$$

where N and K are the creep exponent and the creep parameter. The following parameters have been selected to quantitatively fit the experimental data: $E = 60$ GPa (a reasonable value for NC Au films (Sim and Vlassak, 2014; Hosseinian et al., 2016)), $\sigma_0 = 850$ MPa, $k_{S_1} = 250$, $k_{S_2} = 200$, $n_S = 0.01$, $m_S = 0.01$ as measured by the authors. The rate sensitivity of the creep law is taken according to the experiment $N = 20$, and a value for $K = (1/1300\text{MPa})^N$ is used. The specimen has a thickness over length ratio $\eta = 0.00085$ as in the experiments. No strain gradient plasticity effect is taken into account, and an imperfection equal to f =0.98 is imposed. The predicted strain at necking are shown in Fig 5.4 as a function of strain rate.

The transition in resistance to instability at strain rates below 10^{-4} s^{-1} is well captured. The fact that the predicted necking strain at low strain rates

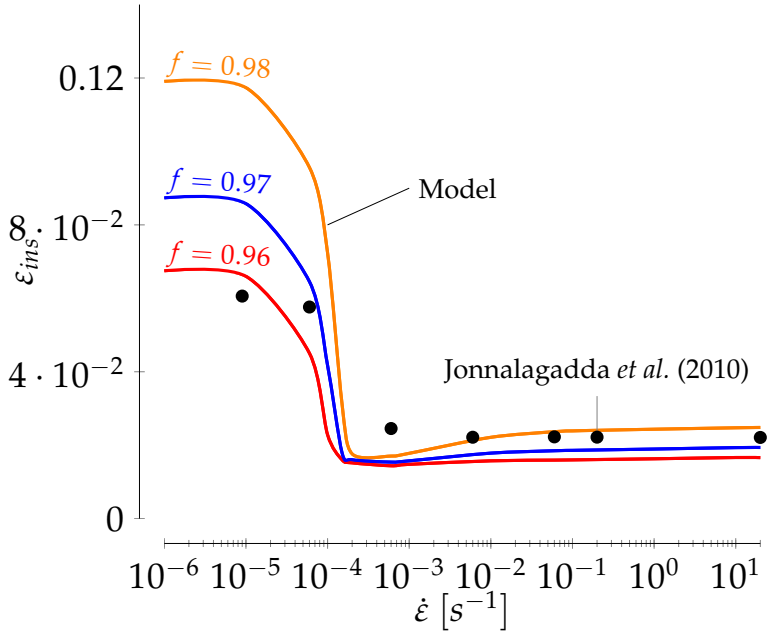

Fig. 5.4: Prediction of the effect of strain rate on the ductility of Au thin films based on experimental data by Jonnalagadda et al. (2010). The material is described by a rate dependent rate Swift hardening law and a creep relaxation law with the following parameters: $E = 60$ GPa, $\sigma_0 = 850$ MPa, $k_{S_1} = 250$, $k_{S_2} = 200$, $n_S = 0.01$, $m_S = 0.01$, $N = 20$ and $K = (1/1300\text{MPa})^N$. $f = 0.98$, 0.97 or 0.96 is imposed

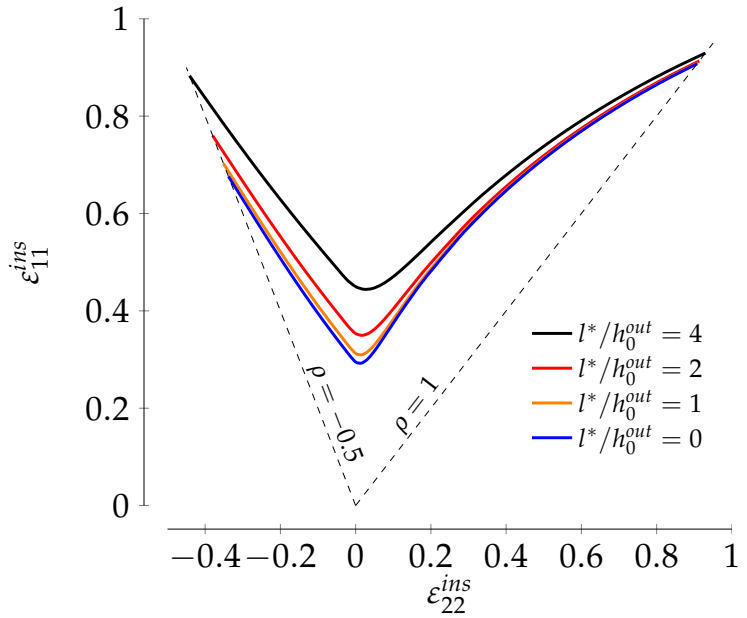

Fig. 5.5: Prediction of the forming limit diagram for a Swift-rate dependent material with $E/\sigma_0 = 125$, $n_S = 0.05$, $m_S = 0.05$ and $k_{S_1} = k_{S_2} = 250$ for different characteristic length l^*. $f = 0.999$.

is larger than the experimental values could be corrected by setting a slightly larger imperfection ($f \sim 0.96-0.97$). The influence of strain rate sensitivity on ductility of material deforming solely by one specific deformation mechanism will be studied in section 5.5.1.

5.4.4 Biaxial loading and forming limit diagram

In various technologies from MEMS applications to purification processes, metallic films are used as membranes undergoing biaxial loading conditions. If the film is sufficiently resistant to cracking by damage accumulation, the failure limiting mechanism will often be localized necking as in macroscopic forming operations. In this section, some trends are showed through forming limit diagrams, unveiling the localization instability for any proportional loading conditions. In order to construct the monotonic forming limit curve, the macroscopic strain mode ρ is imposed :

$$\rho = \frac{D_{22}^{macro}}{D_{11}^{macro}} \tag{5.35}$$

ρ is a constant in the range $-0.5 \leq \rho \leq 1$. The predicted FLD of a Al film with $f = 0.999$ is presented in Figure 5.5. The flow properties are described by the rate dependent Swift law (5.32) with $E/\sigma_0 = 125$, $n_S = 0.05$, $m_S = 0.05$ and $k_{S_1} = k_{S_2} = 250$. The influence of SGP on the delay of necking is also addressed for different characteristic lengths l^*. For any proportional loading, the resistance to plastic instability increases with increasing l^*. This effect is more pronounced in the negative ρ domain, see for example the difference between uniaxial tension $\rho = -0.5$ and biaxial stretching $\rho = 1$. Note that the shape of the simulated FLDs is comparable to the results of earlier works relying on a MK approach (Hutchinson and Neale, 1978a; Eyckens et al., 2009).

5.5 Parameter study

5.5.1 Size independent response

The role of the initial imperfection, strain hardening capacity and rate sensitivity on the resistance to plastic localization, without size effects are illustrated in Figure 5.6 for uniaxial tension. These results are essentially similar to the predictions of localized necking presented by Hutchinson and Neale (1978a,b) or Hosford and Caddell (2011) and in line with the predictions of diffuse necking of Pardoen (2014) but with a factor 2. Indeed diffuse necking, if allowed, occurs at strain twice smaller than localized necking. The flow properties are described by the rate independent Swift law with $E/\sigma_0 = 250$ and $k_{S_1} = 250$. The effect of imperfection is analyzed in Figure 5.6(a) for a rate-independent material with different strain hardening exponent n_S and $\eta = 0.0001$. The hardening capacity has a profound impact on the occurrence of flow instabilities. Moreover, localized necking has strong dependence on the magnitude

of the imperfection. This is a critical point regarding the problem of necking in thin films: grain boundary groove, roughness, lateral lithography error or conformal deposition defect is not unusual, resulting in an imperfection on the order of 1–10 nm which is 1% or more of the typical thin films thickness (between 100 and 500 nm). Material inhomogeneities or nano-porosity can also generate local imperfections.

It is evident from Figure 5.6(b) where a small imperfection $f = 0.999$ is imposed, that strain rate sensitivity strongly delays plastic localization. A fundamental difference between rate-dependent and rate-independent materials arises from Figures 5.6(b) and 5.6(a). Whereas the necking strain of a rate-independent material is bounded by the well defined limit for localized necking, $\varepsilon_{ins} = 2n$ when f tends to 1, the ductility is unbounded for rate-sensitive material. Even a moderate strain rate sensitivity of 0.01 induces an increase of the ductility by a factor 2 or more. These effects are well documented in the literature, see for example, the wide selection of ductile alloys compiled by Woodford (1969).

In section 5.4.3, the competition between two rate dependent mechanisms leads to a variation of m with strain rate, which in turn improves the ductility at slow strain rates. In this specific case, the interesting point is that the rate sensitivity can significantly vary with strain rate. If the strain rate is slow enough, thin films can be prone to diffusional creep due to the small grain size and large surface area (see e.g. Coulombier (2012)) even at room temperature. Specific attention must be paid to this marked transition in ductility between slow and large strain rates when designing thin film based systems. These competitions between different relaxation mechanisms must be taken into account as a function of the type and rate of loading experienced under operation in order to ensure reliability and avoid detrimental creep.

5.5.2 Generic strain gradient plasticity effect

Strain gradients act as an additional source of strain hardening that delocalizes the incipient necking region and postpones unstable flow. The effect of SGP on necking retardation is addressed in Figure 5.7 for a rate-independent material loaded in pure uniaxial tension with a Swift type hardening law (5.33) ($E/\sigma_0 = 250$, $k_{S_1} = 250$ and $n_S = 0.1$). The value of strain corresponding to instability is given as a function of the imperfection f for l^*/h_0^{out} =0, 0.5, or 1. The parallelism between these results and the results of Figure 5.6 is marked. SGP is equivalent to an extra source of strain hardening. Physically, the strain gradients come from the accumulation of GNDs inside the band which accommodate the deformation. SGP effects can thus improve the ductility of a film if the structural length scale of interest is on the order of the characteristic length l^*. The results obtained by Pardoen (2014) are very similar but with a factor 2 (see section 5.5.1).

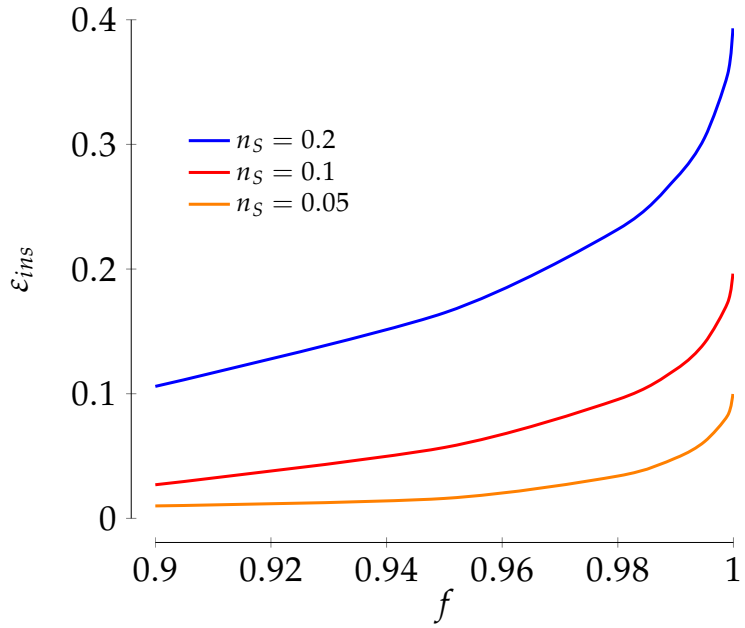

(a) Influence of the strain hardening capacity

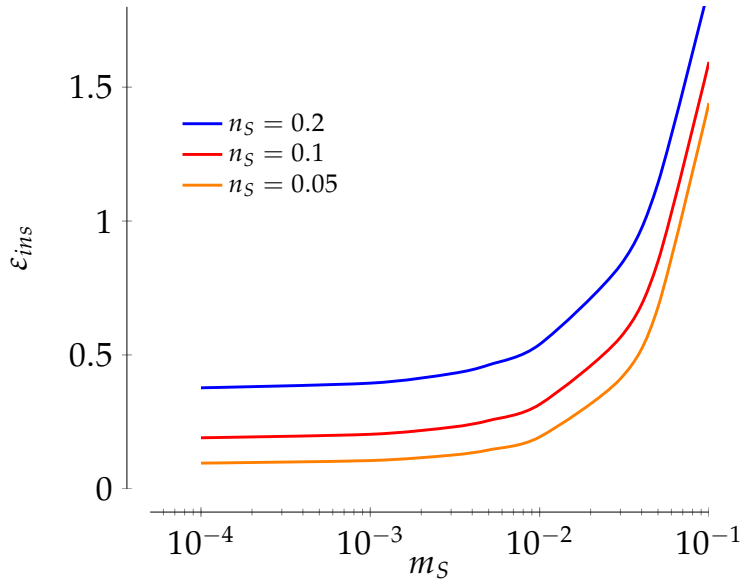

(b) Influence of the strain rate sensitivity

Fig. 5.6: Variation of the strain at necking as a function of the flow properties and imperfection for a Swift hardening law ($E/\sigma_0 = 250, k_{S_1} = 250$). (a) effect of imperfection f on necking strain for various n_S ($m_S = 0.0001$), (b) effect of rate sensitivity m_S on strain at necking for $f = 0.999$ ($k_{S_2} = 250$)

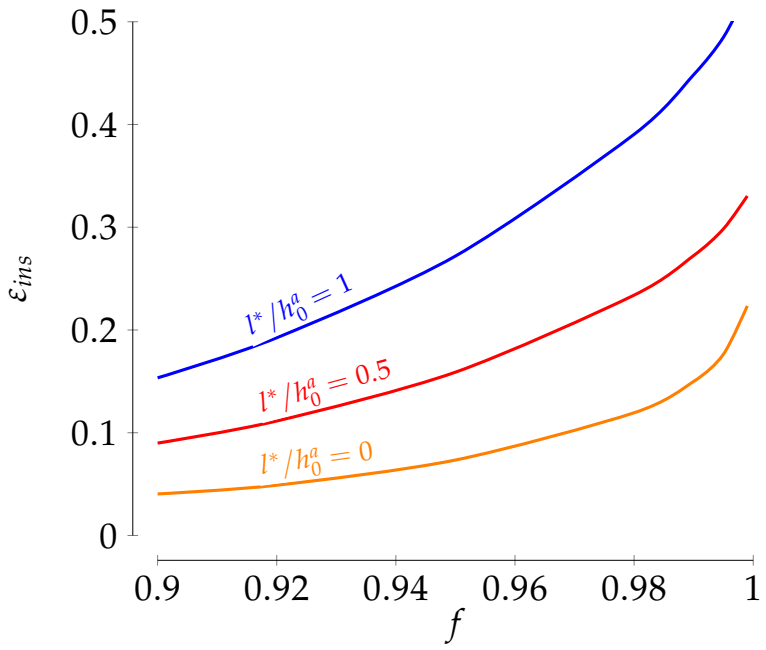

Fig. 5.7: Comparison between the strain at instability for l^*/h_0^{in} =0, 0.5, or 1 in pure uniaxial tension. $E/\sigma_0 = 250$, $\beta = 6$ and $n_S = 0.1$.

5.5.3 Effect of the film thickness on the ductility

In this section, the phenomenological flow parameters are connected to the microstructure of metallic films in which film thickness mostly scales with the grain size. Several parameters of the model vary with the microstructure. The effect of grain size on the strain rate sensitivity, the hardening capacity and the yield strength is depicted in Figure 5.8 for aluminium. In order to study the interplay between increasing yield strength, enhanced strain rate sensitivity and decreasing strain hardening with decreasing grain size, a three step analysis is performed without SGP effects. Firstly, the influence of the grain size on the yield strength is investigated at constant n and m. Then, the effect of grain size on the strain rate sensitivity is introduced while n remains constant. Finally, the grain size dependence of n is included. A Ludwig hardening law is used here in order to differentiate the effect of the grain size on the yield stress and on strain hardening:

$$\sigma_f = \sigma_0 + k_{L_1} \left(p_{dislo}\right)^{n_L} \left(1 + k_{L_2} \dot{p}_{dislo}\right)^{m_L} . \tag{5.36}$$

When SGP effects are considered, it is assumed that the strain hardening part of the Ludwig law is determined using the generalized accumulated plastic strain p^*_{dislo} while the viscous part is influenced by the conventional accumulated plastic strain rate $\dot{p}_{dislo}$. Other formulations can be found in the literature, see e.g (Borg et al., 2006).

The mean grain size as well as the film thickness have an influence on the yield strength σ_0, especially when the film contains only one grain over the

thickness. In thin films technologies, the deposited nanograined microstructures frequently involve one or a few grains along the growth direction. The motion of gliding dislocations is hindered in metallic films by the high density of interfaces and by the large surface to volume ratio. In many small scale systems, passivation or oxyde layers can also act as a barrier to dislocation motion, see e.g. Xiang and Vlassak (2006) and Brugger et al. (2010). The strength may also vary with local porosities resulting from deposition. Following Venkatraman and Bravman (1992) and de Boer et al. (2008b), the yield strength can be related to the grain size d and the film thickness h_0^{out} by the following expression:

$$\sigma_0 = \sigma_{00} + k_{HP1}/\sqrt{d} + k_{HP2}/h_0^{out} \tag{5.37}$$

where σ_{00} is the Peierls stress, and k_{HP1} and k_{HP2} are two empirical parameters. As a first approximation, the film thickness h_0^{out} is assumed here to be equal to the grain size d. The analysis relies on the empirical relation (5.37) and the following parameters are used $\sigma_{00} = 10\ MPa$, $k_{HP1} = 100\ MPa\sqrt{\mu m}$ and $k_{HP2} = 83\ MPa\mu m$ as proposed by de Boer et al. (2008b), based on the experimental data of Venkatraman and Bravman (1992) for Al-0.5% Cu thin films laying between an SiO_2 layer on the substrate and a anodic oxide film grown on the surface. Note that the increase of the yield strength with decreasing grain size is known to reach an upper limit at a grain size in the range of ∼10-30 nm (Meyers et al., 2006).

For the first analysis, the strain hardening capacity is fixed to typical value for pure Al, $n = 0.1$. Figure 5.9 depicts the variation of strain at instability as a function of the film thickness equal to the grain size, with $m_L = 0.003$. At constant strain hardening capacity and strain rate sensitivity, the decrease of ductility when decreasing grain size is significant. The decrease is even more pronounced if we assume that the imperfection consists of a local dimension reduction of 5 nm instead of taking an imperfection $f = 0.999$ while keeping $f = 0.999$ for large grain sizes. As explained in the introduction, such imperfection can easily appear in sub-micron thin films, resulting from GB grooving, from lithography defects or from roughness.

As the grain size decreases, classical forest hardening mechanism is progressively replaced by diffusion and GB meditated mechanisms. These thermally activated mechanisms magnify the strain rate sensitivity. During the last decade, the strain rate sensitivity of nanocrystalline and ultrafine grained metals has been extensively studied using strain rate jumps, nanoindentation or on-chip technique. As listed in section 4.4.2, these studies reported a variety of rate sensitivity exponents, m, for nanocrystalline and ultrafine grained fcc metals, most of which are of the order of 0.015-0.15. Data on thin metallic films is still relatively scarce. The data compiled by Wei (2007) clearly shows a monotonic increase of m with decreasing grain size, even though the underlying rate dependent deformation mechanisms are probably different from

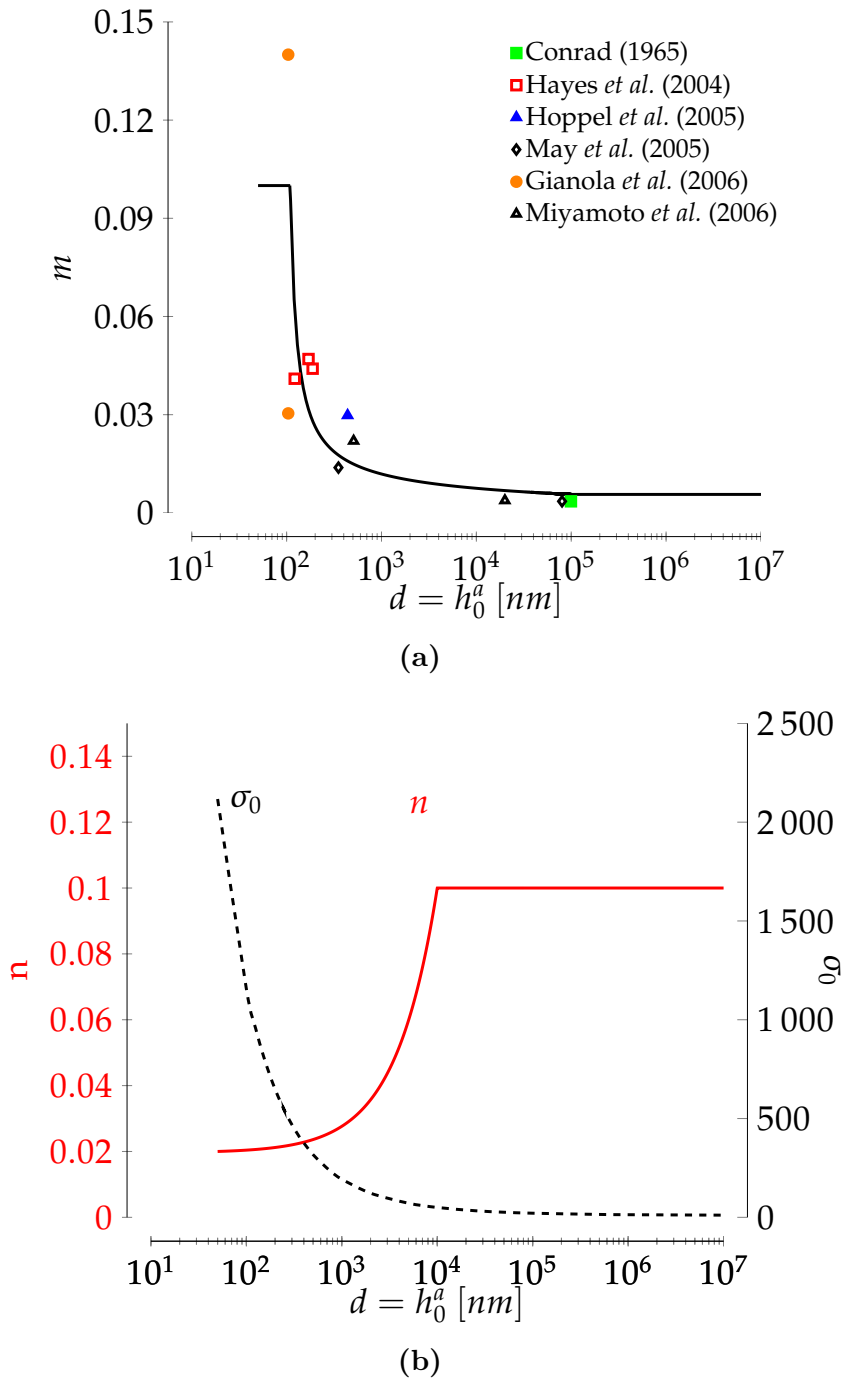

Fig. 5.8: (a) Variation of the strain rate sensitivity as a function of grain size for Al. Marks represent experimental data obtained by Conrad (1965); Hayes et al. (2004); Höppel et al. (2005); May et al. (2005); Gianola et al. (2006); Miyamoto et al. (2006) (b) Evolution of the yield strength and the strain hardening exponent as a function of grain size for Al.

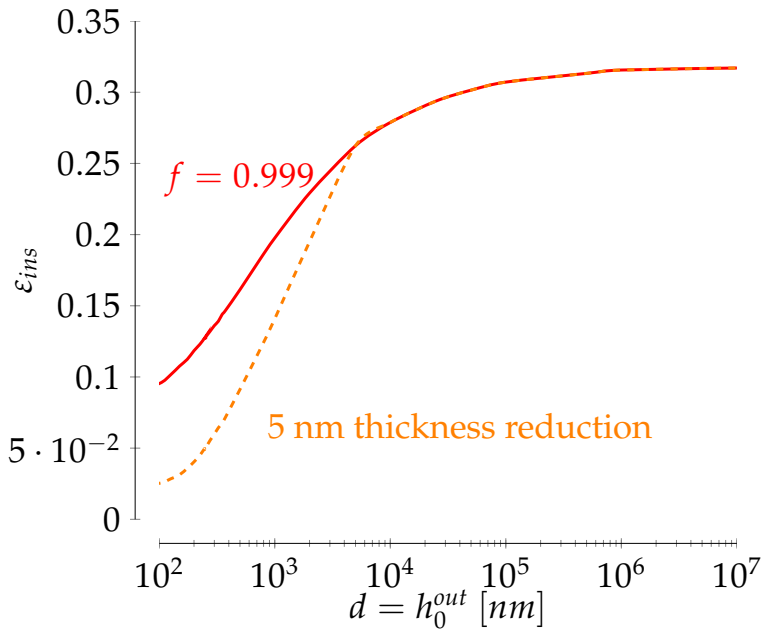

Fig. 5.9: Variation of the strain at necking as a function of the film thickness h_0^{out} taken equal to the grain size d; $n = 0.1$ and yield strength varies with d following equation (5.37): comparison between a constant relative imperfection $f = 0.999$ and a variable imperfection resulting from a constant reduction of 5 nm ($m = 0.003$).

one material to another. Details of the microstructure (purity of the alloys, stacking fault energy of the alloys, presence of solute atoms at GB, etc.) can significantly affect the selection of the dominant deformation mechanism and change the value of m, see for example Tang et al. (2012) and Tian et al. (2016). In order to account for the enhanced rate sensitivity at submicron scale, the following phenomenological expression is chosen following Gu et al. (2007b). Based on the critical stress for the bow-out of an edge dislocation source, Gu et al. (2007b) derived the following expression for the strain rate sensitivity m as a function of the grain size d

$$m = \frac{\sqrt{3} k_B T}{0.36 \mu b^3} \left[\log \left(\frac{c_1 \sqrt{d}}{b} \right) - 1.65\ c_2 \right]^{-1} \tag{5.38}$$

where k_B is the Boltzmann constant, T, the temperature, μ the shear modulus, b the Burger vector and c_1 and c_2 are fitting parameters. $c_1 = 0.118\ \sqrt{nm}$, $c_2 = 1.78$, $\mu = 24$ GPa and $b = 0.286$ nm. m is assumed to saturate at 0.1.

The effective strain hardening capacity varies with grain size too due to complex dislocation/GB interactions, associated with local recovery, dislocation transmission and significant back stress development, see e.g. Sinclair et al. (2006); Duhamel et al. (2010); Massart and Pardoen (2010); Sun et al. (2015); Lemoine et al. (2016). As grain size decreases, the strain hardening capacity is profoundly modified and dictated by dislocation nucleation mechanisms at GBs, replacing the classical forest hardening. These effects are still

not fully understood and not captured by quantitative models. The strain hardening capacity is here decomposed into two contributions: a "forest hardening" capacity and a kinematic hardening contribution due for instance to the storage of dislocation at grain boundaries. When the grain size is larger than 10μm, the effect of back stress vanishes and the "forest hardening" capacity dominates the hardening capacity, $n = n_{forest}$. At grain size lower than 50 nm, back stress becomes dominant and the strain hardening capacity is only dictated by the kinematic hardening, $n = n_{GB}$. Between these two regimes, n is assumed to vary linearly with grain size. In order to make the analysis as realistic as possible, the strain hardening capacity is assumed to be bounded by the two extrema: $n_{GB} = 0.02$ and $n_{forest} = 0.1$.

Figure 5.10 illustrates the variation of the necking strain associated with the increase of rate sensitivity with decreasing grain size, compared to to no change in rate sensitivity for constant or varying strain hardening capacity. The imperfection is taken small $f = 0.999$ and no SGP effects are taken into account. For constant strain hardening capacity, the increased strain rate sensitivity with smaller grain size delays necking formation for any grain size. As the grain size decreases below 10 μm, the yield strength increase is still too pronounced and do not allow to compensate the loss of ductility with a higher rate sensitivity. Below 200 nm, this trend in the evolution of the ductility can be reversed at least in a limited range of grain sizes. The impact of a decrease of strain hardening capacity with grain size accentuates even more the decrease in ductility. Coulombier et al. (2010) found values of strain at instability up to 0.3 for 370 nm thick films for specimens involving the smallest imperfections, which is in the same range as predicted here.

In real thin films, all these effects of imperfection, of increasing strength and rate sensitivity, of decreasing strain hardening capacity with decreasing grain size, and of SGP compete or cooperate all together with relative magnitudes. The question of the limit of validity of SGP theories at low grain sizes has not been much discussed in the literature. Nevertheless, if the deformation mechanism becomes dominated by diffusion, grain growth or grain rotation, GNDs will no longer dictate the deformation process. SGP effects could then be excluded. The following scenario emerges from these considerations and raises two transition lengths l^* and d_c:

- when $h_0^{out} = d < d_c$, strain rate sensitivity increases but SGP are excluded as GB-mediated mechanisms dictate the mechanical response;
- when $h_0^{out} = d > l^*$, the only size effect arises from the Hall-Petch effect;
- when $d_c < h_0^{out} = d < l^*$, SGP effects can ductilize the material.

These transitions are addressed in Figure 5.11 for a material involving a grain size dependent strength, strain hardening capacity and strain rate sensitivity.

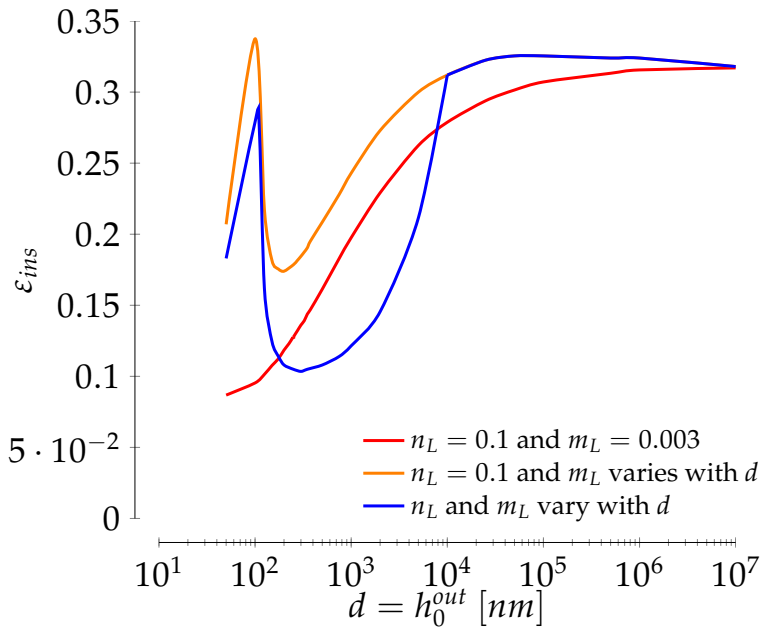

Fig. 5.10: Variation of the strain at localized necking as a function of the film thickness h_0^{out} taken equal to the grain size d; yield strength varies with d following equation (5.37); strain rate sensitivity varies with d following equation (5.38) and n_L varies linearly with d.

Five characteristic lengths are considered: $l^* = 0$, 0.125, 0.25, 0.5 and 1 μm. The SGP effects are turned off below a grain size equal to $d_c = 250$ nm at which the rate dependent thermally activated mechanisms start dominating the deformation process.

The relevance of imposing $h_0^{out} = d$ can be questioned. Depending on the deposition techniques, deposition conditions and the melting temperature of the material, the morphology of the grain can vary between pancaked, equiaxed to moderately elongated in the thickness direction. By depositing a film step by step, with interruptions during the process, it is possible to avoid the propensity to create columnar grain and to produce a thin layer with several grains over the thickness. It is also possible to deposit a thin film with small grain sizes and then perform an annealing in order to increase the grain size. In these cases, the film thickness might significantly differ from the grain size. The trends observed above would remain valid, but the dominant mechanism of deformation would need to be carefully identified. If the grain size becomes too small, SGP might indeed not play a role even if the thickness is in the range of the characteristic length l^*.

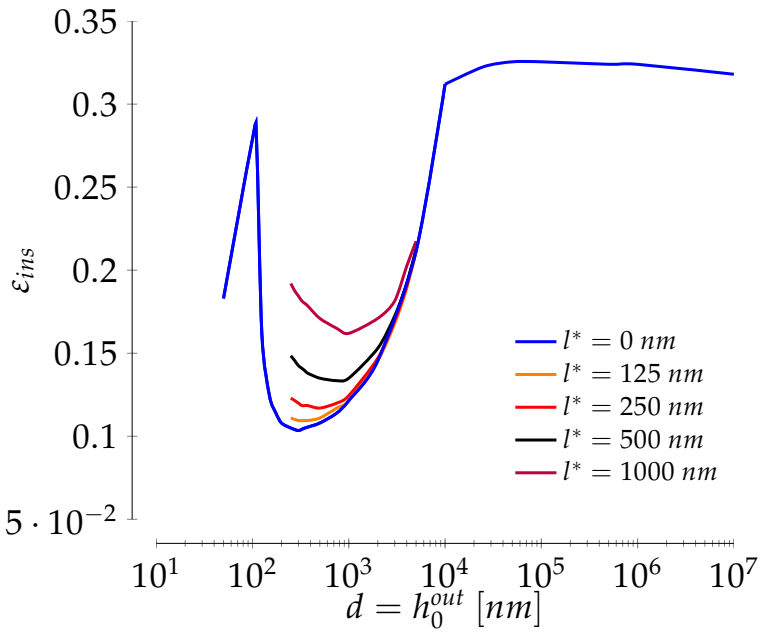

Fig. 5.11: Variation of the strain at localized necking as a function of the film thickness h_0^{out} taken equal to the grain size d in microns for different characteristic length l^*; yield strength varies with d following equation (5.37); strain rate sensitivity varies with d following equation (5.38) and n_L varies linearly with d. The imperfection is taken small $f = 0.999$. The SGP effects are turned off below a grain size equal to $d_c = 250$ nm at which the rate dependent thermally activated mechanisms start dominating the deformation process.

5.5.4 Impact of internal stress on ductility

Most thin films and coatings involve internal stresses which have various origins. Thermal stresses develop due to a thermal mismatch between the film and the substrate as a result of a difference in thermal expansion coefficient during the cooling phase after film deposition on a substrate for instance (Nix, 1989). Other stresses, such as epitaxial stresses, arise during the growth process of the film on the substrate.

Simulations have been designed to check whether or not internal stresses could internal stresses influence the plastic localization process in thin free-standing membranes and affect the measured ductility in tension. The stress state experienced by a thin film during a typical deposition and release process followed by an uniaxial tension test is applied to an Al films. The flow properties are described by the Swift law (5.33) with $E/\sigma_0 = 125$, $n_S = 0.05$ and $k_{S_1} = k_{S_2} = 250$. First, biaxial stretching is applied up to a small strain $\varepsilon_{11} = \varepsilon_{22} = \varepsilon_0$. Negative or positive prestrains ε_0 are generated respectively by tensile and compressive internal stress. Then, uniaxial tension is performed either by imposing $\sigma_{11}^{macro} = 0$, or by imposing the conventional strain mode $\rho = -0.5$ used to characterize uniaxial tension in FLD. The influence of the

prestrain ε_0 on the occurrence of localized necking is depicted in Figure 5.12 for three different strain rate sensitivity $m_S = 0.01$, 0.005 and 0.001. When $\sigma_{11}^{macro} = 0$ is applied, elastic ε_0 has no influence on the necking behaviour but as plasticity is generated by the internal stress, plastic instability occurs earlier during the deformation process. The necking strain decreases with increasing ε_0 for any strain rate sensitivity. When $\rho = -0.5$, the same trend is observed while an elastic ε_0 already induces a lower resistance to plastic localization. In the presence of elasticity, $\rho = -0.5$ does not correspond to a pure uniaxial tension as tensile stress develops in the transverse direction to compensate the constant volume assumption associated to $\rho = -0.5$. The decay of the necking strain with increasing magnitude of ε_0 is more pronounced for positive internal stress. At similar magnitude of prestrains, flow becomes unstable at a same accumulated plastic strain for both tensile or compressive internal stress and the observed variation of ductility can be attributed to the choice of the characteristic strain at necking: $\varepsilon_{ins} = \min_{\phi_0} F_{11}^{ins}$.

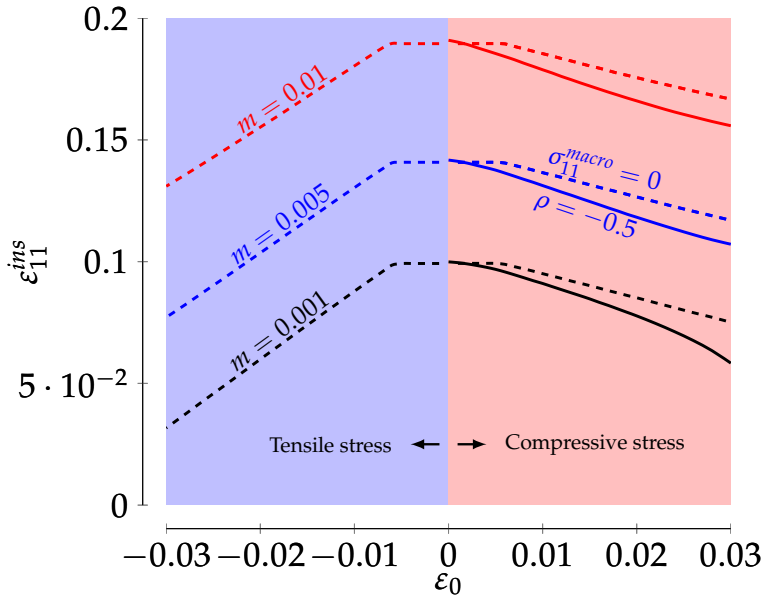

Fig. 5.12: Influence of the biaxial stretching ε_0 on the subsequent uniaxial tensile strain at necking for different m and two tensile loading conditions. The flow properties are described by the Swift law with $E/\sigma_0 = 125$, $n_S = 0.05$ and $k_{S_1} = k_{S_2} = 250$. $f = 0.999$ is imposed.

Internal stresses can induce different well-known undesirable effects in the film/substrate system including film delamination, fracture, buckling and cracks in the film. The present findings add lower necking resistance to this list. The control of internal stress is thus of primary importance for the production of reliable industrial devices based on freestanding thin films.

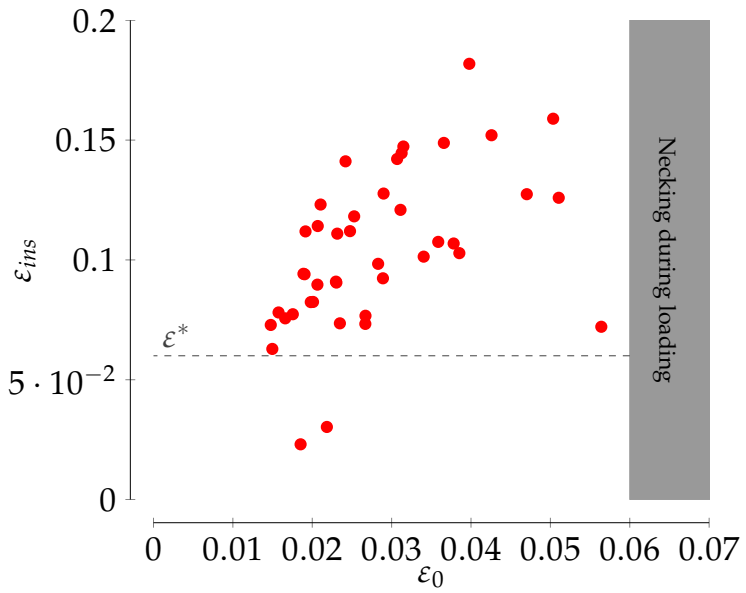

Fig. 5.13: Variation of the strain at instability ε_{ins} during creep/relaxation experiment as a function of the prestrain ε_0 reached during the loading of 170 nm thick freestanding Cu films. ε^* is the necking strain in loading at moderate strain rate.

5.5.5 Lab-on-chip relaxation

The ductility of different thin metallic films in tensile loading and relaxation has been determined by Coulombier et al. (2010) for Al, by Colla (2014) for Pd and by Vayrette et al. (2015) for Cu, using the on-chip uniaxial tension technique. Pd thin films with a thickness between 90 and 480 nm generally show a resistance to plastic localisation up to 5-6% during tensile loading and exhibit for the best cases, high ductility up to 12%. The specimen are then stored for months or even years in clean environment and keep deforming by slow creep. Necking or failure never appeared during this relaxation stage in the unbroken samples and this even though some specimen underwent additional deformation of several percent bringing them to strains larger than 5-6%. 170 nm thick Cu specimens reached more than 5% deformation during the release of the actuator while large ductility up to 20 % was observed during relaxation, indicating that localized necking in Cu thin films is significantly affected by the strain rate. The experimental results of Vayrette et al. (2015) are reproduced in Figure 5.13. Such behaviour has also been reported by Hosseinian et al. (2016) in Au thin films during relaxation experiments. After experiencing successive stress relaxations, these Au films withstand an elongation about ten times larger than the fracture plastic strain under monotonic loading, without failure.

The present section is devoted to the modelling of localized necking under creep/relaxation conditions and aims to provide a better understanding of the experimental results of Vayrette et al. (2015) gathered using the on-chip tech-

nique. The modelling of such on-chip relaxation gives rise to some questions: what is the influence of the actuator spring? How do we select the proper viscoplastic law? based on one or two deformation mechanisms? with a threshold or not?

The principle of the on-chip technique has been presented in chapter 3 so only some specificities of the Cu thin films are outlined here. The copper films of Vayrette et al. (2015) are deposited by e-beam evaporation at room temperature and with a deposition rate of 0.1 nm/s on top of a PECVD SiO_2 sacrificial layer. Etching of the sacrificial layer is fast (etch rate is equal to 0.181 $\mu m.s^{-1}$) and the initial tensile loading rate is around $5\times\ 10^{-3}\ s^{-1}$ for 10 s, with a dependence on sample length. Then, the actuator behaves as a linear spring which slowly contracts while the sample (still loaded in tension) undergoes additional viscoplastic deformation. Due to the critical point dryer step, the first samples are measured three hours after the release. Measurements are then repeated after relaxation times varying from a few hours to several days. At all times, the actuator follows a linear force-displacement relationship and equation (4.1) remains valid. These conditions thus correspond to a creep test performed on a sample attached to a linear spring: stress decreases while strain increases. The relaxation/creep behaviour is dictated by l^a_{nom}/l^s_{nom} ratios which influence the magnitude of the creep strain rates.

The loading path undergone during an on-chip tensile test (moderately fast loading and subsequent relaxation) is modelled using material parameters corresponding to Cu thin films. In order to study the influence of the prestrain ε_0 and of stress relaxation on the ductility of thin films, different constitutive laws are envisaged. First, a purely viscoplastic law corresponding to equation (5.34) is selected. Necking analysis for such constitutive law reveals a stress and rate independent resistance to plastic localization. For any prestrain and thus any stress level reached during the release of the film, the necking strain after relaxation is always the same and equal to the strain at instability reached in loading, denoted ε^*. For a single rate dependent mechanism (and thus a single m value independent of strain rate), there is no change of strain at instability with strain rate in monotonic tensile loading or during the spring-like relaxation where the strain rate evolution with time is dictated by the l^a_{nom}/l^s_{nom} ratio and the subsequent decrease of stress. Some combinations of prestrain and l^a_{nom}/l^s_{nom} ratios do not allow to reach the monotonic necking strain due to the associated very long relaxation time or because the actuator is too short to carry the same level of deformation. This last observation fully agrees with the experiment showing no failure during relaxation. In order to validate the quite surprising stress and rate independence of the ductility obtained within the MK framework, a simple force equilibrium approach is used: a sample with inhomogeneous cross section linked to a purely elastic Si_3N_4 actuator with constant cross section A^a and $E^a = 250$ GPa, is considered. Strain hardening and

elasticity are neglected and the equation (5.34) is rewritten

$$\dot{\varepsilon} = \dot{\varepsilon}_0 \left(\frac{\sigma}{\sigma_0} \right)^{1/m}. \tag{5.39}$$

The sample is divided in two zones, one with an initial cross section A_0^{out} and the other $A_0^{in} = f A_0^{out}$ as for the MK approach. The forces must balance so

$$\sigma^{out} A^{out} = \sigma^{in} A^{in} = F \tag{5.40}$$

where the force F is dictated by the actuator and given by:

$$F = E^a A^a / l^a_{nom} (u^{free} + u). \tag{5.41}$$

The displacement u of the actuator is computed based on the strains of zones *in* and *out*:

$$u = (l_{tot} - (l_0^{out} \exp(\varepsilon^{out}) + l_0^{in} \exp(\varepsilon^{in})) - l_0^a) < 0$$

and

$$u^{free} = l_0^a (\exp(\varepsilon^a_{mis}) - 1). \tag{5.42}$$

Finally, the two differential equations to solve are

$$\dot{\varepsilon^{out}} = (F/\sigma_0/A_0^{out})^{1/m} \exp(\varepsilon^{out}/m), \tag{5.43}$$

$$\dot{\varepsilon^{in}} = (F/\sigma_0/A_0^{in})^{1/m} \exp(\varepsilon^{in}/m). \tag{5.44}$$

These ordinary differential equations are solved using an Adams type algorithm for $\varepsilon^a_{mis} = -0.00315$, $m = 0.05$, $\sigma_0 = 1050$ MPa, $\dot{\varepsilon}_0 = 1s^{-1}$, $l_0^{in} = h_0^{out} = 200$ nm and $l_0^{out} = 25$ μm. Similar tendencies are predicted and the same conclusions can be drawn, validating the extended MK approach. The same applies for $\sigma_f = K p^n \dot{p}^m$. In a second time, a rate dependent Swift law (5.33) is adopted and the same analysis is performed. At constant force, ε^* is recovered for any plastic prestrains. Generally unstable flow never occurs in relaxation except for prestrains around ε^* which lead to ductility equal to ε^*. As a matter of fact, the combined effect of decreasing applied stress and increasing accumulated plastic strain progressively inhibit deformation upon relaxation. This effect is furthermore reinforced by the decreasing rate-dependent effective strain rate sensitivity m_{eff} associated to Swift-type laws:

$$m_{eff} = \frac{d \ln \sigma_f}{d \ln \dot{p}} = m_S \frac{k_{S_2} \dot{p}}{1 + k_{S_2} \dot{p}}. \tag{5.45}$$

These results have been preliminary validated towards a simpler approach involving a band normal to the loading. Such band configuration associated to a rigid plastic material simplifies the equations of the present model and reduces the number of unknowns to 2. Relying solely on one deformation mechanism will not allow a proper reproduction of the experimental results

of Vayrette et al. (2015). As the necking during relaxation never exceeds ε^*, prestrains and relaxation rates only affect the time at which plasticity localizes or not inside the band.

So, the deformation in Cu thin films is supposed to be driven by two deformation mechanisms: a dislocation based mechanism, dominating the mechanical response at moderate strain rate and a diffusive relaxation mechanism at low strain rate. This latter hypothesis is enforced by the diffusion effects observed by Lapouge et al. (2017) for the same Cu thin films. A creep relaxation law (5.34) with $N = 20$ and $K = (1/1050\text{MPa})^N$ and a rate sensitive Voce law:

$$\sigma_f = \left(\sigma_{sat} - (\sigma_{sat} - \sigma_0)\exp\left(-\frac{p}{p_0}\right)\right)(1 + k_V\dot{p})^{m_V} \tag{5.46}$$

with $E = 90$ GPa, $\sigma_0 = 240$ MPa, $\sigma_{sat} = 675$ MPa, $p_0 = 0.02$, $k_V = 750$ and $m_V = 0.02$ are used. The optimized parameters for Voce strain hardening and creep law were obtained in such a way as to fit at best the experimental stress-strain curve and creep curves depicted in Figure 5.14(a) and Figure 5.14(b). A rate dependent Swift hardening law was first assumed but the high apparent strain hardening led to $n_S = 0.25$, predicting unrealistic necking strains. The strong apparent strain hardening in NC materials is generally attributed to a long elasto-plastic transition. A Voce hardening is then adopted because such law limit the apparent hardening by saturating the hardening after $p \sim p_0$. The present model with 2 competing parameters reproduce the experimental trends with realistic parameters. The fitted value of m_V and N are consistent with the literature. The strain rate sensitivity m of nanocrystalline grained Cu thin films usually varies between 0.05 and 0.1 (Lapouge et al., 2017) under relaxation conditions. Wang and Ma (2003) reported that for the nanostructured Cu ($d \sim 190$ nm), m is 0.01 at moderate strain rate $\dot{\varepsilon} \sim 10^{-4}$ s^{-1}.

The resistance to necking of 25 μm long Cu thin films as a function of the initial prestrain and the length of the actuator is depicted in Figure 5.15. The necking strain reached during monotonic tensile loading ε^* is equal to 0.06 for a imperfection $f = 0.94$, corresponding to the experimental value (Vayrette et al., 2015). Depending on the prestrain and on the l^a_{nom}/l^s_{nom} ratios, either no instabilities after 1 year of relaxation, either a drastically improved ductility were predicted. As explained in section 5.4.3, ductility is rate dependent for a material involving two competing mechanisms. During the monotonic loading at moderate strain rate, the dislocation based mechanism is dominant. As the strain rate decreases, the limitation of ductility associated to this mechanism progressively wipes off and the more viscous mechanism ductilizes the film. The competition between these two mechanisms is influenced by the initial prestrain and the actuator length, dictating the decreasing strain rate (see Figure 5.14(b)) and the associated amount of additional elongation needed to trigger instability. For example, if the prestrain is equal to 5% and the actuator

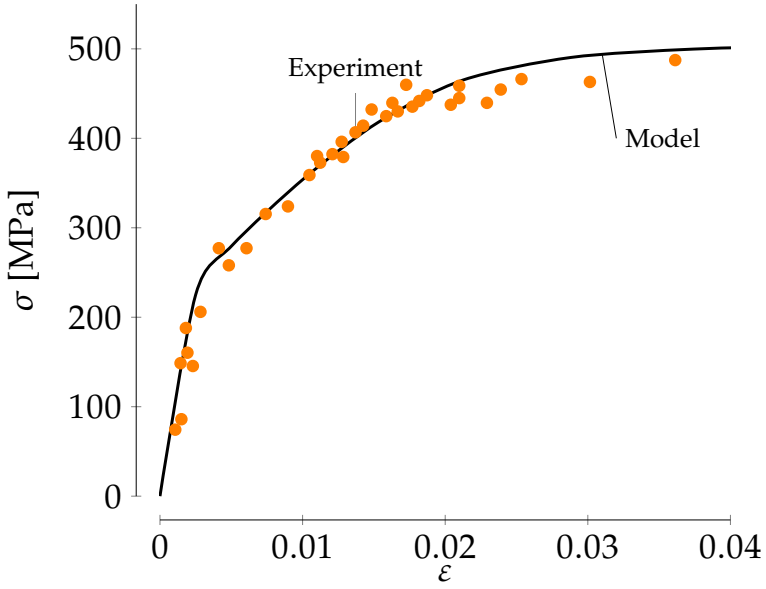

(a) Mechanical response after 3h

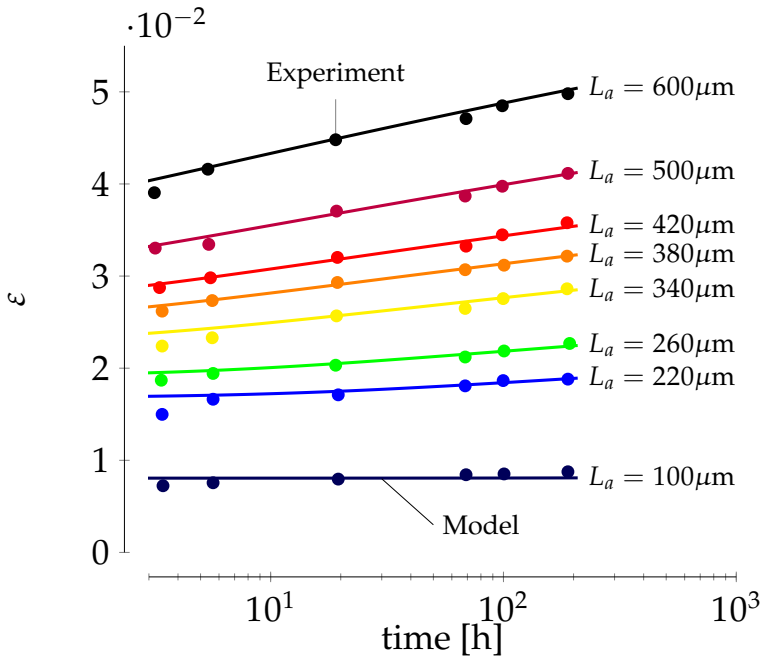

(b) Creep/relaxation behaviour

Fig. 5.14: Comparison between between the experimental and predicted stress strain (a) and the experimental and predicted creep response (b) for Cu thin films with 2 competing mechanisms: a creep relaxation law with $N = 20$ and $K = (1/1050\text{MPa})^N$ and a rate sensitive Voce law with $E = 90$ GPa, $\sigma_0 = 240$ MPa, $\sigma_{sat} = 675$ MPa, $p_0 = 0.02$, $k_V = 750$ and $m_V = 0.02$

is long ($l^a_{nom} = 2500\mu$m), the relaxation strain rate remains nearly equivalent to the loading strain rate during the first hour. The corresponding small activation of the viscous mechanism results in a sightly improved necking strain $\varepsilon_{ins} = 7\%$, which agrees with the singular experimental data point corresponding to $\varepsilon_0 \sim 5\%$ in Figure 5.13. When the prestrain is small compared to ε^*, the relaxed strain needed to reach ε^* is high enough to let sufficient time to activate the viscous mechanism and then improve the ductility by at least a factor 2.5. No necking can even be observed due to low creep rate associated to long relaxation time or low l^a_{nom}/l^s_{nom} ratio, for the sake of simplicity these data have not been reported in Figure 5.13. A small actuator length allows also the activation of the viscous mechanisms by imposing a rapid decrease of the relaxation strain rate. Note that the strain at instability corresponding to the creep mechanism $\varepsilon^{viscous}$ is never reached. As the viscous mechanism is only activated during relaxation, the heterogeneity of deformation generated during the loading remains present during subsequent relaxation and is higher than expected for a material deforming solely by creep mechanism.

Now, the model does not capture the linear relation between prestrain and ductility measured by Vayrette et al. (2015). One may believe that origin of the discrepancy is the following. Assuming that dislocations participate also through recovery and through further nucleation of new dislocations to the relaxation, the activation volume before relaxation should thus be dictated by the dislocation density. Following Cottrell-Stokes law, the activation volume is inversely proportional to the mean spacing between pinning points. Hence, the activation volume decreases with increasing pre-strain, see e.g. chapter 4. Based on the definition of the strain rate sensitivity and the activation volume, a lower activation volume implies a larger m. Here m_V is constant and independent of ε_0. A dislocation based model would intrinsically adapt the strain rate sensitivity m with the initial prestrain and lead to a better resistance to necking, see section 5.5.1. To assess this hypothesis, a J_2 version of the dislocation based model developed in chapter 4 has been implemented and an exploratory work using the same parameters as for Pd has been undertaken. The strain rate writes

$$\dot{p} = \dot{p}_0 \exp\left(-\frac{F_0}{k_B T}\left\{1 - \left(\frac{\sigma_{eq}}{\hat{\sigma}}\right)^{p_i}\right\}^{q_i}\right) \tag{5.47}$$

with $\hat{\sigma} = M\alpha\mu\sqrt{\rho}$ while the evolution of the dislocation density ρ is given by

$$\dot{\rho} = M\left(k_1\sqrt{\rho} - k_2\left\{1 - \left(\frac{k_B T}{F_0}\ln\left(\frac{\dot{p}_0}{\dot{p}}\right)\right)^{1/q_i}\right\}^{-1/p_i}\rho\right)\dot{p}. \tag{5.48}$$

The strains at instability ε_{ins} during creep/relaxation experiment as a function of the initial nominal strain ε_0 of Cu thin films modelled with the dislocation based approach are presented in Figure 5.16. The linear relation between ε_0

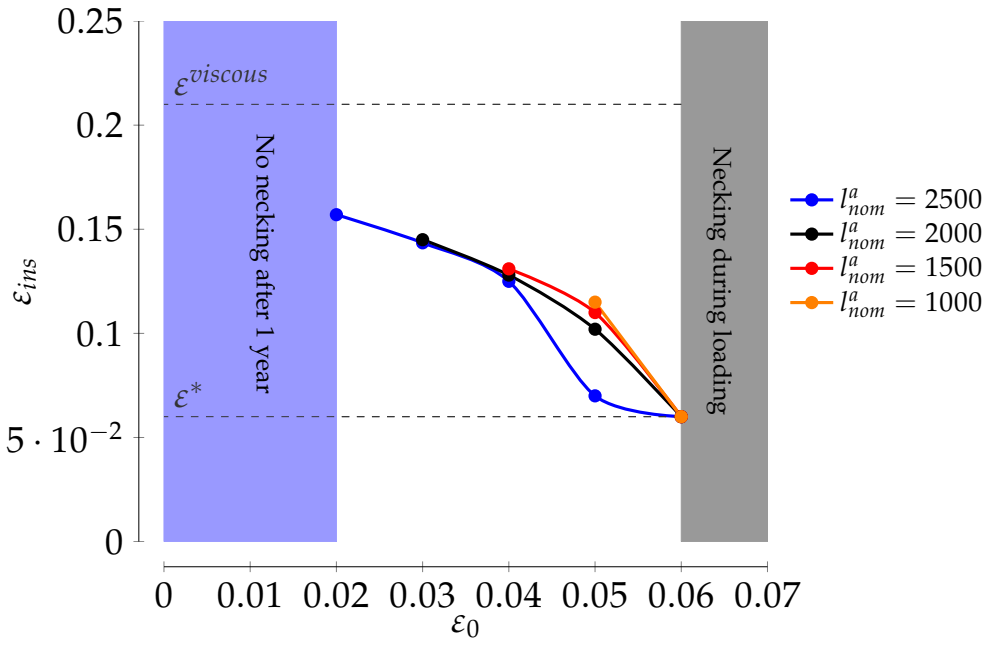

Fig. 5.15: Variation of the strain at instability ε_{ins} during creep/relaxation experiment as a function of the initial nominal strain ε_0 of Cu thin films with 2 competing mechanisms for different actuator lengths l^a_{nom}.

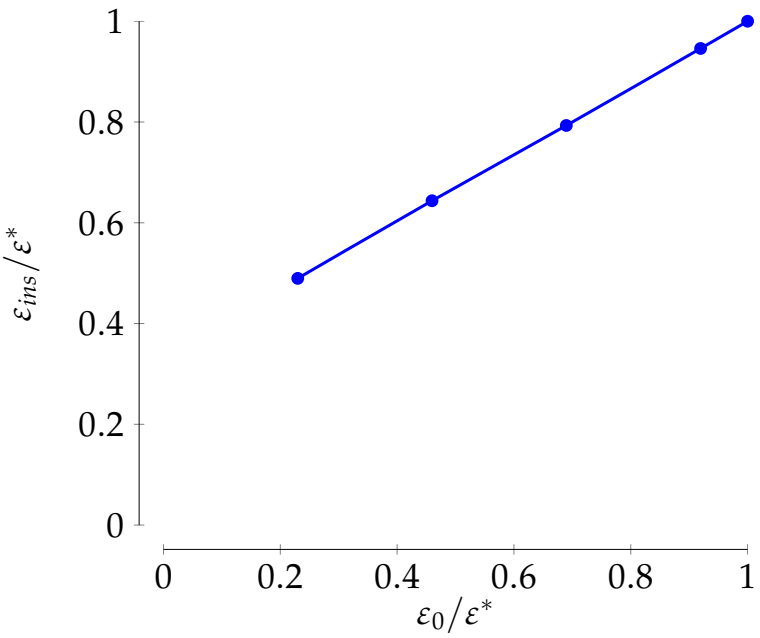

Fig. 5.16: Variation of the strain at instability ε_{ins} during creep/relaxation experiment as a function of the initial nominal strain ε_0 of Cu thin films modelled with a dislocation based approach, normalized by the ductility in monotonic loading ε^*.

and ε_{ins} is recovered but the ductility never exceeds ε^*. The dislocation density contributes well to increase the strain rate sensitivity as a function of the prestrain but does not postpone the occurrence of necking during relaxation. More research into the competition of rate sensitive and rate insensitive deformation mechanisms is still necessary before obtaining a definitive answer to the origin of the prestrain dependent ductility. One question still unanswered is also how prestrains around ε^* can lead to high ductility while all the envisaged constitutive laws predict $\varepsilon_{ins} \sim \varepsilon^*$ in such cases. Imperfections f are maybe statistically distributed and more precisions on the initial dislocation density are required to properly set the rate sensitivity of the dislocation based approach.

5.6 Conclusion

The extended MK based localization model takes into account the effects of elasticity, isotropic strain hardening, strain gradient plasticity, rate sensitivity and imperfection. General trends have been reviewed regarding localized necking in rate independent and dependent materials, with additional effect of SGP. Then, material parameters have been linked to microstructure features. The model has revealed the decrease of ductility with decreasing film thickness and highlighted the possible inversion of this trend when rate-dependent plasticity mechanisms dominate the deformation. Strain gradients plasticity effects can also delay unstable flow in thin films. The competition of deformation mechanisms in NC metallic thin films has been studied: strain rate has a strong influence on the dominating mechanisms, profoundly modifying the necking behaviour. The negative influence of internal stress on the measured ductility in uniaxial tension has also been unveiled. Finally, attention has been devoted to the necking analysis under creep/relaxation conditions but the model predictions do not allow a proper reproduction of all the experimental trends observed by Vayrette et al. (2015).

CHAPTER 6

Conclusion

This thesis, devoted to the study of the mechanical behaviour of metallic face center cubic thin films under tensile static and creep conditions contributes to the development of the on-chip technique and to the modelling of these films within a crystal plasticity framework.

The state of the art related to this work has been presented in chapter 2. The specific deformation mechanisms of nanocrystalline metals have been reviewed as well as their influence on the mechanical properties, depicting the complex interplay of dislocation- and grain boundary- based mechanisms. In the nanocrystalline domain, grain size distributions are such that some grains may experience several competing mechanisms while other grains may deform by conventional dislocation based mechanisms. Such demanding conditions require specific modelling attention and a variety of models relying on various assumptions have been proposed in the literature. An overview of the existing modelling approaches has therefore been provided, showing that dislocation based viscoplasticity models have not been much addressed.

One of the objectives of this thesis was to experimentally study the deformation and the relaxation mechanisms taking place inside nanocrystalline Ni thin films. The adaptation of the internal stress actuated micro-tensile testing method has been unsuccessful. Even if no viable and stable fabrication process has been found, many lessons have been learned. All the aspects of the fabrication process have been detailed in chapter 3. One of the most problematic issues is the control of the internal stress of Ni specimens and the best couple of sputtering power and Ar pressure should be found. The combination of Si sacrificial layer and XeF_2 etchant is believed to become a generic process as

it gives a maximum etching selectivity and avoids temperature variation and the need for a drying process. The knowledge of this process is still limited within the UCLouvain cleanroom facilities and required further investigations in order for instance to prevent undesirable stiction of the structures on the underneath substrate.

Nevertheless, the present thesis contributes to the improvement of this experimental technique by simulating the entire lab-on-chip experiment through finite element modelling. The under-etching of the fixed parts of the specimen and of the actuator, due to the isotropic etching of the sacrificial layer, has been found to profoundly affect the extracted stress and strain while the dog-bone shape of the specimen reinforced this source of inaccuracy. A large scatter in the data has been observed from an instance to another, in agreement with previous experimental results. The possible erroneous determination of material properties caused by these uncertainties has also been emphasized. The relative error on the stress decreases with increasing actuator lengths whereas the extracted specimen strain is more precise as the specimen width increases. Furthermore, the under-etching of the anchoring parts leads to the violation of the condition of application of the Saint Venant principle for small actuator lengths. Therefore, the use of long actuator and wide specimen beams is recommended. A new analytical correction model avoiding any fitting procedure has been proposed in order to address these issues. Even if the correction model improves the precision by a factor 10 and 3-5 for the stress and strain respectively, the procedure is strictly limited to elastic specimen or actuator material. It is also recommended to assess further design improvements of the on-chip technique by FE simulations.

The extension to a 3D version to address the influence of the overlap and of stress gradient through the thickness is one future perspective. The deformation of the specimen and the actuator can potentially be strongly influenced by the stress state in its unreleased configuration. As pointed out by Fang and Wickert (1996), stress gradients can become particularly significant as the film becomes thinner. To properly extract the stress and strain using the lab-on-chip technique, out-of-plane rotation, imposed by internal stress gradients should be accounted for. In FE analysis, internal stress gradient can be generated by imposing a fictitious temperature gradient through the thickness. Such internal stress gradient can be probed experimentally via the MOSS technique (see section 3.3) or via the single cantilever beam deflection technique developed by Fang and Wickert (1996).

On the basis of the lab-on-chip simulations, future work could address the under-etching of the anchoring parts issue. Clearly, further experimental research is needed to limit the under-etching. Selective etching of locally modified sacrificial layer, including for instance doped Si or nanoporous Si, provides a possible direction to solve the problem. Such experimental investigation appears fully justified because no correction on the stress is required

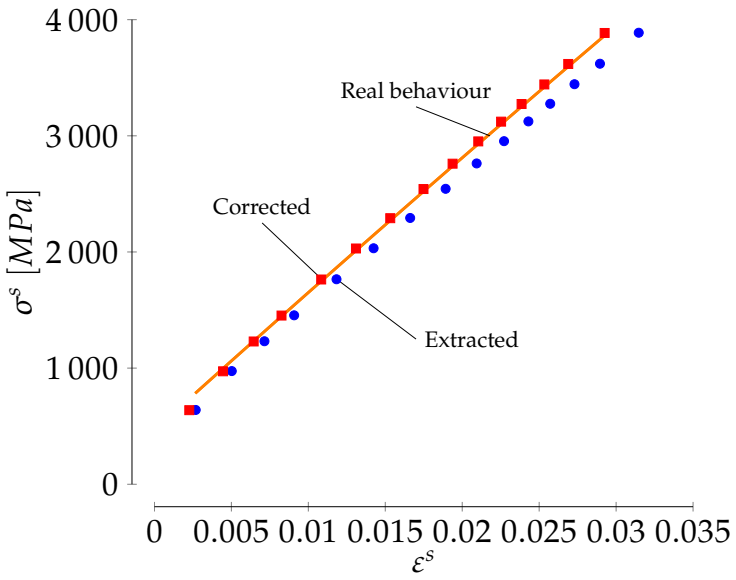

Fig. 6.1: Comparison between the extracted and corrected mechanical behaviour of a purely elastic material via lab-on-chip experiment. No under-etching is imposed.

without under-etching and the correction procedure proposed in this thesis has been found to be very efficient to account for the specimen dog-bone shape (for $l^a_{nom} > 500\mu$m), see Figure 6.1

In chapter 4, a dislocation-informed crystal plasticity model has been developed for metallic thin films, relying on the following observations: (i) the TEM characterization of Pd thin films carried out by Colla et al. (2015) has revealed surprisingly high dislocation densities and dislocation storage inside the grains. (ii) Some grains are initially free from dislocations. (iii) Rate dependent mechanisms are amplified in nanograins. (iv) Pd thin films are subjected to creep/relaxation before the first experimental observations. The developments implemented in the crystal plasticity code previously available at UCLouvain can be summarized as follows: a dislocation evolution law has been established and a physics based rate equation relying on thermal activation has been identified. Furthermore, constitutive laws take into account the effects of grain size distribution and grains free of dislocations. The micro to macro transition is based on the ALAMEL scheme which was for the first time applied to columnar grains. The model has been validated against experimental data on sub-micron Pd films gathered using the lab-on-chip technique. Not only the effect of the film thickness was captured but also the relaxation response and the dislocation density evolution. Although the number of fitting parameters is limited, the parameters of the rate equation (4.4) are extracted from literature. Possible improvement of the model may be provided by a atomistically-informed crystal plasticity approach in which the collective behaviour of dislocations are computed based on atomistic modelling and dislocation dynamics (see e.g. (Amodeo et al., 2016)).

One of the keys element of the model was the presence of grains initially free from dislocations. Indeed, the strain hardening and the thickness effect could only be captured if such extremely resistant grains were present. Such strong assumption requires further TEM investigation to discard possible dislocation emission at GBs. Local stress concentration at triple junction triggers indeed the nucleation of dislocation which are then potentially available for propagation (Bitzek et al., 2008). However this assumption is supported by the Ph.D. of Tummala (2016) on Discrete Dislocation Dynamics (DDD) in FCC metallic thin films. Polycrystalline DDD-FEM simulations based on superposition principle provide an elegant way to study the deformation mechanisms responsible for the strain hardening and thickness dependent response of nanocrystalline thin films. DDD-FEM calculations relying on a distribution of dislocation sources among all the grains did not reproduce the experimental tendencies. Size effects were observed only with simulations involving grains with no initial dislocation sources. Future work could be devoted to explore and compare the mechanical response of 3D polycrystalline thin films within the framework of the classical continuum crystal plasticity developed in this work and discrete dislocation dynamics proposed by Tummala (2016). The model microstructure proposed for such study is a 2D periodic Laguerre-Voronoï tessellation extruded in the growth direction of the film, that reproduce the grain size distribution. Possible statistical comparison are envisaged at macroscopic, grain and microscopic level to evaluate the influence of grain size distribution, grains free of dislocation distribution, grain topology and texture. Discrepancies caused by the discrete nature of plasticity in DDD are expected at grain and microscopic levels as suggested by Šiška et al. (2009). Furthermore, DDD-FEM calculations facilitate the study of the influence of free surfaces and possible dislocation-GB interactions which are not considered in the present work. DDD simulations are also expected to give more insights about the dislocations stored in the vicinity of the boundary and so to possibly enrich the strain hardening law (equation (4.7)) following for instance the work of Sinclair et al. (2006) for UFG materials. Pile-ups will contribute both to isotropic hardening and to the building up of back stresses.

This work contributes to the literature debate to which extent deformation in nanocrystalline materials and thin films is driven or not by dislocation based mechanisms. The dislocation-based deformation mechanism assumption allows the proper reproduction of all the experimental trends, confirming the dominance of a dislocation driven deformation mechanism for the present Pd films with high defects density. Numerical predictions have revealed that texture created during the deposition of a thin film does not significantly influence the creep behaviour and the stress heterogeneity. The model has then been used to address some original experimental evidences involving back stresses, backward creep and strain recovery. Without relying on any complex kinematic hardening formulation, the combination of crystallographic anisotropy and grain size and grains free from dislocations distributions generates such

high level of stress heterogeneity that backward creep and strain recovery are observed. The time dependent plastic response of the Pd films is dominated by the back stresses which originates from a purely composite effect. The grains initially free from dislocation are extremely resistant and remain mainly elastic. The largest grains yield thus much earlier than the hardest ones, inducing a significant kinematic hardening contribution.

According to the model, texture created during the deposition of a thin film does not significantly influence the creep behaviour and the stress heterogeneity. Nonetheless, fibre textures involve significant plastic anisotropy which still need to be confirmed by experiments. Nowadays, the lab-on-chip technique does not allow the measure of the transverse and through the thickness deformations. Future efforts could be devoted to the experimental determination of the Lankford coefficient by, for instance, coupling the Lab-on-chip technique with Digital Image Correlation (DIC) (Jonnalagadda et al., 2010).

In chapter 5, a model initially developed to predict macroscale necking in metal forming applications has been extended to thin films. The extended Marciniak-Kuczynski based localization model aims at accounting for the synergy of elasticity, isotropic strain hardening, strain gradient plasticity, rate sensitivity and presence of imperfection. Generic effects have been reviewed regarding localized necking in rate independent and dependent materials, with additional effect of SGP. Yield strength and strain hardening coefficient have then been linked to grain size and film thickness through empirical laws while the transition of strain rate sensitivity has been addressed through a phenomenological relationship. The model has revealed the loss of ductility associated to decreasing film thickness due to the increasing strength and high relative importance of of imperfections. This deleterious trend can be reversed if rate dependent mechanisms dominate the mechanical response. As reported experimentally in the recent literature, thermally activated deformation mechanisms appear at small grain size and increase the strain rate sensitivity, improving the resistance to plastic instability. Strain gradient plasticity effects can also help to restore the ductility in metallic thin films, but a direct experimental proof of the delay of necking by SGP in small scale systems is still lacking. The complexity of the grain size and thickness effects have also been tackled by introducing multiple deformation mechanisms, based either on dislocation motion or on creep/relaxation. The competition between deformation mechanisms has been investigated and the model predictions have confirmed that ductility is rate dependent in nanocrystalline metallic thin films as observed experimentally. The model has also demonstrated that compressive or tensile internal stress generated during deposition of thin films reduce the measured ductility in uniaxial tension. Finally, efforts have been focussed on applying the necking analysis under creep/relaxation conditions. The question of the most adapted constitutive model appears to be central and the model does not allow to capture all the experimental trends observed with Cu thin

films.

Apart from the fact that J_2 isotropic incremental plasticity is used in this thesis to study localized necking, the question of the most adapted constitutive model is crucial at such small scale. As thin films involve sometimes very sharp crystallographic texture, the crystal plasticity seems to give the more suitable framework to deal with elastic and plastic anisotropy. This last effect is known to postpone plastic instabilities in metal forming operations and is not present in the current formulation. Furthermore, morphological texture of the grains can also affect the necking resistance. For instance, highly textured electro-deposited pure iron exhibiting needle-shape fine grains presented an extraordinarily deep drawability (i.e. necking resistance during deep drawing forming process) (Yoshinaga et al., 2008). The Lankford coefficient r was evaluated to 7, illustrating an incredible plastic anisotropy. Such effect is also expected in thin films with columnar grains and reinforce again the need to determine Lankford coefficient in small scale systems.

Also a statistical treatment of the imperfections is required to set up a predictive model. Here, imperfections f have been chosen arbitrary to reproduce the experimental trends. To justify these choices, f needs to be directly correlated with roughness or material imperfection. Geometrical imperfection can be obtained by mapping the surface roughness using AFM technique whereas material imperfection can be extracted from a RVE calculation, accounting for the grain size distribution and the number of grains across the thickness.

This study has been limited to the question of ductility dictated by plastic localization without addressing damage issues in thin films. At a macroscopic scale, a perspective to combine strain localization and damage could consist in incorporating ductile fracture yield locus such as developed by Bai and Wierzbicki (2008) in the space of equivalent fracture strain, stress triaxiality and the Lode angle parameter. The calibration of such fracture locus is not simple at small scale and may be difficult to set up as it requires tests under different loading configurations. Moreover, local stress concentration at GBs or near impurities can be so large that cleavage occurs. Understanding and modelling of damage and fracture in thin films is also a major challenge for future research (Pineau et al., 2016).

This study on the ductility of thin metallic films essentially shows how complex this problem is. As the dominating mechanism depends on fine microstructure details, a lot of work is still needed to develop mature predictive physics based model for the ductility. However the extended MK imperfection model was implemented in such a way that it can be used in conjunction with any UMAT (User defined Material), offering possibilities for further investigations with more advanced models such as crystal plasticity or homogenized multiphase materials.

Bibliography

Aifantis, E.C., 1984. On the Microstructural Origin of Certain Inelastic Models. Journal of Engineering Materials and Technology 106, 326.

Ames, M., Markmann, J., Karos, R., Michels, A., Tschöpe, A., Birringer, R., 2008. Unraveling the nature of room temperature grain growth in nanocrystalline materials. Acta Materialia 56, 4255–4266.

Amodeo, J., Dancette, S., Delannay, L., 2016. Atomistically-informed crystal plasticity in MgO polycrystals under pressure. International Journal of Plasticity 82, 177–191.

Anderoglu, O., Misra, A., Wang, J., Hoagland, R.G., Hirth, J.P., Zhang, X., 2010. Plastic flow stability of nanotwinned Cu foils. International Journal of Plasticity 26, 875–886.

Aoyagi, Y., Tsuru, T., Shimokawa, T., 2014. Crystal plasticity modeling and simulation considering the behavior of the dislocation source of ultrafine-grained metal. International Journal of Plasticity 55, 43–57.

Argon, A.S., 2008. Strengthening Mechanisms in Crystal Plasticity. Oxford University Press, Oxford.

Asaro, R.J., Krysl, P., Kad, B., 2003. Deformation mechanism transitions in nanoscale fcc metals. Philosophical Magazine Letters 83, 733–743.

Asaro, R.J., Suresh, S., 2005. Mechanistic models for the activation volume and rate sensitivity in metals with nanocrystalline grains and nano-scale twins. Acta Materialia 53, 3369–3382.

Bai, Y., Wierzbicki, T., 2008. A new model of metal plasticity and fracture with pressure and lode dependence. International Journal of Plasticity 24, 1071 – 1096.

Barata da Rocha, A., Barlat, F., Jalinier, J.M., 1985. Prediction of the forming limit diagrams of anisotropic sheets in linear and non-linear loading. Materials Science and Engineering 68, 151–164.

Bardel, D., Mishin, O., Delannay, L., . Prediction of through-thickness heterogeneity after multi-pass rolling of aluminium sheet. International journal of plasticity .

Barlat, F., 1987. Crystallographic texture, anisotropic yield surfaces and forming limits of sheet metals. Materials Science and Engineering 91, 55–72.

Béfahy, S., Yunus, S., Pardoen, T., Bertrand, P., Troosters, M., 2007. Stretchable helical gold conductor on silicone rubber microwire. Applied Physics Letters 91, 1–4.

Bei, H., Shim, S., Pharr, G.M., George, E.P., 2008. Effects of pre-strain on the compressive stress-strain response of Mo-alloy single-crystal micropillars. Acta Materialia 56, 4762–4770.

Benzerga, A., Shaver, N.F., 2006. Scale dependence of mechanical properties of single crystals under uniform deformation. Scripta Materialia 54, 1937–1941.

Benzerga, A.A., 2008. An analysis of exhaustion hardening in micron-scale plasticity. International Journal of Plasticity 24, 1128–1157.

Bitzek, E., Derlet, P.M., Anderson, P.M., Van Swygenhoven, H., 2008. The stress-strain response of nanocrystalline metals: A statistical analysis of atomistic simulations. Acta Materialia 56, 4846–4857.

Blum, W., Eisenlohr, P., 2017. Deformation Strength of Nanocrystalline Thin Films. Journal of Materials Science and Technology 33, 718–722.

de Boer, M.P., Corwin, A.D., Kotula, P.G., Baker, M.S., Michael, J.R., Subhash, G., Shaw, M.J., 2008a. On-chip laboratory suite for testing of free-standing metal film mechanical properties, Part II - Experiments. Acta Materialia 56, 3313–3326.

de Boer, M.P., DelRio, F.W., Baker, M.S., 2008b. On-chip test structure suite for free-standing metal film mechanical property testing, Part I - Analysis. Acta Materialia 56, 3344–3352.

Borg, U., Niordson, C.F., Fleck, N.A., Tvergaard, V., 2006. A viscoplastic strain gradient analysis of materials with voids or inclusions. International Journal of Solids and Structures 43, 4906–4916.

Boudeau, N., Gelin, J., Salhi, S., 1998. Computational prediction of the localized necking in sheet forming based on microstructural material aspects. Computational Materials Science 11, 45–64.

Brandl, C., Derlet, P.M., Van Swygenhoven, H., 2011. Dislocation mediated plasticity in nanocrystalline Al: the strongest size. Modelling and Simulation in Materials Science and Engineering 19, 074005.

Brenner, S., 1956. Tensile Strength of Whiskers. Journal of Applied Physics 27, 1484–1491.

Brugger, C., Coulombier, M., Massart, T., Raskin, J.P., Pardoen, T., 2010. Strain gradient plasticity analysis of the strength and ductility of thin metallic films using an enriched interface model. Acta Materialia 58, 4940–4949.

Caillard, D., Martin, J. (Eds.), 2003. Thermally Activated Mechanisms in Crystal Plasticity. Pergamon Materials Series.

Carsley, J.E., Ning, J., Milligan, W.W., Hackney, S.A., Aifantis, E.C., 1995. A simple, mixtures-based model for the grain size dependence of strength in nanophase metals. Nanostructured Materials 5, 441–448.

Chen, B., Lutker, K., Raju, S.V., Yan, J., Kanitpanyacharoen, W., Lei, J., Yang, S., Wenk, H.R., Mao, H.k., Williams, Q., 2012. Texture of Nanocrystalline Nickel: Probing the Lower Size Limit of Dislocation Activity. Science 338, 1448–1451.

Chen, M., Ma, E., Hemker, K.J., Sheng, H., Wang, Y., Cheng, X., 2003. Deformation Twinning in Nanocrystalline Aluminum. Science 300, 1275–1277.

Cheng, S., Ma, E., Wang, Y.M., Kecskes, L.J., Youssef, K.M., Koch, C.C., Trociewitz, U.P., Han, K., 2005. Tensile properties of in situ consolidated nanocrystalline Cu. Acta Materialia 53, 1521–1533.

Chokshi, A.H., Rosen, A., Karch, J., Gleiter, H., 1989. On the validity of the hall-petch relationship in nanocrystalline materials. Scripta Metallurgica 23, 1679–1683.

Colla, M., Idrissi, H., Malet, L., Godet, S., Raskin, J., Schryvers, D., Pardoen, T., 2015. Dislocation-mediated relaxation in nanograined columnar palladium films revealed by on-chip time-resolved HRTEM testing. Nature Communications 6, 1–8.

Colla, M.S., 2014. Plasticity and creep in thin free-standing nanocrystalline Pd films. Ph.D. thesis. Université catholique de Louvain.

Colla, M.S., Wang, B., Idrissi, H., Schryvers, D., Raskin, J.P., Pardoen, T., 2012. High strength-ductility of thin nanocrystalline palladium films with nanoscale twins: On-chip testing and grain aggregate model. Acta Materialia 60, 1795–1806.

Conrad, H., 1965. The Cryogenic Properties of Materials. by Zackey , 436.

Conrad, H., Narayan, J., 2000. On the grain size softening in nanocrystalline materials. Scripta Materialia 42, 1025–1030.

Coulombier, M., 2012. Nanomechanical Lab On-chip for Tesing Thin Films Marials and Applications to Al-Al(Si). Ph.D. thesis. Université Catholique de Louvain.

Coulombier, M., Boé, A., Brugger, C., Raskin, J.P., Pardoen, T., 2010. Imperfection-sensitive ductility of aluminium thin films. Scripta Materialia 62, 742–745.

Coulombier, M., Guisbiers, G., Colla, M.S., Vayrette, R., Raskin, J.P., Pardoen, T., 2012. On-chip stress relaxation testing method for freestanding thin film materials. The Review of scientific instruments 83, 105004.

Curtin, W.A., Miller, R.E., 2003. Atomistic/continuum coupling in computational materials science. Modelling and Simulation in Materials Science and Engineering 11, R33–R68.

Dalla Torre, F., Van Swygenhoven, H., Victoria, M., 2002. Nanocrystalline electrodeposited Ni: microstructure and tensile properties. Acta Materialia 50, 3957–3970.

Dallatorre, F., Spatig, P., Schaublin, R., Victoria, M., 2005. Deformation behaviour and microstructure of nanocrystalline electrodeposited and high pressure torsioned nickel. Acta Materialia 53, 2337–2349.

Dao, M., Lu, L., Asaro, R.J., De Hosson, J.T.M., Ma, E., 2007. Toward a quantitative understanding of mechanical behavior of nanocrystalline metals. Acta Materialia 55, 4041–4065.

Dao, M., Lu, L., Shen, Y.F., Suresh, S., 2006. Strength, strain-rate sensitivity and ductility of copper with nanoscale twins. Acta Materialia 54, 5421–5432.

Dehm, G., Jaya, B.N., Raghavan, R., Kirchlechner, C., 2017. Overview on micro- and nanomechanical testing: New insights in interface plasticity and fracture at small length scales. Acta Materialia 142, 248–282.

Delannay, L., Jacques, P.J., Kalidindi, S.R., 2006. Finite element modeling of crystal plasticity with grains shaped as truncated octahedrons. International Journal of Plasticity 22, 1879–1898.

Delincé, M., Bréchet, Y., Embury, J.D., Geers, M.G.D., Jacques, P.J., Pardoen, T., 2007. Structure-property optimization of ultrafine-grained dual-phase steels using a microstructure-based strain hardening model. Acta Materialia 55, 2337–2350.

Derlet, P.M., Hasnaoui, a., Van Swygenhoven, H., 2003. Atomistic simulations as guidance to experiments. Scripta Materialia 49, 629–635.

Duhamel, C., Brechet, Y., Champion, Y., 2010. Activation volume and deviation from Cottrell-Stokes law at small grain size. International Journal of Plasticity 26, 747–757.

El-Awady, J.A., 2015. Unravelling the physics of size-dependent dislocation-mediated plasticity. Nature Communications 6, 5926.

El-Sherik, A.M., Erb, U., Palumbo, G., Aust, K.T., 1992. Deviations from hall-petch behaviour in as-prepared nanocrystalline nickel. Scripta Metallurgica et Materiala 27, 1185–1188.

Emery, R.D., Povirk, G.L., 2003. Tensile behavior of free-standing gold films. Part II. Fine-grained films. Acta Materialia 51, 2079–2087.

Ertürk, I., 2012. Modeling creep and anelasticity in particle stregnthened alloys with strain gradient crystal plasticity. Ph.D. thesis. Eindhoven University of Technology.

Ertürk, I., van Dommelen, J.A.W., Geers, M.G.D., 2014. Gradient crystal plasticity modelling of anelastic effects in particle strengthened metallic thin films. Meccanica , 1–29.

Espinosa, H., Prorok, B., Peng, B., 2004. Plasticity size effects in free-standing submicron polycrystalline FCC films subjected to pure tension. Journal of the Mechanics and Physics of Solids 52, 667–689.

Espinosa, H.D., Zhu, Y., Moldovan, N., 2007. Design and operation of a MEMS-based material testing system for nanomechanical characterization. Journal of Microelectromechanical Systems 16, 1219–1231.

Estrin, Y., Mecking, H., 1984. A unified phenomenological description of work hardening and creep based on one-parameter models. Acta Metallurgica 32, 57–70.

Evans, A.G., Hutchinson, J.W., 2009. A critical assessment of theories of strain gradient plasticity. Acta Materialia 57, 1675–1688.

Evers, L.P., Parks, D.M., Brekelmans, W.a.M., Geers, M.G.D., 2002. Crystal plasticity model with enhanced hardening by geometrically necessary dislocation accumulation. Journal of the Mechanics and Physics of Solids 50, 2403–2424.

Eyckens, P., Van Bael, A., Van Houtte, P., 2009. Marciniak-Kuczynski type modelling of the effect of Through-Thickness Shear on the forming limits of sheet metal. International Journal of Plasticity 25, 2249–2268.

Eyckens, P., Van Bael, A., Van Houtte, P., 2011. An extended Marciniak-Kuczynski model for anisotropic sheet subjected to monotonic strain paths with through-thickness shear. International Journal of Plasticity 27, 1577–1597.

Fang, W., Wickert, J.A., 1996. Determining mean and gradient residual stresses in thin films using micromachined cantilevers. Journal of Micromechanics and Microengineering 6, 301–309.

Farkas, D., Mohanty, S., Monk, J., 2008. Strain-driven grain boundary motion in nanocrystalline materials. Materials Science and Engineering A 493, 33–40.

Fleck, N., Muller, G., Ashby, M., Hutchinson, J., 1994. Strain gradient plasticity: Theory and experiment. Acta Metallurgica et Materialia 42, 475–487.

Fleck, N.A., Hutchinson, J.W., 2001. A reformulation of strain gradient plasticity. Journal of the Mechanics and Physics of Solids 49, 2245–2271.

Freund, L., Suresh, S., 2003. Thin Film Materials: Stress, Defect Formation and Surface Evolution. Cambridge University Press, Cambridge.

Frost, H., Ashby, M.F., 1982. Deformation-mechanism maps: the plasticity and creep of metals and ceramics. Pergamon Press.

Fu, H.H., Benson, D.J., Meyers, M.A., 2001. Analytical and computational description of effect of grain size on yield stress of metals. Acta Materialia 49, 2567–2582.

Fu, H.H., Benson, D.J., Meyers, M.A., 2004. Computational description of nanocrystalline deformation based on crystal plasticity. Acta Materialia 52, 4413–4425.

Gao, H., Huang, Y., Nix, W.D., Hutchinson, J.W., 1999. Mechanism-based strain gradient plasticity- I. Theory. Journal of the Mechanics and Physics of Solids 47, 1239–1263.

Geers, M.G.D., Brekelmans, W.A.M., Bayley, C.J., 2007. Second-order crystal plasticity: internal stress effects and cyclic loading. Modelling and Simulation in Materials Science and Engineering 15, S133–S145.

Geuzaine, C., Remacle, J.F., 2009. Gmsh: a three-dimensional finite element mesh generator with built-in pre- and post-processing facilities. International Journal for Numerical Methods in Engineering 79, 1309–1331.

Ghidelli, M., Idrissi, H., Ebastien Gravier, S., Blandin, J.J., Raskin, J.P., Schryvers, D., Pardoen, T., 2017. Homogeneous flow and size dependent mechanical behavior in highly ductile Zr 65 Ni 35 metallic glass films. Acta Materialia 131, 246–259.

Ghosh, A.K., 1977. Tensile instability and necking in materials with strain hardening and strain-rate hardening. Acta Metallurgica 25, 1413–1424.

Gianola, D.S., Eberl, C., 2009. Micro- and nanoscale tensile testing of materials. Jom 61, 24–35.

Gianola, D.S., Mendis, B.G., Cheng, X.M., Hemker, K.J., 2008. Grain-size stabilization by impurities and effect on stress-coupled grain growth in nanocrystalline Al thin films. Materials Science and Engineering A 483-484, 637–640.

Gianola, D.S., Warner, D.H., Molinari, J.F., Hemker, K.J., 2006. Increased strain rate sensitivity due to stress-coupled grain growth in nanocrystalline Al. Scripta Materialia 55, 649–652.

Gravier, S., Coulombier, M., Safi, A., André, N., Boé, A., Raskin, J.P., Pardoen, T., 2009. New on-chip nanomechanical testing laboratory - Applications to aluminum and polysilicon thin films. Journal of Microelectromechanical Systems 18, 555–569.

Gray, G., Lowe, T., Cady, C., 1997. Influence of strain rate & temperature on the mechanical response of ultrafine-grained Cu, Ni, and Al-4Cu-0.5 Zr. Nanostructured Materials 9, 477–480.

Greer, J.R., De Hosson, J.T.M., 2011. Plasticity in small-sized metallic systems: Intrinsic versus extrinsic size effect. Progress in Materials Science 56, 654–724.

Greer, J.R., Oliver, W.C., Nix, W.D., 2005. Size dependence of mechanical properties of gold at the micron scale in the absence of strain gradients. Acta Materialia 53, 1821–1830.

Gu, C., Lian, J., Jiang, Q., Jiang, Z., 2007a. Ductile–brittle–ductile transition in an electrodeposited 13 nanometer grain sized Ni–8.6wt.% Co alloy. Materials Science and Engineering: A 459, 75–81.

Gu, C., Lian, J., Jiang, Z., 2006a. High Strength Nanocrystalline Ni-Co Alloy with Enhanced Tensile Ductility. Advanced Engineering Materials 8, 252–256.

Gu, C., Lian, J., Jiang, Z., Jiang, Q., 2006b. Enhanced tensile ductility in an electrodeposited nanocrystalline Ni. Scripta Materialia 54, 579–584.

Gu, C.D., Lian, J.S., Jiang, Q., Zheng, W.T., 2007b. Experimental and modelling investigations on strain rate sensitivity of an electrodeposited 20 nm grain sized Ni. Journal of Physics D: Applied Physics 40, 7440–7446.

Gürses, E., El Sayed, T., 2011a. A variational multiscale constitutive model for nanocrystalline materials. Journal of the Mechanics and Physics of Solids 59, 732–749.

Gürses, E., El Sayed, T., 2011b. Constitutive modeling of strain rate effects in nanocrystalline and ultrafine grained polycrystals. International Journal of Solids and Structures 48, 1610–1616.

Haque, M.A., Saif, M.T.A., 2002. Application of MEMS force sensors for in situ mechanical characterization of nano-scale thin films in SEM and TEM. Sensors and Actuators, A: Physical 97-98, 239–245.

Haque, M.A., Saif, M.T.A., 2003. Strain gradient effect in nanoscale thin films. Acta Materialia 51, 3053–3061.

Hart, E., 1967. Theory of the tensile test. Acta Metallurgica 15, 351–355.

Hayes, R.W., Witkin, D., Zhou, F., Lavernia, E.J., 2004. Deformation and activation volumes of cryomilled ultrafine-grained aluminum. Acta Materialia 52, 4259–4271.

He, Q., Luo, Z.X., Chen, X.Y., 2008. Comparison of residual stress measurement in thin films using surface micromachining method. Thin Solid Films 516, 5318–5323.

Herrera-Solaz, V., Llorca, J., Dogan, E., Karaman, I., Segurado, J., 2014. An inverse optimization strategy to determine single crystal mechanical behavior from polycrystal tests: Application to AZ31 Mg alloy. International Journal of Plasticity 57, 1–15.

Herrera-Solaz, V., Segurado, J., Llorca, J., 2015. On the robustness of an inverse optimization approach based on the Levenberg-Marquardt method for the mechanical behavior of polycrystals. European Journal of Mechanics, A/Solids 53, 220–228.

Hill, R., 1952. On discontinuous plastic states, with special reference to localized necking in thin sheets. Journal of the Mechanics and Physics of Solids 1, 19–30.

Hill, R., 1957. On uniqueness and stability in the theory of finite elastic strain. Journal of the Mechanics and Physics of Solids 5, 229–241.

Hill, R., 1991. A theoretical perspective on in-plane forming of sheet metal. Journal of the Mechanics and Physics of Solids 39, 295–307.

Hill, R., Hutchinson, J.W., 1975. Bifurcation phenomena in the plane tension test. Journal of the Mechanics and Physics of Solids 23, 239–264.

Höppel, H.W., May, J., Eisenlohr, P., Göken, M., 2005. Strain-rate sensitivity of ultrafine-grained materials. Zeit fur Metallkunde 96, 566–571.

Hosford, W.F., Caddell, R.M., 2011. Metal forming: mechanics and metallurgy. Cambridge University Press.

Hosseinian, E., Legros, M., Pierron, O., 2016. Quantifying and Observing Viscoplasticity at the Nanoscale: Highly Localized Deformation Mechanisms in Ultrathin Nanocrystalline Gold Films. Nanoscale 8, 9234–9244.

Hugo, R.C., Kung, H., Weertman, J.R., Mitra, R., Knapp, J.a., Follstaedt, D.M., 2003. In-situ TEM tensile testing of DC magnetron sputtered and pulsed laser deposited Ni thin films. Acta Materialia 51, 1937–1943.

Hutchinson, J.W., Neale, K.W., 1977. Influence of strain-rate sensitivity on necking under uniaxial tension. Acta Metallurgica 25, 839–846.

Hutchinson, J.W., Neale, K.W., 1978a. Sheet Necking-II. Time-Independent Behavior. Mechanics of Sheet Metal Forming , 127–153.

Hutchinson, J.W., Neale, K.W., 1978b. Sheet Necking-III. Strain-Rate Effects. Mechanics of Sheet Metal Forming , 269–285.

Idrissi, H., Wang, B., Colla, M.S., Raskin, J.P., Schryvers, D., Pardoen, T., 2011. Ultrahigh strain hardening in thin palladium films with nanoscale twins. Advanced materials 23, 2119–22.

Iker, F., André, N., Pardoen, T., Raskin, J.P., 2006. Three-dimensional self-assembled sensors in thin-film SOI technology. Journal of Microelectromechanical Systems 15, 1687–1697.

Inal, K., Neale, K.W., Aboutajeddine, A., 2005. Forming limit comparisons for FCC and BCC sheets. International Journal of Plasticity 21, 1255–1266.

Ivanisenko, Y., Kurmanaeva, L., Weissmueller, J., Yang, K., Markmann, J., Rösner, H., Scherer, T., Fecht, H.J., 2009. Deformation mechanisms in nanocrystalline palladium at large strains. Acta Materialia 57, 3391–3401.

Jang, D., Greer, J.R., 2011. Size-induced weakening and grain boundary-assisted deformation in 60 nm grained Ni nanopillars. Scripta Materialia 64, 77–80.

Jonnalagadda, K., Karanjgaokar, N., Chasiotis, I., Chee, J., Peroulis, D., 2010. Strain rate sensitivity of nanocrystalline Au films at room temperature. Acta Materialia 58, 4674–4684.

Kang, W., Han, J.H., Saif, M.T.A., 2010. A Novel Method for In Situ Uniaxial Tests at the Micro/Nanoscale-Part II: Experiment. Journal of Microelectromechanical Systems 19, 1322–1330.

Kang, W., Saif, M.T.A., 2010. A Novel Method for In Situ Uniaxial Tests at the Micro/Nano Scale-Part I: Theory. Journal of Microelectromechanical Systems 19, 1309–1321.

Kiener, D., Grosinger, W., Dehm, G., Pippan, R., 2008. A further step towards an understanding of size-dependent crystal plasticity: In situ tension experiments of miniaturized single-crystal copper samples. Acta Materialia 56, 580–592.

Kim, H.S., Estrin, Y., Bush, M.B., 2001. Constitutive modelling of strength and plasticity of nanocrystalline metallic materials. Materials Science and Engineering A 316, 195–199.

Knockaert, R., Chastel, Y., Massoni, E., 2002. Forming limits prediction using rate-independent polycrystalline plasticity. International Journal of Plasticity 18, 231–247.

Kocks, U.F., 2001. Realistic constitutive relations for metal plasticity. Materials Science and Engineering A 317, 181–187.

Kocks, U.F., Argon, A.S., Ashby, M.F., 1975. Thermodynamics and kinetics of slip. Pergamon Press, Oxford.

Kocks, U.F., Mecking, H., 2003. Physics and phenomenology of strain hardening: The FCC case. Progress in Materials Science 48, 171–273.

Kohlhoff, S., Gumbsch, P., Fischmeister, H.F., 1991. Crack Propagation in BCC Crystals Studied with a Combined Finite- Element and Atomisitc Model. Phil Mag A 64, 851–878.

Koslowski, M., 2010. Effect of grain size distribution on plastic strain recovery. Physical Review B 82, 1–5.

Kumar, K.S., Suresh, S., Chisholm, M.F., Horton, J., Wang, P., 2003a. Deformation of electrodeposited nanocrystalline nickel. Acta Materialia 51, 387–405.

Kumar, K.S., Van Swygenhoven, H., Suresh, S., 2003b. Mechanical behavior of nanocrystalline metals and alloys. Acta Materialia 51, 5743–5774.

Kuroda, M., Tvergaard, V., 2010. An alternative treatment of phenomenological higher-order strain-gradient plasticity theory. International Journal of Plasticity 26, 507–515.

Lacour, S.P., Wagner, S., Huang, Z., Suo, Z., 2003. Stretchable gold conductors on elastomeric substrates. Applied Physics Letters 82, 2404–2406.

Lambricht, N., Pardoen, T., Yunus, S., 2013. Giant stretchability of thin gold films on rough elastomeric substrates. Acta Materialia 61, 540–547.

Lapouge, P., Onimus, F., Coulombier, M., Raskin, J.P., Pardoen, T., Bréchet, Y., 2017. Creep behavior of submicron copper films under irradiation. Acta Materialia 131, 77–87.

Lapouge, P., Onimus, F., Vayrette, R., Raskin, J.P., Pardoen, T., Bréchet, Y., 2016. A novel on chip test method to characterize the creep behavior of metallic layers under heavy ion irradiation. Journal of Nuclear Materials 476, 20–29.

Lebensohn, R.A., Bringa, E.M., Caro, A., 2007. A viscoplastic micromechanical model for the yield strength of nanocrystalline materials. Acta Materialia 55, 261–271.

Lee, J.H., Holland, T.B., Mukherjee, A.K., Zhang, X., Wang, H., 2013. Direct observation of Lomer-Cottrell locks during strain hardening in nanocrystalline nickel by in situ TEM. Scientific reports 3, 1061.

Legros, M., Gianola, D.S., Hemker, K.J., 2008. In situ TEM observations of fast grain-boundary motion in stressed nanocrystalline aluminum films. Acta Materialia 56, 3380–3393.

Lemoine, G., Delannay, L., Idrissi, H., Colla, M.S., Pardoen, T., 2016. Dislocation and back stress dominated viscoplasticity in freestanding sub-micron Pd films. Acta Materialia 111, 10–21.

Li, J., Weng, G., 2007. A secant-viscosity composite model for the strain-rate sensitivity of nanocrystalline materials. International Journal of Plasticity 23, 2115–2133.

Li, J., Weng, G.J., 2013. A micromechanical approach to the stress–strain relations, strain-rate sensitivity and activation volume of nanocrystalline materials. International Journal of Mechanics and Materials in Design 9, 141–152.

Li, L., Anderson, P.M., Lee, M.G., Bitzek, E., Derlet, P., Swygenhoven, H.V., 2009a. The stress-strain response of nanocrystalline metals: A quantized crystal plasticity approach. Acta Materialia 57, 812–822.

Li, L., Van Petegem, S., Van Swygenhoven, H., Anderson, P.M., 2012. Slip-induced intergranular stress redistribution in nanocrystalline Ni. Acta Materialia 60, 7001–7010.

Li, X., Wei, Y., Yang, W., Gao, H., 2009b. Competing grain-boundary- and dislocation-mediated mechanisms in plastic strain recovery in nanocrystalline aluminum. Proceedings of the National Academy of Sciences of the United States of America 106, 16108–13.

Lian, J., Barlat, F., Baudelet, B., 1989. Plastic behaviour and stretchability of sheet metals. Part II: Effect of yield surface shape on sheet forming limit. International Journal of Plasticity 5, 131–147.

Lian, J., Zhou, D., 1989. Diffuse necking and localized necking under plane stress. Materials Science and Engineering: A 111, 1–7.

Liao, X.Z., Srinivasan, S.G., Zhao, Y.H., Baskes, M.I., 2004. Formation mechanism of wide stacking faults in nanocrystalline Al. Applied Physics Letters 3564, 1–4.

Lin, I.H., Hirth, J.P., Hart, E.W., 1981. Plastic instability in uniaxial tension tests. Acta Metallurgica 29, 819–827.

Liu, P., Mao, S.C., Wang, L.H., Han, X.D., Zhang, Z., 2011. Direct dynamic atomic mechanisms of strain-induced grain rotation in nanocrystalline, textured, columnar-structured thin gold films. Scripta Materialia 64, 343–346.

Liu, Y., Hay, J., Wang, H., Zhang, X., 2014. A new method for reliable determination of strain-rate sensitivity of low-dimensional metallic materials by using nanoindentation. Scripta Materialia 77, 5–8.

Lohmiller, J., Grewer, M., Braun, C., Kobler, A., Kübel, C., Schüler, K., Honkimäki, V., Hahn, H., Kraft, O., Birringer, R., Gruber, P.a., 2014. Untangling dislocation and grain boundary mediated plasticity in nanocrystalline nickel. Acta Materialia 65, 295–307.

Lonardelli, I., Almer, J., Ischia, G., Menapace, C., Molinari, A., 2009. Deformation behavior in bulk nanocrystalline-ultrafine aluminum: in situ evidence of plastic strain recovery. Scripta Materialia 60, 520–523.

Lu, K., Lu, L., Suresh, S., 2009. Strengthening materials by engineering coherent internal boundaries at the nanoscale. Science 324, 349–352.

Lu, L., Schwaiger, R., Shan, Z.W., Dao, M., Lu, K., Suresh, S., 2005. Nanosized twins induce high rate sensitivity of flow stress in pure copper. Acta Materialia 53, 2169–2179.

Ma, E., 2006. Eight routes to improve the tensile ductility of bulk nanostructured metals and alloys. Jom 58, 49–53.

Maier, V., Durst, K., Mueller, J., Backes, B., Höppel, H.W., Göken, M., 2011. Nanoindentation strain-rate jump tests for determining the local strain-rate sensitivity in nanocrystalline Ni and ultrafine-grained Al. Journal of Materials Research 26, 1421–1430.

Marciniak, Z., Kuczyński, K., 1967. Limit strains in the processes of stretch-forming sheet metal. International Journal of Mechanical Sciences 9, 609–620.

Markmann, J., Bunzel, P., Rosner, H., Liu, K.W., Padmanabhan, K.A., Birringer, R., Gleiter, H., Weissmuller, J., 2003. Microstructure evolution during rolling of inert-gas condensed palladium. Scripta Materialia 49, 637–644.

Massart, T.J., Pardoen, T., 2010. Strain gradient plasticity analysis of the grain-size-dependent strength and ductility of polycrystals with evolving grain boundary confinement. Acta Materialia 58, 5768–5781.

May, J., Höppel, H.W., Göken, M., 2005. Strain rate sensitivity of ultrafine-grained aluminium processed by severe plastic deformation. Scripta Materialia 53, 189–194.

Melchior, M.A., Delannay, L., 2006. A texture discretization technique adapted to polycrystalline aggregates with non-uniform grain size. Computational Materials Science 37, 557–564.

Mercier, S., Molinari, A., Estrin, Y., 2007. Grain size dependence of strength of nanocrystalline materials as exemplified by copper: An elastic-viscoplastic modelling approach. Journal of Materials Science 42, 1455–1465.

Meyers, M., Mishra, A., Benson, D., 2006. Mechanical properties of nanocrystalline materials. Progress in Materials Science 51, 427–556.

Meyers, M.A., Ashworth, E., 1982. A model for the effect of grain size on the yield stress of metals. Philosophical Magazine A 46, 737–759.

Milička, K., 1999. Creep behaviour of long range ordered Cu50Zn alloy. Acta materialia 47, 1831–1843.

Miller, R.E., Tadmor, E., 2002. The QuasicontinuumMethod: Overview, applications and current directions. Journal of Computer-Aided Materials Design 9, 203–239.

Mishnaevsky, L., Levashov, E., 2015. Micromechanical modelling of nanocrystalline and ultrafine grained metals: A short overview. Computational Materials Science 96, 365–373.

Miyamoto, H., Ota, K., Mimaki, T., 2006. Viscous nature of deformation of ultra-fine grain aluminum processed by equal-channel angular pressing. Scripta Materialia 54, 1721–1725.

Modlinski, R., Witvrouw, A., Ratchev, P., Jourdain, A., Simons, V., Tilmans, H.A.C., Den Toonder, J.M.J., Puers, R., De Wolf, I., 2004a. Creep as a reliability problem in MEMS. Microelectronics Reliability 44, 1733–1738.

Modlinski, R., Witvrouw, A., Ratchev, P., Puers, R., Den Toonder, J.M.J., De Wolf, I., 2004b. Creep characterization of al alloy thin films for use in mems applications. Microelectronic Engineering 76, 272–278.

Mompiou, F., Legros, M., Boé, A., Coulombier, M., Raskin, J.P., Pardoen, T., 2013. Inter- and intragranular plasticity mechanisms in ultrafine-grained Al thin films: An in situ TEM study. Acta Materialia 61, 205–216.

Needleman, A., 1988. Continuum mechanics studies of plastic instabilities. Revue de Physique Appliquée 23, 585–593.

Nelder, J.A., Mead, R., 1965. A Simplex Method for Function Minimization. The Computer Journal 7, 308–313.

Nicola, L., Xiang, Y., Vlassak, J.J., Van der Giessen, E., Needleman, A., 2006. Plastic deformation of freestanding thin films: Experiments and modeling. Journal of the Mechanics and Physics of Solids 54, 2089–2110.

Niordson, C.F., Redanz, P., 2004. Size-effects in plane strain sheet-necking. Journal of the Mechanics and Physics of Solids 52, 2431–2454.

Niordson, C.F., Tvergaard, V., 2005. Instabilities in power law gradient hardening materials. International Journal of Solids and Structures 42, 2559–2573.

Nix, W.D., 1989. Mechanical Properties of Thin Films. Metallurgical and Materials Transactions A 20, 2217–2245.

Ono, K., 1968. Temperature Dependence of Dispersed Barrier Hardening. Journal of Applied Physics 39.

Pan, D., Nieh, T.G., Chen, M.W., 2006. Strengthening and softening of nanocrystalline nickel during multistep nanoindentation. Applied Physics Letters 88, 161922.

Pardoen, T., 2014. Size and rate dependent necking in thin metallic films. Journal of the Mechanics and Physics of Solids 62, 81–98.

Pardoen, T., Hachez, F., Marchioni, B., Blyth, P.H., Atkins, A.G., 2004. Mode I fracture of sheet metal. Journal of the Mechanics and Physics of Solids 52, 423–452.

Pineau, A., Amine Benzerga, A., Pardoen, T., 2016. Failure of metals III: Fracture and fatigue of nanostructured metallic materials. Acta Materialia 107, 508–544.

Prakash, V., Kaul, P.B., Park, J., Bifano, M.F., 2011. A novel device for in-situ nanomechanics of 1-D nanostructures. Jom 63, 49–56.

Raj, R., Ashby, M.F., 1971. On grain boundary sliding and diffusional creep. Metallurgical Transactions 2, 1113–1127.

Rajagopalan, J., Han, J., Saif, M., 2007. Plastic deformation recovery in freestanding nanocrystalline aluminum and gold thin films. Science 315, 1831–1834.

Rajagopalan, J., Han, J.H., Saif, M.T.a., 2008. Bauschinger effect in unpassivated freestanding nanoscale metal films. Scripta Materialia 59, 734–737.

Rajagopalan, J., Rentenberger, C., Peter Karnthaler, H., Dehm, G., Saif, M.T.A., 2010. In situ TEM study of microplasticity and Bauschinger effect in nanocrystalline metals. Acta Materialia 58, 4772–4782.

Ramesh, K., 2009. Nanomaterials: Mechanics and mechanisms. Springer US, Boston, MA.

Roters, F., Eisenlohr, P., Hantcherli, L., Tjahjanto, D.D., Bieler, T.R., Raabe, D., 2010. Overview of constitutive laws, kinematics, homogenization and multiscale methods in crystal plasticity finite-element modeling: Theory, experiments, applications. Acta Materialia 58, 1152–1211.

Rottmann, P.F., Hemker, K.J., 2017. Experimental quantification of mechanically induced boundary migration in nanocrystalline copper films. Acta Materialia 140, 46–55.

Rudnicki, J.W., Rice, J.R., 1975. Conditions for the localization of deformation in pressure-sensitive dilatant materials. Journal of the Mechanics and Physics of Solids 23, 371–394.

Rupert, T.J., Gianola, D.S., Gan, Y., Hemker, K.J., 2009. Experimental observations of stress-driven grain boundary migration. Science (New York, N.Y.) 326, 1686–1690.

Saada, G., Kruml, T., 2011. Deformation mechanisms of nanograined metallic polycrystals. Acta Materialia 59, 2565–2574.

Schiotz, J., Jacobsen, K.W., 2003. A Maximum in the Strength of Nanocrystalline Copper. Science 301, 1357–1359.

Schwaiger, R., Moser, B., Dao, M., Chollacoop, N., Suresh, S., 2003. Some critical experiments on the strain-rate sensitivity of nanocrystalline nickel. Acta Materialia 51, 5159–5172.

Segurado, J., Llorca, J., 2013. Simulation of the deformation of polycrystalline nanostructured Ti by computational homogenization. Computational Materials Science 76, 3–11.

Sergueeva, A.V., Mara, N.A., Mukherjee, A.K., 2007. Plasticity at really diminished length scales. Materials Science and Engineering A 463, 8–13.

Shan, Z., Stach, E.A., Wiezorek, J.M.K., Knapp, J.A., Follstaedt, D.M., Mao, S.X., 2004. Grain Boundary-Mediated Plasticity in Nanocrystalline Nickel. Science 305, 654–657.

Sharon, J.A., Padilla, H.A., Boyce, B.L., 2013. Interpreting the ductility of nanocrystalline metals. Journal of Materials Research 28, 1539–1552.

Sharpe, W., Yuan, B., Edwards, R., 1997. A new technique for measuring the mechanical properties of thin films. Journal of Microelectromechanical Systems 6, 193–199.

Shen, X., Lian, J., Jiang, Z., Jiang, Q., 2008a. High strength and high ductility of electrodeposited nanocrystalline Ni with a broad grain size distribution. Materials Science and Engineering: A 487, 410–416.

Shen, Y.F., Xue, W.Y., Wang, Y.D., Liu, Z.Y., Zuo, L., 2008b. Mechanical properties of nanocrystalline nickel films deposited by pulse plating. Surface and Coatings Technology 202, 5140–5145.

Shi, J., Zikry, M.A., 2009. Grain size, grain boundary sliding, and grain boundary interaction effects on nanocrystalline behavior. Materials Science and Engineering A 520, 121–133.

Signorelli, J.W., Bertinetti, M.A., Turner, P.A., 2009. Predictions of forming limit diagrams using a rate-dependent polycrystal self-consistent plasticity model. International Journal of Plasticity 25, 1–25.

Sim, G.d., Vlassak, J.J., 2014. High-temperature tensile behavior of freestanding Au thin films. Scripta Materialia 75, 34–37.

Sinclair, C.W., Poole, W.J., Bréchet, Y., 2006. A model for the grain size dependent work hardening of copper. Scripta Materialia 55, 739–742.

Šiška, F., Weygand, D., Forest, S., Gumbsch, P., 2009. Comparison of mechanical behaviour of thin film simulated by discrete dislocation dynamics and continuum crystal plasticity. Computational Materials Science 45, 793–799.

Skrotzki, W., Eschke, A., Jóni, B., Ungár, T., Tóth, L.S., Ivanisenko, Y., Kurmanaeva, L., 2013. New experimental insight into the mechanisms of nanoplasticity. Acta Materialia 61, 7271–7284.

Sluys, L.J., 1998. Computational Modelling of Localisation and Fracture, in: Perzyna, P. (Ed.), Localization and Fracture Phenomena in Inelastic Solids. Springer Vienna, Vienna, pp. 243–299.

Spearing, S.M., 2000. Materials issues in microelectromechanical systems (MEMS). Acta Materialia 48, 179–196.

Spearot, D.E., Tschopp, M.A., McDowell, D.L., 2009. Orientation and rate dependence of dislocation nucleation stress computed using molecular dynamics. Scripta Materialia 60, 675–678.

Sun, Z., Van Petegem, S., Cervellino, a., Durst, K., Blum, W., Van Swygenhoven, H., 2015. Dynamic recovery in nanocrystalline Ni. Acta Materialia 91, 91–100.

Suwas, S., Ray, R.K., 2014. Texture Evolution in Thin Films, in: Crystallographic Texture of Materials. Springer-Verlag. volume 88, pp. 179–194.

Swift, H., 1952. Plastic instability under plane stress. Journal of the Mechanics and Physics of Solids 1, 1–18.

Swygenhoven, H.V., Derlet, P.M., Frøseth, A.G., 2004. Stacking fault energies and slip in nanocrystalline metals. Nature Materials 3, 399–403.

Tang, F., Gianola, D.S., Moody, M.P., Hemker, K.J., Cairney, J.M., 2012. Observations of grain boundary impurities in nanocrystalline Al and their influence on microstructural stability and mechanical behaviour. Acta Materialia 60, 1038–1047.

Thompson, C., Carel, R., 1995. Texture development in polycrystalline thin films. Materials Science and Engineering: B 32, 211–219.

Tian, Y., Shibata, A., Zhang, Z., Tsuji, N., 2016. Ductility Sensitivity to Stacking Fault Energy and Grain Size in Cu–Al Alloys. Materials Research Letters 3831, 1–6.

Tóth, L.S., Hirsch, J., Van Houtte, P., 1996. On the role of texture development in the forming limits of sheet metals. International Journal of Mechanical Sciences 38, 1117–1126.

Tschopp, M.A., Spearot, D.E., McDowell, D.L., 2007. Atomistic simulations of homogeneous dislocation nucleation in single crystal copper. Modelling and Simulation in Materials Science and Engineering 15, 693–709.

Tsuchiya, T., Tabata, O., Sakata, J., Taga, Y., Siga, K., 1998. Specimen size effect on tensile strength of surface micromachined polycrystalline silicon thin films. J. Microelectromech. Syst. 7, 106–113.

Tummala, H., 2016. 3D discrete dislocation dynamics simulations of polycrystalline films and silicon electrostatics. Ph.D. thesis. Université Grenoble Alpes.

Tvergaard, V., 1993. Necking in tensile bars with rectangular cross-section. Computer Methods in Applied Mechanics and Engineering 103, 273–290.

Van Houtte, P., Li, S., Seefeldt, M., Delannay, L., 2005. Deformation texture prediction: From the Taylor model to the advanced Lamel model. International Journal of Plasticity 21, 589–624.

Van Petegem, S., Brandstetter, S., Van Swygenhoven, H., Martin, J.L., 2006. Internal and effective stresses in nanocrystalline electrodeposited Ni. Applied Physics Letters 89, 073102.

Van Swygenhoven, H., 2002. Grain Boundaries and Dislocations. Science 296, 66–67.

Van Swygenhoven, H., 2008. Footprints of plastic deformation in nanocrystalline metals. Materials Science and Engineering A 483-484, 33–39.

Van Swygenhoven, H., Caro, A., Farkas, D., 2001. Grain boundary structure and its influence on plastic deformation of polycrystalline FCC metals at the nanoscale: A molecular dynamics study. Scripta Materialia 44, 1513–1516.

Van Swygenhoven, H., Derlet, P.M., Frøseth, A.G., 2006. Nucleation and propagation of dislocations in nanocrystalline fcc metals. Acta Materialia 54, 1975–1983.

Van Swygenhoven, H., Farkas, D., Caro, A., 2000. Grain-boundary structures in polycrystalline metals at the nanoscale. Physical Review B 62, 831–838.

Van Swygenhoven, H., Spaczer, M., Caro, A., 1999. Microscopic description of plasticity in computer generated metallic nanophase samples: A comparison between Cu and Ni. Acta Materialia 47, 3117–3126.

Vayrette, R., Raskin, J.P., Pardoen, T., 2015. On-chip fracture testing of freestanding nanoscale materials. Engineering Fracture Mechanics 150, 222–238.

Velasco, M., Van Swygenhoven, H., Brandl, C., 2011. Coupled grain boundary motion in a nanocrystalline grain boundary network. Scripta Materialia 65, 151–154.

Venkatraman, R., Bravman, J.C., 1992. Separation of film thickness and grain boundary strengthening effects in Al thin films on Si. Journal of Materials Research 7, 2040–2048.

Viatkina, E.M., Brekelmans, W.A.M., Geers, M.G.D., 2005. A crystal plasticity based estimate for forming limit diagrams from textural inhomogeneities. Journal of Materials Processing Technology 168, 211–218.

Wang, B., Idrissi, H., Galceran, M., Colla, M.S., Turner, S., Hui, S., Raskin, J.P., Pardoen, T., Godet, S., Schryvers, D., 2012a. Advanced TEM investigation of the plasticity mechanisms in nanocrystalline freestanding palladium films with nanoscale twins. International Journal of Plasticity 37, 140–156.

Wang, B., Idrissi, H., Shi, H., Colla, M.S., Michotte, S., Raskin, J.P., Pardoen, T., Schryvers, D., 2012b. Texture-dependent twin formation in nanocrystalline thin Pd films. Scripta Materialia 66, 866–871.

Wang, L., Han, X., Liu, P., Yue, Y., Zhang, Z., Ma, E., 2010. In Situ observation of dislocation behavior in nanometer grains. Physical Review Letters 105, 1–4.

Wang, L., Xin, T., Kong, D., Shu, X., Chen, Y., Zhou, H., Teng, J., Zhang, Z., Zou, J., Han, X., 2017. In situ observation of stress induced grain boundary migration in nanocrystalline gold. Scripta Materialia 134, 95–99.

Wang, Y.J., Ishii, A., Ogata, S., 2013. Entropic effect on creep in nanocrystalline metals. Acta Materialia 61, 3866–3871.

Wang, Y.M., Hamza, A.V., Ma, E., 2006. Temperature-dependent strain rate sensitivity and activation volume of nanocrystalline Ni. Acta Materialia 54, 2715–2726.

Wang, Y.M., Ma, E., 2003. Temperature and strain rate effects on the strength and ductility of nanostructured copper. Applied Physics Letters 83, 3165.

Wang, Y.M., Ma, E., 2004. On the origin of ultrahigh cryogenic strength of nanocrystalline metals. Applied Physics Letters 85, 2750.

Warner, D.H., Molinari, J.F., 2006. A semi-discrete and non-local crystal plasticity model for nanocrystalline metals. Scripta Materialia 54, 1397–1402.

Wei, Q., 2007. Strain rate effects in the ultrafine grain and nanocrystalline regimes—influence on some constitutive responses. Journal of Materials Science 42, 1709–1727.

Wei, Y., Bower, A.F., Gao, H., 2008. Enhanced strain-rate sensitivity in fcc nanocrystals due to grain-boundary diffusion and sliding. Acta Materialia 56, 1741–1752.

Wei, Y., Gao, H., 2008. An elastic–viscoplastic model of deformation in nanocrystalline metals based on coupled mechanisms in grain boundaries and grain interiors. Materials Science and Engineering: A 478, 16–25.

Wei, Y., Su, C., Anand, L., 2006. A computational study of the mechanical behavior of nanocrystalline fcc metals. Acta Materialia 54, 3177–3190.

Woodford, D., 1969. Strain rate sensitivity as a measure of ductility. ASM Trans. Quart 62, 291–293.

Wu, X., Ma, E., Zhu, Y.T., 2007. Deformation defects in nanocrystalline nickel. Journal of Materials Science 42, 1427–1432.

Wu, X.L., Ma, E., 2006. Dislocations in nanocrystalline grains. Applied Physics Letters 88, 231911.

Wu, X.L., Zhu, Y.T., Wei, Y.G., Wei, Q., 2009. Strong Strain Hardening in Nanocrystalline Nickel. Phys. Rev. Lett. 103, 205504.

Xiang, Y., Vlassak, J.J., 2006. Bauschinger and size effects in thin-film plasticity. Acta Materialia 54, 5449–5460.

Yamakov, V., Wolf, D., Phillpot, S.R., Gleiter, H., 2002. Grain-boundary diffusion creep in nanocrystalline palladium by molecular-dynamics simulation. Acta Materialia 50, 61–73.

Yao, H., Cao, J., 2002. Prediction of forming limit curves using an anisotropic yield function with prestrain induced backstress. International Journal of Plasticity 18, 1013–1038.

Yoshinaga, N., Sugiura, N., Hiwatashi, S., Ushioda, K., Kada, O., 2008. Deep Drawability of Electro-deposited Pure Iron Having an Extremely Sharp ‹111›//ND Texture. ISIJ International 48, 667–670.

Yuan, R., Beyerlein, I.J., Zhou, C., 2015. Emergence of grain-size effects in nanocrystalline metals from statistical activation of discrete dislocation sources. Acta Materialia 90, 169–181.

Zhang, K., Weertman, J.R., Eastman, J.A., 2005. Rapid stress-driven grain coarsening in nanocrystalline Cu at ambient and cryogenic temperatures. Applied Physics Letters 87, 1–4.

Zhao, Y.H., Guo, Y.Z., Wei, Q., Dangelewicz, A.M., Xu, C., Zhu, Y.T., Langdon, T.G., Zhou, Y.Z., Lavernia, E.J., 2008. Influence of specimen dimensions on the tensile behavior of ultrafine-grained Cu. Scripta Materialia 59, 627–630.

Zhu, B., Asaro, R.J., Krysl, P., Bailey, R., 2005. Transition of deformation mechanisms and its connection to grain size distribution in nanocrystalline metals. Acta Materialia 53, 4825–4838.

Zhu, B., Asaro, R.J., Krysl, P., Zhang, K., Weertman, J.R., 2006. Effects of grain size distribution on the mechanical response of nanocrystalline metals: Part II. Acta Materialia 54, 3307–3320.

Zhu, L., Ruan, H., Li, X., Dao, M., Gao, H., Lu, J., 2011. Modeling grain size dependent optimal twin spacing for achieving ultimate high strength and related high ductility in nanotwinned metals. Acta Materialia 59, 5544–5557.

Zhu, T., Li, J., Samanta, A., Kim, H.G., Suresh, S., 2007. Interfacial plasticity governs strain rate sensitivity and ductility in nanostructured metals. Proceedings of the National Academy of Sciences of the United States of America 104, 3031–6.

Zhu, Y.T., Liao, X.Z., Wu, X.L., 2008. Deformation twinning in bulk nanocrystalline metals: Experimental observations. Jom 60, 60–64.

Zhu, Y.T., Liao, X.Z., Wu, X.L., 2012. Deformation twinning in nanocrystalline materials. Progress in Materials Science 57, 1–62.